

Lorenza Brusini

# Brain Microstructure: Impact of the Permeability on Diffusion MRI

Ph.D. Thesis

April 4, 2018

Università degli Studi di Verona  
Dipartimento di Informatica

Advisor:  
prof. Gloria Menegaz

Series N°: TD-02-18

Università di Verona  
Dipartimento di Informatica  
Strada le Grazie 15, 37134 Verona  
Italy

*To Fabio,  
because you are my roadmate in the travel of life*



---

## Abstract

Diffusion Magnetic Resonance Imaging (dMRI) enables a non invasive *in-vivo* characterization of the brain tissue. The disentanglement of each microstructural property reflected on the total dMRI signal is one of the hottest topics in the field. The dMRI reconstruction techniques ground on assumptions on the signal model and consider the neurons axons as impermeable cylinders. Nevertheless, interactions with the environment is characteristic of the biological life and diffusional water exchange takes place through cell membranes. Myelin wraps axons with multiple layers constitute a barrier modulating exchange between the axon and the extracellular tissue. Due to the short transverse relaxation time ( $T_2$ ) of water trapped between sheets, myelin contribution to the diffusion signal is often neglected. This thesis aims to explore how the exchange influences the dMRI signal and how this can be informative on myelin structure. We also aimed to explore how recent dMRI signal reconstruction techniques could be applied in clinics proposing a strategy for investigating the potential as biomarkers of the derived tissue descriptors.

The first goal of the thesis was addressed performing Monte Carlo simulations of a system with three compartments: intra-axonal, spiraling myelin and extra-axonal. The experiments showed that the exchange time between intra- and extra-axonal compartments was on the sub-second level (and thus possibly observable) for geometries with small axon diameter and low number of wraps such as in the infant brain and in demyelinating diseases. The second goal of the thesis was reached by assessing the indices derived from three dimensional simple harmonics oscillator-based reconstruction and estimation (3D-SHORE) in stroke disease. The tract-based analysis involving motor networks and the region-based analysis in grey matter (GM) were performed. 3D-SHORE indices proved to be sensitive to plasticity in both white matter (WM) and GM, highlighting their viability as biomarkers in ischemic stroke.

The overall study could be considered the starting point for a future investigation of the interdependence of different phenomena like exchange and relaxation related to the established dMRI indices. This is valuable for the accurate dMRI data interpretation in heterogeneous tissues and different physiological conditions.



---

# Contents

---

## Part I Introduction

---

<b>1</b>	<b>Introduction</b> . . . . .	3
1.1	Diffusion MRI signal modeling and clinical applications . . . . .	3
1.2	Aims of the thesis . . . . .	4
1.3	Main contributions . . . . .	5
1.4	Thesis structure . . . . .	6
1.5	Publications . . . . .	7
<b>2</b>	<b>Background</b> . . . . .	9
2.1	Neuroanatomy . . . . .	9
2.2	Diffusion MRI . . . . .	13
2.2.1	The diffusion process . . . . .	13
2.2.2	Diffusion in cerebral tissues . . . . .	14
2.2.3	The diffusion acquisition . . . . .	15
2.2.4	The propagator formalism . . . . .	18
<b>3</b>	<b>State of the Art</b> . . . . .	21
3.1	Signal reconstruction models in diffusion MRI . . . . .	21
3.1.1	Signal models . . . . .	21
3.1.2	Compartmental models . . . . .	29
3.2	Permeability in dMRI . . . . .	31
3.2.1	Surface relaxivity . . . . .	32
3.2.2	Kärger model . . . . .	38
3.2.3	Other strategies . . . . .	39
3.2.4	Numerical simulation . . . . .	39
3.2.5	The issue of observability . . . . .	40
3.3	Scientific objectives . . . . .	41
3.3.1	Theoretical objectives . . . . .	41
3.3.2	Clinical objectives . . . . .	41

---

## Part II Signal modeling in Diffusion MRI

---

<b>4</b>	<b>Materials and methods</b> .....	45
4.1	Premises .....	45
4.2	Rationale .....	46
4.3	Methods .....	48
4.3.1	Geometry and water dynamics setup .....	48
4.3.2	Estimation of observable $\tau$ .....	51
4.3.3	Signal decay .....	52
4.3.4	Model fitting .....	53
<b>5</b>	<b>Results and discussion</b> .....	55
5.1	Monte Carlo simulator validation .....	55
5.2	Results .....	57
5.2.1	Estimation of observable $\tau$ .....	57
5.2.2	Signal decay .....	58
5.2.3	RD and RK estimates .....	59
5.2.4	$\tau$ estimation .....	60
5.3	Discussion .....	61
5.3.1	Estimation of observable $\tau$ .....	65
5.3.2	Signal decay .....	66
5.3.3	RD and RK estimates .....	67
5.3.4	$\tau$ estimation .....	67
5.3.5	Limitations and bottlenecks .....	68

---

### Part III Clinical applications

---

<b>6</b>	<b>Application: stroke characterization through dMRI indices</b> ....	71
6.1	MRI in stroke disease .....	71
6.2	Materials and methods .....	74
6.3	Signal modeling and microstructural indices derivation .....	74
6.4	Dataset .....	77
6.5	Image preprocessing .....	79
6.5.1	Tract-based analysis on WM tissue .....	79
6.5.2	Region-based analysis on GM tissue .....	80
6.6	Statistical analysis .....	80
6.6.1	Preliminary study .....	80
6.6.2	Networks study .....	82
6.6.3	Comparison between 3D-SHORE indices and tensor FA and MD .....	83
<b>7</b>	<b>Results and discussion</b> .....	87
7.1	Preliminary study .....	87
7.2	Networks study .....	90
7.2.1	Precision of the measurements .....	90
7.2.2	Comparison of absolute indices changes in patients and controls .....	92
7.2.3	Predictive models .....	95
7.3	Comparison between 3D-SHORE indices and tensor FA and MD ..	98



7.3.1 Qualitative assessment of dMRI-based indices ..... 98

7.3.2 Precision of the measurements .....100

7.3.3 Comparison of absolute indices changes in patients and  
controls .....101

7.3.4 Predictive models .....102

7.3.5 Statistical analysis on GM region-based outcomes .....103

7.4 Discussion .....106

7.4.1 Networks study .....106

7.4.2 Comparison between 3D-SHORE indices and tensor FA  
and MD .....110

---

**Part IV Conclusions and achievements**

---

**8 Thesis contributions, open issues and future works** .....119

8.1 Thesis contributions .....119

8.2 Future work .....121

8.3 Achievements .....122

8.4 Publications .....123

**A Appendix** .....127

**References** .....194



## **Part I**

---

### **Introduction**



## Introduction

In the first Chapter of this thesis we briefly introduce the motivations at the basis of this investigation, giving an idea of why the questions here addressed are exciting from both a scientific and a clinical point of view. We also present the aims and main contributions of the work to easily guide the reader into the comprehension of the implications of this study. We finally provide the description of the thesis structure to further aid the reading of the manuscript and the list of publications.

### 1.1 Diffusion MRI signal modeling and clinical applications

The brain is often considered to be the most complex organ of the human being. Its investigation is a fascinating work if we think that it is the control center of our body, of all our actions making us in relationship with the others and with the environment.

In this *scenario*, diffusion magnetic resonance imaging (dMRI) is an important technique to observe the human brain as it is able to capture a view in a non-invasively way. The acquired signal is proportional to water diffusion inside the brain thanks to a particular MRI sequence that in its simplest form employs two gradient pulses in addition to two radiofrequencies (RF). In particular, the combination with mathematical models leads to information extraction from hindrance to the Brownian motion of water molecules from the brain tissue structure. The solution of the inverse problem consents to derive some microstructure measures of the neural environments thanks to the relationship existing between the signal and the ensemble average probability (EAP) of spins displacement within a time interval. The dMRI was firstly introduced by Le Bihan and colleagues in 1985 [130] and rapidly captured the interest of the community. In the following years, many models were developed in order to obtain images of the brain which could be informative about its structure, as well as clinically useful.

Three main big scale objectives are currently pursued: microstructural modeling, structural connectivity and encoding strategies improving. The first aims at the definition of numerical biomarkers. The second targets the definition of the topology of the structural network through the exploitation of the orientation distribution function (ODF), the elementary building block of the tractogram.

The last points at the design of new acquisition sequences with the purpose to increase the specificity of dMRI. Concerning the first, there is a wide variety of indices derivable thanks to signal modeling such as the apparent diffusion coefficient (*ADC*) and the fractional anisotropy (*FA*). These were largely used for comparing and differentiating patients and healthy subjects with diffusion tensor modeling, one of the initial reconstruction methods for the dMRI signal. The calculation of alternative models and indices further aided in understanding diseases from the structural point of view. Tractography is the reconstruction of fiber tracts connecting the various cerebral areas by tracking peaks extracted from the ODFs and it is actually used in surgical planning as well as the basis for pathoconnectomics.

Focusing on microstructural mapping, it must be said that dMRI is evidently sensible to microstructural changes but it is not specific [168, 72]. In one voxel having size of the order of millimeters a lot of different biological structures having size in the order of micrometric scale are present: axons, *somas*, glial cells, free fluid, extracellular tissue, astrocytes as well as others. All these compartments contribute to the overall dMRI signal although with potential different diffusivities, stressing the complexity of resolving the inverse problem that aims to understand the tissue microstructure beyond the signal.

Moreover, the reconstruction models rely on assumptions such as constraining the dMRI signal to a multivariate Gaussian described by one tensor, as in diffusion tensor imaging (DTI); considering a predefined number of compartments; assuming no exchange between intra- and extra-axonal compartments and many others. Despite these assumptions, relevant information could be extracted from models, mirroring the structure and microstructure of the brain. However, the huge complexity of brain tissue must be accounted for in the interpretation of the reconstructed dMRI data, being aware of the inherent limitations of the models and addressing the issue of their reliability.

In this thesis, we aimed at casting light to some of these issues.

## 1.2 Aims of the thesis

In this thesis one of the focuses is on the assumption most often used that is the impermeability of compartment walls in white matter modeling. Myelin is a membranous structure that wraps axons with multiple lipid bilayers [75, 164]. Water in the myelin fills the space left between the bilayers, which MRI has the potential to detect. However, the short relaxation time ( $T_2$ ) [222] makes this task particularly difficult, especially using clinical sequences [8]. For this reason, many signal models used to analyse dMRI data make the assumption that myelin does not contribute to the observed signal. Nevertheless, myelin plays an important role in shaping the signal because it constitutes a significant barrier to the exchange of water molecules from the intra to extra-axonal spaces. In addition, the measure of the exchange time is still an open issue in the literature. When the exchange has been incorporated in the analysis of white matter (WM) dMRI data, a wide range of estimated exchange times was recovered. Nilsson et al. [152] found exchange times in healthy WM in the order of seconds (1.25 – 2.5 s) whereas Nedjati-Gilani et al. [146] found values in the subsecond range (0.5 – 0.6 s). Thus, the first main

aim of this work was to investigate the plausibility conditions of the no-exchange assumption as previously described and to contribute a method for the estimation of the exchange time.

On the same line, this thesis aimed at assessing the myelin structure via exchange studies in dMRI experiments. As a biological barrier, myelin can modify the exchange flux and thus cause a sensible change in dMRI signal implicitly reflecting its geometry. More in detail, this work goes further in the modeling of myelin structure in order to explore the conditions or configurations under which the myelin wrapping permits fast exchange, that is in the sub-second scale. This could be an important prior for guiding the interpretation of dMRI studies involving an altered myelin structure such as during the development of the human brain [54] and in demyelinating diseases like myelinoclastic disorders (e.g. multiple sclerosis) and leukodystrophies (e.g. vitamin B12 deficiency) [126] and thus holds a great translational potential.

The second main aim of the thesis was to address the wide field of computed aid to clinical activity. In particular, we specifically focused on one dMRI signal reconstruction model called three dimensional simple harmonics oscillator-based reconstruction and estimation (3D-SHORE), for its capability in deriving a closed-form analytical derivation of both the signal and the Ensemble Average Propagator (EAP). Some interesting brain microstructure descriptors can be derived grounding on the probability of no net water particles displacement during the time occurring between the gradients of the diffusion weighted imaging (DWI) acquisition. These indices were not fully characterized so far for their ability in differentiating pathological tissues. An extensive study was performed for capturing the contralateral axonal remodeling in case of ischemic stroke [94, 135]. The analysis of their reproducibility, specificity and sensitivity is essential for assessing their exploitability as clinical biomarkers.

Overall, this thesis aimed at shedding light on the plausibility of the assumption of no exchange through the axonal walls and on the conditions for the detectability of such a mechanism, as well as to contributing a pipeline for the assessment of the suitability of microstructural measures as numerical biomarkers. In this way, a complete analysis framework could be defined starting from the acquisition and ending with the assessment of the exploitability of the measures for prognostic purposes. To this end, ischemic stroke was considered as a case study, relying on microstructural features derived under the no-exchange assumption, but the developed framework could be easily adapted to demyelinating diseases relying on new microstructure measure, which is the long-term target of this research and is left for future work.

### 1.3 Main contributions

The main contributions of this thesis are here synthesized.

- **Review of permeability concepts in dMRI**

One contribution of the thesis is a review of the permeability concepts in dMRI that is not actually easily understandable from the literature. In particular, the

concepts involving both the walls relaxivity, the exchange, their relationship and their related models in the state of the art are here reported.

- **Assessment of the plausibility of white matter modeling assumptions**  
Specifically focusing on signal reconstruction assumptions regarding permeability, we provide evidence for their unsuitability in some conditions. Since these conditions reflect particular physiological states, this work emphasizes the importance of a strict collaboration between clinicians and computer scientists for discerning the most effective solution aiming at *ad personam* healthcare.
- **Characterization of dMRI sensitivity to myelin multi-wrappings features via exchange-based studies**

The Monte Carlo simulations under the pulsed gradient stimulated echoes (PG-STE) acquisition scheme followed by reconstruction with diffusion signal models shed light on the relationship between myelin and exchange between intra-axonal and extracellular spaces. In particular, we identify some possible myelin structure conditions where exchange could occur from intra-axonal space towards extracellular tissue.

- **3D-SHORE indices characterization as biomarkers**  
Another contribution of the thesis is the exploitation of 3D-SHORE-based indices in describing *in-vivo* healthy and pathological brain tissues in ischemic stroke disease. More in detail, for the first time is provided their sensitivity to contralateral brain remodeling focusing on cortical and subcortical networks.
  - **Pipeline for biomarker suitability analysis**  
Along with the previous characterization, another contribution is the modality of analysis of the 3D-SHORE indices precision, sensitivity, specificity and predictability of motor outcome proposed for the first time.
  - **Representation by 3D-SHORE indices of different tissues**  
3D-SHORE indices were analysed in white matter (WM) tracts and grey matter (GM) in parallel, proving to be suitable in probing plasticity. Based on this, we could provide additional viability as a novel family of biomarkers.

## 1.4 Thesis structure

This thesis is organized in four main parts. Part I delineates the overall objective, clarifies the central idea of the work and summarizes the main contributions that have been reached (Chapter 1). The background and the state of the art are successively presented in the following two Chapters (Chapters 2 and 3). Part II of the thesis consists of two Chapters (Chapters 4 and 5) targeting the investigation of the exchange mechanisms in the white matter as well as the characterization of the role of the myelin sheet. Moreover, some general considerations about the assumptions usually done in dMRI reconstruction methods are reported along with results. In particular, a numerical method consisting on Monte Carlo simulations is proposed to address these issues, and signal reconstruction models are used to study the induced variations in the estimated parameters.

Part III consists of two chapters (Chapters 6 and 7) in which a wide tract-based study is proposed along with a statistical analysis aiming at exploring the potential of the considered microstructural indices as biomarkers in stroke disease.



More in detail, the diffusion tensor and the 3D-SHORE models were considered opening the way to a future application for exchange models. In addition, a first attempt to use 3D-SHORE indices for characterizing GM plasticity is proposed.

Finally, Part IV derives the conclusions (Chapter 8), summarizes the main open issues and provides some hints for future works.

## 1.5 Publications

The work presented in this thesis was published or submitted to international peer-reviewed journals and international and national conferences.

More in details, the contributions on permeability presented in Chapter 4 and Chapter 5 are mainly represented in [39] as well as in a submitted paper to the European Signal Processing Conference (EUSIPCO) in 2018 and in a journal under submission for the IEEE Transactions on Medical Imaging.

The results on stroke studies by 3D-SHORE indices reported in Chapter 6 and Chapter 5 were published in [229, 37, 156, 38, 31].



## Background

This chapter provides the fundamentals for the two main issues touched by this work: neuroanatomy and dMRI. First, the neuroanatomical perspective is illustrated, starting from the description of the brain to get to the discussion of permeability in the white matter. Successively, the diffusion process is illustrated and the main technical issues of dMRI are briefly illustrated.

### 2.1 Neuroanatomy

The nervous system is basically the control center of the body and all the things that make us in communication with the environment (e.g. eating, sleeping, thinking, moving, etc.). The nervous system is made up of a network of specialized cells called neurons that send and receive signals throughout the body quite rapidly and that we investigate more in detail in the subsequently paragraphs. There are two main parts composing the nervous system: the central nervous system (CNS) and the peripheral nervous system (PNS). The brain and the spinal cord constitute the first, while nerves and ganglia outside the CNS constitute the second one [70]. Exemplifying, the brain communicates with the nerves via the spinal cord receiving sensory informations, integrating them and sending informations in turn. The CNS has four fundamental structures that are common to many species comprising the human: the forebrain, the midbrain, the hindbrain and the spinal cord. Focusing on the first three that constitute the parts on which we are more interested, seventeen structures can be recognized. The first four are the brainstem, the cerebellum, the thalamus and the cerebrum. The brainstem is substantially devoted to involuntary actions like breathing, circulation or digestion and it is the switching center for information from sensory nerves and directed to motor nerves. It includes three parts: the medulla oblongata, the pons and the midbrain. The cerebellum is dedicated to body control and motion memory. The thalamus sorts data and determines where they should go, while a part of it called hypothalamus is principally responsible for homeostasis (e.g. body temperature). Another one called posterior pituitary is a site for the secretion of neurohypophysial hormones (oxytocin and vasopressin) directly into the blood. The cerebrum has the principal function of data integration. It is made up of two hemispheres connected by an

ensemble of nerves called corpus callosum. Below the corpus callosum there are the basal ganglia, constituted by bunches of nuclei with the same function that control different motor actions. Finally the cerebral cortex ( $\sim 80\%$  of the brain) consists of four lobes: the frontal lobe mainly committed to emotional control, the parietal lobe substantially responsible for sensation, the occipital lobe for the vision and the temporal lobe for tasks like language, hearing, memory and many others. Interestingly, on the parietal lobe with the somatosensory cortex and on the motor cortex located on the other side of the gyrus in the frontal lobe, there is the cortical *homunculus* which is a mapping of each part of the body on the brain meaning that there is a dedicated portion of the cortex for controlling each part of our body. In general, the brain can be thought as divided in parts gathering neurons having cytoarchitecture similarity. Alternatively it can be thought divided in parts sharing functional features or again relying on their anatomical localization on the brain structure as well as other similarities [162, 9, 33]. The relationship between structure and function opens the way to exciting investigations of the connections between bunches of neurons leading to the study of structural and functional networks, as well as of their interactions [162, 9, 33].

As previously mentioned, the neuron is the cell constituting the fundamental unit composing the nervous system and is the most complex cell of our organism. Its function is the receiving and sending of informations in a dense communication network. The neuron receives *stimuli* from the environment (e.g. sight, touch, etc.) or from the organism itself (e.g. visceral pain). The parts composing the neuron are the *soma* which is the body of the neuron containing the *nucleus*; the dendrites that are extensions from *soma* creating branchings and for this reason also called dendritic tree (in fact some dendrites originate from *soma*, other from other dendrites); and the axon, which originates from *soma* and is unique. Regarding the information flux, the dendrites are the structures devoted for receiving while the axon is the structure dedicated for sending informations to other neurons through synapses and to muscles. The *soma* of neurons are in high concentration in the cortex that is also called the GM, while the WM is mainly made up of axons.

Going into detail of axons composing the WM, it was shown that they are not limited to drive informations from one point to another, but they process information in at least two or three different domains [109]. The first is the spatial and amplification domain: spatial because the axon maps the position of the cell body into the position of the number of terminals in the area where it terminates, and amplification because not all the terminations receive the same number of synaptic buttons and thus the signal is amplified differentially [107]. The second is the temporal domain because the axons convey the informations to the target in a certain specified time that could be different also for different terminals of the same axon [111]. It is important in the context of axons the role of electricity conduction. Concerning this, Gasser and Erlanger [86] proposed a classification showing that there exists a sort of relationship between average fiber diameters and conduction velocity, added to the type of information they carry. The dMRI potential to recover the axon structure morphology becomes even more fundamental to understand the way this system works. In detail, the morphological basis of temporal computation in axons is  $v = (5.5/g) \times d_{\text{inner}}$  ( $v$  is the velocity,  $d_{\text{inner}}$  is the inner diameter of the axon,  $g$  is the  $g$ -ratio) [108]. The myelin is an important

tissue as it defines the  $g$ -ratio as  $g = d_{\text{inner}}/D_{\text{outer}}$  ( $D_{\text{outer}}$  is the axon diameter comprehensive of myelin). In the CNS there is a very wide spectrum of axon diameters, e.g. in the mouse we can find the peak of the distribution indicating the mean around  $1.0 \mu\text{m}$  while monkey shows also larger axons. Also humans show many differences in axon diameters as will be detailed in what follows.

Studying the evolution of the fiber tracts, two determining phenomena occurred in parallel: the loss of unmyelinated axons and the increase in number of all the axons in the same way. Many of these axons are less than  $2.0 \mu\text{m}$  as showed in [109] and the  $g$ -ratio is interestingly stable across animal systems and across different animals ( $\sim 0.68 - 0.69$ ) and also across diameters ( $\sim 0.71 \mu\text{m}$  in monkey and  $\sim 0.69 \mu\text{m}$  in mouse). In the calculation of the conduction velocity we thus don't need to take the  $g$ -ratio strongly into account. The corpus callosum also reflects the variety of fiber diameters enclosing finer axons arriving from prefrontal cortex and thicker axons from motor cortex [1], emphasizing that different cortical areas communicate through the corpus callosum with different axonal systems of different diameters [197]. In particular, thinner axons connect prefrontal, parietal and temporal association areas while thicker axons connect primary motor, somatosensory and visual areas. Aboitiz and colleagues [1] calculated the distribution of sizes in regions of the human corpus callosum and recovered average diameters around  $4.0 \mu\text{m}$  in genu,  $6.9 \mu\text{m}$  in midbody and  $3.6 \mu\text{m}$  in splenium. In a more recent work, Innocenti et al. found a diameter median value of  $0.89 \mu\text{m}$  in the planum temporal sector of the human corpus callosum [110]. Liewald et al. [133] confirmed this finding measuring the sizes of cortico-cortical fibers and obtaining diameters in a range of  $0.16 - 9 \mu\text{m}$  with average  $< 1 \mu\text{m}$ . Most of these axons are myelinated and only the prefrontal axons in monkey seem to be unmyelinated. The relationship between conduction velocity and diameters determines that there are some areas with faster conduction and other ones with slower conduction. Studying the generated delay ( $delay = L_p/v$ ) requires to employ the length of the pathways ( $L_p$ ) and thus its reconstruction by tracer injection followed step by step from origin to end, which is a very difficult work. In this respect tractography could be of great help once its accuracy and specificity have been demonstrated [49]. This computation can further help to disentangle the structure of the network since big differences were found from callosal midline emphasizing a higher delay than expected, while shorter delays were found in motor and somatosensory areas [50]. The connectome could thus be improved not only by finding which areas connect to which, but also taking into account diameters, that may lead to more informative networks. From this point of view, it seems that the size of axons from the same area can be different for different targets, highlighting in this example a sort of advantage for motor and somatosensory connections. These and other morphological aspects can improve the knowledge about the nervous system and dMRI seems to be on the way of providing some of these estimates *in-vivo* providing crucial information on computational properties of the neurons.

As previously mentioned, a biological structure strictly related to axon is the myelin. The myelin structure is represented in Figure 2.1 and it is an insulatory layer surrounding the axon of neurons that helps the electrical signal travelling more efficiently and quickly along the axon thanks to gaps called nodes of Ranvier, where the axon is exposed to extracellular space. The myelin posed between

the nodes of Ranvier is called internode and the ensemble of internodes lead to a saltatory conduction that makes the transmission faster. The length of an internode goes from  $100.0 \mu\text{m}$  to  $2.0 \text{ mm}$  functionally changing the signal transmission velocity in the axons. In the PNS each internode is constituted by a Schwann cell that wraps the axon in a multilamellar conformation, while in the CNS the myelin is formed by an oligodendrocyte that can construct many internodes of several neurons always wrapping the axon in multiple turns. In this context, it is easily understandable how myelin is a cell with its cytoplasm and membrane forming layers with an almost known structure as illustrated in Figure 2.1. In a theoretical work of 1951, Rushton demonstrated that the conduction velocity is maximal when the  $g$ -ratio is 0.6 [178]. Albert et al. measured the  $g$ -ratio of healthy subjects along with multiple sclerosis patients finding a value of 0.65 in the firsts and a value of 0.76 in axons remyelinated by the repair attempt of the seconds [3]. Edgar and Griffiths reported normal  $g$ -ratios in a range of  $0.6 - 0.7$  [75], while Innocenti reported a theoretical work of the 70s according to which the  $g$ -ratio is a *quasi*-constant parameter with value 0.71 in the monkey and  $0.68 - 0.69$  in the mouse [108]. It is possible to calculate the number of myelin wraps relying on the simple calculation of the myelin thickness  $m_t$  as:

$$m_t = \frac{d_{\text{inner}}(\frac{1}{g} - 1)}{2}, \quad (2.1)$$

and dividing it by one myelin unit depth of  $210 \text{ \AA}$ [164]. Considering an axon diameter of  $0.9 \mu\text{m}$  and  $g$ -ratio of 0.6, 0.65, 0.7 and 0.75, the respective resulting number of wraps is  $\sim 14, 11, 9$  and  $7$ . In the cells membranes of the brain are present water-channel proteins called aquaporins that can modify the membranes permeability to water. In general the topic of permeability and thus also of exchange is important for life as one of its fundamental characteristics beyond being informative about the membrane itself. In this case, studying the possible exchange mechanisms mediated by myelin is an important step in its structure and role understanding.

Several techniques were used to calculate the membrane permeability of the mammalian red blood cell such as diffusion NMR,  $\text{Mn}^{2+}$  doping  $^1\text{H}$  NMR method and diffusion studies with magnetic field inhomogeneity. They all provided similar results, finding a high permeability in the range of  $49 - 112 \mu\text{m/s}$  at  $37^\circ$  in various species. More directly speaking of exchange and in particular of exchange time ( $\tau$ ), to the best of our knowledge it is difficult to find a clear reference for human brain  $\tau$  validated from literature. It was sometimes referred to Pfeuffer et al. [167] and more usually to Quirk's group work [172]: in the first case  $\tau$  was estimated around  $50 \text{ ms}$  through Kärger model fitting to pulsed gradient spin echoes (PGSE) experiments on perfused glial cells; in the second one  $\tau$  was recovered to be around  $550 \text{ ms}$  via Bloch-McConnell exchange modeling of longitudinal relaxation experiments of *in-vivo* rats with injected MR relaxation agent into the extracellular space. More recently, Dortch et al. [71] recovered  $\tau$  in rat optic nerve and frog sciatic nerve *ex-vivo* tissues directly via Relaxation Exchange Spectroscopy (REXS) and found a value of  $138 \pm 15 \text{ ms}$  and  $2046 \pm 140 \text{ ms}$  respectively. When the exchange has been incorporated in the analysis of WM dMRI data, Nilsson et al. found exchange times in healthy white matter in the order of seconds ( $1.25 - 2.5 \text{ s}$ ) using Filtered

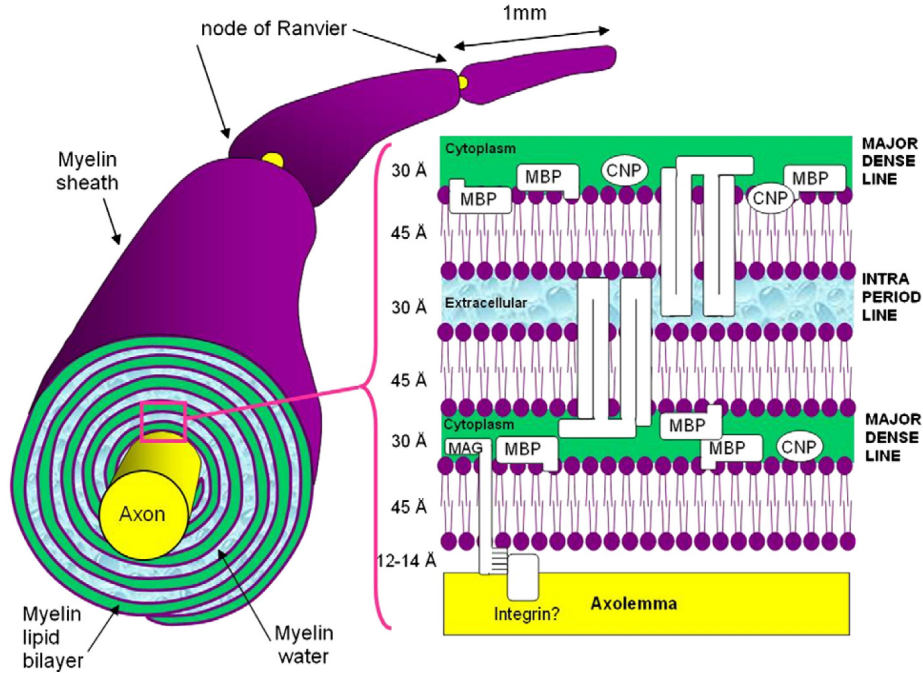


Fig. 2.1: Illustration of myelin structure from the work of Laule and colleagues [129]. An axon wrapped by myelin is shown along with a representation of one myelin bilayer unit.

EXchange Imaging (FEXI) [152] whereas Nedjati-Gilani et al. found values in the subsecond range (0.5 – 0.6 s) using a random forest regressor trained on Monte Carlo simulations [146]. It is evident how this issue is still to solve and requires a wider investigation to disentangle the permeability role in brain diffusion modeling and physiological knowledge.

## 2.2 Diffusion MRI

### 2.2.1 The diffusion process

In 1855, Robert Brown observed the grains of pollen of a plant suspended in water under a microscope and realized that they accomplished a random motion now called Brownian motion [35]. The same physical phenomenon was observed also for water particles which move with microscopic movements without requiring an initial action and without generating a flux, in a scenario called diffusion process. The diffusion coefficient ( $D$ ) describes how fast the molecules diffuse. In 1905, Einstein related the diffusion process to the mean squared displacement [76]:

$$\langle r^2 \rangle = 2DT_D, \quad (2.2)$$

where  $\langle r^2 \rangle$  is the mean squared displacement and  $T_D$  is the time along which it is observed. The  $D$  parameter determines the variance of the displacement distribution describing the observed diffusion process. In case of free diffusion, the longer is  $T_D$  and the higher is the distance displaced by the diffusion process. In restricted diffusion we have the same effect as in free diffusion if observed in short  $T_D$  but for long  $T_D$  the size of the medium makes the process independent from time. In the last context of restriction, if we are able to obtain  $D$  we could extract geometrical information of the medium in which diffusion takes place because of the relationship in Equation 2.2. For this reason is particularly interesting to obtain  $D$  for different  $T_D$ .

### 2.2.2 Diffusion in cerebral tissues

More in detail, the diffusion coefficient for water at 37° is known to be  $3.0 \mu\text{m}^2/\text{ms}$  for free diffusion, while the reduced diffusivity in restricted compartments like in brain tissue becomes informative about the microstructure. The difference between free diffusivity and the diffusivity in a complex medium made up of several barriers provides information on the restriction due to geometrical constraints. In fact, brain tissue as every biological tissue is a highly heterogeneous media consisting of several compartments and barriers leading to different “apparent” diffusivities where exchange can happen and/or where relaxation differences can occur all resulting in one “apparent diffusivity” per voxel. The overall diffusion coefficient obtained by diffusion encoding and resulting from a voxel in the brain is lower than that for free diffusion and is called apparent diffusion coefficient (*ADC*). Looking at the cytohistologic architecture of a biological tissue, it can be generalized as a set of compartments all connected in an arrangement remembering a network. Focusing on the neuronal tissue, the fibrillar structure of the WM consents to assume the nervous tracts as consisting of bundles of packed axons all aligned in a specific direction as cylinders with free diffusion along the axis and restriction in the transversal plane forming the anisotropic signal in dMRI. On the other side, the GM composed by bunches of neurons *soma* can be assimilated to pores permitting a more free diffusion compared to axons. The CSF present in the cavities of brain is characterized by fluid free to diffuse and consequently reasonably regarded as a compartment where the diffusivity can take place. However, the brain tissue is much more complex of what just reported (as illustrated in Figure 2.2) and attention must be paid in resolving of the inverse problem that allows the derivation of the microenvironments description. Due to this complexity, diffusion in brain tissue is usually considered non-Gaussian, term that needs to be clarified. In fact, Gaussian diffusion refers to the case where the displacement probability during diffusion process is Gaussian and thus has a variance that increases linearly with time. This means that there is a single type of diffusing particles and that there are no barriers to the diffusion and it can be referred to as time independent. Non-Gaussian diffusion in brain tissue may arise due to time-dependent diffusion and/or due to multiple compartments. The non-Gaussian behaviour in the first case is due to the variance of the displacement probability during the diffusion process limited by the structure, in the second case the non-Gaussian behaviour of the system is considered due to the heterogeneity of the tissue which can be con-



stituted by different types of particles, all with approximately Gaussian diffusion (i.e. multi-Gaussian).

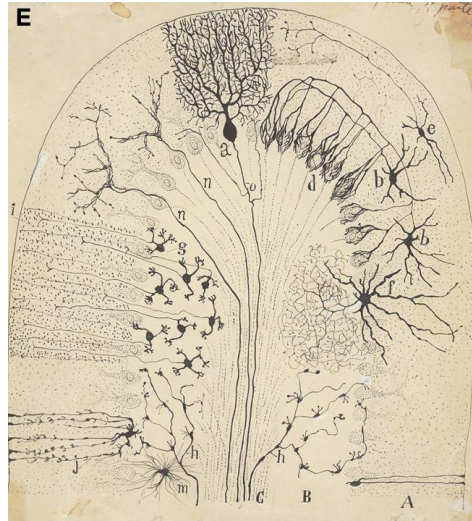


Fig. 2.2: Representation of the neural tissue complexity by the Nobel prize for medicine in 1906 Santiago Ramón y Cajal.

### 2.2.3 The diffusion acquisition

The MRI images ground on the signal emitted by hydrogen nuclei. Their magnetic dipoles, referred to as spins, align with the static magnetic field  $B_0$  generated by the clinical scanner and the perturbations of these alignments through RF and magnetic field gradients are proportional to the detected signal. The RF pulses rotate the spins away from  $B_0$  and the transverse precessing part of the spins contributes to the macroscopic magnetization that decays exponentially with a so-called  $T_2$  time, while the spins realign in  $B_0$  direction with  $T_1$  time, both depending on the tissue composition (mainly determined by the water and fat components). The first is typically on the order of 100 ms, while the second is typically on the order of 1 s [170]. A classical spin-echo sequence consists of one  $90^\circ$  and one  $180^\circ$  RF. The first makes the spins to rotate onto the transversal plane to  $B_0$  and start to dephase due to factors such as magnetic field inhomogeneities and dipolar interactions, the subsequent  $180^\circ$  pulse inverts the dephasing due to magnetic field inhomogeneities and the spins start to rephase causing a signal reproduction [25].

The dMRI is a spin echo sequence with gradient pulses employed to obtain the PGSE [188] as in Figure 2.3. The first gradient after the  $90^\circ$  RF introduces a phase shift dependent on  $G$  at the position of the spins in that temporal instant and, after a waiting time ( $T_D$ ) (during which molecules can either diffuse or stay at the same position), the second gradient after the  $180^\circ$  RF induces a phase shift dependent on the position of the spins in that second temporal instant. The spins that have



Fig. 2.3: Pulsed gradient spin echo acquisition sequence. It is composed by two radiofrequencies at  $90^\circ$  and  $180^\circ$  and two gradient pulses just after them. The two gradient pulses are characterized by a duration  $\delta$  and a strength  $G$ , while  $\Delta$  is the time occurring between them.

displaced during  $T_D$  do not return in the same position and they do not rephase [99]. Assuming gradients short enough to consider negligible diffusion during them, the net phase change induced by the first is  $\phi_1 = -qx_1$  (where  $q = \gamma\delta G$  and  $x_1$  is the “initial” particle position) and  $\phi_2 = -qx_2$  is the net phase change due to the second one. More in detail,  $\gamma$  is the gyromagnetic ratio characteristic of hydrogen atoms of water ( $42.58\text{exp}(6)$  Hz/T), while  $\delta$  and  $G$  are the duration and gradient strength respectively. The phase induced by the magnetic field is ignored since is constant for all spins in the ensemble. The phase change reversion caused by the  $180^\circ$  leads to the net phase change

$$\phi_2 - \phi_1 = -q(x_2 - x_1). \quad (2.3)$$

Because of Equation 2.3, no net phase shift is stored for stationary particles. On the contrary, the signal given by the sum of the magnetic moments of all spins for diffusing particles is attenuated due to the orientation incoherence of individual magnetic moments. The measured signal can be expressed as:

$$S(q, T_D) = S_0 \exp[-(q^2 T_D) ADC] \quad (2.4)$$

where  $T_D = \Delta - \delta/3$  ( $\Delta$  is the time between the two pulses). The only parameters that are possibly tuneable on the MRI scanner are  $q$  and  $T_D$  ( $q^2 \cdot T_D$  is more commonly known as  $b$ -value). The diffusion signal from one voxel, whose dimension is in the order of  $\text{mm}^3$ , reflects all the signal contributions from compartments constituting the tissue microstructure at micrometer and millisecond scale. It is important to highlight that  $q$  determines the maximum displacement that we are sensitive to, while  $T_D$  determines the resolution limit in the size of the microstructural environments probed [188, 74]. The acquisition with gradients in different directions collects the  $ADC$  variation in the three-dimensional space that enables a complete description of the tissue. Another important aspect to

be considered is the role of  $T_2$  relaxation that occurs with the application of the RF pulses as previously described. Taking this factor into account, Equation 2.4 becomes [188, 74]:

$$S(q, T_D) = S_0 \exp [-(q^2 T_D) ADC] \cdot \exp \left( -\frac{TE}{T_2} \right) \quad (2.5)$$

where  $TE$  is the echo time defined as the time from the first  $90^\circ$  RF to the echo. Other issues regard the maximal available  $G$  in clinical scanners that lead to low  $q$ -values implicating no contrast to the smallest diameters, and the finite pulse width that usually ends in  $\Delta \sim \delta$  implying that the diffusion goes on also during the pulse without possibility to be ignored and causing apparently smaller pores sizes derivation [74, 142].

An alternative to PGSE is the PGSTE sequence that takes advantage of the fact that, in this sequence, a slower  $T_1$  decay is more consistent than the  $T_2$  decay during  $T_D$  [194]. More in detail, the sequence is composed by three  $90^\circ$  RF with the first gradient pulse between the first and the second RF and the second gradient pulse after the third RF. The time between the second and third  $90^\circ$  RF is called mixing time (TM) during which the phase encoding is stored along the longitudinal axis and is thus only exposed to the  $T_1$ -relaxation, while  $T_2$  is now present only for  $TE/2$  [43]. The second  $90^\circ$  RF is indeed now used to place the net magnetization back into the transversal plane. The signal becomes:

$$S(q, T_D) = S_0 \exp [-(q^2 T_D) ADC] \cdot \exp \left( -\frac{TE}{2T_2} \right) \cdot \exp \left( -\frac{TM}{T_1} \right). \quad (2.6)$$

The same aforementioned hardware constraints still affect the acquisition and a long  $T_D$  is reached at price of 50% of SNR less than PGSE [74]. Figure 2.4 shows an illustrative PGSTE sequence.

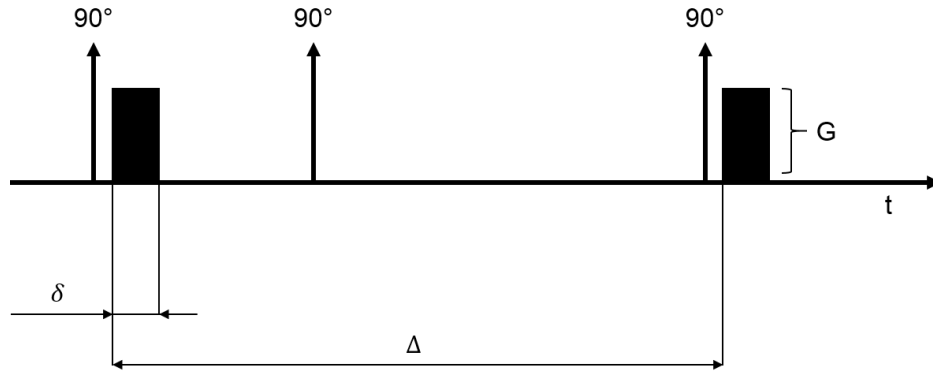


Fig. 2.4: Pulsed gradient stimulated echo (PGSTE) acquisition sequence. It is composed by three radiofrequencies at  $90^\circ$  and two gradient pulses just after the first and third ones. The two gradient pulses are characterized by a duration  $\delta$  and a strength  $G$ , while  $\Delta$  is the time occurring between them.

It must be mentioned that recent advances in developing encoding sequences have been done. In particular, FEXI [128] introduces advantages over PGSE or PGSTE. Its main advantage is the ability to disentangle exchange from restriction employing two PGSE sequences. The two PGSE sequences constitute the diffusion weighting blocks with constant diffusion times while the mixing time between the two is varied. In this way, the first PGSE acts as a low pass diffusion filter attenuating signal from fast diffusing molecules after which exchange takes place restoring the equilibrium between different diffusion components. The second PGSE block provides information for the derivation of the *ADC* varying the mixing time which can be used to quantify the apparent exchange rate (AXR). The AXR depends on characteristics like the cell membrane permeability. FEXY is advantageous also compared to other sequences for exchange filtering like Diffusion EXchange Spectroscopy (DEXSY) [48] or Filter EXchange Spectroscopy (FEXSY) [11]. In fact, it is an even more sparse protocol than FEXSY compared to DEXSY that makes it clinically feasible and advantageous at low SNR.

#### 2.2.4 The propagator formalism

The dMRI signal can be directly related to the probability that particles travel for a certain displacement in a considered direction during the  $T_D$ . This probability was derived in the context of the diffusion process by Einstein [77] as mentioned in Section 2.2.1. The diffusion propagator or EAP from the PGSE signal was formalized by Stejskal and Tanner and is related to the diffusion signal through the Fourier relation [188] when assuming  $\delta$  short enough to be considered negligible:

$$P(\mathbf{r}) = \int_{\mathbf{q} \in \mathbb{R}^3} E(\mathbf{q}) \exp(2\pi i \mathbf{q} \cdot \mathbf{r}) d\mathbf{q} \quad (2.7)$$

where  $E(\mathbf{q}) = S(\mathbf{q})/S_0$  is the normalized diffusion signal.

The collection of a huge amount of data in the  $q$ -space could lead to a direct derivation of the EAP via Fourier transform [47] but the strong influence by the microscopic environment limits this solution due to practical issues related to dMRI sensitivity.

In real condition, the gradient pulse has a finite duration and enables the PGSE spin-echo amplitude expression in terms of the spatial Fourier transform of the center-of-mass propagator [142]. This can be seen as an extension of the aforementioned diffusion propagator since we should consider the additional random walks of duration  $\delta$  with initial points uniformly distributed within the pore. Effect of such acquisition constraint consisting in the finite pulse duration makes the pore appear smaller than its actual size. This issue is relevant since great interest has been devoted in microstructure modeling able to derive, for example, the mean axon diameter. In order to accomplish this effort, more advanced techniques compared to PGSE could be used such as the oscillating gradient spin echo (OGSE) [91, 224]. In fact, OGSE have been developed to reach short diffusion times (e.g. 1 – 2 ms) replacing the diffusion gradients with oscillating diffusion-sensitizing gradients. A temporal diffusion spectrum which is derivable by varying the oscillating frequency should be more sensitive to small axons. Recently, a framework independent from the gradient waveform has been developed for calculating the

lower bound for accurate axon diameter estimate and is referred to as resolution limit [150]. Analysing only the intra-axonal space and assuming the axons as impermeable cylinders, single diffusion encoding sequences resulted as having the lowest resolution limit in case of parallel cylinders while square-wave oscillating gradients were the optimal ones in presence of orientation dispersion. The limit thus depends from factors like the orientation dispersion or the noise level, and for standard clinical MRI was in the range  $4 - 8 \mu\text{m}$  while this was lower for higher gradient strengths.

However, models linking the diffusion process to either the signal or EAP functions from collection of DWIs are being investigated for inferring voxel-averaged microscopic descriptors of the tissue. For example, the Gaussian modeling is largely employed as we will better describe in Chapter 3 and the propagator takes the form:

$$P(r, \mathbf{u}, T_D) = \frac{1}{\sqrt{(4\pi T_D)^3 |\mathbf{D}|}} \exp\left(\frac{-r^2 \mathbf{u}^T \mathbf{D}^{-1} \mathbf{u}}{2T_D}\right) \quad (2.8)$$

where  $\mathbf{D}$  represents the  $3 \times 3$  symmetric matrix describing the diffusion tensor and  $\mathbf{u}$  is the unit vector in the considered direction. In ideal conditions of narrow  $\delta$  and  $T_D \gg a^2/D$  (where  $a$  is the pore characteristic size), the propagator exactly reflects the pore shape as mentioned in Section 2.2.1, enabling the derivation of brain microstructure measures [46]. However, since the nervous tissue architecture is complex within each voxel, many other methods overcoming the derivation of only three parameters as in this technique have been developed and found to be more convenient for the compact representation of the signal as well as of the estimated quantities, while improving the robustness to noise [10, 65, 104]. Moreover, features of the tissue like cell size, shape, and transmembrane exchange following from the restricted character of the diffusion process are extremely important in biomedical applications, and possibly modeled by more complex models as detailed in Chapter 3.



## State of the Art

This chapter aims at illustrating the main dMRI signal reconstruction models currently available in the state of the art as well as the respective derivable microstructural parameters. The most common classification is done on the assumption or not of a generative model of the underlying tissue microstructure [90]. Second aim of the chapter is to introduce the main models assumption and the related limitations.

### 3.1 Signal reconstruction models in diffusion MRI

#### 3.1.1 Signal models

Signal models rely on the representation of the signal as a linear combination of basis. The projection coefficients are most often obtained by fitting the function representing the signal to the measured signal. In describing them, we start from the simplest and most popular Diffusion Tensor Imaging (DTI) and progressively introduce techniques capable to overcome some of its limitations.

#### Diffusion Tensor Imaging

DTI [23, 24] assumes that the dMRI signal can be described by a single multivariate Gaussian function:

$$E(\mathbf{q}) = \exp(-4\pi^2 T_D \mathbf{q}^T \mathbf{D} \mathbf{q}). \quad (3.1)$$

The eigenvalues and the eigenvectors of  $\mathbf{D}$  reflect some microstructural characteristics. More in detail:

$$\mathbf{D} = \lambda_1 \mathbf{v}_1 \mathbf{v}_1^T + \lambda_2 \mathbf{v}_2 \mathbf{v}_2^T + \lambda_3 \mathbf{v}_3 \mathbf{v}_3^T \quad (3.2)$$

where  $\lambda_i$  is the eigenvalue corresponding to the eigenvector  $\mathbf{v}_i$ . In particular, the first eigenvector  $\mathbf{v}_1$  has the highest eigenvalue among the three and thus corresponds to the main diffusion direction in the tissue. Specifically, the eigenvalue  $\lambda_1$  is the *ADC* in the principal diffusion direction. One of the main advantages of DTI is short acquisition time, due to the low number of diffusion gradients that

are required for the tensor estimation. The minimum number of necessary images is six, each corresponding to a different direction, and one baseline image ( $b_0$ ) used for  $S_0$  calculation.  $\mathbf{D}$  is then recovered in each voxel through the determination of its coefficients via the least squares fitting [124]. Information reflecting the underlying microstructure can then be derived from the eigenvalues. In particular, the FA, Mean Diffusivity (MD), Radial Diffusivity (RD) and Axial Diffusivity (AD) can be derived as follows: [22, 123, 220]:

$$FA = \sqrt{\frac{1}{2} \frac{(\lambda_1 - \lambda_2)^2 + (\lambda_1 - \lambda_3)^2 + (\lambda_2 - \lambda_3)^2}{\lambda_1^2 + \lambda_2^2 + \lambda_3^2}} \quad (3.3)$$

$$MD = \frac{\lambda_1 + \lambda_2 + \lambda_3}{3} \quad (3.4)$$

$$RD = \frac{\lambda_2 + \lambda_3}{2} \quad (3.5)$$

$$AD = \lambda_1. \quad (3.6)$$

Figure 3.1 provides an illustration where a high value of FA is representative of a diffusion tensor elongated in one specific direction, that is representative of restricted diffusion with parallel packed compartments (e.g. corpus callosum). The MD is the mean value of the eigenvalues averaged in all the three principal directions. A high value is typical of free diffusion and corresponds to a symmetric (spherical) tensor. The RD and AD give a clearer idea of the diffusion profile shape, respectively disentangling the diffusivity in the transversal plane and along to the main diffusion direction.

The EAP for the DTI model is calculated via Fourier transform and was stated in Equation 2.8. From this Equation is possible to derive the ODF, that is a function on the sphere representing the probability that the water molecules move in a particular direction,  $\mathbf{r}$  in the unit time. As it is well known, the single tensor model is unable to capture multiple peaks of diffusivity in regions with complex architectures like fiber crossing or fanning (e.g. corona radiata) [28, 60, 114].

The Multi-Tensor model can be seen as a natural extension of DTI [203, 180]. The signal is modeled as the sum of the signal contributions arising from the different compartments in the underlying tissue assuming no exchange:

$$E(\mathbf{q}) = \sum_{i=0}^M \nu_i \exp(-4\pi^2 T_D \mathbf{q}^T \mathbf{D}_i \mathbf{q}) \quad (3.7)$$

where  $M$  is the number of compartments,  $\nu_i$  is the volume fraction and  $\mathbf{D}_i$  is the diffusion tensor associated with the  $i_{th}$  compartment. Generally, the propagator, the ODF and each index of the Multi-Tensor model can be computed as the sum of the single tensor contributions. The Multi-Tensor model has two principal limitations: the number of compartments in each voxel is different and unknown *a-priori*, and its fitting procedure for finding volume fractions and diffusion tensors is non-linear leading to a high number of required samples spread on multiple shells.



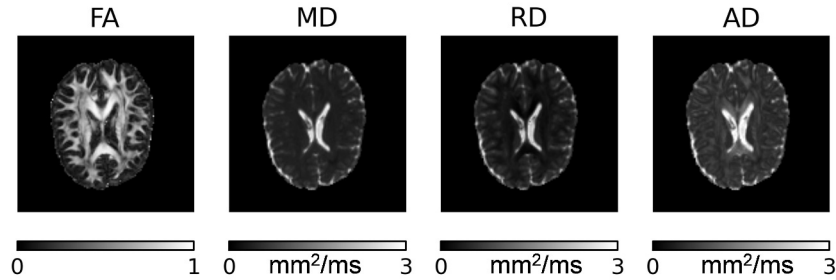


Fig. 3.1: DTI indices calculated on one healthy subject data. The subject underwent DWI acquisition on a 3T Philips clinical scanner providing written informed consent to the University Hospital of Verona. The acquisition scheme consisted of 7 images at  $b = 0 \text{ s/mm}^2$  and two shells with  $b = 700 \text{ s/mm}^2$  and 24 diffusion gradients ( $\Delta = 0.0579 \text{ ms}$  and  $\delta = 0.0138 \text{ ms}$ ), and  $b = 2000 \text{ s/mm}^2$  and 48 diffusion gradients ( $\Delta = 0.0458 \text{ ms}$  and  $\delta = 0.0283 \text{ ms}$ ) respectively;  $TR/TE = 8500/91 \text{ ms}$ ,  $FOV = 230 \times 230 \text{ mm}$ , 120 slices,  $2 \times 2 \times 2 \text{ mm}$  resolution. Data were pre-processed applying topup, eddy current-induced distortions, and subject movement corrections.

### Diffusion Kurtosis Imaging

The use of higher order tensors allows a finer dMRI signal representation, emphasizing tissue characteristics due to non Gaussian diffusion [89]. Diffusion Kurtosis Imaging (DKI) grounds on the fourth order tensor corresponding to kurtosis [113]. The signal model is:

$$S(b) = S_0 \cdot \exp \left( -b \sum_{i,j=1}^3 D_{ij} g_i g_j + \frac{b^2}{6} MD^2 \sum_{i,j,k,l=1}^3 W_{ijkl} g_i g_j g_k g_l \right) \quad (3.8)$$

where  $D_{ij}$  are the coefficients of  $\mathbf{D}$ , and  $W_{ijkl}$  are the coefficients of the fourth order cumulant kurtosis tensor. Since the symmetric kurtosis tensor is of dimensions  $3 \times 3 \times 3 \times 3$ , at least fifteen diffusion directions and two baseline images need to be acquired. DKI characterizes the kurtosis of the signal highlighting whether the departure from Gaussian behaviour is in a negative (platykurtic distribution) or positive (leptokurtic distribution) sense. From kurtosis tensor, indices similar to those derived from DTI can be obtained that are Mean Kurtosis (MK), Radial Kurtosis (RK) and Axial Kurtosis (AK) [82, 192] (Figure 3.2).

One of the limitations of the DKI model is the long image acquisition time compared with that for DTI [189]. A minimum of images in different directions bigger than those for DTI are required to calculate the added higher order kurtosis tensor. Another limitation is the complexity of the DKI model compared to DTI considering that it relies on 21 independent parameters instead of 6 [189].

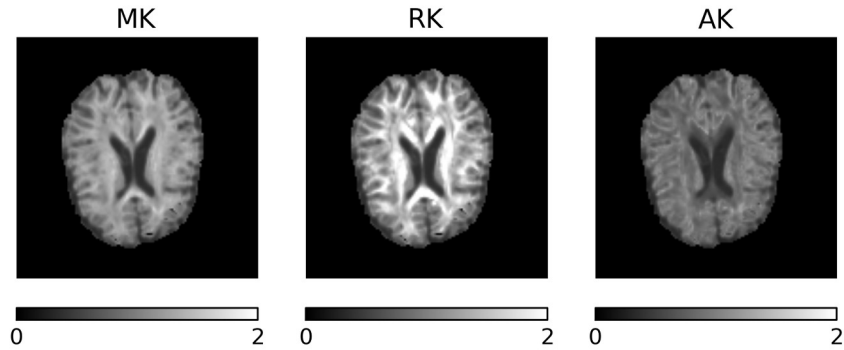


Fig. 3.2: DKI indices calculated on one healthy subject data. The subject underwent DWI acquisition on a 3T Philips clinical scanner providing written informed consent to the University Hospital of Verona. The acquisition scheme consisted of 7 images at  $b = 0 \text{ s/mm}^2$  and two shells with  $b = 700 \text{ s/mm}^2$  and 24 diffusion gradients ( $\Delta = 0.0579 \text{ ms}$  and  $\delta = 0.0138 \text{ ms}$ ), and  $b = 2000 \text{ s/mm}^2$  and 48 diffusion gradients ( $\Delta = 0.0458 \text{ ms}$  and  $\delta = 0.0283 \text{ ms}$ ) respectively;  $TR/TE = 8500/91 \text{ ms}$ ,  $FOV = 230 \times 230 \text{ mm}$ , 120 slices,  $2 \times 2 \times 2 \text{ mm}$  resolution. Data were pre-processed applying topup, eddy current-induced distortions, and subject movement corrections.

### Diffusion Spectrum Imaging

As mentioned in the previous Sections, the Stejskal-Tanner formalism enables the direct estimation of the EAP from the signal. Diffusion Spectrum Imaging (DSI) derives it by Fast Fourier Transform [215] without making any assumption on the diffusion process. A discrete  $q$ -space sampling on a Cartesian grid is performed, which is required to be dense for a good approximation of the EAP. Many diffusion directions are acquired up to high  $b$ -values (typically  $8000 \text{ s/mm}^2$ ) in order to resolve very small features of the tissue from EAP. Moreover, the desirable short  $\delta$  for satisfying the narrow pulse approximation (NPA) further prompts to high  $|\mathbf{G}|$ . Unfortunately, the required conditions make acquisition times and  $b$ -values hardly feasible in clinical conditions due to long scan durations, high impact Eddy current distortions and possibly harmful electric fields in the subject caused by the coils movement in the attempt to reach these strong gradients in short times (in some works, more than 500 DWIs were acquired and  $b_{max} = \sim 20000 \text{ s/mm}^2$  was used) [218, 215].

### Orientation Distribution Function driven methods

The importance of the ODF derivation for performing tractography also in cases of crossing fibers is such that some reconstruction methods were developed with the aim to just obtaining a high resolution ODF. From the EAP it is possible to

derive the ODF, that maps the EAP on the sphere and can be seen as the radial average of the EAP. It is obtained as the integral of the EAP along its radius:

$$ODF(\mathbf{u}) = \int_0^\infty P(r\mathbf{u})r^2dr. \quad (3.9)$$

In q-ball Imaging (QBI), the diffusion signal is described through real symmetric spherical harmonics (SH) basis. The  $q$ -space is sampled on a single shell and only the angular part of the signal is modeled [202, 65]. Specifically, the diffusion signal is represented as:

$$E(\mathbf{u}, q) = \sum_{l=0, \text{even}}^N \sum_{m=-l}^l c_{lm} Y_l^m(\mathbf{u}) \quad (3.10)$$

where  $c_{lm}$  are the coefficients associated to the SH function  $Y_l^m$  and their number is  $(l+1)(l+2)/2$ . The SH coefficients are retrieved via regularized least squares methods and are used to approximate the ODF using the Funk-Hecke Theorem.

The ODF can be seen as a blurred version of the fiber ODF (fODF) that represents the principal directions of diffusion corresponding to the peaks of the ODF. More in detail, the signal is assumed as given by a spherical convolution between the response function of an ideal single fiber bundle (e.g. corpus callosum), a kernel generally assumed constant for the whole WM, and a spherical density function which is the fODF representing the distribution of the fiber orientations in the voxel. This model was first described in [211]. The deconvolution process allows to retrieve the underlying fODF starting from the signal and the known single fiber signal diffusion kernel (acting as a response function). The two principal techniques used for the deconvolution are a modified Richardson-Lucy deconvolution algorithm [2, 161] and the Constrained Spherical Deconvolution (CSD) using the SH basis [200, 199]. In CSD, the single fiber response function is assumed to be axially symmetric and it is estimated from voxels with high FA values and thus most probably containing only single fiber bundles. The fODF is modeled as a sum of Dirac delta functions and the deconvolution problem is linearly solved by representing the signal, the fODF and the response function in the SH basis. The fODF is obtained by an iterative regularisation process. Recently, a multi-shell multitissue CSD (MSMT-CSD) generalization involving a multi- $q$ -shell spherical deconvolution was proposed [115] which is able to discern also between cerebrospinal fluid (CSF), GM and WM crossing fibers [115] besides providing improved performance [67].

From the ODF it is possible to derive a measure of anisotropy calculated as its “variance” called Generalized FA (GFA):

$$GFA = \sqrt{\frac{n \sum_{i=1}^n \psi(\mathbf{u}_i) - \langle \psi \rangle^2}{(n-1) \sum_{i=1}^n \psi(\mathbf{u}_i)^2}} \quad (3.11)$$

where  $\psi(\mathbf{u}_i)$  is the ODF sampled along direction  $i$  and  $\langle \psi \rangle$  is its mean over all directions. GFA was first introduced by Tuch [202] when he formalized the QBI. The method reconstructs the signal acquired with multiple  $b$ -values and directions [High Angular Resolution Diffusion Imaging (HARDI) signal] via Funk-Radon

transform leading to resolve multiple fiber orientations within the voxel. The  $b$ -value dependence of GFA is consequence of the same ODF dependence from which is derived and thus is consequence of the reconstruction model used. For example, Tournier et al. [201] have shown that 4000 s/mm<sup>2</sup> was the minimum  $b$ -value required for resolving 45° crossing with QBI, while 2000 s/mm<sup>2</sup> was sufficient with CSD although a bias in the orientations could be introduced. The main cause of this difference is the fact that lower  $b$ -values lead to a more blurred QBI ODF from which the presence of two peaks could be indistinguishable. On the other hand, too high  $b$ -values could result in the fitting of noise instead of signal. Therefore, it is important for results interpretation task to discern among the optimal and acceptable acquisition parameters required depending on the reconstruction method.

### Methods based on functional basis

Many analytical approaches for calculating EAP were proposed in literature. These reconstruction methods allow the interpolation of the data in both the  $q$ -space and the real space since the signal is represented with functional basis having analytical or closed forms Fourier transformations. More in detail, functional bases decompose the diffusion signal  $E(\mathbf{q})$  as a linear combination of functions  $\Psi_n(q\mathbf{u})$ :

$$E(\mathbf{q}) = \sum_{n=0} c_n \Psi_n(q\mathbf{u}) \quad (3.12)$$

and the coefficients  $c_n$  are recoverable using regularized least squares optimization [65, 141] or quadratic programming [159]. The EAP is then calculated by applying the Fourier transform to Equation 3.12.

Among these, the 3D-SHORE is of particular interest for its approximation capabilities. It employs a monoexponential decaying function in the radial direction modulated by Laguerre polynomials  $L$ , and an angular profile described by spherical harmonics as functional basis [158]. Specifically, the basis functions are:

$$\Psi_{jlm}(\zeta, q\mathbf{u}) = \left[ \frac{2(j-l)!}{\zeta^{3/2} \Gamma(j+3/2)} \right]^{1/2} \left( \frac{q^2}{\zeta} \right)^{l/2} \exp\left( \frac{-q^2}{2\zeta} \right) L_{j-l}^{l+1/2} \left( \frac{q^2}{\zeta} \right) Y_l^m(\mathbf{u}) \quad (3.13)$$

where  $\zeta$  is a scaling parameter and  $j$ ,  $l$  and  $m$  are the indices for the representation of the series involving spherical coordinates.

The same model expressed in terms of Cartesian coordinates is the Mean Apparent Propagator MRI (MAP-MRI) model [159]. In this case, three scaling parameters  $\zeta_x$ ,  $\zeta_y$  and  $\zeta_z$  are enabled along the three principal directions, as opposed to the case of SHORE where a single scaling parameter  $\zeta$  can be used. The separable solution in the Cartesian space was then introduced leading to a Hermite polynomial series representation:

$$\Psi_{k_1 k_2 k_3}(\mathbf{Z}, \mathbf{q}) = \psi_{k_1}(\zeta_x, q_x) \psi_{k_2}(\zeta_y, q_y) \psi_{k_3}(\zeta_z, q_z) \quad (3.14)$$

with

$$\psi_k(Z, q) = \frac{i^{-k}}{\sqrt{2^k k!}} \exp(-2\pi^2 q^2 \zeta^2) H_k(2\pi q \zeta) \quad (3.15)$$

with  $\mathbf{Z} = [\zeta_x, \zeta_y, \zeta_z]^T$  and  $H_k$  the  $k_{th}$  order Hermite polynomial. Zucchelli et al. [230] proposed an extension of the MAPMRI model called Multi-Tensor MAPMRI (MT-MAPMRI). MT-MAPMRI improves the reconstruction for crossing fibers which takes advantage on the initial single tensor fitting by fitting more than one axially symmetric tensors.

Other models based on functional basis that is worth mentioning are the Diffusion Propagator Imaging (DPI) where the diffusion signal equation is obtained by solving the Laplace equation in spherical coordinates [66]; the Bessel Fourier Orientation Reconstruction (BFOR) model where the full and analytical Fourier transform in spherical coordinates were derived from the heat equation [105]; and the Spherical Polar Fourier Imaging (SPFI) using a Gauss-Laguerre representation with its full analytical Fourier transformation [16, 51, 58, 57].

It is important to say that the accuracy of signal description by the basis obviously depends on the basis parameters and moreover on the fitting of the coefficients through the optimization [79, 141]. The number of coefficients depends on the maximal basis order  $N$  and must not exceed the number of DWIs for a reliable fitting.

#### *Microstructural descriptors*

From the aforementioned methods, microstructural indices can be derived from the EAP. Among these are the Return To Origin Probability (RTOP) or the Mean Squared Displacement (MSD), the Return To Axis Probability (RTAP), the Return To Plane Probability (RTPP), the Propagator Anisotropy (PA) and the Non-Gaussianity (NG) [159].

The RTOP is the probability that the particles do not move during the observed diffusion time and it is formalized as:

$$RTOP = P(\mathbf{0}) = \int_{\mathbb{R}^3} E(\mathbf{q}) d^3 \mathbf{q}. \quad (3.16)$$

Under assumptions of narrow pulses and long diffusion time, RTOP is proportional to the reciprocal of the apparent pore volume in which diffusion is supposed to take place and thus can be considered as a measure of restriction. It was firstly introduced in Özarslan et al. [159] along with RTAP and RTPP that are respectively the integral of the EAP along the main diffusion direction and over the plane passing through the origin and perpendicular to the main diffusion direction:

$$RTAP = \int_{\mathbb{R}} P(\mathbf{r}_{\parallel}) d\mathbf{r}_{\parallel} = \int_{\mathbb{R}^2} E(\mathbf{q}_{\perp}) d^2 \mathbf{q}_{\perp} \quad (3.17)$$

$$RTPP = \int_{\mathbb{R}^2} P(\mathbf{r}_{\perp}) d^2 \mathbf{r}_{\perp} = \int_{\mathbb{R}} E(q_{\parallel}) dq \quad (3.18)$$

where  $P(\mathbf{r}_{\parallel})$  is the propagator along the main diffusion direction  $\mathbf{r}_{\parallel}$ , while  $P(\mathbf{r}_{\perp})$  indicates the propagator over the plane through the origin and along  $\mathbf{r}_{\perp}$  which is the direction perpendicular to the main one;  $\mathbf{q}_{\perp}$  is the plane passing through the origin and perpendicular to the main diffusion direction and  $q_{\parallel}$  is the main diffusion direction. Also RTAP and RTPP are proportional to the inverse of the apparent cross-sectional area and the apparent mean length of the compartment

where diffusion takes place under the aforementioned conditions. All the indices of no net displacement between the two gradient pulses are illustrated in Figure 3.3.

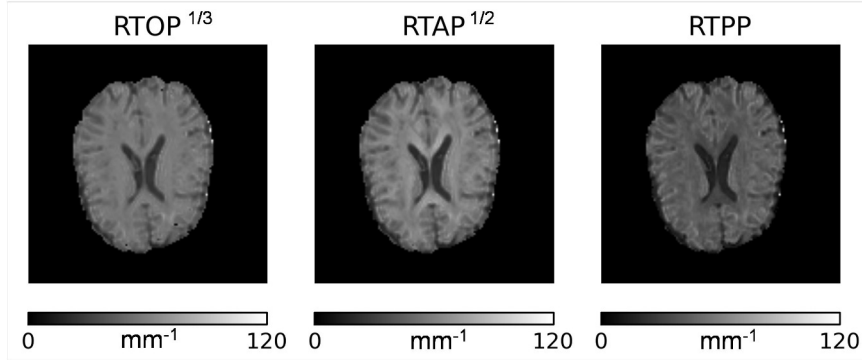


Fig. 3.3: 3D-SHORE indices of no net displacement calculated on one healthy subject data. The subject underwent DWI acquisition on a 3T Philips clinical scanner providing written informed consent to the University Hospital of Verona. The acquisition scheme consisted of 7 images at  $b = 0 \text{ s/mm}^2$  and two shells with  $b = 700 \text{ s/mm}^2$  and 24 diffusion gradients ( $\Delta = 0.0579 \text{ ms}$  and  $\delta = 0.0138 \text{ ms}$ ), and  $b = 2000 \text{ s/mm}^2$  and 48 diffusion gradients ( $\Delta = 0.0458 \text{ ms}$  and  $\delta = 0.0283 \text{ ms}$ ) respectively;  $TR/TE = 8500/91 \text{ ms}$ ,  $FOV = 230 \times 230 \text{ mm}$ , 120 slices,  $2 \times 2 \times 2 \text{ mm}$  resolution. Data were pre-processed applying topup, eddy current-induced distortions, and subject movement corrections.

The PA represents an index that relates the entire three-dimensional apparent propagator to a measure of anisotropy that can be expressed as an angular metric between the propagator and its isotropic counterpart:

$$PA = \sigma(\sin\theta_{PO}, \epsilon) \quad (3.19)$$

where  $\sigma(\cdot)$  is a scaling function  $\left[\sigma(t, \epsilon) = \frac{t^{3\epsilon}}{1-3t^\epsilon+3t^{2\epsilon}}\right]$  ( $t$  is the quantity to scale, e.g.  $\sin\theta_{PO}$ ) and  $\epsilon$  is a positive-valued shape parameter that determines the range of values to be emphasized by the transformation.

Finally, the NG is an index that quantifies the dissimilarity between the propagator  $P(\mathbf{r})$  and its Gaussian part  $G(\mathbf{r})$  readily available from a diffusion tensor analysis. The NG is defined as  $NG = \sin\theta_{PG}$  and can be seen as an alternative measure to kurtosis [159].

MSD has been proven to be closely related to the classical MD index, sharing similar patterns and representing the net mean square displacement of the water molecules in the unit time [223]. MSD is computed as follows:

$$MSD = \int_{\mathbb{R}^3} P(\mathbf{r}) \mathbf{r}^2 d^3\mathbf{r} \quad (3.20)$$

It has been shown that when reconstructing with partial data at lower  $b$ -values, scalar maps of indices derived by MAPMRI (in particular PA) are affected even if they are similar to the original ones [159]. Aiming to investigate a clinical feasible protocol for accurately reconstructing signal with MAPMRI, Avram et al. [17, 18] demonstrated that reducing the number of DWIs does not significantly affect the indices derivation when high  $b$ -values are included. MAPMRI optimal protocol can thus be accelerated taking advantage by reducing the number of acquisition but keeping relatively large  $b$ -values. In particular subsampled datasets containing only 150 DWIs converged to within 5% error when images with  $b > 4000$  s/mm<sup>2</sup> were included.

### 3.1.2 Compartmental models

The idea beyond the compartmental reconstruction methods is the assumption of a generative model of the tissue microstructure. The compartmental models aid in the disentanglement of some phenomena otherwise hardly distinguishable like the presence of a slow and fast diffusions observable in normal diffusion signal from cerebral tissue, or the partial volumes between GM and WM or CSF. These fall in the category of biophysical models as assumptions are made on the different compartments contributing to the signal and the corresponding signal contribution.

In what follows, the main compartmental models are briefly summarized.

Generally, diffusion in cerebral tissue is considered to take place in three principal conditions: *restricted* in compartments where only one main diffusion direction is allowed, like axons, *hindered* in compartments where diffusion is still not Gaussian yet less restricted, like extracellular tissue or cells present in WM as the glial cells, and *free* in compartments where free diffusion can be allowed, like the CSF.

The simplest biophysical model is the Ball&Sticks that models the restricted diffusion as a tensor with  $\lambda_1 = 1, \lambda_2 = \lambda_3 = 0$  (the 'sticks') along the main diffusion direction for the intracellular compartment while an isotropic Gaussian (the 'ball') is used to model the unrestricted diffusion [27]. A more realistic representation of fiber bundles can be obtained by extending the model for accounting for the distribution of fiber orientations.

In the Composite Hindered and Restricted Model (CHARMED) the restricted diffusion compartment is a cylinder with a fixed diameter and the hindered diffusion one is a diffusion tensor [14]. The signal model is then represented by:

$$E(\mathbf{q}) = \nu_h E_h(\mathbf{q}) + \nu_r E_r(\mathbf{q}) \quad (3.21)$$

where  $E_h$  is the model of the signal coming from the hindered compartment,  $E_r$  is the model of the signal coming from the restricted one and  $\nu_h + \nu_r = 1$  are the volume fractions.

AxCaliber then introduced an alternative to CHARMED, allowing to estimate the diameters of parallel structural components when a diffusion gradient perpendicular to the main diffusion direction is applied [13]. More in detail, the fiber population diameters are assumed as coming from a Gamma distribution and the restricted signal is represented via Callaghan's model under short gradient pulse assumption [46].

ActiveAx is another improvement of the CHARMED method assuming four tissue compartments: the axons represented by Gaussian phase distribution approximation [145] of the signal from particles in a cylinder [205], the extra-axonal water represented by a diffusion tensor, the CSF modeled through an isotropic Gaussian and the stationary water as in glial cells represented by a constant signal equal to 1 [6].

The Neurite Orientation Dispersion and Density Imaging (NODDI) model allows the cylinders (again represented as sticks) to disperse. The three main compartments in which the overall diffusion signal is divided are the free water compartment, the intra-neurite compartment and the extra-neurite one. The signal is [225]:

$$E(\mathbf{q}) = (1 - \nu_{iso})(\nu_{in}E_{in} + (1 - \nu_{in})E_{en}) + \nu_{iso}E_{iso} \quad (3.22)$$

where the subscript *iso* is for the free water compartment, *in* is for the intra-neurite compartment and *en* is for the extra-neurite compartment. A linear optimization for the fitting of these parameters was also provided with the advantage of greatly reducing the computational time. The dispersion of cylinders is modeled by the Watson distribution [226]. Recently, Lampinen et al. [127] have demonstrated the invalidity in brain and gliomas of NODDI constraints. More in detail, the intracellular volume fraction directly connected to the mean diffusivity of the tissue by tortuosity assumption leads to greater water levels with microscopic diffusion anisotropy in GM and glioma tumors. To obtain more data-driven estimates, they proposed the employment of *b*-tensors with variable shape.

Typical biomarkers derivable from the aforementioned models are the volume fractions of the isotropic, the intra-neurite and the extra-neurite compartments as illustrated in Figure 3.4, obviously in addition to all the parameters let free in the fitting. NODDI also introduced the Orientation Dispersion Index (ODI) which describes the neurites direction distribution [225]. A further evolution of the model was then provided by replacing the Bingham with the Watson distribution [117].

Extracellular tissue compartment is usually assumed Gaussian and thus generally modeled as a tensor independent by diffusion time [7, 13, 15, 226]. Recently, it has been shown that this compartment diffusion in the orthogonal plane to the main fiber orientation is dependent from time [155]. Moreover, it can generate a bias in axon diameter and density estimates if not considered in the modeling [155]. Based on this, De Santis et al. [63] proposed a two compartment model composed by the restricted and the hindered compartments, where the novelty was the modeling of the hindered compartment representative of the extracellular tissue described by:

$$S_h(\mathbf{q}, \Delta) = \exp[-4\pi^2(\Delta - \delta/3)\mathbf{q}^T \mathbf{D}_h \mathbf{q}], \quad (3.23)$$

where

$$\mathbf{D}_h = \begin{pmatrix} D_{h,\parallel} & 0 & 0 \\ 0 & D_{h,\infty} + A \frac{\ln(\Delta/\delta)+3/2}{\Delta-\delta/3} & 0 \\ 0 & 0 & D_{h,\infty} + A \frac{\ln(\Delta/\delta)+3/2}{\Delta-\delta/3} \end{pmatrix}. \quad (3.24)$$

$D_{h,\parallel}$  can be chosen as free parameter like in CHARMED [15] or linked to the longitudinal diffusion in the restricted compartment via tortuosity approximation



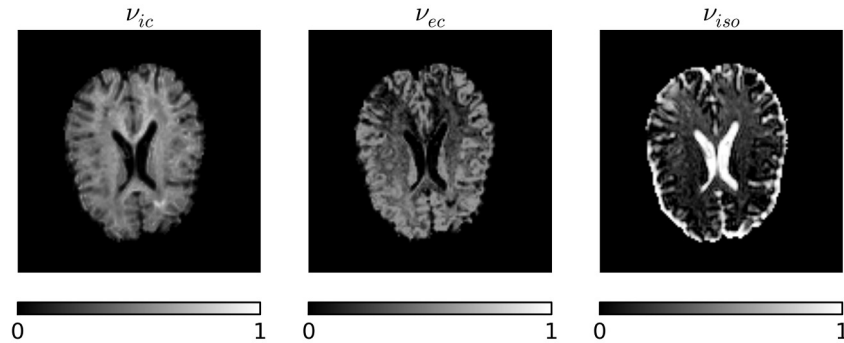


Fig. 3.4: NODDI indices of volume fraction calculated on one healthy subject data. The subject underwent DWI acquisition on a 3T Philips clinical scanner providing written informed consent to the University Hospital of Verona. The acquisition scheme consisted of 7 images at  $b = 0$  s/mm<sup>2</sup> and two shells with  $b = 700$  s/mm<sup>2</sup> and 24 diffusion gradients ( $\Delta = 0.0579$  ms and  $\delta = 0.0138$  ms), and  $b = 2000$  s/mm<sup>2</sup> and 48 diffusion gradients ( $\Delta = 0.0458$  ms and  $\delta = 0.0283$  ms) respectively;  $TR/TE = 8500/91$  ms,  $FOV = 230 \times 230$  mm, 120 slices,  $2 \times 2 \times 2$  mm resolution. Data were pre-processed applying topup, eddy current-induced distortions, and subject movement corrections.

[191] like in NODDI [227].  $D_{h,\infty}$  is the bulk diffusion constant while  $A$  is the characteristic coefficient for  $\ln(\Delta/\delta) + 3/2$  (used when  $\Delta/\delta \gg 1$  [42]). For a wider understanding of such a modeling, Fieremans et al. [81] provided an investigation comparing the conventional two-compartment model in which time-dependence is considered only for the intra-axonal compartment and the extra-axonal time-dependent model at the basis of the aforementioned study.

All the signal reconstruction models just mentioned consider the restricted compartments representing WM as completely impermeable. With the aim of overcoming such a limitation, in this work, a wide-spectrum review of the literature regarding permeability/relaxivity was performed. Next Section provides an overview on the topic.

### 3.2 Permeability in dMRI

Talking about permeability, a distinction must be done on the difference between osmotic and diffusional permeability. Osmotic permeability takes place when an osmotic pressure gradient is present over the membrane and is generally greater than the diffusional one [209]. The dMRI experiments are assumed to be done in absence of osmotic permeability and thus we generally refer to diffusional permeability throughout the thesis. In this thesis we aim at shedding light on strategies

used to extract information on the brain tissue depending on the permeability. In some cases, it was difficult distinguishing the proper studies on the topic due to the used nomenclature. In particular, this was the case of studies on surface relaxivity that is a microscopic phenomenon that is correlated to the permeability from a macroscopic point of view but from which is important making a distinction. Among these studies on the surface relaxivity we investigated the Multiple Propagator [59] and the Multiple Correlation Function [95, 96]. More properly, diffusional permeability implies an exchange and thus multiple compartments through which this has place. The Kärger model [119] is a multi-compartment reconstruction method grounding on this phenomenon. Other strategies different from the signal modeling to assess cerebral microstructure characteristics depending on permeability are proposed. This is the case of specific acquisition sequences and optimization routines, together with numerical simulations to realize the exchange as a flux through the barriers. Figure 3.5 represents the entire picture of strategies described above.

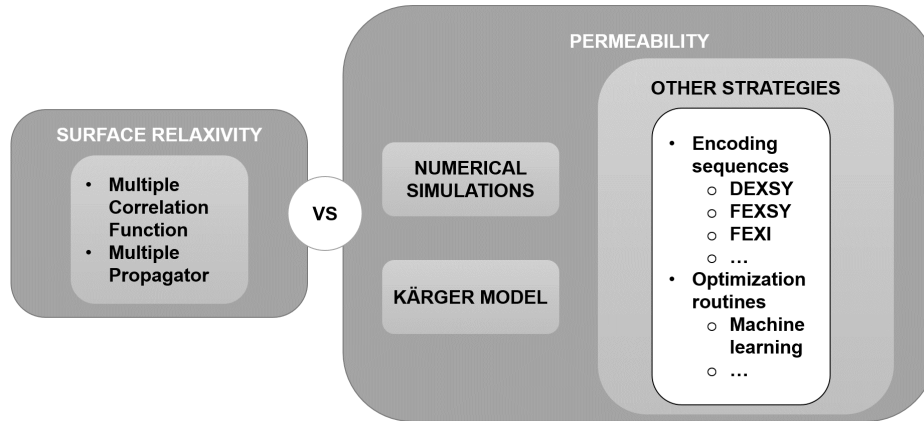


Fig. 3.5: schema representing the review of permeability in dMRI. The Multiple Correlation Function and the Multiple Propagator are methods for investigating surface relaxivity that must be distinguished from permeability which implies exchange through multiple compartments. Among the methods used to investigate this topic we see the Kärger model for reconstructing the signal, numerical simulations and other strategies such as new acquisition sequences and optimization routines.

### 3.2.1 Surface relaxivity

In the study of this phenomenon, the reference system is placed inside a particular geometry (e.g. typically slab, cylinder, sphere) and the world system is confined within the walls of the considered shape. In this case, the collision of the water particles with the walls gives information about the properties of the boundaries.

More in detail, these impacts cause a loss of magnetization depending on the surface relaxivity which have the same effect of permeability if considered from a macroscopic point of view. The signal attenuation is thus modeled through relaxivity and is modulated by the surface-to-volume ratio of the compartment in which the world system is placed.

The parameter involved in the study of this mechanism is:

$$M = \frac{1}{s} \int \mu(\mathbf{r}) df \quad (3.25)$$

where  $M$  [cm/s] is the average value of the surface sink strength density  $\mu(\mathbf{r})$  over the active surface  $s$  ( $df$  is the surface element) [36]. The signal attenuation mechanism due to surface relaxivity is governed by a dimensionless variable  $h = \frac{Ma}{D}$ .

Limiting the investigation to WM diffusion signal reconstruction models and considering the cylinder as the more suitable geometry for representing the axon, Callaghan was one of the firsts to derive the PGSE nuclear magnetic resonance signal under conditions of wall relaxation [44]. Together with Codd, he also proposed a matrix formalism named Multiple Propagator [59] to simulate the PGSE signal in a general gradient waveform. Successively, Grebenkov proposed another matrix formalism based on the Laplacian operator and called Multiple Correlation Function [95, 96].

### Multiple Propagator

The assumption of the NPA allows re-writing Equation 2.7 as [188, 46]:

$$E(\mathbf{q}, \Delta) = \int \int \rho(\mathbf{r}, 0) P(\mathbf{r}|\mathbf{r}', \Delta) \exp[i2\pi\mathbf{q} \cdot (\mathbf{r}' - \mathbf{r})] d\mathbf{r}d\mathbf{r}' \quad (3.26)$$

where the propagator is formalized as a conditional probability that a molecule starting from  $\mathbf{r}$  at  $t = 0$  arrives in  $\mathbf{r}'$  at  $t = \Delta$ , and  $\rho(\mathbf{r}, 0)$  is the starting spin density that may be considered as the pore molecular density function  $\rho(\mathbf{r})$  indeed thanks to NPA.

Since the basic differential equation governing the propagator is the Fick's law, the propagator can be developed by Eigenmode expansion [44]:

$$P(\mathbf{r}|\mathbf{r}', t) = \sum_{n=0}^{\infty} \exp(-\lambda_n t) u_n(\mathbf{r}) u_n^*(\mathbf{r}') \quad (3.27)$$

where  $u_n(\mathbf{r}')$  are an orthonormal set of solutions to the Helmholtz equation parameterized by the eigenvalues  $\lambda_n$ . Since  $P(\mathbf{r}|\mathbf{r}', 0) = \delta(\mathbf{r} - \mathbf{r}')$ , the eigenfunction expansion of  $P$  is derived for the identity  $\delta(\mathbf{r}|\mathbf{r}') = \sum_{n=0}^{\infty} u_n(\mathbf{r}) u_n^*(\mathbf{r}')$ . The eigenvalues  $\lambda_n$  depend on the Robin boundary condition for the case of relaxing walls:

$$D\hat{\mathbf{n}} \cdot \nabla P + MP = 0 \quad (3.28)$$

where  $\hat{\mathbf{n}}$  is the outward surface normal,  $\nabla P$  is the gradient of the propagator along the same direction. For  $M = 0$  we retrieve the NPA echo-attenuation as defined

by Tanner and Stejskal [195]. In case of cylindrical pore the typical length  $a$  is the radius and the eigenfunction expansion of  $P$  is given by:

$$P(\mathbf{r}|\mathbf{r}', \Delta) = \sum_{nk}^{\infty} \exp[-\beta_{nk}^2 D \Delta / a^2] J_n(\beta_{nk} \mathbf{r} / a) J_n(\beta_{nk} \mathbf{r}' / a) A_{nk}^2 \cos(n\theta) \cos(n\theta') \quad (3.29)$$

where

$$A_{nk}^2 = (2/\pi a^2)(\beta_{nk}^2 / J_n^2(\beta_{nk})) / [(Ma/D)^2 + \beta_{nk}^2 - n^2] \quad (3.30)$$

$$A_{0k}^2 = (1/\pi a^2)(\beta_{0k}^2 / J_0^2(\beta_{0k})) / [(Ma/D)^2 + \beta_{0k}^2] \quad (3.31)$$

where  $J_n$  are the Bessel functions and the eigenvalues  $\beta_{nk}$  are obtained by solving:

$$\beta_{nk} J_{nk}'(\beta_{nk}) / J_{nk}(\beta_{nk}) = -Ma/D. \quad (3.32)$$

The final cylindrical NMR signal equation with relaxing walls and assumed NPA is [44]:

$$\begin{aligned} E(q, \Delta) &= \sum_k 4 \exp[-\beta_{0k}^2 D \Delta / a^2] \frac{\beta_{0k}^2}{[(Ma/D)^2 + \beta_{0k}^2]} \\ &\times \frac{[(2\pi qa) J_0'(2\pi qa) + (Ma/D) J_0(2\pi qa)]^2}{[(2\pi qa)^2 - \beta_{0k}^2]^2} \\ &+ \sum_{nk} 8 \exp[-\beta_{nk}^2 D \Delta / a^2] \frac{\beta_{nk}^2}{[(Ma/D)^2 + \beta_{nk}^2 - n^2]} \\ &\times \frac{[(2\pi qa) J_n'(2\pi qa) + (Ma/D) J_n(2\pi qa)]^2}{[(2\pi qa)^2 - \beta_{nk}^2]^2}. \end{aligned} \quad (3.33)$$

In case of the common NPA assumption violation, Codd and Callaghan proposed a matrix formalism in 1999 [59]. In particular, the gradient waveform was subdivided in steps short enough to make valid such assumption and some matrices describing the different attenuation mechanisms were obtained by the aforementioned eigenfunction expansion [45]. More in detail,  $S$  represents the spectral component of the phase factor and is dependent on the specific geometry under examination,  $R$  is for including the time evolution associated with diffusion and  $A$  is for the phase evolution associated with the gradient impulse:

$$E = S(\mathbf{q}) R [A(\mathbf{q})]^{m_2} \dots R [A(\mathbf{q})]^{m_n} \dots R [A(\mathbf{q})]^{m_N} R S^\dagger(-\mathbf{q}) \quad (3.34)$$

where  $\mathbf{q}$  is the smallest impulse used to digitize the waveform,  $m_n$  are the indices used to summarize the shape of the waveform and  $S^\dagger$  is the Hermitian conjugate of  $S(\mathbf{q})$ .

The formulation of the matrices for the case of cylinder with relaxing walls are given in [59].

### Multiple Correlation Function

Grebenkov proposed a formalism called Multiple Correlation Function for the simulation of the diffusion signal with the possibility to add the surface relaxation [95].

In a confining domain with Neumann boundary conditions (i.e. without surface relaxation) the evolution of the transverse magnetization is described by an initial state due to diffusion and a perturbation state due to encoding (Bloch-Torrey equation) [198]. The initial state is given by the diffusive migration of the spin-bearing particles and is represented by the diffusion coefficient  $D$  and the Laplace operator that measures the caused change [177, 147, 36]. The perturbation state is due to the magnetic encoding, when the spins acquire the phase shift resulting from their precession. Since the Laplace operator has a complete set of eigenfunctions (in all the three possible boundary conditions: Neumann, Dirichlet and Robin), it can be used as a basis to decompose the transverse magnetization [29]. Similarly to the approach used in the Multiple Propagator, matrices depending on the pore geometry and representative of each attenuation mechanism of the diffusion signal can be derived [95]. The matrix formalism can be used for any gradient waveform, for example in the classical PGSE we have:

$$E = U \exp [-(p\Lambda + iq\mathcal{B})\delta/T_{tot}] \exp [-p\Lambda(T_{tot} - 2\delta)/T_{tot}] \exp [-(p\Lambda - iq\mathcal{B})\delta/T_{tot}] \tilde{U} \quad (3.35)$$

where  $U$  represents the initial spin density,  $\Lambda$  is the matrix for the attenuation due to pure diffusion,  $\mathcal{B}$  is the matrix for the attenuation due to phasing,  $p$  and  $q$  are the dimensionless variables respectively corresponding to  $p = DT_{tot}/L^2$  and  $q = \gamma GaT_{tot}$ ,  $i$  is such that  $i^2 = -1$ ,  $T_{tot}$  is the total time observed and finally  $\tilde{U}$  is the sampling function. In the matrices multiplication we can see that the first exponential represents the first gradient pulse in which diffusion together with dephasing are present, the second exponential is for calculating the pure diffusion that has elapsed during  $\Delta$  and the last exponential is the same of the first but it has different sign due to the rephasing [95].

Up to this point, no surface relaxation was considered. To do this, Grebenkov proposed two alternative methods [95]. Similarly to [59], the first one assumes a uniform surface relaxation taking into account the magnetization in case of Robin boundary condition. In this case all the governing matrices have to be re-written in order to be put in the form described above [95]. In the alternative perspective, a real coefficient  $\kappa$  for the phasing attenuation mechanism is assumed instead of the imaginary part ( $iq$ ), which corresponds to a pure relaxation mechanism. The limitation of this mechanism only in the boundaries space allows the insertion of the surface relaxation mechanism in the aforementioned formalism. In this case, the PGSE formulation becomes:

$$E = U \exp [-(p\Lambda + iq\mathcal{B} + ph\tilde{\mathcal{B}}^s)\delta/T_{tot}] \exp [-(p\Lambda + ph\tilde{\mathcal{B}}^s)(T_{tot} - 2\delta)/T_{tot}] \times \exp [-(p\Lambda - iq\mathcal{B} + ph\tilde{\mathcal{B}}^s)\delta/T_{tot}] \tilde{U} \quad (3.36)$$

where  $\tilde{\mathcal{B}}^s$  is the matrix for the walls relaxivity and  $ph$  corresponds to the real term  $\kappa$  just discussed and it is equal to  $MT_{tot}/a$ .

Starting from conditions as reported by Callaghan in 1995 [44], we reproduced the cylindrical dMRI signal in case of surface relaxivity different from zero with NPA. Figure 3.6.A illustrates the signals obtained from five different  $\Delta$  times with-

out surface relaxation, for comparison with Figure 3.6.B where a surface relaxation leading to  $h = 2$  was introduced.

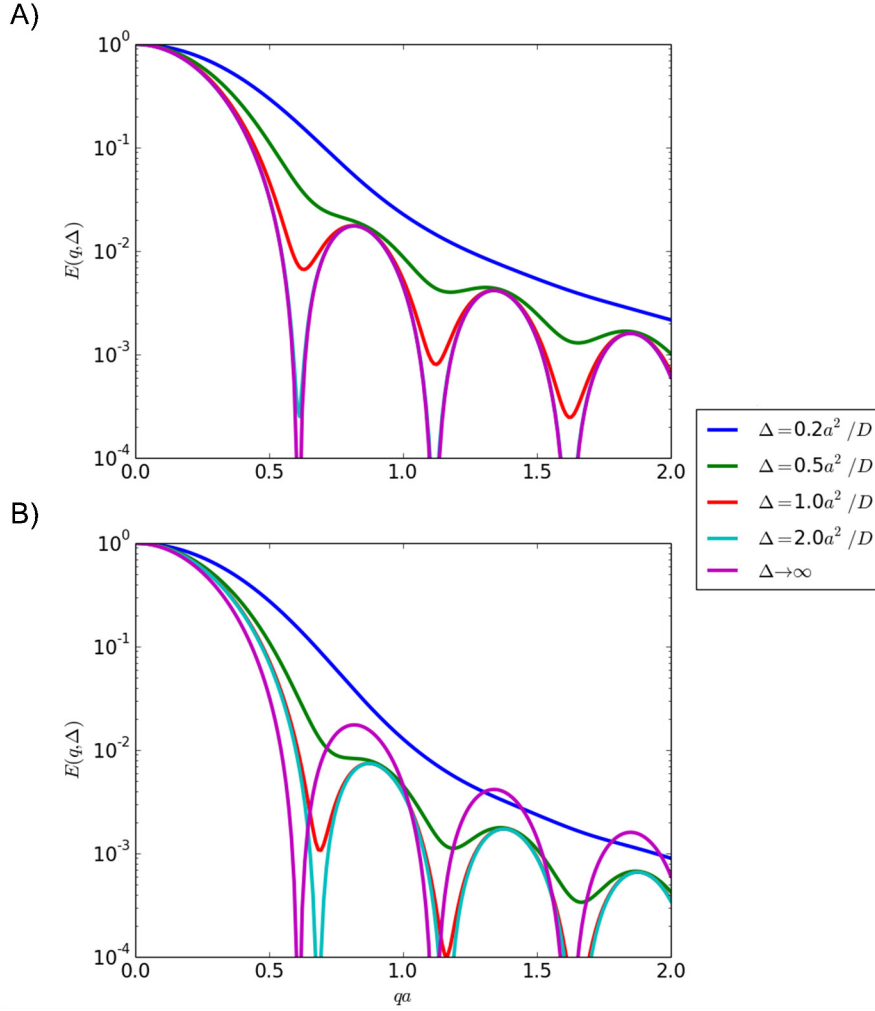


Fig. 3.6: Diffusion MRI signal from cylindrical pore without walls relaxivity (A) and with walls relaxivity leading to  $h = 2$  (B). Differences in  $\Delta$  times are color-coded.

Figure 3.6.A shows the well known dependence from  $T_D$ , that is equal to  $\Delta$  since in this experiment  $\delta$  is negligible. It is interesting to observe how the diffraction pattern reflecting the size of the cylinder becomes evident with  $\Delta$  that only slightly overcomes  $a^2/D$  (the condition according to which the particles are allowed to hit the surface). Figure 3.6.B shows the ideal signal obtained in case of NPA and

$\Delta \gg a^2/D$  without surface relaxivity. In particular it highlights, in case of the surface relaxation, the diffraction effect still evident also when  $\Delta$  only slightly exceeds  $a^2/D$ . Evidently, the relaxation reduces the magnitude of the peaks and shifts the diffraction minimum to higher values of  $q$  highlighting that the estimated apparent radius would be reduced if this effect was ignored.

We also reproduced other experiments done by Codd and Callaghan in 1999 [59] using the Multiple Correlation Function from Grebenkov [95]. In particular, in these experiments the surface relaxation was taken into account in simulations employing finite gradient pulses duration. Figure 3.7 illustrates the cylindrical dMRI signals at varying  $\Delta$ , gradient strength and surface relaxation.

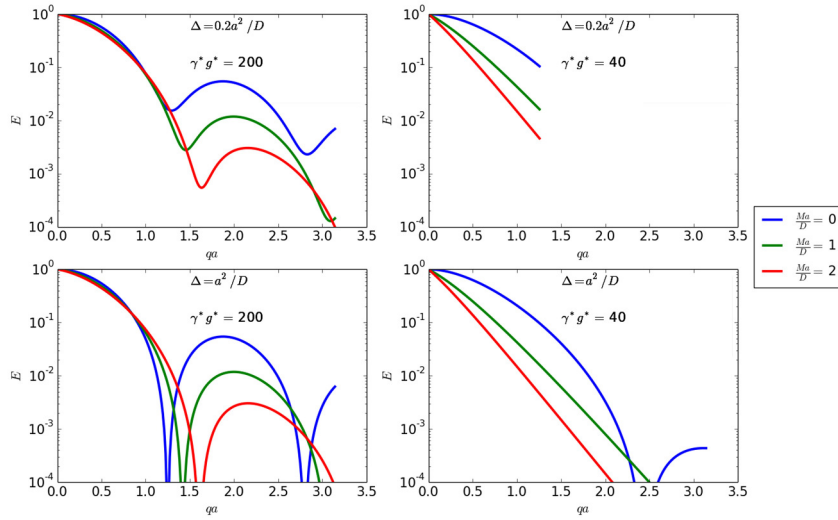


Fig. 3.7: Diffusion MRI signal from cylindrical pore varying  $\Delta$  along the rows and gradient strength along the columns. Differences in walls relaxation are color-coded.

Note that in Figure 3.7  $\gamma^*g^* = \gamma ga^3/D$  is a dimensionless gradient amplitude. As expected from the previous calculations, the walls relaxation results in an apparent narrowing of the pore and a decrease in signal magnitude.

The surface relaxivity studies are important for deep understanding the signal trend in a simple situation, but in a realistic situation such as the nervous tissue, where many micrometric structures are highly probably present in one voxel, the multi-compartment models are to be preferred.

### 3.2.2 Kärger model

The Kärger model is a multi-compartment model that represents permeability as the result of an exchange mechanism among compartments, that is throughout a diffusion flux through the walls modulated by membranes properties. The work proposed on this thesis grounds on this assumption and explores the potential of the Kärger model in predicting the exchange rate in a specific condition that will be detailed in what follows. In addition, The DKI model [113] will be considered for the estimation of the kurtosis to characterize the diffusion process. A Monte Carlo-based simulation will be used for signal generation allowing to set the reference values for the parameters of interest. Numerical simulations will be also performed on multi-compartment geometries to build a reference ground truth.

The diffusional exchange can be modeled by first order exchange kinetics equations:

$$\frac{dS_1}{dt} = -q^2 D_1 S_1 - k_{12} S_1 + k_{21} S_2 \quad (3.37)$$

$$\frac{dS_2}{dt} = -q^2 D_2 S_2 - k_{21} S_2 + k_{12} S_1. \quad (3.38)$$

These equations basically say that in the first compartment the signal is lost during the time interval due both to diffusion and to spins flowing out of this compartment (described by exchange coefficient  $k_{12}$ ) and is gained due to spins flowing back from the second compartment into the first compartment. Similarly, in the second compartment signal decay is described through inward and outward flow of spins through the permeable boundary that is ruled by the same mechanism through the exchange coefficient ( $k_{21}$ ). When this model is applied to two-compartment systems the Kärger model is retrieved [119]. The Kärger model assumes two compartments with free diffusion and no exchange during the pulses that thus must be narrow enough (or the exchange must be slow enough). The two aforementioned exchange coefficients become  $k_{ie}$  and  $k_{ei}$  to indicate the flux through intra- and extracellular spaces. Modifications to this model exist in order to account for restricted diffusion and exchange during the pulses. Among these modifications, the most used is written in a simple matrix exponential form as subsequently shown [228]. The concepts just illustrated are graphically represented in Figure 3.8.

The matrix exponential form is the following:

$$S(q, T_D) = S_0 \mathbf{1}^T \cdot \exp((-2\pi q)^2 \mathbf{D} + \mathbf{K}) T_D) \cdot \mathbf{f} \quad (3.39)$$

where  $\mathbf{1}$  is a column vector of ones,  $\mathbf{D} = \text{diag}(D_1, D_2, \dots, D_n)$  and  $\mathbf{f} = [\nu_1 \nu_2 \dots \nu_n]$  are the diffusivities and the volume fractions of the considered compartments. The exchange matrix  $\mathbf{K}$  for a two-compartment system is:

$$\mathbf{K} = \begin{bmatrix} -k_{ie} + k_{ei} \\ +k_{ie} - k_{ei} \end{bmatrix} \quad (3.40)$$

with  $\nu_i k_{ie} = \nu_e k_{ei}$  in equilibrium conditions. The exchange time is derived as  $\tau = k_{ie}^{-1}$  and it will be detailed in the Section 3.2.4. The restriction is accounted for through the diffusivity in the compartments as dependent by the diffusion time.



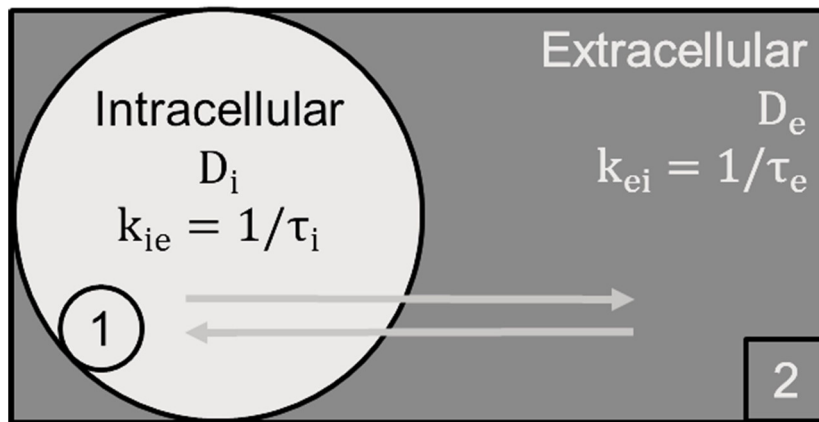


Fig. 3.8: Illustration of the two-compartments exchange model on which Kärger model grounds.

### 3.2.3 Other strategies

It is important to say that other strategies different from the explicit modeling of the more classical PGSE diffusion signal were recently employed for extracting parameters related to permeability.

Except for the numerous different implementations of the numerical simulations in which what substantially varies is the considered geometry, a strategy recently employed is based on machine learning. This allows to avoid direct signal modeling by learning a mapping between microstructural parameters of interest and features derived by DWI data rather than from Monte Carlo simulations. One example is the training of a random forest regressor on simulations where exchange was allowed as in numerical simulation method and then applied to real data to extract the intracellular residence time [146].

Another important strategy is grounded on the recent imaging techniques as described in Section 2.2.3 such as FEXI which is able to retrieve the AXR that is proportional to the total exchange rate constant. However, the recruitment of specialised diffusion encoding sequences were out of scope of this thesis [128, 152].

### 3.2.4 Numerical simulation

Numerical simulations like Monte Carlo can be used to mimick the dynamics of the spins following a given model. From a microscopic point of view, permeability is the probability that a spin that moves from the intracellular to the extracellular compartment completes the transition. The exchange time  $\tau$  is expressed as the probability of the transition to take place in the unit time. Formally [149]:

$$p_{ic2ec} = \left( \frac{n_{tot}}{n_{out}} \right)_{ic} \frac{\Delta t_{ic}}{\tau_{ic}} \quad (3.41)$$

where  $n_{tot}$  is the total number of particles in the intracellular compartment,  $n_{out}$  is the total number of particles that exit the intracellular compartment,  $\Delta t_{ic}$  is the simulation unit time, that is the intracellular compartment time step and  $\tau_{ic}$  is the intracellular residence time. Similarly, the probability that the particle completes a transition from the extracellular compartment to the intracellular compartment is obtained by multiplying it by the ratio between discretization times (they could be different). In terms of membrane permeability,  $p_{ic2ec}$  is derived as [149]:

$$p_{ic2ec} = \frac{K \Delta x}{D_{ic}} = \frac{2n_d V}{\Delta x A} \frac{\Delta t_{ic}}{\tau_{ic}}. \quad (3.42)$$

When assuming  $K = \left( \frac{1}{\tau_{ic}} \right) \cdot \left( \frac{V}{A} \right)$  ( $V$  and  $A$  are the volume and surface of the compartment respectively) and  $n_d = 2$  (the number of system dimensions) [174], Equation 3.42 is approximately equivalent to Equation 3.41.  $\Delta x$  is the space discretization of the simulation and  $D_{ic}$  is the diffusivity. Barzykin et al. [21] already formalized this relationship as the diffusional permeability for a cell.

Further details on some of the used simulation models in the field of permeability in WM will be provided in Section 4.2.

### 3.2.5 The issue of observability

Given the interest in interpreting data regarding an organ with such a complex tissue like the brain where a very high number of structures are continuously in communication, our attention focused on multi-compartment models of permeability that, in our opinion, better represent the issue that we would like to address.

In this context, it is important to explore some conditions of observability of the permeability parameters and in particular of the exchange time. Moreover, some limitations regarding the Kärger model are here reported for a better understanding of the most common used model for the exchange time estimation.

Generally, an accurate estimate of the exchange time requires experiments employing long diffusion times and high values of gradient pulse strength [152]. Nilsson and colleagues [149] found that exchange time based on simulations resulted accurate when in the same order of magnitude of the diffusion time, which is easily understandable thinking to the impossibility of being sensible to an exchange time much longer than the observed. Furthermore, the high gradient pulse strength allows for the observability of fast exchange since it becomes potentially more sensible to finer structures as suggested by the higher kurtosis of the diffusion signal [131, 83].

A consequent issue with these conditions is about the MRI scanner constraints, in particular with the difficulty to impose long diffusion times and high gradient strength in a clinical setting. As simple example, the long diffusion time can dramatically increase the acquisition time which can easily become unfeasible in a clinical setting. Another important factor that cannot be neglected is  $T_2$  relaxation during the diffusion time acting as a strong attenuation of the diffusion

signal and that can only be partly avoided by using PGSTE instead of classical PGSE.

In addition, the Kärger model originally grounds on assumptions like the mixing of the exchanging compartments in order to have equal transition probability for all the particles [119]. In this context, the parameters calculation can suffer because of the restriction of the brain tissue. However, the restriction can be added as mentioned in the previous Section, but Fieremans et al. [83] already commented on the need of having the intracellular exchange time  $\tau_i$  satisfying the condition  $\tau_i \gg d^2/2D_i$  ( $d$  is the axon size and  $D_i$  the intracellular diffusivity) which translates in having a barrier limited exchange in a compartmental system.

In this scenario, it is thus even more relevant to understand the effective sensitivity of the dMRI signal in affordable situations. The numerical simulations can be really helpful in this study to understand the extent to which the parameters of interest can be reliably inferred.

### 3.3 Scientific objectives

The state of the art summarized here highlights the extended use of simplifications in models for the dMRI reconstruction. In consequence, care must be taken in the interpretation of the results. One of this simplification is the assumption of perfectly reflecting and impermeable axon walls despite some experiments highlighted the limitations implied by such assumption [152, 146]. The investigation through models involving the possible exchange between compartments allows us to bring novelty in theoretical and clinical areas.

#### 3.3.1 Theoretical objectives

More in detail of theoretical objectives of this thesis, the overall objective is to shed light on the reliability of no-exchange assumption in the WM tissue. First we aim at investigating the permeability concept in dMRI. This is important for shedding light on the interpretation of real data in which exchange can plausibly play a role.

The exploration of the sensitivity of the dMRI signal to such mechanism should open the way to added awareness to be exploited in new signal models. Therefore, we want to characterize when exchange is necessary in WM modeling.

Another objective concerns the strict relationship between exchange and barrier through which it takes place, and thus we are interested in a deepening in the myelin impact in dMRI as constituting the most important biological barrier in WM.

#### 3.3.2 Clinical objectives

From a clinical perspective, the investigation of the relationship between the tissue structure and the model derived indices (such as the FA) becomes particularly relevant in interpreting data from subjects with pathologies (e.g. stroke). In this context the definition of indices holding the potential for being possible biomarkers

would be important in the clinical practice. Then, we explore 3D-SHORE indices for characterizing their potential as biomarkers in stroke disease.

Aiming at this objective, a pipeline is proposed able to quantify this suitability through the calculation of their precision, sensitivity, specificity and predictability of clinical outcome.

Another important step to reach the first objective is the specific tissue representation by model-based indices that we explore via analysis on WM and GM separately.

**Signal modeling in Diffusion MRI**



## Materials and methods

In this Chapter, first, the premises and rationale of the proposed study are discussed. Then, the proposed methods are presented, together with the motivations at the basis of our choices and the details of the experiments are provided. The contents of this Chapter are in part published in an accepted abstract to ISMRM conference [39], a submitted paper to EUSIPCO and a submitted journal to TMI.

### 4.1 Premises

Diffusion in brain depends on the neural tissue morphology. In the ventricular system, where the space is constituted by cavities, the CSF is free to diffuse in all directions according to Brownian motion. In the *soma* of the neurons water equally diffuses in all directions displacing distances confined by the *quasi*-spherical shape of the cell. The same probably happens also in all the other cells of the neural tissue such as the neuroglial cells. Differently, in the axons forming fibers, diffusion takes place in an elongated structure and results in an anisotropic process being the diffusion approximately free along the tract and restricted in the radial direction.

The water exchange through barriers is another kind of diffusion extremely important for maintaining the water level constant in spite of its loss or formation caused by the metabolic processes. Even if the biological lipid membranes are a significant barrier for movements into and out of cells due to their characteristic hydrophobicity, a low permeability is anyway present. Furthermore, thanks to Fick's law according to which the rate of diffusion is proportional to the concentration gradient, the naturally high ratio between cells surface area and volume and high concentration of water molecules inside cells facilitate this phenomenon [52]. Moreover, an important role is played by a family of proteins called "aquaporins" (AQP) which regulates the transport through membranes. In particular, three different types of aquaporins were found in brain and participate to its physiological functioning demonstrating their potential as target for drug discovery [193]. Badaut and colleagues [19] showed that the inhibition of the expression of one of this three types arousing a 27% aquaporin silencing caused a 50% decrease in *ADC* values despite the tissue remained intact. This proves the dMRI sensi-

tivity to diffusional exchange through the brain barriers, boosting the interest of discovering specific descriptors for permeability modeling in the nervous system.

Myelin constitutes a barrier to exchange between axon and extracellular tissue having a particular multi-wrappings structure in the direction transversal to the length of the axon and interrupted along its length in nodes of Ranvier [75, 164]. Nilsson and colleagues [148] showed by Monte Carlo simulations that these gaps constitute a possible exchange mechanism especially necessary for small axons having diameters below  $4.0 \mu\text{m}$  and short nodal distances below  $100.0 \mu\text{m}$  for which the exchange time ( $\tau$ ) is in the 10-400 ms range. Moreover, a study by Guo et al. [98] demonstrated the possible rise of myelin permeability due to deficiency of the peripheral myelin protein-22 (PMP22) according to which myelin remains intact but the myelin junctions are disrupted. This augmented permeability constitutes a realistic biological case in which the role of the barrier might be investigated. However, the multi-wrapping myelin nature effect on dMRI signal remained unexplored apart one case in which this conformation was only implicit [101]. Specifically, Harkins and Does represented the anisotropy of this structure allowing a circumferential diffusion higher than radial one and they highlighted how myelin can slightly influence DWI. Furthermore, they hypothesized that myelin water exchange can complicate the interpretation of dMRI sensitivity to myelin.

Another complication factor is  $T_2$  relaxation. More in detail,  $T_2$  describes the loss of phase coherence in the transverse magnetization and depends on several factors including the tissue density or the lipid composition among others [64]. The richness of lipids in myelin sheath is considered to be one of the main factors responsible for the WM shorter  $T_2$  compared to GM [163]. This reason led to the assumption that the signal contribution due to myelin is not observable in the observation time and thus to not take it into account in signal modeling.

However, the relationship between  $T_2$  and exchange seems to be more complex and its role deserves further investigation. In particular, Levesque and Pike [132] performed pathology-inspired analyses on simulations representing disease arousing increased exchange. They found that myelin water fractions and  $T_2$  values decreased for greater exchange concluding that myelin water fractions could be incorrectly related to changes in myelin content. Harkins et al. [102] also studied this relationship finding a linear correlation between  $T_2$  profile and water volume fractions as measured by histological studies of rat spinal cord. They nevertheless found an overestimation of water fractions that could be reasonably attributed to exchange since other myelin markers did not explain the changes in myelin contents.

## 4.2 Rationale

The microstructure characterization of the neural tissue based on a given signal in dMRI research is an inverse problem. Jelescu et al. [112] showed how the signal models seen in Chapter 3 suffer from the lack of specificity although they are sensitive to the microstructural modifications. They correctly said that, for example, given a FA or MK change from a portion of WM we cannot determine if it was due to demyelination, axonal degeneration, inflammation, as well as others.



There are some examples of studies highlighting this: Paus discussed the inherent ambiguity in the interpretation of the DTI-derived metrics changes in WM growing in adolescent brain, making impossible to disentangle between myelin- or axon-related processes [164]. Norris showed how similar microstructural indices alterations can have different causes at a mesoscale level (e.g. lower permeability and cell swelling) [154]. Badaut et al. found that MD decreased after the inhibition of specific brain membrane proteins for the water transport. Nevertheless, many dMRI signal models do not take into account the permeability [19]. In this context, simulations and numerical methods are very useful tools for a controlled exploration of a model performance, and therefore they aid in the understanding of the possible tissue configurations. For this reason, in this work, numerical simulations were used for investigating the spiraling myelin as a model to explain the exchange mechanism. This allows characterizing the dMRI sensitivity to specific myelin structure changes being aware of the limitations of the model.

Prior works have often modelled exchange as a direct jump from the intra-axonal to extracellular space, without considering a volume for the third compartment representing the myelin. As example, Fieremans et al. [83] investigated the relationship between Kärger model and a WM-inspired geometry by randomly packed identical parallel cylinders with permeable walls. Nilsson et al. in a first work compared the estimation of Kärger model in uniformly sized cylinders with different diameters and exchange, and the  $\tau$  estimates obtained by fitting *in-vivo* dMRI data of the corticospinal tract [151]. In a second work they evaluated the performance of the same model against a model based on a collection of simulations from different instances of the same aforementioned substrate [149]. Nedjati-Gilani and colleagues [146] extracted  $\tau$  from healthy and multiple sclerosis diseased subjects using either the Kärger model or a random forest regressor trained on simulated collections of non-abutting parallel cylinders with radii drawn from a gamma distribution having different values of surface permeability. They concluded that machine learning improves the estimation of exchange time but care must be taken about the dependence on the substrate used for the regressor training that makes the sensitivity highly specific. Some approaches have included more complex simulations. Nilsson et al. investigated water exchange only at the interruptions of myelin called nodes of Ranvier [148]. Other approaches treated the myelin as a third compartment with free diffusion whose own diffusion coefficient could have an effect on the overall DWI signal. More in detail, Hwang et al. [106] developed an image-based diffusion simulation method which allowed the generation of substrate on the basis of histologic images with different diffusivity in each compartment including the myelin sheath; Sen and Bassler [182] proposed a model for diffusion in white matter as an array of identical thick-walled cylindrical tubes periodically arranged in a regular lattice and inserted in a outer medium; Peled [165] studied a tensor model with an added baseline correlating with intra-axonal water volume on a geometry composed by coated parallel identical cylinders in a hexagonal lattice where particles were allowed to diffuse inside and through compartments; Baxter and Frank [26] added, to the analysis described by Sen and Bassler, the observation of different spin concentration for each compartment effect. To the best of our knowledge, only the aforementioned study by Harkins and Does [101] paid attention to the multi-wrappings nature of the myelin, albeit implicitly, by

modelling diffusion in myelin as anisotropic with a higher diffusivity in the tangential compared to radial direction [101]. However, the latter works modeling myelin sheath volume investigated its impact from a limited point of view without paying attention to  $\tau$  estimation.

Our work goes further in the modeling of myelin structure in order to explore the conditions or configurations under which the myelin wrapping permits fast exchange, defined as sub-second  $\tau$ . The strategy chosen was to perform Monte Carlo simulations in which the myelin was realized as a spiral along which the water molecules could diffuse freely. This approach thus reproduced the histologically known structure of myelin. The dependence of the intra-to-extra axonal  $\tau$  was explored while varying parameters of the geometry. Diffusion-weighted signals from a PGSTE sequence [194] were then simulated with experimental parameters applicable with clinical MRI scanners. The data were subsequently analysed with the DKI model [113] and the modified Kärger model [118]. DKI was fitted aiming to understand the dMRI signal model specificity in capturing myelin modifications by effects on the most popular brain descriptors such as apparent diffusion coefficient and apparent kurtosis; Kärger model is instead the most used method for specifically capturing exchange time despite the limitations already discussed in Chapter 3. Effects of  $T_2$  relaxation on the signal were also investigated in order to explore a realistic situation.

### 4.3 Methods

We can summarize our strategy in the following pipeline illustrated in Figure 4.1 as follows:

- i) Definition of the geometrical substrate and simulation of water dynamics using Monte Carlo according to the chosen acquisition sequence;
- ii) Recording of the number of intra-axonal particle concentration as a function of time;
- iv) Fitting of the Kärger and DKI models to the resulted signal and corresponding microstructural indices derivation;
- v) Evaluation of models performance by comparison between the substrate parameters and the fitted ones.

#### 4.3.1 Geometry and water dynamics setup

Starting from the first step of our pipeline, we constructed the spiraling myelin simulation geometry as comprising three compartments: intra-axonal, extra-axonal and myelin, as illustrated in Fig. 4.2. We chose the simplest representation of WM constituted by parallel identical cylinders since in this work we just wanted to investigate the suitability of spiraling myelin as exchange mechanism. We leave for the future work a more complex implementation in order to see the interaction of the many variables that naturally affect the biological tissue. In the following Section we describe the details of the geometry implementation from a top-down

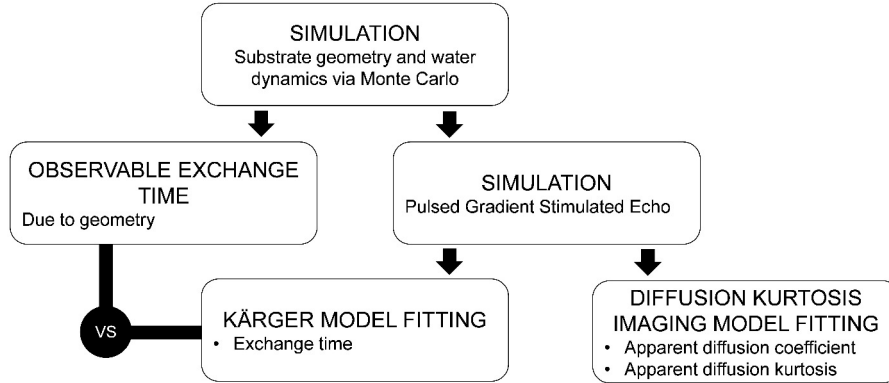


Fig. 4.1: Pipeline for investigating spiraling myelin feasibility as exchange mechanism.

perspective in three levels of in-depth analysis: i) the periodic structure, ii) the substrate, iii) the myelin.

The periodic structure was managed by imposing periodic boundary conditions and consisted in an infinite number of two-dimensional transversal sections of parallel “axons”. More in detail, the periodic boundaries were implemented by updating the absolute  $x$ - and  $y$ -coordinates of the spins with the addition or subtraction of one step according to the respectively reached upper or lower bound of the cell unit. A second pair of variables representing the  $x$ - and  $y$ -coordinates within the cell unit were updated adding or subtracting the entire cell unit width according to the reached lower or upper bound.

In detail, the substrate consisted of unit cells where each unit cell consisted of a square tile modeling the extracellular tissue surrounding the axon (intra-axon and myelin) placed at the center. The width of the square ( $s_{\text{width}}$ ) was a turneable parameter, together with the axon inner diameter ( $d_{\text{inner}}$ ) and the  $g$ -ratio ( $g$ ). The  $g$ -ratio corresponded to  $g = d_{\text{inner}}/D_{\text{outer}}$ , where  $D_{\text{outer}}$  was the diameter of the structure including both axon and myelin. Tuning the three aforementioned variables was thus possible to assign the desired volume fractions to the substrate and viceversa, with the limits given by the space discretization. Another turneable parameter was the number of myelin wraps ( $n_{\text{wraps}}$ ) around the axon of the considered thickness. Therefore, the variables of the model were:  $s_{\text{width}}$ ,  $d_{\text{inner}}$ ,  $g$ -ratio and  $n_{\text{wraps}}$ . Throughout this work, the  $g$ -ratio was set to  $g = 0.7$  as discussed in Section 2.1. Then,  $\nu_{ic}$  was set to  $\nu_{ic} = 0.45$  and  $s_{\text{width}}$  was derived accordingly, while  $d_{\text{inner}}$  and  $n_{\text{wraps}}$  were varied. Figure 4.2.A shows an example of the geometry varying  $d_{\text{inner}}$  and  $n_{\text{wraps}}$ , maintaining  $g$ -ratio and  $s_{\text{width}}$  constant. Figure 4.2.B shows a portion of the substrate with infinite size resulting from the application of periodic boundaries to the unit cell.

Going into details of myelin implementation, a one-dimensional spiraling compartment was chosen for its model. This choice was done to overcome the space representation limit due to difference in size between axon and myelin which cov-

ers several orders of magnitude. An idea of this difference is given by the size of extracellular space placed between the myelin wraps that is around 30.0 nm [164] and the axon diameters which generally measure up to 4.0  $\mu\text{m}$  [133]. Figure 4.2.C illustrates the geometrical equivalence of the described substrate model.

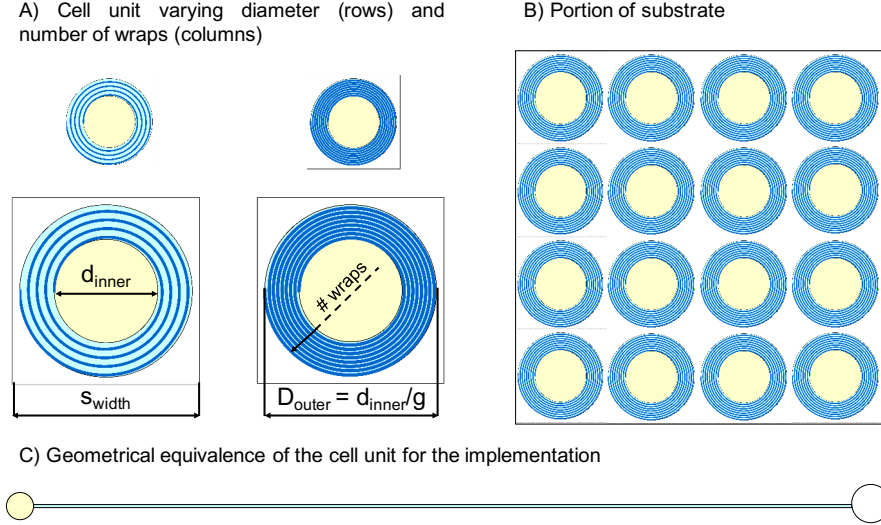


Fig. 4.2: Simulation setup. A) Changes of the axon diameter and number of wraps are illustrated across rows and columns, respectively. B) Periodic boundary conditions. C) Rectified myelin wraps as in the implementation.

After the geometry specification, we go into details of the water particles dynamics. Specifically, this implementation involved the definition of three principal conditions of possible movements.

The first and more common condition was the case of particles moving inside axonal or extra-axonal space. All particles positions were incremented of one step along a direction randomly chosen in the  $xy$ -plane at each time step.

The second condition is peculiar for particles movements inside the myelin. Positions within the myelin spiral were parameterized as

$$x = \left( \frac{d_{\text{inner}}}{2} + s\theta \right) \cos(\theta) \quad (4.1)$$

$$y = \left( \frac{d_{\text{inner}}}{2} + s\theta \right) \sin(\theta) \quad (4.2)$$

where  $s$  was the spacing between each arm [ $s = (D_{\text{outer}} - d_{\text{inner}})/(4\pi n_{\text{wraps}})$ ] and  $\theta$  the angle turned by the spiral. The length of the spiral was calculated by solving

$$L = \int_0^{2\pi n_{\text{wraps}}} \sqrt{s^2 + \left( \frac{d_{\text{inner}}}{2} + s\theta \right)^2} d\theta. \quad (4.3)$$

The length of the spiral was divided by  $\Delta x$  that is the space discretization of the simulation, and the particles were then allowed to diffuse along  $L$ . Positions of the particles inside the myelin were updated according to  $x$ - and  $y$ -coordinates obtained by cosine and sine of the angle just turned calculated as

$$\theta_i = l_i \Delta x / L n_{\text{wraps}} 2\pi \quad (4.4)$$

where  $l_i$  is the position along the spiral.

Exchange was implemented by allowing transition from axon to myelin ( $p_{a2m}$ ), from myelin to axon ( $p_{m2a}$ ), from extra-axon to myelin ( $p_{e2m}$ ) and from myelin to extra-axon ( $p_{m2e}$ ) at specific points in the axon and extra-axonal space (Figure 4.3). These probabilities were constrained by equilibrium conditions of mass balance according to:

$$m_m \cdot p_{m2a} = m_a \cdot p_{a2m} \quad (4.5)$$

$$m_m \cdot p_{m2e} = m_e \cdot p_{e2m} \quad (4.6)$$

where  $m_m$ ,  $m_a$  and  $m_e$  are the total number of particles ("masses") in the myelin, axon and extra-axonal space, respectively. Since the myelin space was represented differently from the axon and extracellular spaces, the initial particle concentrations in each space was computed by counting pixels (the volume units in the two-dimensional model) occupied by each compartment multiplied by its water concentration. For myelin, the concentration depended on the ratio between the probability to enter and leave it. These were computed as follows:

$$p_{m2a} = 1.0 \quad (4.7)$$

$$p_{a2m} = p_{m2a} \cdot \frac{a_m}{a_a}$$

$$p_{m2e} = 1.0$$

$$p_{e2m} = p_{m2e} \cdot \frac{a_m}{a_e}$$

These probabilities depend on the exchange rate and the permeable area, according to which they are directly proportional as discussed in Section 3.2.4 [11]. We assumed no hindrance for particles entering the myelin, except that the "cross sectional area" of the myelin layer was smaller than the simulated voxels. Thus, the axon-to-myelin transition area ( $a_m$ ) was computed as the width of the passage into myelin relative to pixel size (discretizing the size of the extracellular space existing between myelin wraps that is 30.0 nm [164]). The myelin-to-axon and myelin-to-extra transition areas ( $a_a$  and  $a_e$ ) were defined as the fraction of steps that yield a transition.

### 4.3.2 Estimation of observable $\tau$

The second step of our pipeline was the computation of the observable exchange times by recording the flow of intra-axonal particles through the spiralling barrier as a function of time.

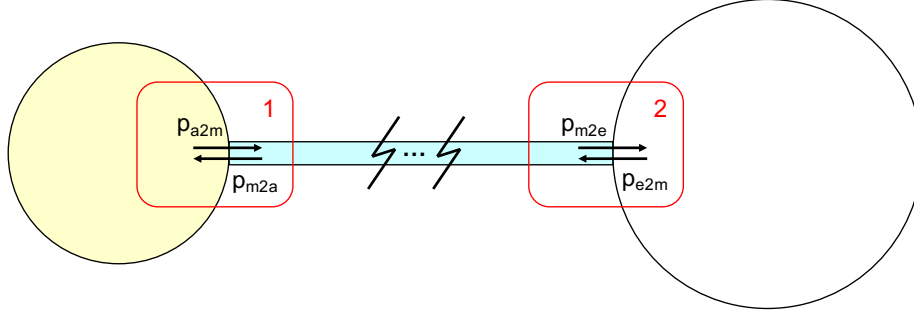


Fig. 4.3: Exchange setup. Referring to the geometrical equivalence of the cell unit for the implementation, the impermeability of the myelin walls is shown except for the myelin-to-axon and the myelin-to-extra areas highlighted by areas 1 and 2 respectively. In these areas, particles flow is allowed in both the directions.

The first set of numerical experiments were designed to probe how the intra-axonal residence time depends on myelin properties. Particles were here initialized in the intra-axonal and myelin compartments only. Flow to the extra-axonal space was allowed, but particles were not allowed to re-enter. This setup gives an unbiased measure of the exchange time [149]. Random walks were then simulated for a period of 200 ms and the number of intra-axonal particles as a function of time was recorded. The exchange time  $\tau$  was estimated from the following relation,

$$n(t) = n_0 \exp(-t/\tau), \quad (4.8)$$

via polynomial fitting in a least-squares sense, where  $n(t)$  is the number of resident particles at time  $t$ .

Effects on the exchange time were investigated in two conditions. First we investigated the impact of the number of myelin wraps ( $\tau$  versus  $n_{\text{wraps}}$ ), and then of the axon diameter ( $\tau$  versus  $d_{\text{inner}}$ ). In the first case,  $d_{\text{inner}}$  was varied between 1.0 and 2.0  $\mu\text{m}$  and  $n_{\text{wraps}}$  was set to 1, 2, 4, 8, 16 and 32. In the second case  $n_{\text{wraps}}$  was varied between 1 and 4 and  $d_{\text{inner}}$  was 1.0, 2.0 and 4.0  $\mu\text{m}$ .

The results were related to values found in literature or to values derived from our calculations from Equation 2.1 in Section 2.1 reporting a review on myelin structure characteristics (i.e. diameter, number of wraps, etc.).

### 4.3.3 Signal decay

Microstructure information in dMRI is encoded in the signal attenuation due to a phase dispersion caused by the interaction of magnetic field gradients and diffusing spins. The Monte Carlo simulations model the process by using particles mimicking the behaviour of the spins and carrying the phase information  $\phi$ . Then, the signal is derived as

$$S(G) = \frac{1}{n} \sum_{k=1}^n \exp(-i\phi_k), \quad (4.9)$$

where  $n$  is the number of particles,  $i^2 = -1$ , and

$$\phi_k = \gamma \sum_i^m g_i x_i \Delta t \quad (4.10)$$

where  $\gamma$  is the gyromagnetic ratio,  $g_i$  the magnetic-field gradient discretized into  $m$  time points,  $x_i$  the position of the particle, and  $\Delta t$  is the time discretization of the Monte Carlo simulation.

The acquisition sequence was the PGSTE which uses two  $90^\circ$  RF pulses replacing the  $180^\circ$  one and a spoiler gradient. This led to a higher signal conservation than the classical PGSE for large enough diffusion time, which is an advantage when  $T_2$  is short as in myelin [5]. The signal is commonly analysed as a function of the  $b$ -value, given by [188]:

$$b = \gamma^2 \delta^2 G^2 T_D. \quad (4.11)$$

The attenuation due to  $T_2$  relaxation was accounted for. In particular, the time spent in each compartment was tracked for each particle and the corresponding diffusion signal was multiplied by  $\exp(-\Delta t/T_2)$ , where  $T_2$  was the relaxation time that depends on the compartment [101]. The use of the PGSTE sequence allowed us to avoid  $T_2$  decay during time between the two gradient pulses.

Therefore, the overall simulated signal is

$$S(G) = \frac{1}{n} \sum_{k=1}^n \exp(-i\phi_k) \exp(-\Delta t/T_2). \quad (4.12)$$

The aforementioned geometries with varying  $d_{\text{inner}}$  and  $n_{\text{wraps}}$  underwent one-dimensional PGSTE acquisition in perpendicular direction with respect to the main diffusion direction. The diffusion times were  $\delta = 15$  ms and  $\Delta = 25, 55$  and  $225$  ms, respectively.

#### 4.3.4 Model fitting

We fitted our data with two different models: DKI and Kärger models. The two models allow the estimation of different parameters from the same data enabling the study of the same experimental condition from two different perspectives. More in detail, the DKI model permitted the derivation of  $RD$  and  $RK$ , while the Kärger model allowed the  $\tau$  calculation among the others.

#### RD and RK estimates

The DKI model [113] was fitted to the PGSTE simulated signal for  $\delta = 15$  ms and  $\Delta = 25$  ms for two different choices of myelin  $T_2$  relaxation [101, 190, 137, 206]: short ( $T_2 = 15$  ms) and long ( $T_2 = 85$  ms).  $T_2$  of axon and extra-axon compartments were both set to 85 ms as in [101].

Since we are focusing on one-dimensional acquisitions perpendicular to the axis of the axons, Equation 3.8 can be reformulated as in [113] replacing the two tensors with  $RD$  and  $RK$  respectively:

$$S(b) = S_0 \cdot \exp \left[ -b \cdot RD + (b \cdot RD)^2 RK/6 \right] \quad (4.13)$$

where  $RD$  and  $RK$  were respectively the radial diffusivity and kurtosis. The free parameters of the model are  $S_0$ ,  $RD$  and  $RK$  and were retrieved through nonlinear curve-fitting in least-squares sense via the Levenberg-Marquardt algorithm.

In addition, the apparent fiber density ( $AFD$ ) was calculated as the diffusion signal value at the highest  $b$ -value (in this case equal to 2500 s/mm<sup>2</sup>). It was already demonstrated that this measure calculated in radial direction with respect to the substrate is a measure of  $\nu_{ic}$  [173].

### $\tau$ estimation

The PGSTE simulated signals were used to fit the Kärger model [118]. More in detail, the two-compartments model was the same as defined by Nilsson et al. [149] and already illustrated in Section 3.2.2. The two-compartments version of Equation 3.39 can be re-written as:

$$S(b) = S_0 \begin{bmatrix} 1 & 1 \end{bmatrix} \exp(-b \cdot \mathbf{ADC} + \mathbf{K} \cdot T_D) \begin{bmatrix} \nu_{ic} \\ \nu_{ec} \end{bmatrix}. \quad (4.14)$$

The  $\mathbf{D}$  matrix in Equation 4.14 is defined as follows:

$$\mathbf{ADC} = \begin{bmatrix} ADC_{ic} & 0 \\ 0 & ADC_{ec} \end{bmatrix} \quad (4.15)$$

with  $ADC_{ic}$  calculated as in [149] and thus as  $ADC_{ic} = [d \cdot \kappa(\alpha, \beta)]^2 / 2T_D$  where  $\kappa(\alpha, \beta)$  is the Gaussian phase distribution approximation [205].  $ADC_{ec}$  is one of the free parameters of the model and is formalized as  $ADC_{ec} = D_{ec}/\lambda^2$ , where  $\lambda$  is the tortuosity factor of the extracellular space. The  $\tau$  parameter to be estimated is embedded in the  $\mathbf{K}$  matrix. This matrix describes the exchange between two compartments through exchange rates between the intra- and the extracellular compartments. In the equilibrium condition, no net flux is present thus the following relation holds:  $k_{ec}\nu_{ec} = k_{ic}\nu_{ic}$ . Reminding that the permeability  $K$  can be written as in Section 3.2.4 as  $K = k_{ic} \left(\frac{V}{A}\right)$  [21] and is expressed in  $\mu\text{m}/\text{s}$ ,  $k_{ic}$  is the reciprocal of a time and in particular of  $\tau$  that is the intra-axonal residence time.

Overall, the free parameters  $S_0$ ,  $ADC_{ec}$ ,  $\tau$  and  $\nu_{ic}$  can be recovered by nonlinear curve-fitting in the least-squares. In our implementation this was performed by the trust-region-reflective algorithm [149]. Usually, the diameter is a free parameter of the Kärger model. However, in our implementation it was set to  $\sim 0$  because it would not have been observable under the considered experimental condition [150].

500 instances of Gaussian noise ( $SNR = 40$ ) were added to each instance of the resulting diffusion signal and the 5<sup>th</sup> and 95<sup>th</sup> percentiles of the estimated parameters distributions were calculated.



---

## Results and discussion

In the following Sections we first demonstrate the reliability of our simulator by some unit tests. Then, the results obtained from the experiments illustrated in Chapter 4 are reported and discussed.

### 5.1 Monte Carlo simulator validation

The number of particles used in the next unit tests and experiments was 100000,  $D = 2.0 \mu\text{m}^2/\text{ms}$ ,  $\Delta x = 0.05 \mu\text{m}$  and 100 equally spaced  $b$  values were chosen from 0 to 2500  $\text{s}/\text{mm}^2$ . The same classical pulsed gradient spin echo (PGSE) acquisition sequence [188] was employed with the pulses duration chosen as short as possible for comparing our simulation with the theoretical signals under the NPA [ $\delta \sim 1.5 \exp(-2)$  ms], while the delay between the pulses was  $\Delta = 20.0$  ms.

#### *Free diffusion*

Free diffusion was characterized through particles placed in the extra-axonal space. The recovered signal was compared to the theoretical one  $S(b) = \exp(-bD)$  by computing the mean square error ( $MSE = \frac{\sum_{i=1}^N (sim_i - the_i)^2}{N}$ , where  $sim_i$  and  $the_i$  are the  $i$ th element of the simulated and theoretical signal respectively and  $N$  corresponds to their length). The width of the substrate unit was  $100.0 \mu\text{m}$  and  $d_{\text{inner}} = 0.5 \mu\text{m}$ . Therefore, the simulation geometry had preponderance of extracellular tissue and movements were allowed only within it since the particles were initialized only in this compartment and the transition probabilities were zero-outed. The simulated and theoretical signals representing free diffusion are reported in Figure 5.1. The  $MSE = 2.6 \exp(-5)$  proves the goodness of the simulation.

#### *Restricted diffusion*

Restricted diffusion signal was characterized from particles placed inside the axon. The theoretical diffusion signal inside a cylinder was used as reference [140]:

$$S = \left( \frac{2 \cdot J_1(\pi q d_{\text{inner}})}{\pi q d_{\text{inner}}} \right)^2 \quad (5.1)$$

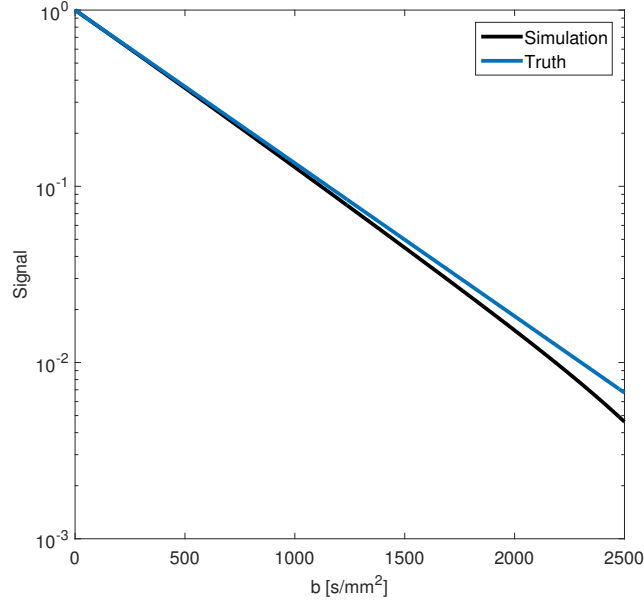


Fig. 5.1: Free diffusion signal simulation (*black*) and theoretical one (*blue*).

where  $J_1$  was the Bessel function of the first kind and order 1. The simulation geometry had  $d_{\text{inner}} = 2.0 \mu\text{m}$ , and zero-outed transition probabilities. The restricted diffusion signals corresponding to Monte Carlo simulation and Equation 5.1 are shown in Figure 5.2. The corresponding MSE was  $MSE = 6.0 \exp(-7)$ .

#### *Transition between compartments*

The transition between compartments was tested initializing the particles in the whole substrate and recording their number in the different compartments during 200 ms. The test was performed for two cases: transition probabilities different from zero, and equal to zero, respectively. Figure 5.3 represents the number-of-particles versus time curve for each compartment in both the aforementioned cases. The slope of each curve was computed as the rise over run and resulted  $\sim -2$  for the curves representing the extra- and intra-axon trends and  $\sim 3$  for myelin one in the exchange condition, and  $\sim 0$  for the three ones in the no-exchange condition. Correctly, the curves do not show decay or other variations as expected at equilibrium in the case of allowed transition. The same is expected also in the case of no-exchange due to absence of transition and thus no concentration variations in time.

#### *Time tracking*

The same simulation set of the restricted diffusion validation test was also used to check the particle time tracking with particles distributed in all compartments.

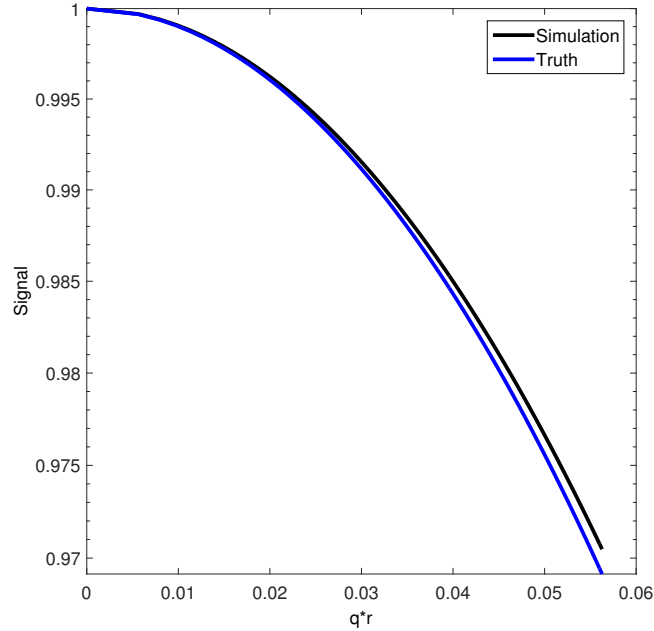


Fig. 5.2: Restricted diffusion signal simulation (*black*) and theoretical one (*blue*).

The time spent in each compartment was compared to the total time required for the acquisition sequence ( $T_{\text{tot}}$ ). Since no transition was allowed, the two times should both result equal to  $T_{\text{tot}} = 2\delta + \Delta$  ( $\sim 20$  ms). The satisfaction of this relation proved the correctness of the time tracking in our framework.

### $T_2$ relaxation

Free and restricted diffusion with addition of  $T_2$  relaxation of 85 ms [166] were tested to evaluate this effect on simulations. More in detail, the theoretical diffusion signals of the two validation tests were respectively multiplied by  $\exp(-T_{\text{tot}}/T_2)$  where  $T_2$  was the relaxation time of the compartment in exam. The signals were compared by computing MSE. Figure 5.4 illustrates the simulated and theoretical signals normalized to the maximum value respectively for both cases of free and restricted diffusion with  $T_2$  relaxation. The computed MSEs were respectively  $1.6 \exp(-5)$  and  $5.5 \exp(-7)$  demonstrating the good performance of the Monte Carlo simulator.

## 5.2 Results

### 5.2.1 Estimation of observable $\tau$

Figure 5.5A shows observable  $\tau$  values as a function of  $n_{\text{wraps}}$  for two different  $d_{\text{inner}}$ . In particular, water particles flow out from axons with a lower rate adding

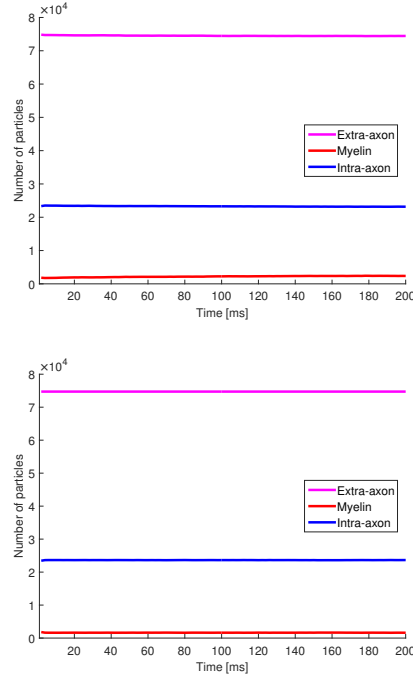


Fig. 5.3: Extra-axonal (*magenta*), myelin (*red*) and intra-axonal (*blue*) concentration trends in case of exchange (*top*) and no exchange (*bottom*).

wraps and  $\tau$  values were systematically higher with greater  $d_{\text{inner}}$ . Figure 5.5B reports the axon water number of particles versus time decaying trend from an axon having  $d_{\text{inner}} = 1.0 \mu\text{m}$  and  $n_{\text{wraps}} = 4$ . The annotation in Figure 5.5B reports Equation 4.8 from which  $\tau$  was recoverable via polynomial fitting.

Figure 5.6 illustrates observable  $\tau$  values versus  $d_{\text{inner}}$  and again the exchange time increases with axon diameter and the number of myelin wraps.

In both cases,  $y$ -axis was limited to 3500 ms to highlight only configurations with  $\tau$  observable using clinical MRI acquisitions [152]. More in detail, the feasibility of exchange time measurements is increased for small  $d_{\text{inner}}$  and low  $n_{\text{wraps}}$ .

### 5.2.2 Signal decay

The PGSTE simulated diffusion signals are illustrated in Figure 5.7. It can be observed that less myelin wraps lead to increased signal decay. The signal corresponding to geometries with large number of wraps was not sensitive to  $T_D$ , while the dependence on  $T_D$  could be observed by reducing  $n_{\text{wraps}}$ . The smaller  $n_{\text{wraps}}$ , the higher the signal decay. Moreover, differences in Figure 5.7A and 5.7B highlighted a larger sensitivity to  $n_{\text{wraps}}$  variation when  $d_{\text{inner}}$  was small.

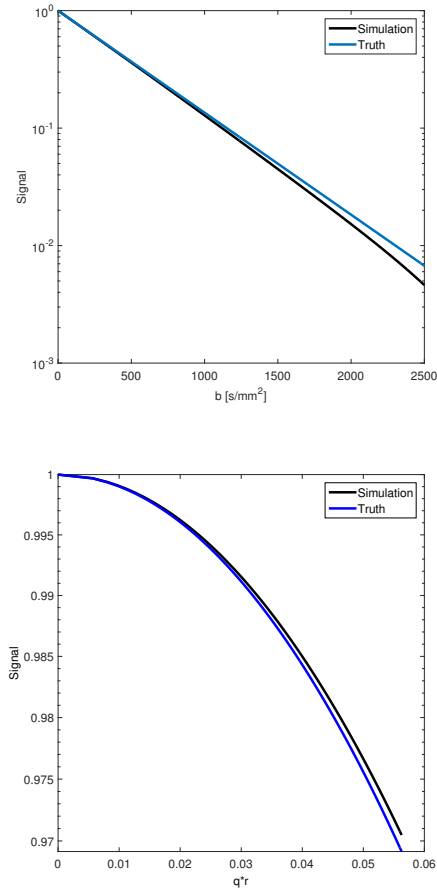


Fig. 5.4: Simulated (*black*) and theoretical (*blue*) signal in case of  $T_2$  relaxation for free (*top*) and restricted diffusion (*bottom*) normalized to the respective maximum value.

### 5.2.3 RD and RK estimates

The parameters estimated via the DKI model fitting are reported in Figure 5.8A and 5.8B, together with the signal value calculated at highest  $b$ -value ( $b = 2500$   $\text{s}/\text{mm}^2$ ) as in Figure 5.8C and referred to as  $AFD$ . As it can be observed,  $RD$  generally decreased adding  $n_{\text{wraps}}$  in the range  $0.46 - 0.62$   $\mu\text{m}^2/\text{ms}$ , while  $RK$  and  $AFD$  increased showing an almost equal trend and specular to the  $RD$  one. More in detail,  $RK$  varied in the range  $1.75 - 2.67$  and  $AFD$  in the range  $0.42 - 0.56$ . A larger slope of  $RD$ ,  $RK$  and  $AFD$  versus  $n_{\text{wraps}}$  curves was also observed in case of longer myelin  $T_2$  relaxation than for shorter one. Moreover, in long myelin  $T_2$  relaxation the curve representing small axons intersected the bigger axon curve at lower  $n_{\text{wraps}}$  (16 wraps) compared to short myelin  $T_2$  relaxation for all parameters.

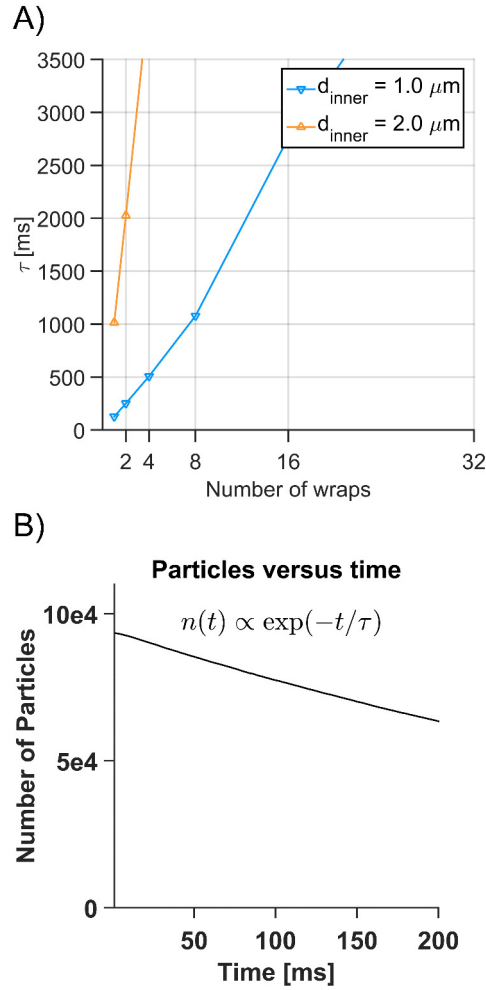


Fig. 5.5: A) Exchange time observed as the time employed by water particles to flow out from axon into extra-axonal compartment depending on the number of wraps in case of axon diameter 1.0 and 2.0  $\mu\text{m}$ . B) Number of particles within the axon as a function of time in case of axon diameter 1.0  $\mu\text{m}$  and 4 wraps.

#### 5.2.4 $\tau$ estimation

Figure 5.9 shows the parameters estimated via Kärger model fitting. The estimated  $\nu_{ic}$  slightly increased with  $n_{\text{wraps}}$ , and almost negligible error areas were identified ranging from 0.41 to 0.52. As expected, no high differences were found in  $\nu_{ic}$  estimation when changing  $d_{\text{inner}}$  since the volume fractions were maintained constant in all the studied frameworks as reported in Section 4.3.1.

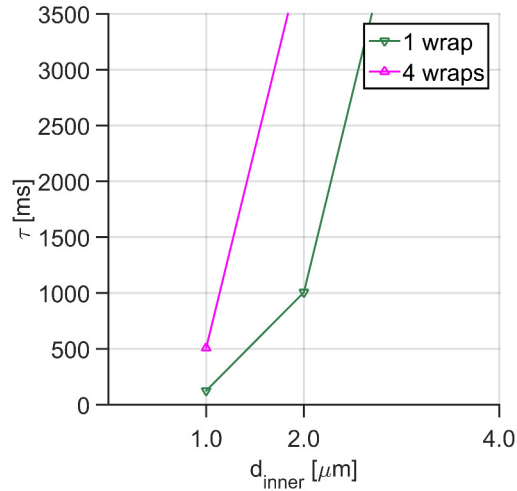


Fig. 5.6: Exchange time observed as the time employed by water particles to flow out from axon into extra-axonal compartment depending on the axon diameter in case of 1 and 4 myelin wraps.

The  $ADC_{ec}$  estimate was not highly sensitive to  $n_{wraps}$  neither to  $d_{inner}$  variations, although it was a little bit lower for smaller axons in the range  $1.06 - 1.13 \mu\text{m}^2/\text{ms}$ . The error areas were negligible also for  $ADC_{ec}$  estimate.

The  $\tau$  estimation followed the same trend as observable ones as reported in Figure 5.5A, showing systematically higher values to greater  $d_{inner}$  and  $n_{wraps}$ . Figure 5.9 reveals progressively wider error areas for larger  $n_{wraps}$  that highlights that  $\tau$  estimates become less reliable counting up  $n_{wraps}$ . Numerical details are provided in Table 5.1 where observable and estimated  $\tau$  values are compared. A larger correlation is generally retrieved for small axon diameters and low numbers of wraps.

### 5.3 Discussion

This work targeted the modeling of myelin structure by representing its spiraling nature through Monte Carlo simulations. To the best of our knowledge, it was the first time that the multi-wrapping nature of myelin was directly mimicked apart from one other case in which this effect was indirectly introduced through a compartment with different diffusivity in radial and circumferential direction [101]. Noteworthy, Harkins and Does did not use their simulation for estimating exchange time. In fact, the strategy followed here consented to compute a ground truth for the exchange mechanism depending on myelin wraps around the axons. More in detail, the observable  $\tau$  exclusively due to the particular geometry was calculated for different morphological conditions. This enabled the definition of a

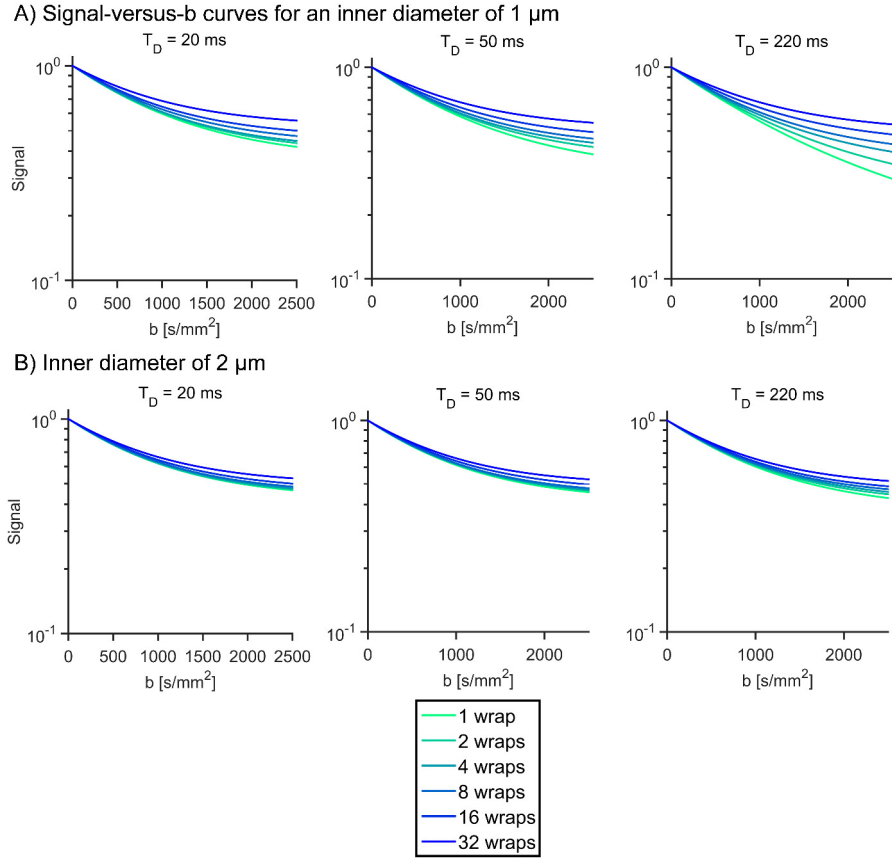


Fig. 5.7: PGSTE simulated diffusion signal for different numbers of myelin wraps (*light blue - blue colors*) and diffusion time (*columns*) in axons having diameter A)  $1.0\ \mu\text{m}$  and B)  $2.0\ \mu\text{m}$ .

reference condition allowing to derive a set of measures of  $\tau$  (observable  $\tau$ ) to be used as a benchmark for the estimation of such parameters using the Kärger model. Controlling  $\tau$  through simulations is important because of the lack of agreement on the value of such parameter in the literature as already discussed in Section 2.1. Moreover, the flexibility of the geometry allowed to explore the effects of such exchange mechanism on the diffusion signal in different conditions. In particular, this study was designed following a possible clinical setting ( $T_D = 20\ \text{ms}$ ,  $b \in [0 - 2500]\ \text{s/mm}^2$ ) with possibly realistic  $T_2$  relaxations, allowing the characterization of  $RD$  and  $RK$  [113] together with  $AFD$  [173] variations to myelin structure modifications. In addition, the possibility to create a ground truth for axonal residence time enabled the possibility to evaluate the performance of the Kärger model [118] in estimating  $\tau$  values, as mentioned before.



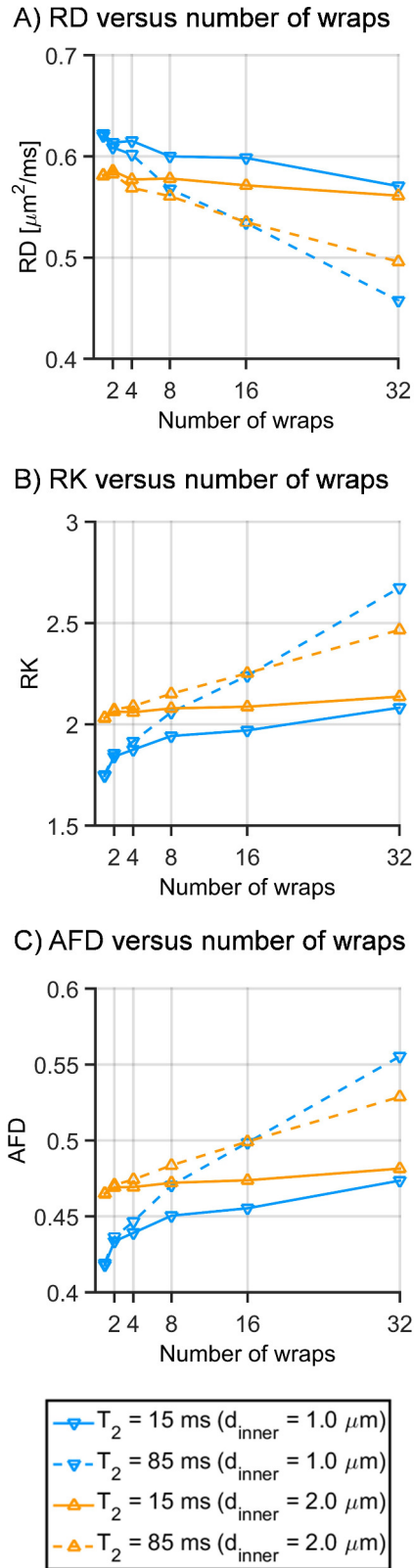


Fig. 5.8: DKI model estimated parameters in case of axon diameter 1.0 and 2.0  $\mu\text{m}$  and short (*solid line*) and long (*dashed line*) myelin  $T_2$  relaxation: A) radial diffusivity, B) radial kurtosis and C) apparent fiber density.

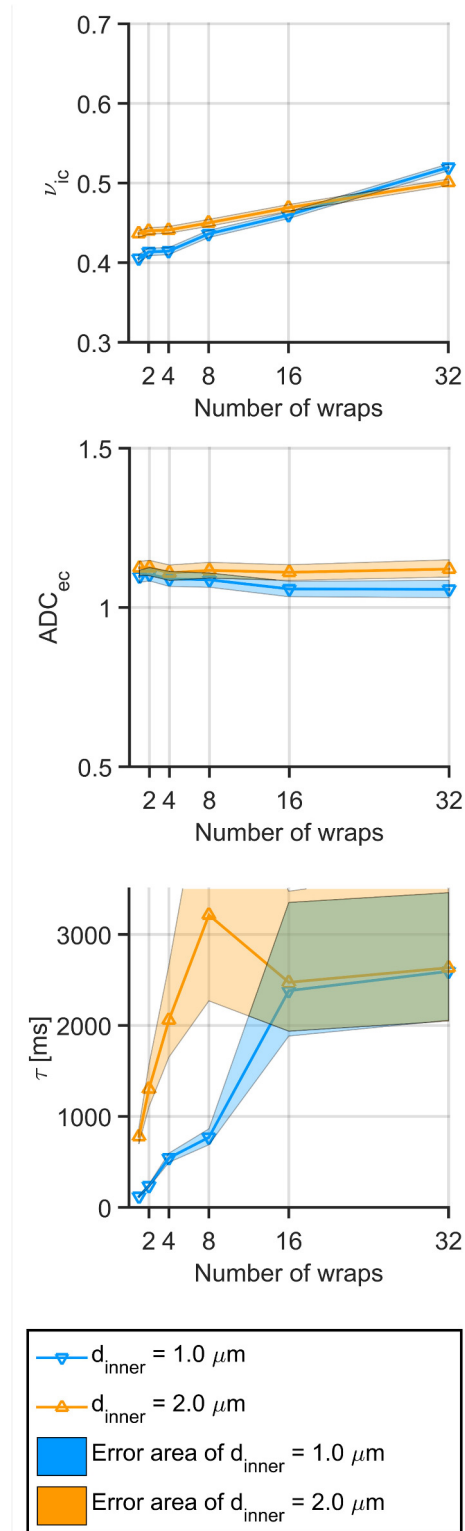


Fig. 5.9: Kärger model estimated parameters in case of axon diameter 1.0 and 2.0  $\mu\text{m}$ : A) intracellular volume fraction, B) extracellular apparent diffusion coefficient and C) exchange time. Error areas are bounded by 5<sup>th</sup> and 95<sup>th</sup> percentiles computed on 500 noisy instances of signal ( $SNR = 40$ ).

$d_{\text{inner}}$ [ $\mu\text{m}$ ]	$n_{\text{wraps}}$	Obs $\tau$ [ms]	Est $\tau$ ( $5^{\text{th}}$ – $95^{\text{th}}$ ) [ms]
1.0	1	126	120 (112 – 130)
	2	251	237 (223 – 255)
	4	507	543 (495 – 596)
	8	1077	770 (688 – 863)
	16	2761	2381 (1883 – 3351)
	32	5254	2608 (2057 – 3458)
2.0	1	1015	780 (702 – 882)
	2	2026	1301 (1105 – 1569)
	4	4104	2059 (1652 – 2664)
	8	9005	3215 (2270 – 5103)
	16	16718	2473 (1937 – 3475)
	32	19805	2681 (2047 – 3717)

Table 5.1: Observable and estimated exchange time with  $5^{\text{th}}$  and  $95^{\text{th}}$  percentiles reported for each axon diameter and number of wraps.

### 5.3.1 Estimation of observable $\tau$

The exchange times increased with the number of wraps and for bigger axons. This is intuitively understandable since the length of the path the spins have to travel to quit the axon through the myelin sheet increases with  $n_{\text{wraps}}$ , and thus the time spent in the spiral. The exchange time was also greater in bigger axons, still easily understandable thinking about the lower probability for a particle to reach the boundary besides the fact that bigger axons imply longer spiral myelin length. Our findings were in line with what observed by Dula et al. [73] and Harkins [102] according to which exchange is longer in big axons and thick myelin. More in detail, Dula et al. [73] observed by quantitative MRI measures of multi-exponential  $T_2$  relaxation (MET<sub>2</sub>) a lower underestimation of the myelin water fraction, which is larger in big axons and thick myelin and they supposed the longer exchange time as cause. They performed this analysis on *ex-vivo* rat tissue and subsequently retrieved the same effects further enhanced in *in-vivo* tissue [102]. Harkins et al. [102] also highlighted some abnormal results on the human corpus callosum and they hypothesized different characteristics of the myelin in different tracts of the brain as justification. Since the large majority of human brain axons have diameter below 1.0  $\mu\text{m}$  (as seen in Section 2.1), and the number of myelin wraps in human brain is normally around 10 according to Edgar et al. [75, 54] and in agreement with the results following Section 2.1, our results suggest that exchange times are not clinically observable as they overcome the sub-second scale. The measurement of exchange time could become clinically feasible in case of myelin turns lower than expected. In a reasonable normal situation in humans, the results were more in line with the findings of Nilsson and colleagues [152] than with those of Nedjati-Gilani [146]. Specifically, we calculated  $\tau$  in the order of second as in [152] supposing a typical human axon with  $d_{\text{inner}} < 1.0 \mu\text{m}$  and  $n_{\text{wraps}} \sim 9$  as discussed in Section 2.1. Probably, the difference observed with  $\tau$  recovered in [146] was due to the assumed structure model at the basis. In particular, Nedjati-Gilani and colleagues did not take into account myelin multi-wrappings nature and volume. Results in our work were also within the same order of magnitude of  $\tau$  retrieved via the rat

model having axon with  $d_{\text{inner}} = 1.0 \mu\text{m}$  and  $n_{\text{wraps}} < 8$  [172, 71]. Quirk’s group work [172] also recovered  $\tau$  in the sub-second scale (around 550 ms) via Bloch-McConnell exchange modeling of longitudinal relaxation experiments injecting MR relaxation agent into the extracellular space, but they performed experiments on *in-vivo* rats with potentially smaller axons and consequently potentially lower number of myelin turns than in humans [75]. Doing the same consideration, also Dortch et al. [71] recovered fast  $\tau$  in rat optic nerve *ex-vivo* tissue directly via Relaxation Exchange Spectroscopy (REXS) and they found a value of  $138 \pm 15$  ms.

From our results, we can extrapolate some scaling laws that govern how the spiraling myelin impacts the exchange time. From Equation 3.42 and knowing that the surface-to-volume ratio in a cylinder is determined by the radius as  $A/V = 4/r$ , we can say that  $\tau \propto r/K$  considering permeability along the whole membrane and thus equal permeability for all points on the area. In the case here examined of a cylinder covered by a spiraling membrane, we have a high permeability where the spiral opens, and a lower or absent permeability otherwise. Assuming that the exchange through the lipid bilayers forming the myelin membranes is much slower than the diffusion around a full spiral and thus negligible, the factor governing the exchange rate will be the width of the space between myelin turns in which extracellular water is trapped. This is known to be approximately 30.0 nm [164] in normal conditions. We thus get  $A_m \approx 30.0 \text{ nm}$  leading to  $\tau \propto r^2/K_m A_m$  that explains the results in Figure 5.5, where twice the inner diameter results in four times the exchange time. Moreover, Figure 5.5.A illustrates that exchange time scales approximately with the logarithm of the number of wraps.

Another generalization that can be made is that diameters of above approximately 2 micrometers, or more than approximately 8 layers, are sufficient to lead to exchange times longer than a second. This is important, because some tracts like spinal cord, brainstem or cerebellar peduncles contain axons with diameters up to  $10.0 \mu\text{m}$  [75] and diameters up to  $9.0 \mu\text{m}$  were found also in the human superior longitudinal fascicle [133]. The number of myelin turns in normal human brain was already calculated to be  $\sim 9$  in Section 2.1 further confirmed by literature [75, 54] as mentioned before. In normal conditions, our results thus support the assumption of slow (negligible) exchange in WM. However, during development or degeneration, these numbers can change [54, 3, 20] and thus affect the observable exchange times aiding the interpretation for experiments in these cases.

### 5.3.2 Signal decay

The signal versus  $b$  curves showed higher decay for smaller number of myelin wraps and smaller axons, accentuated in longer diffusion times. The results are in agreement with the findings of Harkins and Does [101] according to which a slowly diffusing myelin (in this study given by many  $n_{\text{wraps}}$ ) accounted for more signal coming from water staying in the multi-wrappings compartment. The higher emphasis of this phenomenon provided by longer  $T_D$  did not surprise given that long diffusion times allow to detect permeability effects as already discussed by Stanisz et al. [186]. In fact, the longer the observation times, the more probable it is that the water particles bump into a transition. The last consideration could

also explain the lower decay observed in bigger axon where water particles had not the time to experience exchange in the considered  $T_D$  resulting in almost restricted signals.

### 5.3.3 RD and RK estimates

The  $RD$  decrease along with the  $RK$  and  $AFD$  increase were more evident for small axons and low number of wraps, otherwise the short myelin  $T_2$  makes negligible these variations. The  $RD$  and  $RK$  estimates resulted in ranges of values similar to those found by Harkins and Does [101]. Moreover, our findings were in line with their results, showing respectively a decreased  $RD$  and increased  $RK$  adding  $n_{wraps}$  (corresponding to the slower myelin diffusivity in [101]). The recovered  $AFD$  was already discussed by Raffelt et al. [173] as being approximately linearly related to  $\nu_{ic}$ . In this study,  $AFD$  resulted close to the volume fraction set of 0.45 and comprehensive of both axon and myelin. The observed increase with  $n_{wraps}$  was possibly caused by the preponderance of water in axon or more probably in myelin as discussed before referencing to the work of Harkins and Does [101]. This enhances the signal coming from those compartments. The increment of  $AFD$  to  $n_{wraps}$  was also in line with what found by Peled [165] according to which a reduced permeability caused an increase of her model baseline tensor that correlated with intra-axonal water volume in her definition. Concerning the differences in myelin  $T_2$ , in this work we observed that parameters estimation was much more different across  $n_{wraps}$  in long  $T_2$  than in short although some interesting slight differences could be observed for lower number of wraps in clinical acquisition setting. It was also noted a greater slope for curves representing smaller (and also the most frequent [133]) axons in human brain, further confirming the reasonable potential of accounting for water exchange.

### 5.3.4 $\tau$ estimation

In this work, the Kärger model well fitted to all the diffusion signals reporting reliable estimates of exchange times for small axons and number of wraps up to 8. Concerning  $\nu_{ic}$ , the estimated values had negligible error areas, quite insensible to  $d_{inner}$  and slightly more sensible to  $n_{wraps}$ , with values in a range comprehending the ground truth value of 0.45 and trends close to  $AFD$  previously discussed. Also  $ADC_{ec}$  findings were stable, showing a very slight dependence from  $d_{inner}$  while it resulted independent from  $n_{wraps}$ . The resulting values were in agreement with  $D/\lambda$  ( $\lambda$  corresponding to tortuosity factor) as in [149]. The  $\tau$  estimates were closer to the respective observable counterparts and also more stable for  $d_{inner} = 1.0 \mu\text{m}$  and  $n_{wraps} = 1, 2, 4$  and  $8$  and  $d_{inner} = 2.0 \mu\text{m}$  and  $n_{wraps} = 1$ . The decreased reliability of  $\tau$  estimates for larger  $d_{inner}$  were possibly due to the fact that longer  $T_D$  are required to study exchange in this case, while the same effect observed for many  $n_{wraps}$  can be due to the almost impermeability of the myelin that causes a failure in Kärger model fitting [83]. An important implication derived by our work is added evidence of the capability of Kärger model to retrieve the exchange time for those cases in which  $n_{wraps}$  could be lower than expected like in developing brain or demyelinating diseases [54, 3]. Furthermore, even if relaxometry was not

included in experiments observing exchange, in case of low  $n_{\text{wraps}}$  and small axon it is influential as seen from the previous DKI fitting experiments.

### 5.3.5 Limitations and bottlenecks

A limitation of the present study was the oversimplification of the substrate, in particular the assumption of constant diameter across axons and the square packaging. The square packaging allows a maximum  $\nu_{ic}$  without substrates overlapping lower than, for example, the hexagonal one, allowing more realistic simulations of the WM [100]. Moreover, the diameter variation could add similarity to histologic data as shown in the work of Aboitiz [1], and the coexistence of these parameters in the overall signal can make the signal interpretation further difficult. However, the obtained results could be reasonably retained with the aim to explore multi-wrapping myelin and conditions in which this is a possible exchange mechanism able to influence dMRI signal.

Future work could include a study of the different parameters here analyzed and their dependence from  $TE$ , recently considered as an interesting biomarker for myelin-dependent process [134]. In particular, Lin et al. [134] highlighted a sensitivity of  $TE$  dependence to the change of  $g$ -ratio. Qin et al. [171] already demonstrated the dependence of the tensor-derived indices on  $TE$ , attributing this effect to the different transverse relaxation within the tissue although this requires more specific investigation. Several works suggest the possibility to obtain more trustworthy results by including compartment-specific  $T_2$  and by studying the relationship between  $TE$  and diffusion experiments [208, 196, 78].

Furthermore, a study on real data and especially on subjects in which myelin is plastic or damaged would be required for assessing the sensitivity and specificity of the proposed method in realistic contexts [54, 20]. More specifically, we can search for the same trend variations in estimated parameters and eventually correlate the findings with results from multi-modal imaging for being more specific on the nature of these modifications. As example, Magnetization Transfer Ratio (MTR) imaging, Multiexponential  $T_2$  ( $MET_2$ ), and many others are used for myelin water imaging [8].

**Clinical applications**





## Application: stroke characterization through dMRI indices

In this chapter we describe the methods used for defining the indices derived from the promising SHORE model as potential biomarkers. This was done aiming at exploring a possible strategy for validating the clinical relevance of dMRI signal measures, opening the way to application also for different models like the ones for permeability. In order to check the suitability of the indices as biomarkers, the model must be fitted also on data from pathological subject. The stroke disease was investigated for this purpose. The content of this Chapter has been published in journals [37, 31] and [38, 156] papers.

### 6.1 MRI in stroke disease

The blockage of blood (e.g. due to a clot) or the rupture of an artery (e.g. due to an aneurysm burst or a vessel leak) causes the lack of oxygen to brain cells and subsequently their death in a phenomenon called stroke (when it is consequence of the first cause is named ischemic, otherwise is named hemorrhagic). The symptoms can be the loss of speech, weakness, or paralysis of one side of the body. Stroke is the second most common cause of morbidity worldwide and is the leading cause of acquired disability [69]. Following initial damage, stroke patients can recover to some extent, partially due to the resolution of edema and possibly because of structural and functional modifications in surviving brain tissue. In particular, several experimental studies on both animal models and patients showed that this spontaneous recovery mainly depends on brain plastic reorganization of the infarct and peri-infarct areas [68, 144]. Figure 6.1 illustrates the qualitative structural differences between a healthy and a diseased subject.

Important insights into the underlying remodeling and reorganization processes of functional recovery can nowadays be derived in human patients via advanced neuroimaging methods and brain mapping [175]. In addition, the recent developments in connectivity analyses from multiple MRI data have provided new details about the network pathophysiology and stroke recovery, although the role of the non-injured hemisphere in this process is still controversial. At functional level, positron emission tomography (PET) and subsequently functional MRI (fMRI) studies have evidenced task-related brain activations in both lesional and con-

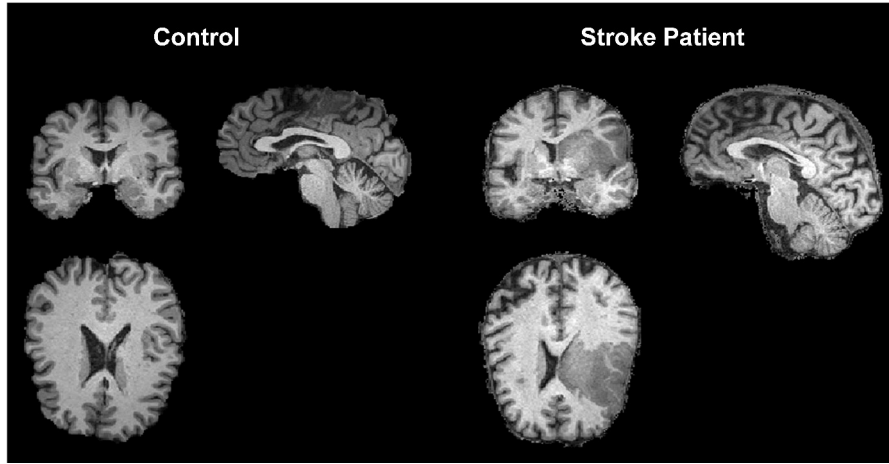


Fig. 6.1: Coronal, lateral and axial views of the structural image of one healthy and one stroke patient. They were acquired with the high-resolution 3D  $T_1$ -weighting protocol described in Section 6.4.

tralateral hemispheres, which were highly dependent on the degree of brain damage [219, 176]. In particular, Ward et al. [214] investigated a series of patients who went through a good recovery after stroke and suggested that the recruitment of other contralateral motor-related networks would have subserved the recovery and played an essential role for compensation of the impaired functions.

At structural level, dMRI has recently generated considerable interest due to its ability to disclose early pathophysiological changes in acute stroke, both in terms of structural changes of fiber tracts and microstructural properties of the tissues. Several studies demonstrated structural remodeling in ipsilateral and contralesional corticospinal tracts [41] and changes in the number of neural pathways in areas both ipsilateral and contralateral to the stroke [87], especially for the specific fiber trajectories connecting cortical regions in both hemispheres [61]. In addition, dMRI studies performed in well-recovered stroke patients revealed increased FA in both ipsi- and contralesional corticospinal tracts in comparison to controls, and that tracts' FA asymmetries in the contralateral corticospinal tract may play a role in motor recovery after unilateral stroke [179]. Connectivity remodeling after stroke has been reported in both injured [184] and uninjured hemispheres [94, 135]. GFA had previously been successfully exploited to provide evidence of plasticity in the uninjured motor network in stroke patients with motor deficits [94, 135]. Current literature works suggest that dMRI may be one of the most sensitive neuroimaging biomarkers of vascular damage in stroke patients [143].

Among the different variants currently available, DSI is a particular technique that is sensitive to intra-voxel heterogeneities in diffusion directions caused by crossing fiber tracts and thus allows more accurate mapping of axonal trajectories than other diffusion imaging approaches [216]. Although anisotropy is the most

widely studied diffusion index, there is a growing interest in investigating WM microstructural properties and changes by analyzing different diffusion indices. To this end, the application of a recently proposed new analytical reconstruction model referred to as 3D-SHORE [157] can provide a set of new generation indices describing different microstructural properties. Even though many factors affect the accuracy of such an estimation, including acquisition parameters such as diffusion time, diffusion gradient duration, gradient strength, partial volume effects due to limited resolution and, last but not least, the presence of crossing fibers, this measure is of particular interest because it is sensitive to WM microstructural changes. Although the available findings for these numerical indices are encouraging, a quantitative comparison with the classical tensor-derived metrics is currently lacking but essential to further probing their potentialities as biologically specific markers. Regardless of the aforementioned issues, MD and FA remain indeed the standard measures in clinical settings, especially for acute stroke imaging. Therefore, 3D-SHORE-based indices have to be carefully related to these tensor-derived indices in terms of precision, consistency, discriminative and predictive power in patients, all essential requirements for being considered good biomarkers. Avram and colleagues [18] reported a first attempt to assess within a clinically appropriate scanning time the feasibility of novel EAP-indices (from MAP-MRI modeling rather than 3D-SHORE) in comparison to classical DTI indices, demonstrating good consistency across subjects and reproducibility in test-retest experiments on three controls. However, despite the promising results, we dealt with a very limited number of healthy subjects and relied on qualitative visual comparisons, acknowledging the need for further studies on patient populations that, to the best of our knowledge, are still missing in recent literature.

Despite its relevance in stroke disease, the microstructural modeling of GM is still largely unexplored. In fact, there is a growing need for a more comprehensive assessment of GM tissue changes using dMRI despite its intrinsic complexity given by the lack of coherent tissue orientation and the unproven suitability of the currently available models. Some previous studies with classical DTI indices have highlighted MD as a promising marker of GM diffusivity changes in several pathologies as Alzheimer disease [221], multiple sclerosis [53] and Parkinson [121]. However, DTI is scarcely employed in the assessment of GM regions, especially in the cortex, and its ability of capturing microstructural features and feature modulations in GM is still under debate. Conversely, thanks to the ability of capturing the EAP in complex tissue microstructures, the 3D-SHORE model might allow characterising the signatures of hindered diffusion in GM regions and/or provide information about GM changes occurring over time. In particular, we target the plasticity process taking place in the case of stroke. Very little is known about possible GM modifications in the contralateral hemisphere with respect to the lesion, as these tissues have been widely disregarded as considered normal and not directly involved in any rearrangement process [138, 160]. Indeed, to the best of our knowledge, all the models present in the state-of-the-art were tailored on WM, often relying on simplistic assumptions such as predefined pore geometry, limited number of diffusion compartments and absence of water exchange. Even though these hardly cope with the complex GM structure, it is worth assessing the exploitability of such models for deriving measures that could be useful indicators

of tissue alterations. This might be useful for detecting the occurrence of different pathologies as well as for characterizing the recovery due to treatment in longitudinal studies. Otherwise stated, the goal of this work was not to derive measures that could directly express biophysical tissue properties but suitable detectors of microstructural features modulations due to different possible causes with the aim of improved personalized health care and treatment.

In this chapter, we framed the study at three levels of complexity. In a first and preliminary investigation, we aimed at exploring whether the measures could reveal contralesional structural changes along intracallosal connections after stroke, whether they correlate with the well established GFA index and if they allow to predict motor outcomes jointly with clinical status. In a successive step we widened the investigation by including the transcallosal circuit and the subcortical motor loops as well as multiple temporal scales from injury. Finally, we propose the comparative analysis of the 3D-SHORE-derived microstructural descriptors with respect to the classical tensor-derived indices (MD and FA) and the analysis of the ability of the considered indices to detect plasticity processes in GM.

## 6.2 Materials and methods

The following Sections describe the characterization of the dMRI indices as potential biomarkers for stroke pathology.

Briefly summarizing, structural ( $T_1$ ) and dMRI data from ischemic stroke patients and healthy subjects were collected at different timepoints. The firsts were employed as reference for brain parcellation and registration of dMRI data, while the seconds were fitted with 3D-SHORE model to derive the indices under analysis and the tractography. We could then extract the variations of the indices along the desired tracts connecting different regions across time and in both controls and patients. The statistical analysis was then provided for quantifying these variations and the indices capability as biomarkers. The entire pipeline here briefly described is represented in Figure 6.2 while the following Sections describe each step in more detail.

## 6.3 Signal modeling and microstructural indices derivation

The dMRI signal is represented as in Equation 3.12. In this case,  $\Phi_n(q\mathbf{u})$  is the family of functional basis functions and, in detail, they are the solutions for the 3D quantum harmonic oscillator ( $\mathbf{u}$  is the unit vector). The EAP is obtained by applying the inverse Fourier transform to Equation 3.12:

$$P(\mathbf{r}) = \sum_{n=0}^N c_n \mathcal{F}[\Phi_n(q\mathbf{u})] = \sum_{n=0}^N c_n \Psi_n(r\mathbf{u}) \quad (6.1)$$

where  $\Psi_n(r\mathbf{u})$  are the Fourier transforms of the basis functions  $\Phi_n(q\mathbf{u})$ . The 3D-SHORE model is expressed in spherical coordinates. Separability holds the radial

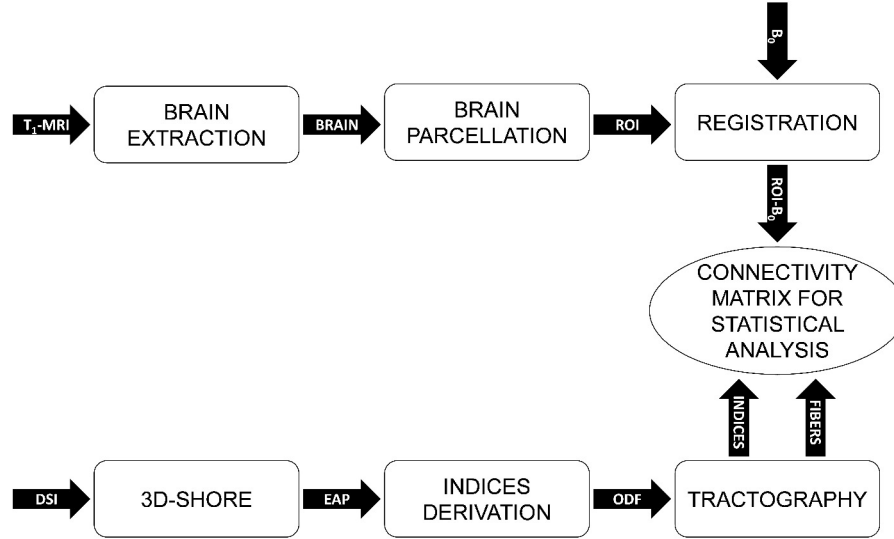


Fig. 6.2: Scheme of the pipeline employed to address the study reported in this Chapter.

and angular coordinates which prevents the independent scaling of the basis functions along the main coordinate axes. Following the formulation in [56], the basis functions  $\Phi_n(q\mathbf{u})$  can be written as

$$\Phi_n(q\mathbf{u}) = R_n(q)Y_n(\mathbf{u}) \quad (6.2)$$

where  $R_n(q)$  models the radial part of the signal and  $\{Y_n(\mathbf{u})\}$  are the real spherical harmonics of even order [65]. After a reordering of the terms, the signal model becomes

$$E(q\mathbf{u}) = \sum_{l=0, \text{even}}^{N_{max}} \sum_{n=l}^{(N_{max}+l)/2} \sum_{m=-l}^l c_{nlm} \Phi_{nlm}(q\mathbf{u}) \quad (6.3)$$

$$\begin{aligned} \Phi_{nlm}(q\mathbf{u}) = & \left[ \frac{2(n-l)!}{\zeta^{3/2} \Gamma(n+3/2)} \right]^{1/2} \left( \frac{q^2}{\zeta} \right)^{l/2} \exp\left( \frac{-q^2}{2\zeta} \right) \times \\ & \times L_{n-l}^{l+1/2} \left( \frac{q^2}{\zeta} \right) Y_l^m(\mathbf{u}) \end{aligned} \quad (6.4)$$

where  $N_{max}$  is the maximal order in the truncated series and  $\Phi_{nlm}(\mathbf{q})$  is the orthonormal 3D-SHORE basis,  $\Gamma$  is the Gamma function,  $L$  is the Laguerre polynomial and  $\zeta$  is an isotropic scaling parameter. The coefficients are determined by quadratic programming and positivity constraints are imposed to the EAP. The first  $N_{max}/2 + 1$  functions are isotropic ( $l = 0$  and  $m = 0$ ) and  $\zeta$  was derived by the zero order term  $\Phi_{000}$  to be the DTI-derived Gaussian function leading

to  $\zeta = 1/(8\pi^2 T_D D)$  (where  $D$  is diffusivity) [229]. In case of isotropic scaling the MAPMRI formulation [159] is equivalent to this one. Accordingly, the scale factor depends on two parameters: the diffusion time and the diffusivity. In the 3D-SHORE model the diffusivity is assumed to be constant across the angular directions, which corresponds to isotropic diffusion, and is calculated as the diffusion tensor derived mean diffusivity. We are aware of the fact that such an assumption is not suitable where diffusion is either restricted or hindered as it is the case in WM and, to a lesser extent, in GM [159]. This constraint cannot easily be removed because the radial term of the 3D-SHORE model is not separable since it only depends on the norm of the reciprocal vector. Angular dependency is recovered by SH. In case of high anisotropy this limits the accuracy of the signal representation. Nevertheless, the 3D-SHORE model provides competitive performance in terms of both signal reconstruction error and estimation of main fiber directions [80, 153].

The corresponding EAP is recovered by Fourier transformation

$$P(r\mathbf{u}) = \sum_{l=0, \text{even}}^{N_{max}} \sum_{n=l}^{(N_{max}+l)/2} \sum_{m=-l}^l c_{nlm} \Psi_{nlm}(r\mathbf{u}) \quad (6.5)$$

$$\begin{aligned} \Psi_{nlm}(r\mathbf{u}) = & (-1)^{n-l/2} \left[ \frac{2(4\pi^2\zeta)^{3/2}(n-l)!}{\Gamma(n+3/2)} \right]^{1/2} \left( 4\pi^2\zeta r^2 \right)^{l/2} \exp\left( 4\pi^2\zeta r^2 \right) \times \\ & \times L_{n-l}^{l+1/2} \left( 4\pi^2\zeta r^2 \right) Y_l^m(\mathbf{u}) \end{aligned} \quad (6.6)$$

where, due to the linearity of the transform operator, the coefficients  $c_{nlm}$  are the same as in Equation 6.4.

The RTOP, RTAP and RTPP indices can then be derived starting from Equations 3.16 and 3.18 as follows [159]

$$RTOP = \sum_{n=0}^{N_{max}/2} c_{n00} (-1)^n \left[ \frac{4\pi^2\zeta^{3/2}(n)!}{\Gamma(n+3/2)} \right]^{1/2} L_n^{1/2}(0) \quad (6.7)$$

$$\begin{aligned} RTAP = & \sum_{l=0, \text{even}}^{N_{max}} \sum_{n=l}^{(N_{max}+l)/2} \sum_{m=-l}^l c_{nlm} \times \\ & \times \left[ \frac{\zeta^{1/2} 2^{l+3} \pi^2 \Gamma(l/2+1)^2 \Gamma(n+3/2)}{(n-l)! \Gamma(l+3/2)^2} \right]^{1/2} \times \\ & \times {}_2F_1(l-n, l/2+1, l+3/2, 2) P_l(0) Y_l^m(\vec{u}_{\parallel}) \end{aligned} \quad (6.8)$$

$$\begin{aligned} RTPP = & \sum_{l=0, \text{even}}^{N_{max}} \sum_{n=l}^{(N_{max}+l)/2} \sum_{m=-l}^l c_{nlm} \times \\ & \times \left[ \frac{\Gamma(l/2+1/2)^2 \Gamma(n+3/2) 2^l}{\zeta^{1/2} (n-l)! \Gamma(l+3/2)^2} \right]^{1/2} \times \\ & \times {}_2F_1(l-n, l/2+1/2, l+3/2, 2) Y_l^m(\vec{u}_{\parallel}) \end{aligned} \quad (6.9)$$

where  ${}_2F_1$  is the Gaussian hypergeometric function and  $P_l(0)$  is the  $l$ -degree Legendre polynomial in zero. Özarlan et al. [159] proved the equivalence between RTOP, RTAP, and RTPP and the reciprocal of the ensemble average of the pores' geometrical properties under assumption of long  $T_D$ , NPA, homogeneous pores in the voxel and sufficiently precise fitting of the signal. In particular, RTOP, RTAP, and RTPP respectively represent the estimation of the reciprocal of the mean apparent volume ( $1/\langle V \rangle$ ), cross-sectional area ( $1/\langle A \rangle$ ), and length ( $1/\langle L \rangle$ ) of the compartment in which diffusion takes place. Thus, the estimation of the apparent mean axon's diameter can be obtained as  $D = 2R = 2\sqrt{1/(\pi RTAP)}$  (where  $D$  and  $R$  will be the diameter and the radius in the rest of the thesis). It is important to note that the assumptions for deriving microstructural indices are strong and thus normally of difficult reaching. Despite this, we can observe the sensitivity of these descriptors to microstructural modifications and discussing on their interpretation basing on their theoretical meaning.

The PA index represents the measure of the anisotropy of the EAP and is defined similarly to the tensor FA. It is calculated as the weight of the isotropic part of the propagator, corresponding to the first 3D-SHORE coefficient

$$PA = \sqrt{1 - \frac{\sum_{n=0}^{N_{max}} c_{n00}^2}{\sum_{l=0,even}^{N_{max}} \sum_{n=l}^{(N_{max}+l)/2} \sum_{m=-l}^l c_{nlm}^2}}. \quad (6.10)$$

Other indices that we calculated from 3D-SHORE EAP were the more well established GFA [202] and MSD which general formulas were already seen in Equation 3.11 and Equation 3.20 respectively.

## 6.4 Dataset

Ten ischemic stroke patients (6 males, mean age:  $60.3 \pm 12.3$  years) and ten age- and gender-matched healthy subjects were enrolled in the study and underwent longitudinal MRI acquisitions on a 3T Siemens scanner (Trio, Siemens, Erlangen, Germany) equipped with a 32-channel head coil, as firstly reported in [94]. Patients were affected by ischemia infarction in the motor cortex or subcortical structures involved in motor control, while subjects with brainstem and cerebellar infarcts or with massive edema causing midline shift were excluded [94]. Moreover they should not have history of previous stroke or generally neurological, psychiatric or major system disorder. Acquisitions were performed at three time points in patients (within one week ( $tp1$ ), one month ( $\pm$  one week,  $tp2$ ), and six months ( $\pm$  fifteen days,  $tp3$ ) after the injury), and at two time points in controls (one month apart,  $tp1c$  and  $tp2c$ ). The same structural imaging protocol was used in all cases. In particular, Diffusion Spectrum Imaging (DSI), a high angular resolution diffusion technique [217], was performed using a single-shot spin-echo echo-planar imaging (EPI) product sequence and the following parameters:  $TR/TE = 6600/138$  ms,  $FOV = 212 \times 212$  mm<sup>2</sup>, 34 slices,  $2.2 \times 2.2 \times 3$  mm<sup>3</sup> resolution,  $GRAPPA = 2$ , scan time = 25.8 min. The sampling scheme consisted of a keyhole Cartesian acquisition with 258 diffusion directions covering a half q-space 3D grid with radial

grid size of 5. Thirty-four different  $b$ -values (from 300 up to 8000 s/mm<sup>2</sup>) were included in the acquisition and one image was acquired at  $b$ -value=0 s/mm<sup>2</sup> ( $b_0$  volume). Because of the inherent antipodal symmetry, the signal was duplicated on the other hemisphere yielding to 515 points. High-resolution 3D  $T_1$ -weighted images were also included ( $TR/TE = 2300/3$  msec,  $FOV = 256 \times 256$  mm<sup>2</sup>, 160 slices,  $1 \times 1 \times 1.2$  mm<sup>3</sup> resolution, scan time = 6.13 min). Besides MRI acquisitions, patients underwent clinical neurological assessment following the National Institutes of Health Stroke Scale (NIHSS) at each  $tp$ . They all received antiplatelet treatment and standard rehabilitation program. Only the motor part of the NIHSS score was retained for further analysis. Stroke volumes were derived from the individual high-resolution  $T_1$ -weighted images using the statistical parametric mapping (SPM) lesion segmentation toolbox ([www.fil.ion.ucl.ac.uk/spm/](http://www.fil.ion.ucl.ac.uk/spm/)). All the subjects signed the written informed consent to the imaging and the Lausanne University Hospital approved the protocol. Patient demographics and main clinical information are reported in Table 6.1.

Patient	Gender	Age	Stroke Location	Arteries Involved	NIHSS Motor			Stroke Size (# voxels)
					<i>tp1</i>	<i>tp2</i>	<i>tp3</i>	
1	F	25	L cortico-subcortical	L MCA	13	4	3	8032
2	M	66	L subcortical	L MCA	5	2	2	1112
3	F	39	R cortico-subcortical	R MCA	7	4	3	76568
4	F	49	R cortico-subcortical	R MCA	8	3	1	15408
5	M	76	L subcortical	L MCA	6	2	2	7520
6	M	73	L subcortical	L MCA L ACA	3	1	0	9400
7	F	67	L cortico-subcortical	L MCA	7	3	1	19336
8	M	62	R cortico-subcortical	R MCA	8	5	4	69832
9	M	35	R cortico-subcortical	R MCA	16	7	4	101360
10	M	69	R cortico-subcortical	R MCA	4	2	2	8752

Table 6.1: Patient demographics and clinical characteristics where the following abbreviations are used: right middle cerebral artery (R MCA), left middle cerebral artery (L MCA) and left anterior cerebral artery (L ACA).



## 6.5 Image preprocessing

For each subject, dMRI images were processed using the Diffusion Toolkit (CMTK; [www.cmtk.org](http://www.cmtk.org)) in order to derive the ODFs needed for fiber tracking, subsequently performed via a streamline-based algorithm. Individual high-resolution  $T_1$ -weighted images were parcellated using Freesurfer (<http://surfer.nmr.mgh.harvard.edu/>) and the Desikan-Killiany anatomical atlas at 83-region scale (64 cortical and 19 subcortical regions) plus the Corpus Callosum was employed. The FLIRT tool from the FMRIB FSL software ([www.fmrib.ox.ac.uk/fsl](http://www.fmrib.ox.ac.uk/fsl)) was used for the linear (affine) registration of the  $T_1$ -weighted scan to diffusion data. In particular, the diffusion baseline images ( $b_0$  volumes) were considered as reference images for estimating the registration transformation subsequently applied to back-project the subject-specific anatomical parcellation into the DSI space.

The tissues analysis is then divided in tract-based analysis characterized on WM tissue, and in region-based analysis characterized on GM tissue. The difference in diffusion properties at the basis of the two requires a substantially different point of view in the investigation choices and interpretation.

### 6.5.1 Tract-based analysis on WM tissue

In a first preliminary study, only the primary motor area (M1), supplementary motor area (SMA), somatosensory cortex (SC) and thalamus (Thl) were considered in the analysis. More precisely, GFA, RTAP, D, and PA values were collected only along intracallosal fiber bundles connecting those regions to the corpus callosum (CC) in the contralateral (non-lesioned) hemisphere.

Widening the study, a series of networks involved in different motor skills were identified in collaboration with an expert. These networks were practically created by selecting the respective regions of interest (ROIs) from the whole set of regions derived from the automatic brain parcellation and all the analysis were performed on these networks in order to study the specific contralateral motor mechanisms. The considered cortical and subcortical ROIs include M1, SMA, SC and premotor area (PM), Thl, caudatus (Cau), putamen (Put) and globus pallidus (GPi). In particular, the following ensembles of tracts were considered: (1) the set of connections between each region cited above in the contralesional area and the corpus callosum (Figure 6.3a), that we call here transcallosal circuit (CC); (2) the ensemble of connections linking the cortical regions, that we define cortical loop (CORT) (Figure 6.3b); (3) the ensemble of connections linking subcortical regions called subcortical loop (SUBCORT) (Figure 6.3c). The latter has been further investigated, identifying its five main sub-networks, in order to provide a more detailed description of the SUBCORT motor pathways: (a) M1 loop (Figure 6.3d), (b) SMA1 loop (Figure 6.3e), (c) SMA2 loop (Figure 6.3f), (d) PM1 loop (Figure 6.3g), (e) PM2 loop (Figure 6.3h).

The microstructural indices previously computed were collected along the different pairs of ROI links shaping each of the aforementioned networks. To this end, an in-house software was used to extract the mean of values along each fiber connecting two specific ROIs. After that, the mean of fibers' values was calculated for each fiber bundle to obtain a value for each index and each particular connection of the considered networks.

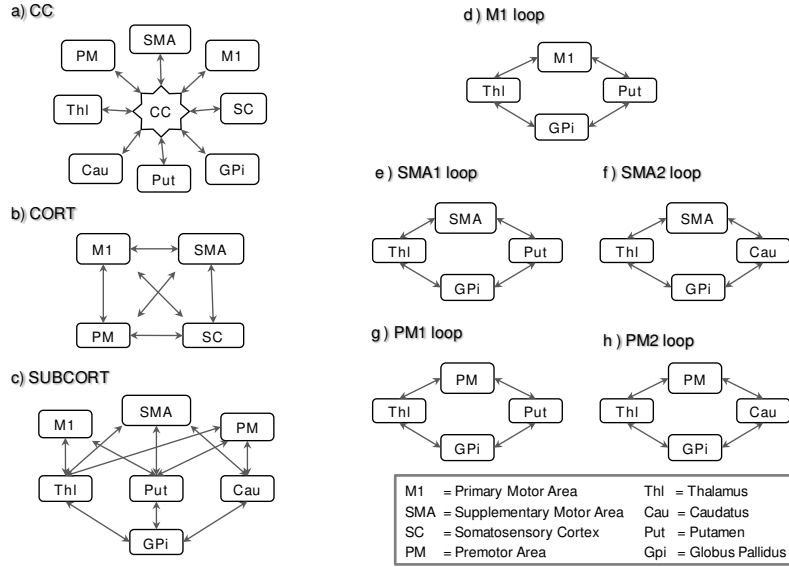


Fig. 6.3: Schematic representation of the transcallosal (CC), cortical (CORT) and subcortical (SUBCORT) networks. The five sub-networks of this latter circuit are also reported on the right panel (d-h).

### 6.5.2 Region-based analysis on GM tissue

The individual high-resolution  $T_1$ -weighted images were segmented into WM, GM and CSF tissues using the SPM toolbox [85]. A binary mask was derived for GM using a conservative 95% threshold on the individual probability maps aiming to avoid partial volume effects. Eighty regions from the Freesurfer parcellation were considered (brainstem and corpus callosum were excluded) and masked with the binary GM mask. Four small subcortical regions per hemisphere resulted to be empty after GM masking and were excluded from further analyses, for a total of seventy-two regions. For all indices, the mean GM value across each masked ROI was then calculated. In particular, average measures were calculated across corresponding regions in both hemispheres for controls, while averaging was constrained to the contralateral hemisphere for patients, leading in both cases to thirty-six representative GM values for each index and subject. The list of the considered regions and relative abbreviations is provided in Table 6.2.

## 6.6 Statistical analysis

### 6.6.1 Preliminary study

In the preliminary study of this investigation [38], the reproducibility of mean GFA, RTAP, D, and PA values along motor tracts was assessed by evaluating statistical differences between  $tp1c$  and  $tp2c$  using a paired  $t$ -test ( $p > 0.05$ ) after

<b>ROI</b>	<b>Abbreviation</b>
Banks of superior temporal sulcus	bSTS
Caudal anterior cingulate cortex	cACC
Premotor area	PM
Cuneus	Cun
Entorhinal cortex	EC
Fusiform gyrus	FuG
Inferior parietal lobe	IPL
Inferior temporal gyrus	ITG
Isthmus cingulate gyrus	IGG
Lateral occipital cortex	LOC
Lateral orbito frontal cortex	lOFC
Lingual gyrus	LgG
Medial orbito frontal cortex	mOFC
Middle temporal gyrus	MTG
Parahippocampal gyrus	PHG
Supplementary motor area	SMA
Pars orbitalis	PORB
Pars triangularis	PTRI
Pericalcarine	PERI
Sensory cortex	SC
Posterior cingulate cortex	PCC
Primary motor area	M1
Precuneus	PCN
Rostral anterior cingulate cortex	rACC
Rostral middle frontal gyrus	rMFG
Superior frontal gyrus	SFG
Superior parietal lobe	SPL
Superior temporal gyrus	STG
Supramarginal gyrus	SMG
Frontal pole	FP
Temporal pole	TP
Thalamus	Thal
Caudate	Cau
Putamen	Put
Hippocampus	Hipp
Amygdala	Amg

Table 6.2: List of the thirty-six regions and relative abbreviations considered for the region-based analyses.

a Kolmogorov-Smirnov normality test. Percentage absolute changes in mean values between time points were evaluated for each index on both groups as

$$\begin{aligned}
\Delta_{tp12c}(m) &= |(m_{tp2c} - m_{tp1c})|/m_{tp1c} \\
\Delta_{tp12}(m) &= |(m_{tp2} - m_{tp1})|/m_{tp1} \\
\Delta_{tp23}(m) &= |(m_{tp3} - m_{tp2})|/m_{tp2} \\
\Delta_{tp13}(m) &= |(m_{tp3} - m_{tp1})|/m_{tp1}
\end{aligned}
\tag{6.11}$$

where  $m$  denotes the mean value of the considered index along the fibers of a given connection, and the subscript  $c$  denotes the control group. Normality test (Kolmogorov-Smirnov) revealed that the values were normally distributed enabling the use of parametric statistics. Accordingly, the unpaired  $t$ -test with  $p < 0.05$  was performed to establish the significant differences between  $\Delta_{tp12c}(m)$  and  $\Delta_{tp12}(m)$ . With the purpose to further characterize the indices, Spearman correlation with GFA was performed. In addition, for each patient, the  $z$ -score of the mean absolute changes of each index and connection with respect to the same measurement on the control group was calculated in order to highlight and visually render in an intuitive way the distance between each patient and the control group as well as individual changes over time. Finally, the predictive value of each metric was assessed by a linear regression model where the motor outcome at six months after stroke ( $tp3$ ) was the dependent variable and the mean values of each index for all the connections at  $tp1$ , age, stroke size, and NIHSS motor scores at  $tp1$  and  $tp2$  were the predictors. A backward selection process was used to select the optimal predictor model with  $p = 0.05$  as significance threshold.

### 6.6.2 Networks study

In the next step, the analysis was extended to other microstructural indices that are RTOP and RTPP, and an additional statistical analysis was performed, as detailed in what follows [37].

#### Precision of the measurements

In order to demonstrate the longitudinal stability of the different indices, a repeatability analysis was performed on the test-retest data from the control group. First, for each index and each network the degree of correlation as assessed by the square of the Pearson's correlation coefficient ( $R^2$ ) was calculated between  $tp1c$  and  $tp2c$  data. Second, the Bland-Altman plot was derived for illustrating the variations of the differences between paired data for each of the main networks, together with the percent coefficient of intra-subject variation ( $CV_{intra}\%$ ), and the intra-class correlation coefficient (ICC). More in details, the ICC estimates the reliability of the measurements by comparing the within-subject (WS) to the between-subject (BS) variability:

$$ICC = \frac{BSMSS - WSMSS}{BSMSS + WSMSS} \quad (6.12)$$

where  $MSS$  represents the mean sum of squares and is calculated for the  $WS$  and the  $BS$  as follows:

$$WSMSS = \frac{\sum_{i=1}^N \sum_{k=1}^2 (m_{ik} - \bar{m}_i)^2}{N} \quad (6.13)$$

$$BSMSS = \frac{\sum_{i=1}^N 2(\bar{m}_i - \bar{m})^2}{N - 1} \quad (6.14)$$

where  $N$  is the number of subjects,  $m_{ik}$  is the value of the  $k$ th measurement session for subject  $i$ ,  $\overline{m}_i$  is the mean of the measurements for subject  $i$  across all sessions and  $\overline{m}$  the overall mean across all subjects and sessions. The ICC values were interpreted as follows:  $> 0.75$  as excellent,  $0.40 - 0.75$  as fair to good and  $< 0.40$  as poor [84].

### Comparison of absolute indices changes in patients and controls

After the stability analysis, on both groups the percentage absolute changes in mean values between time points were calculated for each index and each network as in Equation 6.12 averaging the values from all the tracts belonging to the same network. Since Kolmogorov-Smirnov normality test informed about the normal distribution of the percentage values, unpaired  $t$ -test (corrected for multiple comparisons with a false discovery rate of 0.05) was performed to detect significant differences between  $\Delta_{tp12c}(m)$  and  $\Delta_{tp12}(m)$ ,  $\Delta_{tp12c}(m)$  and  $\Delta_{tp23}(m)$ , and  $\Delta_{tp12c}(m)$  and  $\Delta_{tp13}(m)$ .

### Predictive models

In order to assess the predictive power of the 3D-SHORE indices, different linear regression models were considered for prediction of the motor outcome at six months after stroke (NIHSS at  $tp3$ ). First, a linear regression model including only age, stroke size, and NIHSS motor scores at  $tp1$  as predictors was calculated. Then, for each of the three main networks, the mean value of each index along the connections of the set at  $tp1$  was calculated and included as predictor together with age, stroke size and NIHSS motor scores at  $tp1$ . Moreover, a predictive model was derived for each index separately using its  $\Delta_{tp12}$  values and including all the networks shown in Fig. 6.3 and NIHSS at  $tp1$ . The optimal model was identified by a backward selection process (significance threshold:  $p = 0.05$ ).

#### 6.6.3 Comparison between 3D-SHORE indices and tensor FA and MD

In comparing the 3D-SHORE indices with the classical tensor FA and MD [31] we decided to insert the MSD which has a more explicit and directly correlation with MD [223]. Moreover, to avoid overfitting in some analyses due to the large number of considered indices we decided to retain only RTAP and RTPP discarding RTOP as being the composition of the previous ones and thus already implicitly described. The major part of the analysis was the same as already written except for the GM analysis, thus the subsequent Sections evidenced only the additions to the pipeline.

### Precision of the measurements

The variability and longitudinal stability analyses were performed for all the microstructural indices, relying on all the representative measures coming from both tract-based and region-based analysis on GM. In addition to ICC and  $CV_{intra}$

calculated as aforementioned, the inter-subject coefficient of variation was added ( $CV_{inter}$ ) [30, 55, 169].

Specifically, the  $CV_{inter}$  (between-subject CV) measures the variability across subjects, reflecting the inter-individual variability and being indicative of data consistency across subjects. The  $CV_{inter}$  was computed for each session as follows:

$$CV_{inter} = \frac{\sigma}{\mu} \cdot 100 \quad [\%] \quad (6.15)$$

where  $\mu$  and  $\sigma$  are the mean and standard deviation of each index measure across subjects. For biological measurements from MRI,  $CV_{intra} \leq 10\%$  and  $CV_{inter} < 15\%$  are considered as acceptable [139, 103]. For tract-based measures,  $CV_{intra}$  and ICC were a single measure for each loop, as all the connections belonging to the corresponding network were considered together for providing a global representative measure of network reproducibility. Conversely, the  $CV_{inter}$  metric was first computed for each tract as the mean of the corresponding  $CV_{inter}$  values of the two sessions and then summarized for each loop by the mean  $\pm$  standard deviation (SD) values across connections. This has been done to better appreciate the variability across these structural links. For region-based analysis,  $CV_{intra}$  and ICC were computed for each ROI individually (mean  $\pm$  SD values across GM ROIs), while the  $CV_{inter}$  metric was initially derived calculating it for each region, after averaging the  $CV_{inter}$  metrics of the two sessions, and then reported as mean  $\pm$  SD values across GM ROIs.

### Comparison of absolute indices changes in patients and controls

Concerning this analysis, everything remained unchanged with respect to the previous Section apart from a more stringent correction for multiple comparisons across indices that is Bonferroni adjustment at  $\alpha = 0.05$ .

### Predictive models

In addition, in order to assess the predictive power of both tensor-derived and 3D-SHORE-derived indices, different linear regression models were considered and their performance in predicting the clinical motor outcome at six months (NIHSS at  $tp3$ ) was tested. For each of the three networks, three regression models were built:

- Tensor-based model (TBM): the average across all the connections of the considered loop at  $tp1$  was calculated for each index (MD, FA) and both mean values were included as predictors along with age, stroke size and NIHSS at  $tp1$ .
- 3D-SHORE-based model (SBM): the average across all the connections of the considered loop at  $tp1$  was calculated for each index (GFA, PA, RTAP, RTPP, MSD) and these mean values were included as predictors along with age, stroke size and NIHSS at  $tp1$ .
- Global microstructural model (GBM): all the indices (both tensor-derived and 3D-SHORE-derived) were included as predictors, after having calculated their individual mean value across all the connections of the considered loop. No clinical information was added.

The optimal model was always identified by a backward selection process (significance threshold:  $p = 0.05$ ).

### **Statistical analysis on GM region-based outcomes**

After the reproducibility assessment, also for the GM region-based measures the statistical analyses were performed for depicting differences between patients and controls and detecting possible plasticity changes in contralateral GM tissues. First, a three-way mixed (within-between) analysis of variance (ANOVA) was performed for each microstructural index to test the significance of different factors, using the mean index value as dependent variable. Three independent variables were considered: Time with two levels and Region with thirty-six levels (within-subject factors) plus Group with two levels as between-subject factor. In addition, a further two-way repeated measures ANOVA was performed on the patient group data in order to assess for the presence of longitudinal changes in contralateral GM structures across all temporal scales. Also in this case the mean value for each index was used as dependent variable in the corresponding ANOVA, while two independent variables were included: Time with three levels and Region with thirty-six levels. For each ANOVA, Mauchly's test was used to assess the sphericity assumption and Greenhouse-Geisser epsilon adjustments for nonsphericity were applied where appropriate. Post-hoc tests adjusted for multiple comparisons with the Bonferroni correction were used when significant interactions were found. For all statistical tests,  $p < 0.05$  was considered to be significant.





## Results and discussion

Following Chapter 6, here below we show all the results obtained and we discuss them aiming at emphasizing the 3D-SHORE indices potential as biomarkers for stroke disease. The structure of this Chapter reflects the subdivision proposed in Chapter 6 starting from the preliminary study exploring only some indices and single connections and successively widened considering collections of connections and more indices, that were also characterized against well established DTI indices.

### 7.1 Preliminary study

#### *Reproducibility of index values in controls.*

In controls, reproducibility of the mean GFA, RTAP, D and PA values was observed as confirmed by *t*-test which showed no statistical significant differences between *tp1c* and *tp2c* ( $p > 0.05$ ). The mean absolute GFA, RTAP, D, and PA changes calculated for all the motor connections between the two time points were: *GFA* :  $0.0248 \pm 0.0074$ , *RTAP* :  $0.0290 \pm 0.0082$ , *D* :  $0.0205 \pm 0.0047$ , *PA* :  $0.0241 \pm 0.0072$  (mean $\pm$ SEM). Among connections, the largest variability was recorded for SC.

#### *Comparison of absolute GFA, RTAP, D, and PA changes in patients and controls.*

Figure 7.1 illustrates the mean absolute percent changes of the different indices for patients and controls. For each index, absolute changes between *tp1* and *tp2* in patients' connections were significantly different from the absolute changes between the same regions in controls between *tp1c* and *tp2c* ( $0.01 \leq p \leq 0.05$ ). However, the thalamic intracallosal connection failed to reach significance in all conditions, and SC-CC did not reach significance for RTAP and D. As it is apparent from Figure 7.1, PA shows the highest sensitivity in differentiating the patients from the control group, outperforming GFA in the SMA-CC connection and having the same performance for the other considered ones. In particular, both are able to differentiate the groups for the M1 and SC intracallosal connections. RTAP and D also allow differentiating between the two groups for M1 and SMA, while they could not highlight differences for SC. In connections where RTAP and D are able

to split patients and controls, 3D-SHORE-based indices allow for a more accurate description of the microstructural changes in patients.

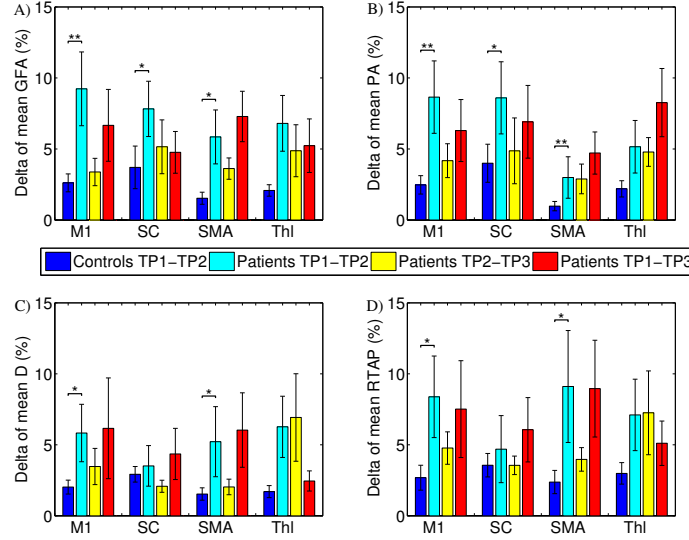


Fig. 7.1: Longitudinal changes in percent mean absolute values in controls and patients (\* $p < 0.05$ , \*\* $p < 0.01$ ). (A) *GFA*; (B) *PA*; (C) *D*; (D) *RTAP* [38].

#### *Correlations of each absolute descriptor changes with GFA.*

For both controls and patients, Spearman's correlation  $\rho$  showed a significant ( $p < 0.05$ ) monotonic relationship between the mean absolute changes of each index and GFA changes. The overall correlation among all the intracallosal connections was assessed, showing the following results: 1) *RTAP*:  $\rho_{tp12c} = 0.48$ ,  $\rho_{tp12} = 0.74$ ,  $\rho_{tp23} = 0.38$ ,  $\rho_{tp13} = 0.65$ ; 2) *D*:  $\rho_{tp12c} = 0.43$ ,  $\rho_{tp12} = 0.76$ ,  $\rho_{tp23} = 0.37$ ,  $\rho_{tp13} = 0.40$ ; and 3) *PA*:  $\rho_{tp12c} = 0.51$ ,  $\rho_{tp12} = 0.74$ ,  $\rho_{tp23} = 0.40$ ,  $\rho_{tp13} = 0.64$ . In all cases results were significant with  $p < 0.05$ .

#### *Longitudinal changes in patients.*

Figure 7.2 highlights the pattern of the longitudinal changes in the different connections for individual patients with respect to the control group, that appeared to be patient-specific. The largest changes were observed in patients with the more severe motor deficit. The pattern is similar for the different indices providing evidence of the ability to capture the microstructural alterations due to white matter plasticity in the contralesional area. In particular, *PA* closely reproduces the pattern of *GFA*, while *RTAP* and *D* appear to be less sensitive especially for *SC*, coherently with the observation that for *SC* no significant difference between patients and controls could be detected by these two indices (see Figure 7.1). An increase in axon diameter is seen in patients over time. This could reveal axonal

outgrowth and myelin increase due to plasticity as activated in the rehabilitation process [135], [204].

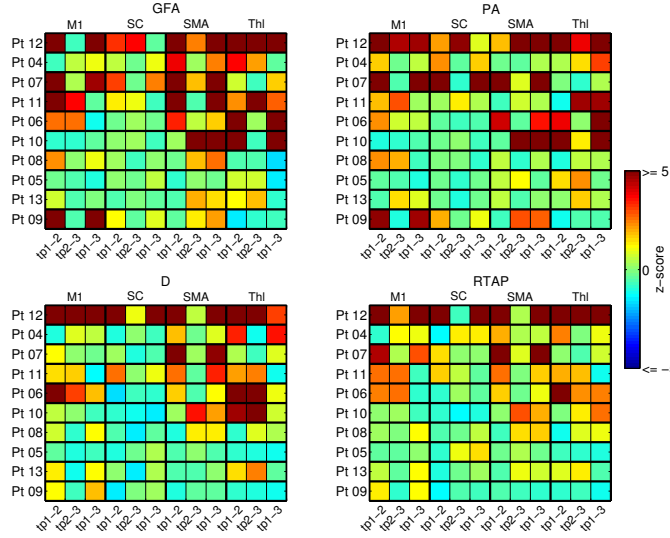


Fig. 7.2: Patients’ individual profiles of mean absolute changes between  $tp1$  and  $tp2$  (first column),  $tp2$  and  $tp3$  (second column), and  $tp1$  and  $tp3$  (third column). Changes were compared to the corresponding controls’ mean changes using  $z$ -scores. Patients are ordered according to the initial NIH Stroke Scale (NIHSS) [38].

*Prediction of clinical outcomes in patients for each index.*

In the patients’ group, a linear regression model including only age and NIHSS at  $tp1$  and  $tp2$  gave low correlation as well as a model including only NIHSS at  $tp1$  and  $tp2$  as reported in Table 7.1 ( $R^2 = 0.691$ ; adjusted  $R^2 = 0.652$ ). Conversely, for each index, the models including also its mean values across the different connections were able to predict the NIHSS at  $tp3$  with higher significance (Table 7.2). In particular, the best prediction model was obtained for D ( $R^2 = 0.998$ ; adjusted  $R^2 = 0.990$ ,  $p = 0.008$ ). However, all models led to high significance, with adjusted  $R^2 > 0.8$ , confirming the importance of GFA and 3D-SHORE-based indices for an early prediction of the patient clinical outcome. Moreover, although GFA and PA are both anisotropy indices, PA has a higher prediction significance pointing at a stronger reliability of this new descriptor.

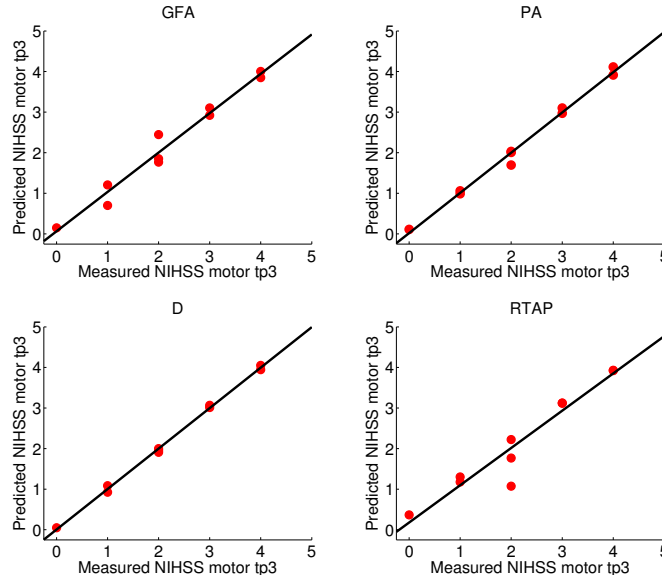
Table 7.1: Prediction model based only on *Age + NIHSS*

Coefficients	Estimate	SE	$t$	$p$	Confidence interval
<i>NIHSS tp2</i>	0.62	0.15	4.23	0.003	0.28, 0.96

The prediction model was statistically significant  $F(1, 8) = 17.86$  with  $p = 0.003$ ; RMSE: 0.78

Table 7.2: Performance of each prediction model

Index	Multiple $R^2$	Adjusted $R^2$	$p$
GFA	0.970	0.932	0.004
RTAP	0.919	0.818	0.026
D	0.998	0.990	0.008
PA	0.991	0.973	0.004

Fig. 7.3: Representation of the measured and predicted NIHSS at  $tp3$  using the models described above.

## 7.2 Networks study

### 7.2.1 Precision of the measurements

The repeatability of the measurements was assessed on the three main networks using the Bland-Altman plots.

The Bland-Altman plots comparing the mean index values across the CC connections for  $tp1c$  and  $tp2c$  are reported in Figure 7.4. The corresponding correlation scatter plots are provided in Figure 7.5. As shown in Table 7.3, a strong correlation between  $tp1c$  and  $tp2c$  was detected for all the indices. The best degree of association was achieved for GFA ( $r^2 = 0.85$ ,  $p < 0.05$ ), followed by PA ( $R^2 = 0.83$ ,  $p < 0.05$ ) while  $R$  showed the lowest correlation value ( $r^2 = 0.78$ ,  $p < 0.05$ ). High ICC values, close to unity, were found in all cases, with GFA and  $R$  showing also the highest and lowest ICC values (0.92 and 0.88), respectively. Regarding the relative variability expressed by the CV index, RTPP resulted the index with the best performance and lowest value, below 3%. In all cases, the Bland-Altman plots showed a mean difference close to zero (except for RTOP, due to the high values' range for this index) with a limited spread of values.

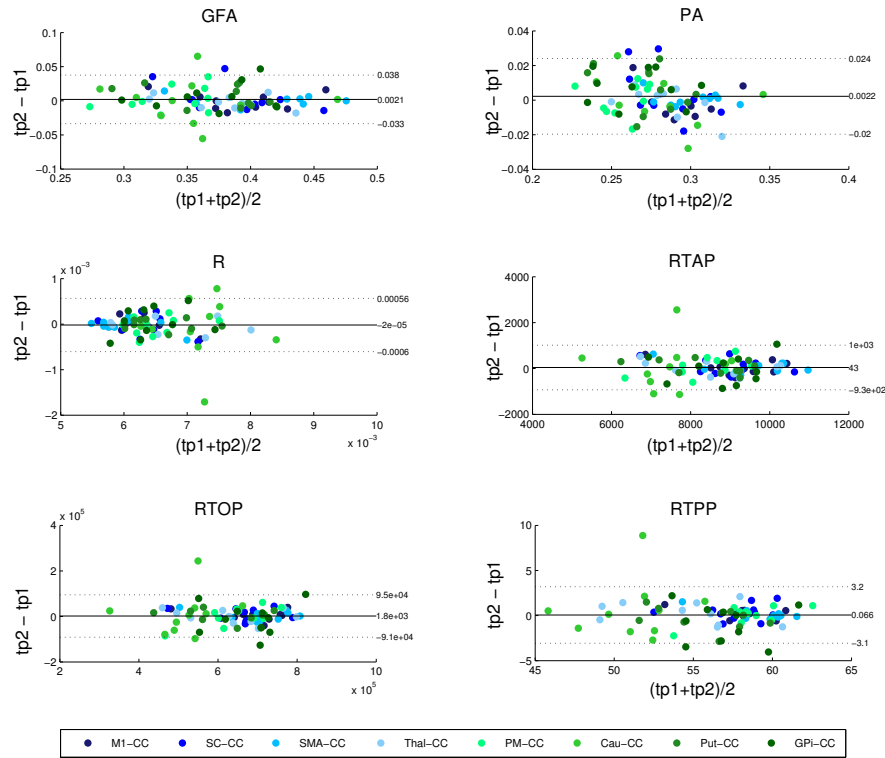


Fig. 7.4: Bland Altman plot for each index in the transcallosal (CC) network. The *solid line* represent the mean value, while the *dashed lines* represent the  $\pm 1.96$  SD values, respectively [37].

The Bland-Altman plots for the CORT and SUBCORT loops are reported in Figures 7.6 and 7.7, respectively, while the corresponding repeatability indices are given in Table 7.3. For the CORT network, the correlation plots evidenced a positive association between time points for all the indices (see Figures 7.8 and 7.9), with the highest correlation obtained for RTOP ( $r^2 = 0.82, p < 0.05$ ), while RTPP showed a poor degree of correlation between values along time. RTOP and RTPP also displayed, respectively, the highest and lowest agreement in terms of ICC values between repeated measures in the test-retest procedure (0.91 and 0.59, respectively). For all the indices, the CV values between the repeated measures were well below 6%. Also in this network, the Bland-Altman plots confirmed a good reproducibility for all the indices, with a limited spread of the values around the mean (close to zero) and almost entirely within  $\pm 1.96$  SD.

For SUBCORT, PA showed the highest temporal stability both in terms of correlation and ICC ( $r^2 = 0.90, p < 0.05$ ; ICC = 0.96). Differently from the other two sets of connections, RTPP and RTOP showed, respectively, the lowest correlation and repeatability values relatively to the other indices (RTPP  $r^2 = 0.73, p < 0.05$ ;

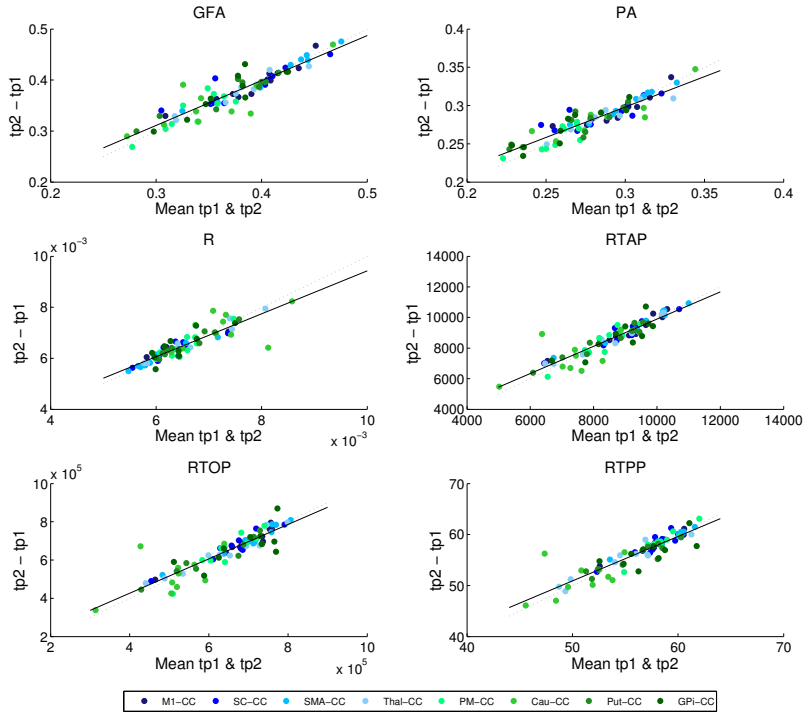


Fig. 7.5: Correlation plot for each index in the CC set [37].

RTOP ICC = 0.85). RTOP also showed a larger CV value in comparison with the other networks (11%). The good reproducibility of the indices for this loop was further confirmed by the Bland-Altman plots, with almost all the values concentrated within the agreement limits for all the indices.

Overall, all the microstructural indices resulted to be stable across acquisition sessions guaranteeing precise measurements.

### 7.2.2 Comparison of absolute indices changes in patients and controls

The mean absolute percent changes for  $\Delta_{tp12c}$ ,  $\Delta_{tp12}$ ,  $\Delta_{tp23}$  and  $\Delta_{tp13}$  for each index and for each of the main networks are reported in Figure 7.10. Regarding the CC network, a significant difference was reached in all the comparisons between temporal changes.

In particular, a marked statistically significant difference was detected in all the indices, except R, between the pairs  $\{\Delta_{tp12c}, \Delta_{tp12}\}$  and  $\{\Delta_{tp12c}, \Delta_{tp13}\}$  with the same range of  $p$  values ( $0.001 < p \leq 0.01$ , corrected) while  $\Delta_{tp23}$  appeared to be less different from the control variations in this loop. Regarding the CORT network, this failed to show statistically significant differences for RTPP at all time scales as well as for the pair  $\{\Delta_{tp12c}, \Delta_{tp23}\}$  in all the considered indices.

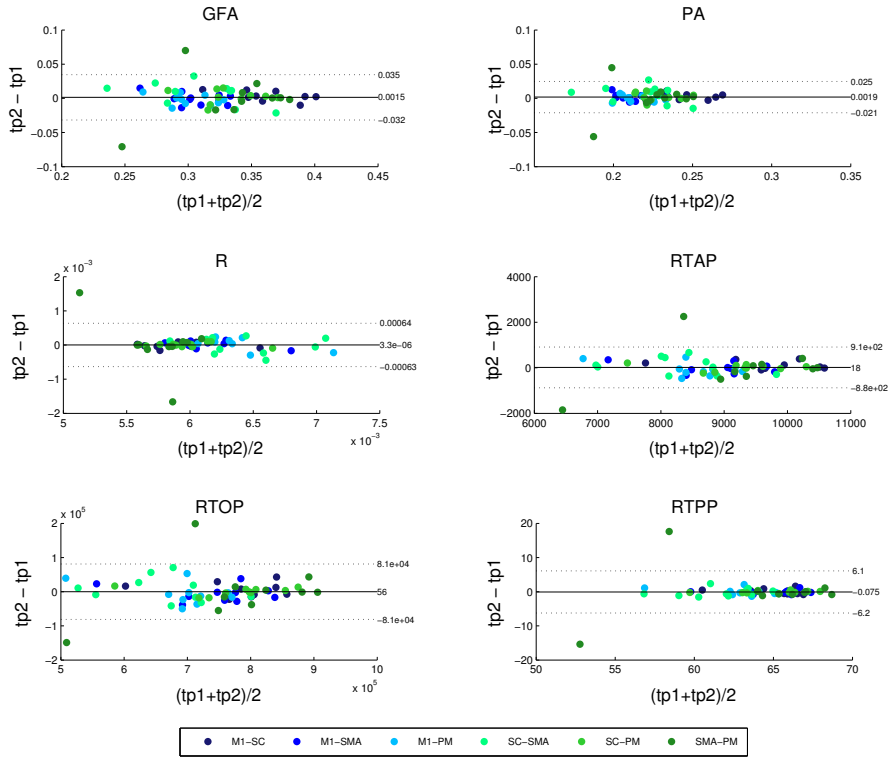


Fig. 7.6: Bland-Altman plot for each index in the cortical (CORT) network. The *solid line* represents the mean value, while the *dashed lines* represent the  $\pm 1.96$  SD values, respectively [37].

In the other cases, the differences with the control group appeared to be equally or less strongly significant in comparison with the other two networks at all the time scales. Finally, the SUBCORT network presents the same results as for the CC connections for GFA and R. A lower significance than for the CC network could be observed for PA and RTAP for the comparison between  $\Delta_{tp12c}$  and  $\Delta_{tp12}$  and also for the comparison between  $\Delta_{tp12c}$  and  $\Delta_{tp23}$  in RTPP. Moreover, RTOP had no significant differences except for the pair  $\{\Delta_{tp12c}, \Delta_{tp13}\}$ .

RTPP results revealed that this index has lower percentage absolute changes over time in comparison with the other indices, both for controls and patients, while RTOP trends in all the networks are in line with those of RTAP.

Overall, mean absolute changes of the set of microstructural indices along the CORT network resulted less effective in discriminating patient and control groups. We thus decided to investigate further the role of the SUBCORT network by considering the five SUBCORT loops that are illustrated in Figure 6.3. This allows a finer granularity in the analysis while still keeping the loop as the basic structural element.

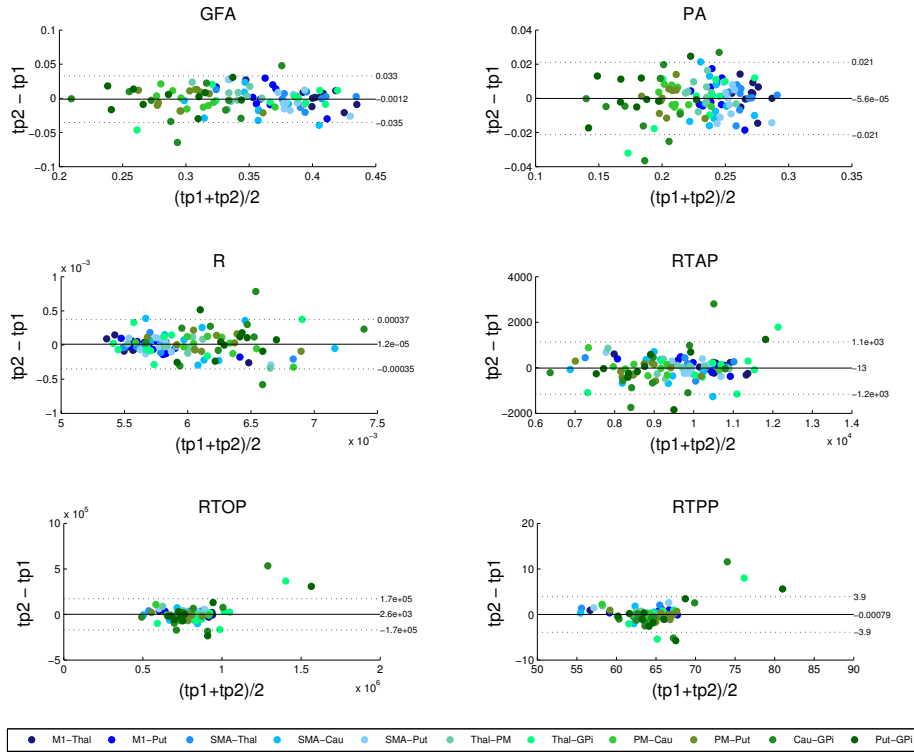


Fig. 7.7: Bland-Altman plot for each index in the subcortical (SUBCORT) network. The *solid line* represents the mean value, while the *dashed lines* represent the  $\pm 1.96$  SD values, respectively [37].

Splitting the SUBCORT network to the set of five sub-network components (Figures 6.3d-h, 7.11) highlighted the leading role of the M1 loop since it allowed discriminating the two groups at all time scales for GFA, PA and R ( $p < 0.05$ ). On the other end, the PM2 sub-network had a less prominent role detecting significant differences only at longer time scales using PA and RTAP as shown in Figure 7.11.

Focusing on the indices, GFA was highlighted as the index reaching the highest significant differences for all the three temporal conditions and all the sub-networks. Furthermore, R showed a good ability to differentiate controls from patients in all loops, followed by PA and, to a lesser extent, RTAP. Finally, RTOP and RTPP changes failed to reach significance in all conditions, namely for all sub-networks and temporal scales. However, a positive trend could be observed in the absolute percent change  $\Delta_{tp13}$  between  $tp1$  and  $tp3$  in patients, which indicates a change in the absolute value of the corresponding index. Even though such changes did not reach statistical significance, they witness the ability of RTOP and RTPP indices of capturing microstructural remodeling in patients. It could be useful to highlight that the method used for correction for multiple comparisons strongly



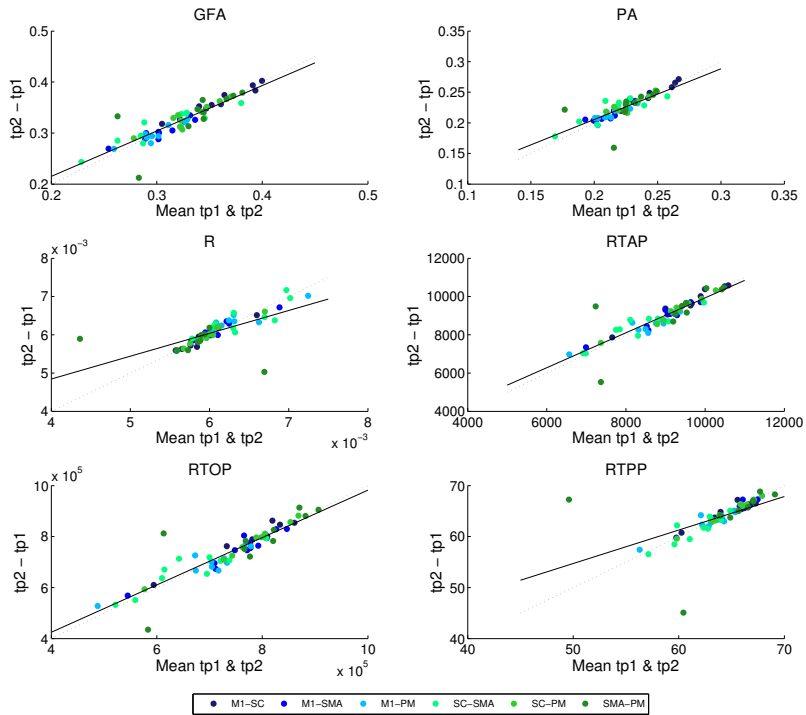


Fig. 7.8: Correlation plot for each index in the CORT set [37].

influences the results. A clear indication does not emerge from the literature in this respect so far.

### 7.2.3 Predictive models

Two families of predictive models were considered: the first targeting the identification of the networks playing a dominant role in the prediction of the clinical outcomes at  $tp3$  and the second aiming at disambiguating the role of a specific index in the same predictive task by gathering the different circuits.

In the patients cohort, a linear regression model including only age, stroke size and NIHSS at  $tp1$  has shown to predict the NIHSS outcome at  $tp3$  with low correlation ( $R^2 = 0.546$ ; adjusted  $R^2 = 0.489$ ;  $p = 0.772$ ). The R index was not considered because of its dependence on RTAP [38]. Conversely, the construction of a predictive model for each of the three networks including all together the corresponding  $tp1$  values of GFA, PA, RTAP, RTOP, and RTPP, increased the prediction capability, except for the CORT loop, as shown in Figure 7.12 ( $R^2 = 0.558$ ; adjusted  $R^2 = 0.431$ ;  $p = 0.057$ ). Notably, the best results were obtained in the SUBCORT set ( $R^2 = 0.997$ ; adjusted  $R^2 = 0.988$ ;  $p = 0.009$ ), even though the regression model for the CC network proved to have a high correlation as well ( $R^2 = 0.994$ ; adjusted  $R^2 = 0.973$ ;  $p = 0.021$ ). Moreover, all the prediction models

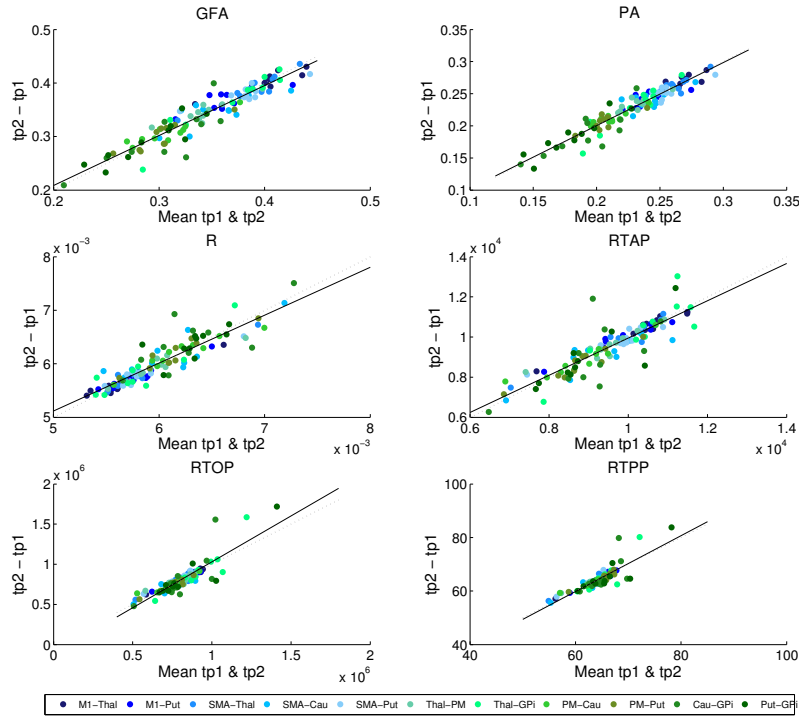


Fig. 7.9: Correlation plot for each index in the SUBCORT set [37].

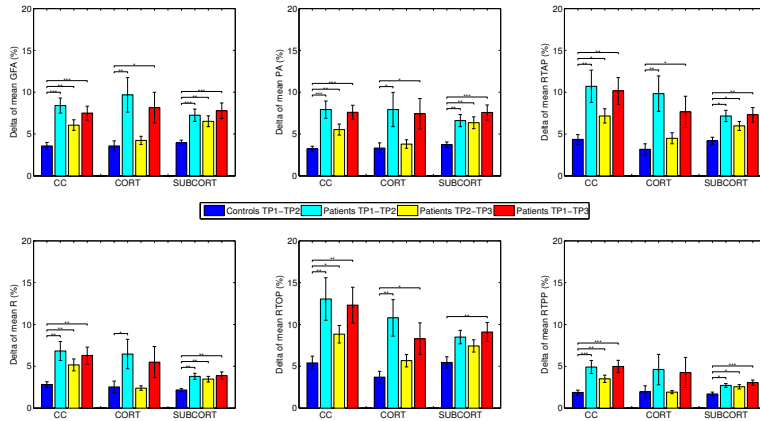


Fig. 7.10: Longitudinal changes in percent mean absolute values in controls and patients for each index in transcallosal (CC), cortical (CORT), and subcortical (SUBCORT) networks ( $*p < 0.05$ ,  $**p < 0.01$ ,  $***p < 0.001$ ) [37].

Table 7.3: Repeatability performance in terms of correlation coefficient ( $R^2$ ), intra-class correlation coefficient (ICC), and coefficient of variation (CV%) for all the indices for each set of connections.

Network	Index	$r^2$	ICC	CV %
CC	GFA	0.85	0.92	4.8
	PA	0.83	0.90	4.0
	R	0.78	0.88	4.6
	RTAP	0.84	0.91	5.7
	RTOP	0.81	0.90	7.4
	RTPP	0.82	0.90	2.8
CORT	GFA	0.80	0.89	5.2
	PA	0.68	0.82	5.2
	R	0.49	0.69	5.3
	RTAP	0.79	0.89	5.1
	RTOP	0.82	0.91	5.6
	RTPP	0.35	0.59	4.9
SUBCORT	GFA	0.88	0.94	5.0
	PA	0.90	0.96	4.7
	R	0.82	0.91	3.1
	RTAP	0.77	0.88	6.2
	RTOP	0.76	0.85	11.0
	RTPP	0.73	0.88	3.1

Table 7.4: In all the networks, correlation values were statistically significant ( $p < 0.05$ ).

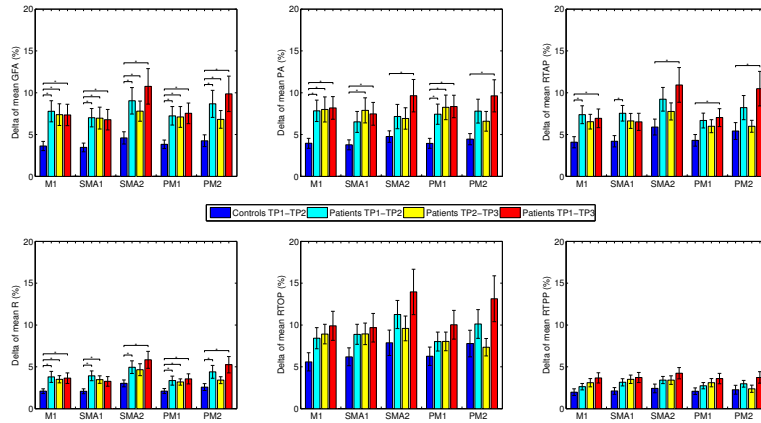


Fig. 7.11: Longitudinal changes in percent mean absolute values in controls and patients for each index in the five sub-networks ( $*p < 0.05$ ,  $**p < 0.01$ ,  $***p < 0.001$ ) [37].

retained RTOP as a significant predictor while GFA was the only one rejected in the model composed by SUBCORT connections.

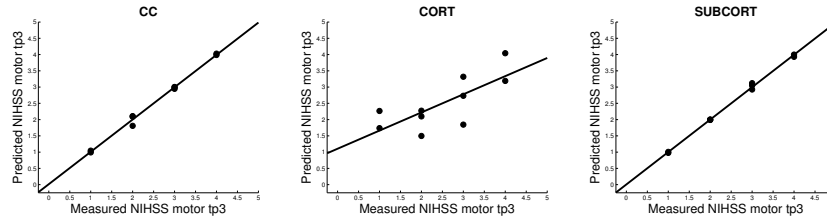


Fig. 7.12: Representation of the measured and predicted NIHSS at  $tp3$  using the models described above [37].

When the 3D-SHORE indices were considered separately, the advantage of taking into account RTOP to determine a good prediction of clinical outcome was further confirmed as appears in Figure 7.13. Indeed, the predictive model for this index showed the highest correlation value ( $R^2 = 0.998$ ; adjusted  $R^2 = 0.983$ ;  $p = 0.096$ ). The models using GFA ( $R^2 = 0.992$ ; adjusted  $R^2 = 0.976$ ;  $p = 0.003$ ), RTPP ( $R^2 = 0.956$ ; adjusted  $R^2 = 0.802$ ;  $p = 0.146$ ), and PA ( $R^2 = 0.861$ ; adjusted  $R^2 = 0.688$ ;  $p = 0.073$ ) also showed a good correlation and prediction power. Conversely, no meaningful prediction models could be derived for RTAP using these sets of connections.

For all the different optimal models, the relative importance of each predictor was evaluated by the Fisher test.

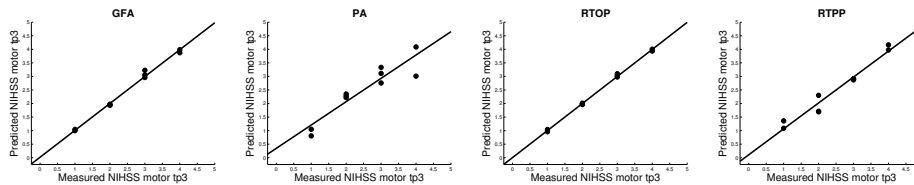


Fig. 7.13: Representation of the measured and predicted NIHSS at  $tp3$  for each index [37].

## 7.3 Comparison between 3D-SHORE indices and tensor FA and MD

### 7.3.1 Qualitative assessment of dMRI-based indices

Classical tensor-derived and 3D-SHORE-derived indices were estimated in all subjects and  $tp$ . Figures 7.14 and 7.15 show the different maps calculated for each

index across times in a representative control and a representative ischemic stroke patient, respectively. For ease of visualization and for the sake of clearer presentation, the three anisotropy measures were normalized to the respective maximum index value, while the square-root of the RTAP maps was extracted to report the values in the same range of RTPP, as in [18]. All the anisotropy measures as well as RTAP and RTPP maps revealed high values in WM, while lower values were reached in GM and especially in voxels with strong CSF contribution. The opposite pattern was visible in MD and MSD maps, where WM appeared to be hypointense due to restricted diffusion while higher values were reached in GM and CSF tissues. These patterns were consistent across subjects and temporal scales. Comparing GFA, PA and FA, both control and patient representative slices revealed a higher WM/GM contrast for the normalized 3D-SHORE-derived anisotropy measures that also appeared to be less noisy and more uniform throughout WM in comparison to the classical FA. Moreover, FA appeared to have lower values in regions with large fiber orientation dispersions where the single tensor representation precludes the possibility to cope with complex structures leading to drops. RTAP maps were hyperintense in regions of coherently packed WM fibers, while RTPP was similar in GM and WM tissues. Finally, MSD and MD visually demonstrated a correlated behaviour, appearing brighter in regions where water particles are free to diffuse like ventricles and darker in regions of restriction like WM. In the stroke patient reported in Figure 7.15, a large ischemic lesion can be appreciated in the left hemisphere (cortico-subcortical areas) and the modulation of tissue microstructure is visible across the different  $tp$ . The lesion was hypointense in GFA, PA, MSD, FA and MD at  $tp1$ , while markedly brighter than the other tissues in RTAP and RTPP. After one month from the injury ( $tp2$ ), the contrast was reversed for these two indices, such that the lesion appeared hypointense as in the anisotropy measures, where hyperintensities within the lesion became visible in MSD and MD. Such a trend persisted at six months after the initial brain damage ( $tp3$ ). For all the subsequent quantitative analyses, we investigated the contralateral hemisphere only, where microstructural changes after stroke might be subtle and not visually detectable.

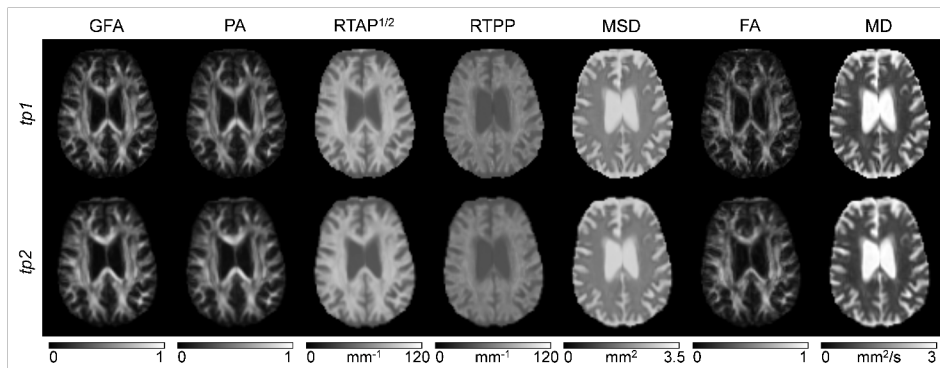


Fig. 7.14: Axial slices of a representative control for each index (columns) and each time point (rows). Images are displayed in radiological convention [31].

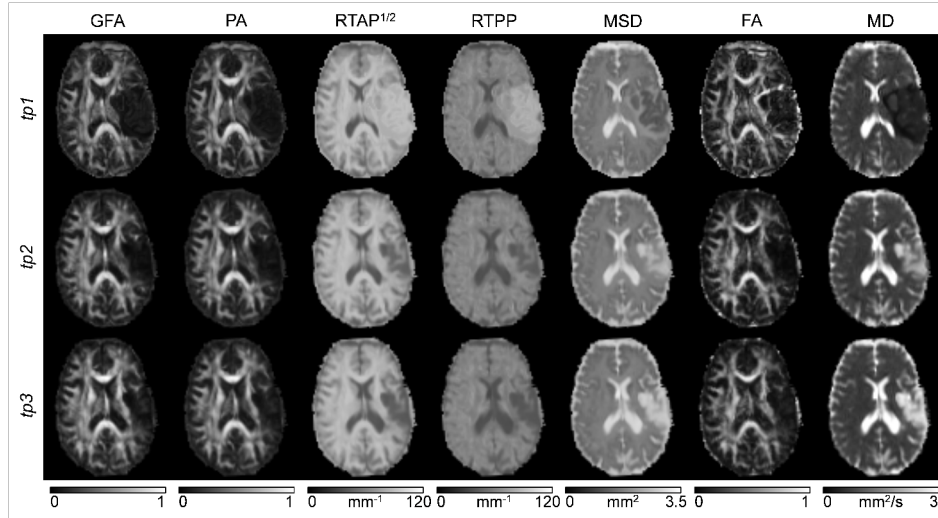


Fig. 7.15: Axial slices of a representative patient (ischemic stroke in left cortico-subcortical areas) for each index (columns) and each time point (rows). Images are displayed in radiological convention [31].

### 7.3.2 Precision of the measurements

In terms of test-retest reproducibility, tract-based results highlighted excellent consistency across sessions in the three networks for tensor-derived as well as 3D-SHORE indices, with  $ICC > 0.8$  in almost all cases and values close to unity for the SUBCORT loop (Table 7.5). Indeed, the highest  $ICC$  was obtained for PA in SUBCORT ( $ICC = 0.96$ ), followed by MSD in the same network ( $ICC = 0.95$ ). Conversely, MSD together with RTPP reached the lowest values in CORT, although still amenable to be judged as having good reliability ( $ICC = 0.67$  and  $ICC = 0.59$ , respectively). This high reliability was matched with high intra-subject stability across sessions as measured by  $CV_{intra}$  values, well below 10% and, in most of the cases, also below 5%. The lowest stability was found in the CC loop for MD ( $CV_{intra} = 7.7\%$ ), while MSD resulted to be the index with the highest stability in all the loops, reaching a remarkable 1.1% within-subject variability in the SUBCORT network.

GM region-based reproducibility results are reported in Table 7.6 in terms of mean and SD values across ROIs. RTAP, RTPP, MSD and MD reached excellent consistency, with mean  $ICC > 0.90$  and very low SD across ROIs ( $< 0.10$ ). Conversely, all the anisotropy measures showed only good reliability and more variability across the different GM structures. This was further confirmed by the  $CV_{intra}$  measure, reporting mean values  $< 10\%$  in all cases albeit higher for GFA, PA and FA in comparison to the other microstructural indices. Also in this case, MSD reached the lowest variability values with a limited spread around the mean.

Figure 7.16 shows the inter-subject variability results ( $CV_{inter}$ ) represented as mean  $\pm$  SD across all the connections of a given loop for tract-based analysis, and

Table 7.5: Tract based reproducibility.

		Tract-based		
		CC	CORT	SUBCORT
<i>GFA</i>	<i>ICC</i>	0.92	0.89	0.94
	$CV_{intra}$	4.83	5.23	5.03
<i>PA</i>	<i>ICC</i>	0.90	0.82	0.96
	$CV_{intra}$	3.98	5.23	4.71
<i>RTAP</i>	<i>ICC</i>	0.91	0.89	0.88
	$CV_{intra}$	5.72	5.10	6.16
<i>RTPP</i>	<i>ICC</i>	0.90	0.59	0.88
	$CV_{intra}$	2.83	4.92	3.10
<i>MSD</i>	<i>ICC</i>	0.83	0.67	0.95
	$CV_{intra}$	2.06	3.40	1.13
<i>FA</i>	<i>ICC</i>	0.90	0.91	0.93
	$CV_{intra}$	4.77	4.31	4.89
<i>MD</i>	<i>ICC</i>	0.85	0.89	0.94
	$CV_{intra}$	7.74	3.73	3.50

Table 7.6: Grey matter reproducibility.

	ICC	$CV_{intra}$
<i>GFA</i>	$0.63 \pm 0.22$	$7.36 \pm 2.96$
<i>PA</i>	$0.61 \pm 0.24$	$6.82 \pm 2.42$
<i>RTAP</i>	$0.91 \pm 0.07$	$3.40 \pm 1.63$
<i>RTPP</i>	$0.92 \pm 0.07$	$1.73 \pm 0.78$
<i>MSD</i>	$0.93 \pm 0.09$	$1.97 \pm 0.75$
<i>FA</i>	$0.66 \pm 0.17$	$9.25 \pm 3.59$
<i>MD</i>	$0.94 \pm 0.08$	$3.09 \pm 1.71$

across ROIs for region-based analysis on GM. As expected, the between-subject variability was higher than the within-subject, although the mean  $CV_{inter}$  values were  $\leq 15\%$  in all cases. Regarding the network analysis, similar patterns in the three loops were observed for each index, with RTPP and MSD featuring the lowest variability across subjects (RTPP:  $CV_{inter} = 4.67 \pm 2.53\%$  in CORT; MSD:  $CV_{inter} = 2.36 \pm 1.82\%$  in SUBCORT). Conversely, RTAP was the index showing more variability in all loops, especially in CC. The same trend was observed in the ROI-based analysis on GM, where the  $CV_{inter}$  values were similar to those resulting from tract-based analysis with RTPP and MSD reaching the highest stability (RTPP:  $CV_{inter} = 4.87 \pm 1.34\%$ ; MSD:  $CV_{inter} = 6.49 \pm 1.72\%$ ). It is worthy of note that all the values were within the recommend 15% range [139, 103], even though tensor-derived indices featured relatively lower stability across subjects in GM, with the highest values reached by FA ( $CV_{inter} = 11.68 \pm 3.09\%$ ).

### 7.3.3 Comparison of absolute indices changes in patients and controls

For each index and network, the mean of the percentage absolute changes between  $tp$  is reported in Figure 7.17 along with SD across subjects. The  $p$ -values resulting from the statistical analysis are shown as stars with three levels of significance

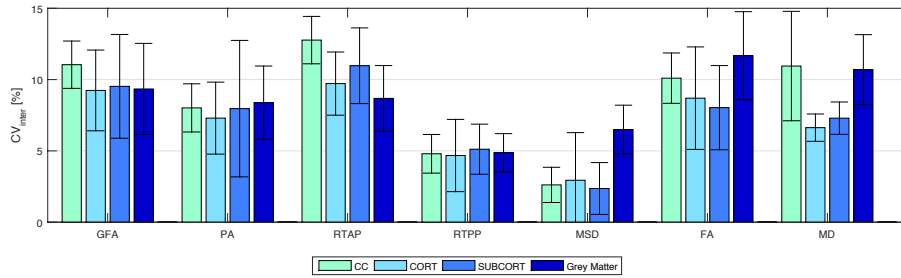


Fig. 7.16: Reproducibility in terms of inter-subject coefficient of variation ( $CV_{inter}$ ) for all the indices and for all the outcome measures. Results are expressed as percentage and reported as mean  $\pm$  standard deviation across connections (for tract-based) and regions (for region-based on grey matter), respectively. CC = transcallosal network; CORT = cortical network; SUBCORT = subcortical network [31].

(\* $p < 0.05$ , \*\* $p < 0.01$ , \*\*\* $p < 0.001$ ). In all the cases, data from the control group confirmed the limited percentage changes between time points, with mean values  $< 5\%$ , in agreement with the reproducibility results from the previous Section. Regarding the CC network, all the anisotropy measures (GFA, PA and FA) reached the highest significance when comparing  $\Delta_{tp12c}$  and  $\Delta_{tp12}$  as well as  $\Delta_{tp12c}$  and  $\Delta_{tp13}$  ( $p < 0.001$ ). Moreover, GFA and FA showed higher significance than the other microstructural indices in the comparison between  $\Delta_{tp12c}$  and  $\Delta_{tp23}$  ( $p < 0.01$ ). MSD and MD highlighted the same patterns across time and the same statistical differences, with not significant changes between  $\Delta_{tp12c}$  and  $\Delta_{tp23}$ . In the CORT network, only few significant differences were detected between controls and patients ( $\Delta_{tp12}$ ) by GFA and RTAP, while for all the other indices the longitudinal changes, although appreciable, did not reach the statistical threshold. Conversely, several significant differences were detected again in the SUBCORT loop by all the indices at multiple time scales, except for RTAP and RTPP which did not depict significant changes between  $\Delta_{tp12c}$  and  $\Delta_{tp23}$ . All the anisotropy measures confirmed the presence of marked changes over time involving also this network, with similar patterns to the findings shown in CC.

### 7.3.4 Predictive models

Extending the preliminary analyses, the tract-based results in patients were further used to predict the clinical motor outcome at  $tp3$  by relying on several regression models. The reference linear regression model including only clinical variables at baseline (age, stroke size and NIHSS motor score at  $tp1$ ) and avoiding microstructural indices could predict the NIHSS outcome at  $tp3$  with low correlation ( $R^2 = 0.546$ ; adjusted  $R^2 = 0.489$ ;  $p < 0.05$ ). The TBM, enclosing MD-FA at  $tp1$  plus the clinical variables, allowed increasing the prediction capability of the reference model in the CORT and SUBCORT networks (Figure 7.18, first row). In detail, the TBM for SUBCORT presented the best performance ( $R^2 = 0.975$ ;



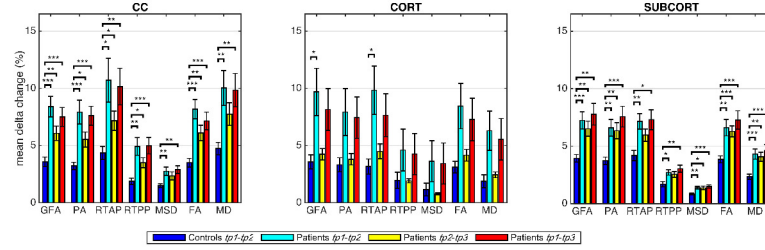


Fig. 7.17: Longitudinal changes in percent absolute values in controls and patients with significant differences between cohort distributions ( $*p < 0.05$ ,  $**p < 0.01$ ,  $***p < 0.001$ ) for each index in transcallosal (CC), cortical (CORT), and subcortical (SUBCORT) networks. Mean  $\pm$  standard deviation values across subjects are reported [31].

adjusted  $R^2 = 0.955$ ;  $p < 0.001$ ) holding MD, FA, stroke size and age as relevant predictors. In the case of the CORT network, a higher correlation than the reference model was found with the TBM retaining only stroke size and MD as significant predictors ( $R^2 = 0.700$ ; adjusted  $R^2 = 0.614$ ;  $p < 0.05$ ). Conversely, the tensor-based model for CC did not include any microstructural index, returning the reference model as the optimal one. The SBM, embedding the five 3D-SHORE indices at  $tp1$  plus the clinical variables, reached the highest correlation in the SUBCORT network ( $R^2 = 1$ ; adjusted  $R^2 = 0.998$ ;  $p < 0.001$ ) (Figure 7.18, second row). The optimal predictive model held clinical variables plus GFA, MSD, RTPP and PA as significant predictors. The SBM for CORT excluded all the microstructural indices, leading to the reference model as the optimal one. Finally, in the CC network the SBM presented a slightly lower correlation than the reference ( $R^2 = 0.454$ ; adjusted  $R^2 = 0.385$ ;  $p < 0.05$ ) but highlighting RTPP as the only significant predictor. The GBM, including only the dMRI-based indices, allowed to substantially increase the capability to timely predict the motor outcome compared to the clinical reference model (Figure 7.18, third row). In detail, the SUBCORT network provided again the highest correlation ( $R^2 = 0.728$ ; adjusted  $R^2 = 0.694$ ;  $p < 0.01$ ) keeping only RTPP as significant predictor. The predictive model for the CC network also featured high correlation ( $R^2 = 0.713$ ; adjusted  $R^2 = 0.631$ ;  $p < 0.05$ ) maintaining MD and RTPP as predictors, while GFA, RTAP and MD were retained in the predictive model for CORT. This network led to the GBM with the lowest correlation ( $R^2 = 0.724$ ; adjusted  $R^2 = 0.586$ ;  $p < 0.05$ ), but still higher than the reference model.

### 7.3.5 Statistical analysis on GM region-based outcomes

Regarding the control vs patient analyses on the outcomes from the region-based quantification in GM tissues, the mixed ANOVA revealed a significant three-way interaction between Group, Time (TP) and Region (ROI) for all the anisotropy measures (GFA, PA, and FA) and RTPP. Details about these statistical results are reported in Table 7.7. For the four indices, post-hoc Bonferroni tests revealed significant between-group differences in several regions at both time scales, showing

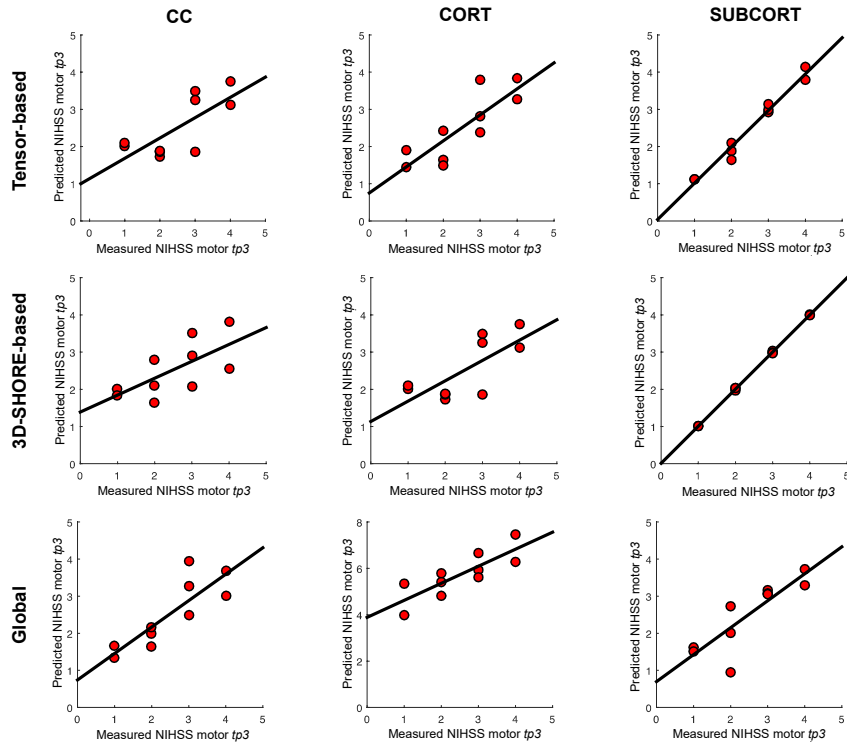


Fig. 7.18: Representation of the measured and predicted NIHSS at  $tp3$  using tensor-based, 3D-SHORE-based and global predictive models [31].

in these cases higher values in patients than controls (Figure 7.19.A,B). While the most widespread changes were detected in terms of anisotropy at  $tp1$ , four common regions were identified as significantly altered (Patients > Controls) also by RTPP. While the most widespread changes were detected in terms of anisotropy at  $tp1$ , four common regions were identified as significantly altered (Patients > Controls) also by RTPP. In detail, the Inferior Temporal Gyrus (ITG) and the Lateral Occipital Cortex (LOC) were in common at both  $tp$ , while the Lateral Orbitofrontal Cortex (lOFC) and the Middle Temporal Gyrus (MTG) presented high significance ( $p \leq 0.01$ ) at  $tp1$  and  $tp2$  in GFA, PA and RTPP and only at  $tp1$  in FA (Figure 7.19.C). RTPP changes were more visible at  $tp2$ , with several regions showing higher values in patients compared to controls and non-significant anisotropic differences. The remaining indices failed to reach a significant three-way interaction even though control vs patient differences can be visually appreciated in Figure 7.19.A. In particular, for RTAP a similar trend to the anisotropy measures was detected in all the regions, especially at  $tp1$  over motor areas and subcortical nuclei as PM, SMA, SC, M1 and Th1, Cau and Put (Patients > Controls). For MSD, while few ROIs presented relatively higher values in patients at  $tp1$ , there was an overall increase in all regions at  $tp2$  (Patients > Controls), except for the temporal

pole where lower values were found over time in this group. Finally, MD patterns were in line with MSD results, although with less marked changes between groups. Moving a step backwards in the mixed ANOVA, all the indices except RTAP revealed a significant two-way interaction between Group and ROI confirming that, considering the overall time scales, there were differences in specific GM regions between the two groups (Table 7.7; Figure 7.20). The anisotropy measures were highly consistent, with FA highlighting more widespread increased values in GM for patients as before. Finally, only GFA, PA and FA revealed an overall significant main effect of Group (between-subject factor), as reported in Table 7.7.

	Between-subject		Within-subject			
	Group		Group*ROI		Group*TP*ROI	
	F-ratio (1,18)	<i>p</i> -value	F-ratio (35,630)	<i>p</i> -value	F-ratio (35,630)	<i>p</i> -value
GFA	6.205	0.023*	2.340	< 0.001*	2.235	< 0.001*
PA	6.256	0.022*	2.218	< 0.001*	1.669	0.010*
RTAP	1.548	0.229	1.249	0.157	1.326	0.102
RTPP	2.064	0.168	2.152	< 0.001*	1.843	0.003*
MSD	2.681	0.119	2.601	< 0.001*	0.552	0.990
FA	7.346	0.014*	2,082	< 0.001*	2.731	< 0.001*
MD	0.186	0.671	1.825	0.003*	1.105	0.314

Table 7.7: ANOVA results (three-way mixed ANOVA) for the control vs patient comparison of grey matter outcomes. The three independent variables were Group (between-subject factor), Time Point (TP) and Region (ROI) (within-subject factors), while the dependent variable was the mean index value. Group\*ROI and Group\*TP\*ROI interactions are expressed in terms of F-ratio(df,error) and *p*-values.

Considering the longitudinal analysis on the patient measures only, again all the anisotropy indices along with RTPP and MD revealed a significant interaction between TP and ROI. In details, GFA  $F(70, 630) = 1.61$ ,  $p = 0.002$ ; for PA  $F(70, 630) = 1.52$ ,  $p = 0.006$ ; for RTPP  $F(70, 630) = 1.47$ ,  $p = 0.01$ ; for FA  $F(70, 630) = 1.92$ ,  $p < 0.0001$ ; and for MD  $F(70, 630) = 1.76$ ,  $p = 0.0003$  (Table 7.8). Post-hoc Bonferroni tests (Figure 7.21) highlighted for the three anisotropy measures consistently significant differences over the lingual gyrus (LgG) for  $tp1$  vs  $tp2$ , and in the medial orbitofrontal cortex (mOFC) for  $tp1$  vs  $tp3$ . Moreover, FA presented LgG differences for  $tp1$  vs  $tp3$ , and in the precuneus (PCN) for both  $tp1$  vs  $tp2$  and  $tp1$  vs  $tp3$ . In all these statistically significant changes, higher values were detected just after the stroke event ( $tp1$ ) in comparison to  $tp2$  and  $tp3$ . Conversely, an opposite trend was found for RTPP detecting a single region [frontal pole (FP)] with higher values at  $tp2$  compared to  $tp1$ . For MD, despite the significant interaction no regions survived the Bonferroni corrections of the post-hoc paired tests (Figure 7.21.B,C). When using a less conservative approach [Least Significant Different (LSD) post-hoc tests], five regions, including PM, SC and Thal, turned out to be significantly increased at  $tp3$  compared to  $tp2$  and  $tp1$  (Figure 7.22). Applying LSD post-hoc tests also to the other indices, the

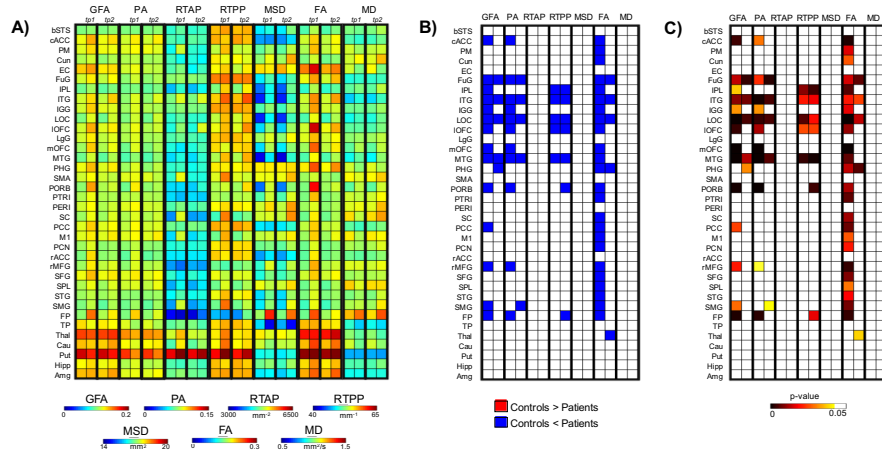


Fig. 7.19: Post-Hoc test results for the three-way mixed ANOVA (controls vs patients). A) For each index and each time point (*tp*) block, the first column represents the mean index values for the controls while the second column the mean values for the patients. B) Post-hoc results of the significant interactions between Group, TP and Region (ROI), expressed in red if the difference between control and patient mean values is positive (controls > patients) and in blue if the difference is negative (controls < patients). (C) Corresponding *p*-values for the significant ROI resulting from the post-hoc tests. These values ( $p < 0.05$ ) are Bonferroni corrected for multiple comparisons [31].

anisotropy measures revealed more widespread regions of increased values in the early phase (*tp1*) in comparison to the other two time points, consistently with the results from the mixed ANOVA. GFA and PA, in addition, showed higher values at *tp3* compared to *tp2* over two motor regions, e.g. Put and M1, respectively. Finally, RTPP confirmed a significant increase over time (both *tp2* and *tp3*) in comparison to *tp1* in the FP region. Regarding the other two indices that did not show a significant interaction (RTAP and MSD) and were thus precluded to be evaluated with post-hoc tests, a different trend was visible across time with a series of appreciable longitudinal differences (Figure 7.21.A). In particular, RTAP revealed a similar behaviour to the anisotropy measures, with higher values at *tp1* that decreased over time, especially at *tp3*. Conversely, MSD highlighted higher values over time, as in the case of MD, with marked visual increases at *tp3* over several regions (as PM, SC, FP, Thal, Put, Cau).

## 7.4 Discussion

### 7.4.1 Networks study

This longitudinal study on motor stroke patients demonstrates the suitability of 3D-SHORE indices for characterizing the contralesional structural changes of

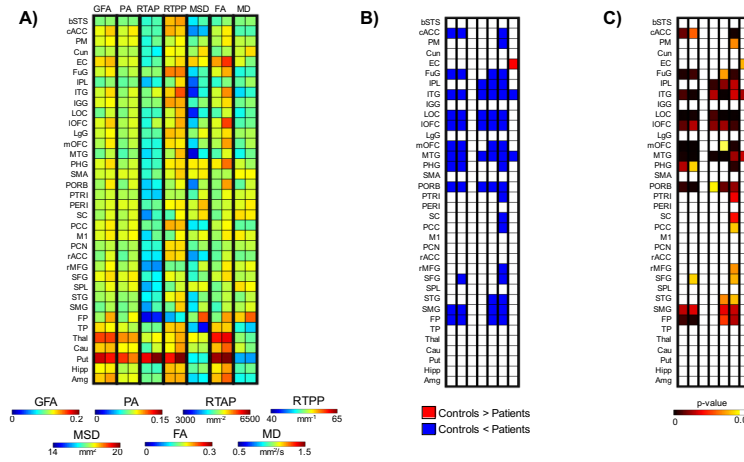


Fig. 7.20: Post-Hoc test results for the three-way mixed ANOVA (Controls vs Patients). A) For each index, the first column represents the mean index values for the controls while the second column the mean values for the patients, averaged across the first two time points. B) Post-hoc results of the significant interactions between Group and Region (ROI), expressed in red if the difference between control and patient mean values is positive (Controls > Patients) and in blue if the difference is negative (Controls < Patients). (C) Corresponding  $p$ -values for the significant ROI resulting from the post-hoc tests. These values ( $p < 0.05$ ) are Bonferroni corrected for multiple comparisons [31].

TP*ROI		
	F-ratio (1,18)	$p$ -value
GFA	1.611	0.002*
PA	1.515	0.006*
RTAP	1.161	0.184
RTPP	1.467	0.010*
MSD	0.983	0.520
FA	1.918	< 0.001*
MD	1.756	< 0.001*

Table 7.8: ANOVA results (two-way ANOVA for repeated measures) for the longitudinal evaluation of grey matter outcomes in the patient group. The two independent variables were Time Point (TP) and Region (ROI), while the dependent variable was the mean index value. The TP\*ROI interaction is expressed in terms of F-ratio(df,error) and  $p$ -values.

the main motor pathways. In particular, our findings suggest that the complete microstructural characterization provided by these indices over the contralateral white matter connections can enable a more detailed knowledge of axonal remodeling after stroke, confirming and extending recent studies based on anisotropy

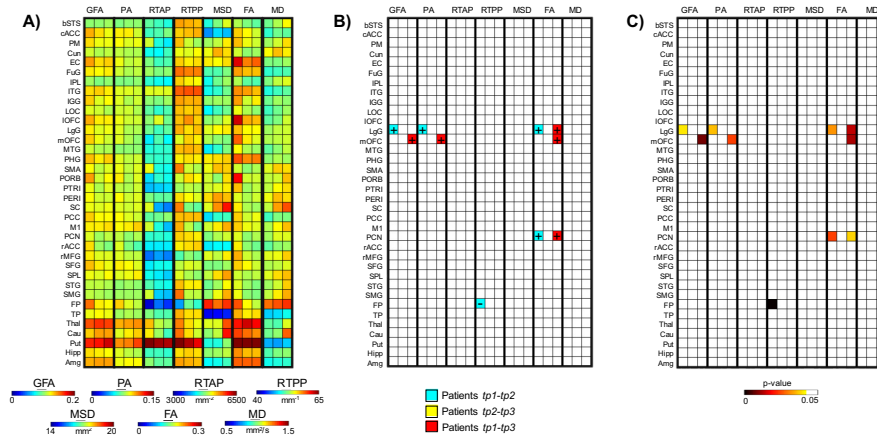


Fig. 7.21: Post-Hoc test results for the two-way ANOVA for repeated measures. A) For each index, the first column represents the mean index values at  $tp1$ , the second column at  $tp2$  and the third at  $tp3$ . B) Post-hoc results of the significant interactions between Time Point (TP) and Region (ROI) for the different time scales (light blue:  $tp1 - tp2$ ; yellow:  $tp1 - tp2$ ; red:  $tp2 - tp3$ ), expressed with their sign as positive or negative depending on the difference results. (C) Corresponding  $p$ -values for the significant ROI resulting from the post-hoc tests. These values ( $p < 0.05$ ) are Bonferroni corrected for multiple comparisons [31].

measures [94, 135] and on a different and less extended set of microstructural indices [38].

The potential of 3D-SHORE derived indices as new markers of disease-induced changes has been further demonstrated by the test-retest study on healthy volunteers which proved the stability of all these indices over time. Finally, our results stress the indication that the different 3D-SHORE measures within 1 week from the insult, combined with clinical status in the acute phase, can predict the motor outcome at 6 months after stroke with strong correlation.

While previous studies focused on the plastic changes considering individually the contralateral intra-hemispheric and interhemispheric motor connections [176, 61, 94], here the concept of network has been introduced and fully investigated. Acute ischemic strokes can indeed disrupt the nodes and edges of the circuits and lead to time- and recovery-dependent changes in the specific structural network characteristics [125]. Thus, studying different CORT and SUBCORT circuits we could identify which are more involved in the recovery process and which allow to more clearly discriminate acute stroke patients from controls. Our findings demonstrate the detection of microstructural changes in all the considered networks. More in details, the changes in all the indices of the CC and SUBCORT network loops, which differ substantially between patients and healthy subjects, put forth the important role played by these two interacting networks which have been largely neglected for a long time. Our results about the CC network are in line with previous findings from functional imaging and electrophysiological studies

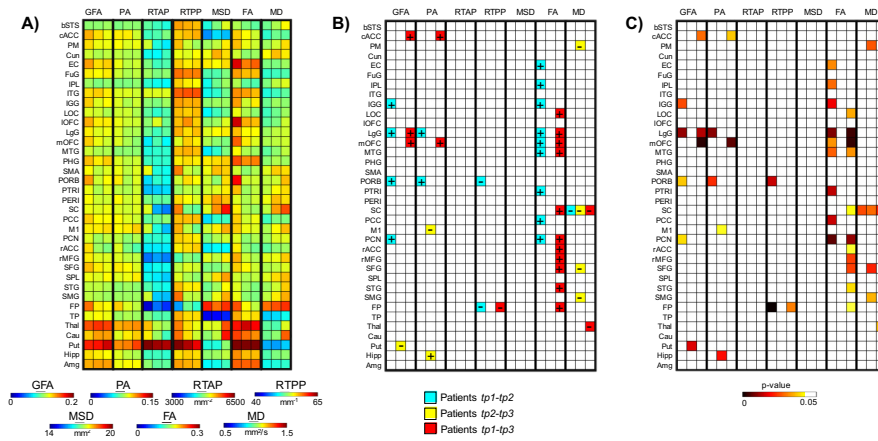


Fig. 7.22: Post-Hoc test results for the two-way ANOVA for repeated measures. A) For each index, the first column represents the mean index values at  $tp1$ , the second column at  $tp2$  and the third at  $tp3$ . B) Post-hoc results of the significant interactions between Time Point (TP) and Region (ROI) for the different time scales (light blue:  $tp1 - tp2$ ; yellow:  $tp1 - tp3$ ; red:  $tp2 - tp3$ ), expressed with their sign as positive or negative depending on the difference results. (C) Corresponding  $p$ -values for the significant ROI resulting from the post-hoc tests. These values ( $p < 0.05$ ) are derived using Fisher’s LSD (Least Significant Difference) [31].

applying transcranial magnetic stimulation (TMS) that have suggested a critical importance of interhemispheric connections for stroke recovery [181].

Regarding the different indices, GFA and PA appeared to be the most sensitive to longitudinal changes in stroke patients, and the most specific in discriminating patients from controls for all the loops. The remodeling of the contralesional white matter in post-stroke functional improvement was reported in many studies [176, 87, 179, 136] and specified as possibly caused by axonal sprouting, axonal outgrowth, dendritic plasticity, or new connections [93, 204]. The new indices, in particular RTAP, RTOP, and RTPP, help us to disentangle the different sources of the contralesional compensation. More in details, GFA permits to only enhance differences in the diffusivity while RTAP, RTOP and RTPP can specify the changes in the axonal structures.

In terms of longitudinal stability and repeatability, the statistical measures applied to the test-retest data from the control group confirmed strong and significant correlations between time points for all the indices and sets of connections, with higher and consistent values for the interhemispheric connections and SUBCORT loop. The ICC values for these two circuits demonstrated excellent agreement for all the indices, while those for the CORT network resulted to be slightly inferior for R and RTOP, although still excellent for the remaining four indices. Finally, the Bland-Altman plots further elucidated a strong repeatability of the indices in test-retest trials showing narrow limits of agreement and small mean differ-

ences between the two repetitions. Overall, the CC and SUBCORT connections appeared to be the most stable and reproducible networks for all the indices, suggesting their importance as circuits to take into consideration for assessing patients' changes over time.

Regarding the prediction power of these indices, the predictive models introduced in this study further demonstrated how 3D-SHORE measures calculated over specific circuits, in combination with clinical and functional status, can provide a powerful and easy-to-use tool to evaluate acute stroke patients and predict their motor recovery. In particular, two types of models have been presented. First, a predictive model for each of the three main networks have been derived, considering all the indices' values at *tp1* together. Again, the interhemispheric (CC) circuit and the SUBCORT loop highlighted the beyond suspicious importance of taking into account these brain circuits. For these models, the inclusion of RTOP as predictor in all the regressions, instead of the conventional GFA, evidenced the role played by the 3D-SHORE indices in the creation of an effective prediction model. Second, we defined a predictive model for each index, considering all together the circuits as predictors. However, here we considered the mean absolute changes rather than the individual values at *tp1* and only included the clinical variables at *tp1* demonstrating that early changes can provide a good prediction of the clinical outcome. While GFA results further confirmed previous findings in literature about its strong prediction power [94, 135], RTOP and RTPP results are novel and permit an improved prediction in comparison to the conventional models including only clinical variables and/or GFA measures. Future studies will be performed to broaden both the inclusion criteria and the number of patients, in order to fully validate these promising findings for a wider clinical use and for a better planning of the rehabilitation processes in stroke patients.

#### 7.4.2 Comparison between 3D-SHORE indices and tensor FA and MD

Our results suggest that 3D-SHORE-based microstructural descriptors obtained from DSI data are capable to quantify the remodeling of both WM tracts and GM regions involved in motor recovery after ischemic stroke. 3D-SHORE-based indices proved to perform similarly to the classical DTI indices (FA and MD) and revealed common patterns across the networks and ROI evaluated in the analyses. Considering their performance and different nature, their combination in clinical studies would allow to provide a more detailed and specific tissue characterization, allowing to disentangle different conditions where tensor-based indices take the same values. For instance, DTI cannot distinguish between a reduction of FA caused by crossing fibers and one caused by a decrease of neural density in a voxel. Conversely, the joint exploitation of RTAP and RTPP can allow disentangling such ambiguity, as RTAP and RTPP both diminish in the case of neuronal density reduction, while RTAP decreases and RTPP increases for crossing fibers, as previously reported [229]. In addition, the combination of tensor-based and SHORE-based indices in the linear regression models allowed to greatly increase their ability to predict the clinical motor outcome in all the considered networks. To the best of our knowledge, this is the first study focusing on the quantitative comparison between 3D-SHORE-based and tensor-based descriptors in healthy



subjects and in a patient population, aiming at demonstrating their behaviour in different brain conditions/tissues and accomplishing an essential step towards their applicability as viable tissue markers.

A growing body of literature is currently reporting the advantages of using multiple  $b$ -values in terms of both detecting fiber crossings [185, 115] and recovering the tissue microstructure [12, 227, 116]. Because of these facts, nowadays, sampling schemes presenting higher  $b$ -values (as DSI and multi-shell) are becoming popular in research and started to appear also in clinical application. In order to fully exploit advanced dMRI datasets, reconstruction models that require multiple  $b$ -values such as the 3D-SHORE are necessary and therefore will become more common in this field. In this context, it is therefore necessary to provide an extensive characterization of these indices in describing tissues in physiological and pathological condition, as we did for stroke patients. In line with the findings firstly described by Özarslan and colleagues [158, 159], our results suggest that 3D-SHORE-based indices can provide a wide set of information, reflecting meaningful tissue properties as visually appreciable from the different maps. In particular, the values estimated in our healthy population for each index and their spatial distribution across the different anatomical structures appear to be in agreement with the available literature results [159, 229, 18], with a high consistency across subjects and time also at a visual inspect. GFA and PA are able to more properly quantify the anisotropy, presenting more contrast between the GM and regions with multiple fiber crossings in which the FA usually results in the same value. The two zero-displacement probability measures derived from SHORE reflect diffusion restriction in different directions, respectively radially (RTAP) and axially (RTPP) to the main diffusion direction [159]. Consistently, RTAP maps exhibited high values in regions of coherently packed WM fibers, as the corpus callosum which is less contaminated by partial volume effects. RTPP values were similar in both GM and WM tissues featuring less WM/GM contrast. This could suggest similar apparent axial diffusivity for WM and GM, even though the mapping of this measurement to real tissue microstructural properties is still an open issue. Finally, MSD and MD were consistently higher in regions featuring free diffusion, like the CSF and in areas with ischemic oedema [4]. These two indices are directly related via the Einstein diffusion equation as reported in the works of Wu and Alexander [223] and Hosseinbor et al. [105] and, accordingly, are visually correlated. Evaluating qualitatively the longitudinal maps derived from the stroke patients, the microstructural indices exhibited a different behaviour in the voxels belonging to the damaged area but with a consistent pattern. Indeed, while all the anisotropy measures revealed low values within the lesion that persisted over time, RTAP and RTPP shifted from initial hyperintensities towards hypointensities after one month from the event ( $tp2$ ), highlighting an opposite trend for anisotropy and restriction. This stresses the complementarity of the information brought by those indices. Furthermore, considering their opposite trend in comparison to MSD and MD (from hypo- to hyperintensities) and the ischemic nature of the stroke these findings support the hypothesis of Avram et al. [18] according to which the zero-displacement measures are more specific biomarkers of the presence of restricting barriers to diffusion. Interestingly, RTAP and RTPP featured the highest values at  $tp1$  highlighting restricted diffusion in the lesion. Moreover, we found MSD to

be more contrasted than MD inside the ischemic lesion in all cases. In particular, this index seems to identify and characterise different portions of the lesion, while MD appears to be more homogeneous in the same areas. Some patients (mainly those with extensive lesions) also revealed increased MSD values in the periphery. However, as this pattern was not confirmed in all cases, a larger sample size and more focused analyses on the stroke lesion would be necessary to draw robust conclusions on this aspect, possibly pointing at an inflammatory reaction which has been previously described [213, 122]. Finally, the heterogeneous patterns of RTAP, RTPP and MSD visible within the lesion one week after stroke could be of help for distinguishing the ischemic core from the penumbra area. This issue deserves further investigation.

The quantitative analysis of possible plasticity processes focused on the contralateral hemisphere to the stroke and exhibited high reproducibility in both 3D-SHORE-based and DTI indices, as quantified by ICC, and high stability, as quantified by intra/inter-subject CV parameters, on both tract and region-based outcomes. Interestingly, for tract measures the 3D-SHORE index MSD, rarely considered in previous studies, showed the lowest intra-subject variability ( $CV_{intra}$ ) in all cases, and the highest reliability (ICC) in CC and SUBCORT. Conversely, it revealed lower, although still good, ICC values in CORT along with RTPP that resulted to be the index with the lowest reliability in this network. This is possibly related to the fact that these two indices exhibited here a relatively higher within-subject SD for repeated measurements than in the other cases, which resulted to be closer to the between-subject SD values and therefore led to lower ICC values for this loop. Despite this consideration concerning the CORT loop only, the reliability and discriminative power of MSD and RTPP were not compromised as further proven by the other group-based analyses performed in this study. Other studies have quantified the reproducibility of 3D-SHORE-based metrics across subjects and sessions. Moreover, the previous reports aiming at quantifying the reliability of classical tensor-based measures generally focused only on few major fiber tracts (e.g. corpus callosum, cingulum, fornix and arcuate fasciculus) [103, 62, 212] rather than considering specific brain networks with different sets of tracts. Despite this main difference, our findings are in line with the results of these studies, which demonstrated reliable measurements for FA and MD featuring both inter-session  $CV_{intra} \leq 10\%$  and  $ICC \geq 0.70$ , with some variability related to the considered tract. Regarding region-based outcomes, the reproducibility analysis in GM ROIs revealed a higher intra-subject variability for the three anisotropy measures (GFA, PA and FA) in comparison to the other indices, with mean values still well within the 10% range, matched with a good reliability from ICC. This is possibly due to the lack of directed orientation in a tissue as GM [25] and is in agreement with previous studies showing a two-three times higher variation of FA in regions of GM compared to WM structures [210, 32]. Conversely, MSD and RTPP appeared again as featuring the lowest intra-subject variability and, along with MD, reached the highest ICC reliability values. The performance of FA for GM ROIs appears to be in line with previous reports evaluating DTI indices in this tissue [207, 97], showing higher  $CV_{intra}$  values for the whole GM than for MD (8 – 11% vs 2 – 5%, respectively) and a wide range of variation across the different GM structures (3.3 – 19.2%). Conversely, no studies have previously quantified the measurement

precision of 3D-SHORE-based indices in GM regions, therefore our findings add an important step to the current literature on the topic and their reassurance in terms of reliability encourages their use for evaluating GM tissues as well. Considering as additional reliability measure the between-subject variability, we found average  $CV_{inter}$  values well below the 15% threshold for both tract- and region-based outcome. Among the seven variables, RTPP and MSD generally had lower  $CV_{inter}$  than the other metrics with average values  $\leq 6\%$ . Tensor-based measures revealed overall lower between-subject stability than 3D-SHORE-based indices, especially in the GM ROIs where the average values were around 10%. Previous studies have indicated FA and MD as the measures with lower  $CV_{inter}$  in different WM fiber tracts, for example Wang and colleagues [212] reported average values in the range 2.4–7.6% for FA and 1.7–9.9% for MD respectively, while Grech-Sollars et al. [97] showed mean inter-subject values  $< 6\%$  for the whole GM and WM regions (not tracts). Our results confirmed the good inter-subject stability for FA and MD but demonstrated that the 3D-SHORE-based indices improve on the classical measures in terms of between-subject variability in most of the cases. The latter observation demonstrated the gain in using a multi- $b$ -values model such as 3D-SHORE. In particular, GFA and MSD were already defined the analogues of FA and MD for multi- $b$ -values acquisitions by Hosseinbor and colleagues [105]. The combined high stability over time, relatively higher inter-subject variability ( $CV_{intra} \ll CV_{inter}$ ) shown by the 3D-SHORE based indices, which is a pattern that can help detecting group differences between subjects, and excellent inter-session ICC values for most of the cases reinforce their potentialities as microstructural biomarkers for revealing longitudinal changes.

Longitudinal group-based analyses were performed to statistically compare the mean absolute changes between time points calculated for each network. Regarding 3D-SHORE-based indices, the Bonferroni corrected  $t$ -tests revealed several highly significant differences between patients and controls in the SUBCORT and CC networks, also for the newly introduced MSD index. These findings further confirm and strengthen our results on a subset of 3D-SHORE indices [37], where the  $t$ -tests were corrected for multiple comparisons with FDR. Conversely, a more conservative correction was employed here in order to quantify with additional confidence the longitudinal changes detected by the different indices and to reduce false positive results. Tensor-derived indices also exhibited similar patterns to 3D-SHORE descriptors, in terms of both evolutions of changes over time and level of significance. In all cases, the highest levels of significance were reached in the patient group for the  $tp1$ - $tp2$  and  $tp1$ - $tp3$  relative changes, suggesting the presence of marked modifications in the contralateral hemisphere just one week after the stroke event ( $tp1$ ). Interestingly, 3D-SHORE-based indices appeared to be the only capable of depicting statistically significant changes across the CORT loop. Indeed, only GFA and RTAP found a significant patient vs control difference in the first phase ( $tp1$ - $tp2$ ), further highlighting the relevance of this time scale in the course of the disease. These findings are in line with the few previous works reporting changes in the WM tracts of the contralesional hemisphere after stroke. Indeed, the possible modifications in the contralateral hemisphere with respect to the lesion have been scarcely investigated in literature, especially in humans, as these tissues have been widely disregarded as considered healthy and not directly

involved in any rearrangement process [138, 160]. However, as the field moved forward, it became apparent that also the non-injured hemisphere undergoes marked changes and has a fundamental role in stroke recovery, as recognised by several authors relying on different MRI techniques [214, 88, 61, 94, 135]. Specifically, Crofts and colleagues [61] showed how communicability values, derived from complex network analysis, were reduced in both ipsilateral and homologous contralateral regions. Moreover, Granziera et al. [92] reported significantly increased apparent diffusion coefficient (*ADC*) values in the infarct region (in both GM and WM tissues) moving from acute to chronic, whereas WM FA significantly decreased in the mirror regions. Our study extends the available literature on the topic and the novel biomarkers derived by the 3D-SHORE model possibly add new metrics that can be employed in this context (for a detailed overview see Kim and Winstein [120]). In addition, the predictive power of all the microstructural indices for patient motor outcome at *tp3* were investigated relying on the tract-based values and comparing several regression models for the prediction. Notably, among the three loops, the SUBCORT was the only one for which all the three types of models created (tensor-based model, 3D-SHORE-based model, global microstructural model) reached excellent performance. In particular, the 3D-SHORE-based model, combining a subset of these indices together with clinical patient information, led to the best linear regression model featuring a very high predictive power ( $R_{adj}^2 = 0.998$ ,  $p < 0.001$ ), which slightly outperformed the optimal model we found in our previous work ( $R_{adj}^2 = 0.988$ ,  $p = 0.009$ ) [37]. The set of indices in the optimal model of this work embeds MSD, suggesting that this index holds a higher potential in probing stroke-induced microstructural changes during the early phase. The model using all the microstructural indices led to the best performance in the SUBCORT loop, reaching the highest correlation score ( $R_{adj}^2 = 0.694$ ,  $p < 0.01$ ) and keeping RTPP as key predictor. The relevance of RTPP for subcortical WM tracts appears to be coherent with another observation of Avram and colleagues [18] according to which RTPP is very sensitive to deep structures, showing higher intensity in nuclei like thalamus. RTPP also highlighted high predictive power in CC, contributing to the optimal model for both the 3D-SHORE-based and global model, in combination with MD in this latter case. These results, jointly with the high precision and the ability to detect significant changes between patients and controls, stress the potential of this index in the considered task.

Besides evaluating the performance of the different indices along the WM connections of specific brain networks, we performed a quantitative comparison of their patterns within contralateral GM regions. GM tissue changes related to the disease are generally quantified by volume or density analyses and are very rarely investigated with dMRI-based indices. A growing body of literature is emerging to endorse the use of dMRI techniques for detecting microscopic changes in GM in different disorders. Indeed, the analysis of diffusivity GM changes using MD has shown to be promising for detecting abnormalities in Alzheimer disease [221] and multiple sclerosis [53]. GM FA alterations were also demonstrated in schizophrenic patients in [183], reporting increased MD and decreased FA values in patients compared to controls. In stroke patients, studies in GM are less consistent and generally consider the tissues in the contralateral hemisphere as normal, although regions remote (upstream or downstream) from the infarct have been demonstrated to

undergo marked changes over a time course of 2 days to 1 year [184]. In one of these studies using the contralateral part as reference, Maniega et al. [138] showed a trend of increased MD/decreased FA values within the lesion, which just started the first week from the event. In our study, the longitudinal analyses on the patient group demonstrated a similar pattern but in the contralateral hemisphere, revealing an increase in MD values over time which mainly involved GM motor regions. Conversely, FA exhibited an initial widespread increase at *tp1* over temporo-frontal and motor areas, followed by a gradual decrease towards normality at *tp3*. This was further confirmed by the group-based comparisons with ANOVA, highlighting in most of these regions significantly higher FA values at *tp1* in patients vs controls, whereas the increased pattern remained restricted to few ROIs when *tp2* values were evaluated. Similar patterns of alterations were detected also by SHORE-based indices, in particular by GFA, PA, RTPP and MSD. The group comparisons one week after the stroke revealed several GM regions (cACC, FuG, IGG, mOFC, PORB, rMFG, FP, ITG, LOC, IOFC, MTG) in which the patients exhibit significantly higher values for all the anisotropy indices (GFA, PA, FA) with respect to the controls. Considering that in the same regions, at the same time point, the MD and MSD appear to be increasing (Figure 7.19.A), although not significantly, we can speculate that we are observing a general increase of the diffusivity along the main diffusion direction in the GM. More difficult to interpret is the simultaneous increase of the RTPP in some of these regions (ITG, LOC, IOFC, MTG). RTPP is generally inversely proportional to anisotropy in WM, e.g RTPP is low in single fiber bundle areas such as the CC, and higher in crossing regions [159, 229, 18]. Understanding the possible causes of this contemporary increase of RTPP and anisotropy in the GM will be one of the aims of our future works. Contralateral changes in GM involved not only regions in the motor systems, but also areas playing an important role in cognition and behaviour, as the FP and frontal areas, supporting the hypothesis of extensive rearrangements during stroke recovery. These indices therefore confirm their potentialities in describing not only WM but also GM properties, with high reliability and discriminative power. However, RTAP and MSD, which resulted to be suitable to characterize WM tracts in all the networks, appeared to be less sensitive to GM changes. Indeed, these indices failed to highlight statistically significant differences in the GM areas, especially when comparing the patient data over time. However, they deserve further investigations considering their good stability over time and their physiological relevance. It is worth mentioning that the impact of partial volume effects was minimized by restricting the analysis to voxels where the GM contribution was above the 95%. This strengthens the hypothesis of extensive contralateral changes involving also the GM, reducing the contamination by other tissues. As a side note, we also extracted for each patient and time point the average volumes of GM ROIs (results not shown). However, when statistically compared by means of a two-way repeated measure ANOVA, no significant changes were detected, possibly because of the small sample size and the limitations of such morphometric measure that might be not sensitive enough to subtle changes in the contralateral hemisphere. A larger sample size and more sophisticated analyses, for example based on cortical thickness measures or voxel-based morphometry, might be more suitable for depicting GM longitudinal changes following stroke, as often done in literature

[187, 34]. Our results, though preliminary, support the hypothesis that SHORE-based indices might hold the potential of revealing GM plasticity processes in the contralesional stroke area. We are aware of the fact that the interpretation in terms of geometrical restriction of the diffusion of the SHORE-derived indices in GM is prone to criticism because the real tissue architecture cannot be directly mapped to the underlying reference model (i.e. the pore). However, the fact that differences across time within a patient population and across groups can be detected using such indices provide evidence in favour of their exploitability as potential numerical biomarkers for GM plasticity in disease, leaving their interpretation in terms of microstructural properties an open issue.

Some limitations have to be acknowledged. This work has to be considered as a preliminary comparison between DTI and SHORE-based EAP derived indices in stroke. Here, we considered only the two most used DTI derived indices (FA and MD) and some of the principal EAP derived indices (RTAP, RTPP, MSD, PA, GFA). However, it will be interesting to extend the analyses to further indices that can be derived, e.g. the radial and axial diffusivity for the DTI, RTOP and the MAP-MRI non-gaussianity for the EAP. Moreover, our findings are based on the comparison between ten healthy subjects and ten ischemic stroke patients. A higher number of subjects would be necessary in future studies to fully exploit the potentialities and discriminative/predictive power of these rather novel indices. In particular, the linear regression analyses have to be carefully evaluated bearing in mind they are preliminary, although encouraging, findings. Indeed, the limited sample size precluded the possibility of identifying the optimal model in a subset of the population and testing it in a different validation cohort, as normally does in the machine learning/classification field. Moreover, a large number of predictors was initially included in the models, possibly leading to over-fitting problems that should be carefully considered when dealing with a limited number of subjects. Adding more data will allow to increase the power of the statistical analyses performed in this work and to further validate the promising findings about contralateral WM and GM changes suggesting the presence of plasticity processes.

**Conclusions and achievements**





## 8.1 Thesis contributions

### *Theoretical contributions*

This thesis aimed at investigating the plausibility conditions of the no-exchange assumption in dMRI signal reconstruction in white matter, as well at the definition of a model allowing to assess the myelin structure. To this end, the present study investigated for the first time the spiraling myelin as a possible mechanism for modeling water exchange between intra and extra axonal environments, as well as its influence on the dMRI signal.

- **Review of permeability concepts in dMRI**

In Chapter 3 and in Chapter 4 we proposed a review regarding the topic of permeability. The distinction between surface relaxivity and exchange flux through barriers in relation to permeability is shown. This preliminary overview can help the non-expert reader to appreciate the main contributions of this thesis, summarized in what follows.

- **Design and implementation of a multi-wrap model for myelin**

A novel multi-wrapping model for myelin was proposed and implemented. To the best of our knowledge, it was the first time that this implementation was performed and studied from the diffusional exchange perspective.

- **Assessment of the plausibility of white matter modeling assumptions**

Our white matter model showed that although exchange can be neglected in a reasonable normal human brain using clinical acquisitions, this assumption can fail in some abnormal conditions like the infant brain and in demyelinating diseases. According to our findings, in those cases the exchange time could be estimated from clinically feasible MRI protocols. The work also emphasized the need of accounting for myelin  $T_2$  in white matter modeling. Indeed, a  $T_2$  modulation of the considered microstructural parameters that is  $\nu_{ic}$ ,  $ADC_{ec}$  and  $\tau$  was observed.

- **Characterization of dMRI sensitivity to myelin multi-wrappings features via exchange-based studies**

A periodic substrate mimicking a three compartments environment was designed allowing to control the parameters ruling the exchange and leading to

observations of the exchange time in a set of different conditions. The same parameter was estimated from signal instances using the Karger model and other parameters including apparent radial diffusion coefficient and kurtosis were also derived from the DKI model. Our analysis predicts sub-second exchange times for small axons and low number of myelin turns, more specifically up to  $\sim 500$  ms for diameters of  $1.0 \mu\text{m}$  and 4 myelin wraps. As discussed in Chapter 6, a number of myelin wraps lower than expected can be reasonably found in the developing and demyelinating tissues, and the exchange time can be estimated with high confidence using the Kärger model. In the same conditions of small axons and number of wraps, we also provided evidence for  $RD$ ,  $RK$  and  $\nu_{ic}$  dependence on myelin structure changes since in these configurations the  $T_2$  influence resulted to be negligible, as discussed in Chapter 5.

The theoretical contributions are supported by an accepted abstract to International Society for Magnetic Resonance in Medicine (ISMRM) in 2018, a paper submitted to EUSIPCO conference and a journal submitted to IEEE of Transactions on Medical Imaging.

#### *Clinical study*

Regarding the clinical applications, the recent 3D-SHORE indices were widely investigated for characterizing the contralateral brain plasticity in motor recovery after ischemic stroke. To the best of our knowledge, this was one of the first times that these indices were employed as potential biomarkers in pathological human brain.

- **3D-SHORE indices characterization as potential numerical biomarkers**

The 3D-SHORE indices convey information regarding the cerebral microstructure enabling a more thorough characterization of the type of microscopic differences that arise between healthy and diseased subjects and opens the way for an accurate automatic discrimination. Overall, the 3D-SHORE indices could be a support for clinical activity, and in particular in the prognosis formulation.

- **Pipeline for biomarker suitability analysis**

A novelty proposed in this thesis was the implementation of a pipeline for analysing the potential of microstructural features of interest as biomarkers. We combined the classical tract-based analysis with the use of the recent 3D-SHORE indices, obtaining the connectivity matrices from which we extracted the values that underwent statistical analysis. Another contribution was to bring this WM analysis at different levels of detail based on the group categorization: single connections, subnetwork, network. Our study revealed the advantage of using network and subnetwork information rather than single connections, emphasizing the highly cooperation among different parts of the brain. Moreover, it was the first time that these indices were quantitatively characterized from the point of view of a GM region-based analysis. Another contribution is in the exhaustive characterization of the prognostic power of the considered microstructural indices through the design of different predictive models exploiting different combinations of

indices and WM tract group. In particular, 3D-SHORE-based indices and single connections, 3D-SHORE-based indices and networks, tensor-based indices and networks, 3D-SHORE and tensor-based indices and networks were considered as well as many others.

– **Representation by 3D-SHORE indices of different tissues**

The reproducibility of the indices as evidenced by the repeatability analyses, the precision in the estimation of microstructural features and the capability to predict the clinical outcome proved the suitability of dMRI-based microstructural indices in probing plasticity in both WM tracts and GM tissue in ischemic stroke patients. The detection of significant changes in GM across groups and in the patient longitudinal comparison provides a new perspective along the path of characterizing disease-related microstructural modulations which deserves further investigation. The 3D-SHORE-derived indices performed as well as classical tensor-derived indices (FA and MD). In particular, it was highlighted the importance of having more information than standard clinical variables to predict the clinical outcome at 6 months after the onset of a stroke as early as the first week of affection of the injury.

The clinical study contributions are supported by publications in peer-reviewed journals as well as international and national conferences [31, 229, 37, 156, 38].

## 8.2 Future work

This work opened the way to other important aspects and perspectives that may be worth to explore. Concerning the theoretical contributions, in Chapter 4 the investigation of walls relaxivity via multiple propagator and multiple correlation function was performed only from a qualitative point of view. Further investigation would be required for a complete analysis. Moreover, the relationship between the walls relaxivity and the permeability characteristic of the barrier would deserve further investigation.

Regarding the white matter model proposed in this thesis, a possible extension would be the addition of complexity to our numerical model of myelinated substrate such as adding the third dimension. This would allow to simulate the node of Ranvier thus opening the way to combine different exchange mechanisms for dMRI investigation. In addition, the model should be extended for accounting for the axons diameter distribution in the substrate.

Obviously, the availability of in-vivo measurements would be needed for the assessment of the performance of the proposed method. This could be done in a multi-modal framework where results from different imaging modalities such as techniques for myelin water imaging [i.e. Magnetization Transfer Ratio (MTR) imaging, Multiexponential  $T_2$  (MET<sub>2</sub>), etc.] acquired on healthy rather than pathological subjects like multiple sclerosis diseased would be available.

The implications on the relationship between  $T_2$  and exchange mechanisms emphasized by this thesis suggest a potential fruitful study of their interaction with other acquisition parameters such as  $T_D$  and TE. The recent interest of the scientific community on this issue and evidences about TE impact on the

considered variables [134, 208, 196, 78] encourage us to extend the exploration of this topic through the joint analysis of these parameters.

The addition of complexity to our simulated substrate could also be in adding further information coming from histology. Following the idea exposed by Nedjati-Gilani et al. [146], machine learning method trained on Monte Carlo simulations could be considered. To this extent, the big effort remains the validation challenge as already mentioned in the previous Section.

Moreover, the pipeline exposed in the Chapter 6 of this thesis could be profitably exploited in the context of permeability. The wide investigation of the exchange time comprehensive of a detailed statistical analysis would allow for the assessment of the suitability of the derived microstructural indices as biomarker. More in detail, this can be particularly useful for diseases affecting the myelin structure.

The study exposed by this thesis could be the starting point for a future work in which 3D-SHORE indices are studied in relationship with the various confounders typical of heterogeneous tissue like partial volume, relaxation, exchange, mixture of isotropic and anisotropic structures. This would be valuable for interpretation of dMRI data. As example, another interesting confounder that could be possibly explored is the axonal beading. Recently, Budde and Frank [40] have shown that the reduced *ADC* observed after a few minutes from the injury could be explained either as cell swelling or axonal beading providing a biophysical model of neurite beading. More in detail of exchange topic afforded in this work, it would be of interest the investigation of exchange integration in 3D-SHORE modeling leading to a further advancement in the state of the art.

These and many other additional analysis are possible and particularly fascinating in this field, that could be helpful for the improvement of health care. Citing Rita Levi Montalcini, “progress depends on our brain. The most important part of our brain, that which is neocortical, must be used to help others and not just to make discoveries.”

## 8.3 Achievements

### Awards

- Student Travel Award, MICCAI 2015

### Grants

- Cooperint, 2015: public competition for the financing of projects with the purpose to stimulate international relationships in the research environment.  
4 January 2016 – 30 April 2016, INRIA Sophia Antipolis – Mediterranean research center  
Local supervisor: Prof. Rachid Deriche  
Description: study and implementation of different analytical simulations of diffusion MRI signal in cylindrical pores in the extra-ordinary case of permeable walls.
- Educational Stipend, ISMRM 2015
- Educational Stipend, ISMRM 2018

## Visits

- INRIA Sophia Antipolis Mediterranean research center, 4 January 2016 – 30 April 2016  
Local supervisor: Prof. Rachid Deriche  
Description: study and implementation of different analytical simulations of diffusion MRI signal in cylindrical pores in the extra-ordinary case of permeable walls.
- Lund University, 6 February 2017 – 16 February 2017  
Local supervisor: Prof. Markus Nilsson  
Description: implementation of spiraling myelin for studying this exchange mechanism on dMRI experiments.

## 8.4 Publications

### Journals

- SUBMITTED: Journal to Transactions on Medical Imaging – Brusini, L., Menegaz, G., Nilsson, M. *Monte Carlo simulations of water exchange through myelin wraps: Implications for diffusion MRI*
- Boscolo Galazzo, I., Brusini, L., Obertino, S., Zucchelli, M., Granziera, C., Menegaz, G. *On the viability of diffusion MRI-based microstructural biomarkers in ischemic stroke*, Journal to Frontiers in Neuroscience, 12, 92 (2018)
- Zucchelli, M., Brusini, L., Mendez-Guerrero, A., Daducci, A., Granziera, C., Menegaz, G.: *What lies beneath? Diffusion EAP-based study of brain tissue microstructure*, Medical Image Analysis, 32, 145-156 (2016)

### Invited journals

- Brusini, L., Obertino, S., Boscolo Galazzo, I., Zucchelli, M., Krueger, G., Granziera, C., Menegaz, G.: *Ensemble average propagator-based detection of microstructural alterations after stroke*, Int J CARS, 11, 1585-1597 (2016)

### Conferences

- International Proceedings
  - SUBMITTED: Paper to EUSIPCO Conference – Brusini, L., Menegaz, G., Nilsson, M.: *Assessing the non-Gaussian Nature of Signal Decay in a Permeable Environment by Diffusion MRI*
  - Obertino, S., Brusini, L., Boscolo Galazzo, I., Zucchelli, M., Granziera, C., Cristani, M., Menegaz, G.: *Shore based biomarkers allow patients versus control classification in stroke*, ISBI, Prague, 2016
  - Brusini, L., Obertino, S., Zucchelli, M., Boscolo Galazzo, I., Krueger, G., Granziera, C., Menegaz, G.: *Assessment of Mean Apparent Propagator-based Indices as Biomarkers of Axonal Remodeling After Stroke*, MICCAI, Munich, 2015
  - Zucchelli, M., Brusini, L., Mendez, C.A., Menegaz, G.: *Multi-Tensor MAPMRI: how to estimate microstructural information from crossing fibers*, CDMRI 2015

- Abstracts
  - Brusini, L., Menegaz, G., Nilsson, M. *Monte Carlo simulations of diffusion in myelin spirals: Impact on diffusional water exchange*, ISMRM, Paris, 2018
  - Brusini, L., Zucchelli, M., Obertino, S., Menegaz, G.: *Characterization of diffusion MRI signal non Gaussianity using MAPMRI*, ISMRM Workshop, Lisbona, 2016
  - Zucchelli, M., Brusini, L., Menegaz, G.: *Detection of fiber crossing and fanning using the Multi-Tensor Distribution Model*, ISMRM Workshop, Lisbona, 2016
  - Obertino, S., Brusini, L., Boscolo Galazzo, I., Zucchelli, M., Daducci, A., Menegaz, G., Granziera, C.: *Cortico-Subcortical motor network integrity relates to functional recovery after stroke*, ISMRM, Singapore, 2016
  - Brusini, L., Zucchelli, M., Daducci, A., Granziera, C., Menegaz, G.: *Are SHORE-based biomarkers suitable descriptors for microstructure in DSI?* ISMRM, Toronto, 2015
  - Brusini, L., Zucchelli, M., Granziera, C., Menegaz, G.: *Microstructural description of cerebral tissues from diffusion spectrum imaging data*, ICHI, Verona, 2014
- National Congresses
  - Brusini, L., Zucchelli, M., Daducci, A., Granziera, C., Menegaz, G.: *Diffusion MRI sensitivity to contralateral GM modulations after stroke*, GNB, Milano, 2018
  - Brusini, L., Cruciani, F., Boscolo Galazzo, I., Galbusera, A., Borin, M., Diana, G., Buffelli, M., Gozzi, A., Menegaz, G.: *Assessing the effects of synaptic plasticity using structural MRI in the mouse*, GNB, Milano, 2018
- National Abstracts
  - SUBMITTED: Abstract to ISMRM Italian Chapter Zucchelli, M., Brusini, L., Menegaz, G.: *Two-parameters compartmental models for diffusion MRI: a comparative analysis*
  - Brusini, L., Zucchelli, M., Daducci, A., Granziera, C., Menegaz, G.: *Diffusion MRI characterization of stroke lesions using 3D-SHORE microstructural indices*, Italian Chapter ISMRM, Bologna, 2016
  - Zucchelli, M., Ricciardi, G.K., Brusini, L., Pizzini, F., Montemezzi, S., Menegaz, G.: *Diffusion MRI characterization of glioma using MAPMRI reconstruction: a preliminary study*, Italian Chapter ISMRM, Bologna, 2016
  - Brusini, L., Zucchelli, M., Ricciardi, G.K., Pizzini, F., Montemezzi, S., Menegaz, G.: *In-Vivo Quantification of Brain Microstructure: a Preliminary Analysis using SHORE Diffusion Model*, Italian Chapter ISMRM, Verona, 2015

### Presentations

- Brusini, L., Obertino, S., Zucchelli, M., Boscolo Galazzo, I., Krueger, G., Granziera, C., Menegaz, G.: *Assessment of Mean Apparent Propagator-based Indices as Biomarkers of Axonal Remodeling After Stroke*, MICCAI, Munich, 2015. TRADITIONAL POSTER AND TEASER

- Brusini, L., Zucchelli, M., Daducci, A., Granziera, C., Menegaz, G.: *Are SHORE-based biomarkers suitable descriptors for microstructure in DSI?* ISMRM, Toronto, 2015. E-POSTER
- Brusini, L., Zucchelli, M., Ricciardi, G.K., Pizzini, F., Montemezzi, S., Menegaz, G.: *In-Vivo Quantification of Brain Microstructure: a Preliminary Analysis using SHORE Diffusion Model*, Italian Chapter ISMRM, Verona, 2015. ORAL PRESENTATION
- Brusini, L., Zucchelli, M., Granziera, C., Menegaz, G.: *Microstructural description of cerebral tissues from diffusion spectrum imaging data*, ICHI, Verona, 2014. TRADITIONAL POSTER





A

---

Appendix

# Assessment of Mean Apparent Propagator-Based Indices as Biomarkers of Axonal Remodeling after Stroke

Lorenza Brusini<sup>1</sup>, Silvia Obertino<sup>1</sup>, Mauro Zucchelli<sup>1</sup>, Ilaria Boscolo Galazzo<sup>2</sup>, Gunnar Krueger<sup>3</sup>, Cristina Granziera<sup>4</sup>, and Gloria Menegaz<sup>1</sup>

<sup>1</sup> Dept. of Computer Science, University of Verona, Italy

<sup>2</sup> Institute of Nuclear Medicine, University College of London, UK

<sup>3</sup> Siemens Healthcare USA, Boston, USA

<sup>4</sup> Dept. of Clinical Neuroscience, CHUV and University of Lausanne, Switzerland

**Abstract.** Recently, a robust mathematical formulation has been introduced for the closed-form analytical reconstruction of the signal and the Mean Apparent Propagator (MAP) in diffusion MRI. This is referred to as MAP-MRI or 3D-SHORE depending on the chosen reference frame. From the MAP, microstructural properties can be inferred by the derivation of indices that under certain circumstances allow the estimation of pores' geometry and local diffusivity, holding the potential of becoming the next generation of microstructural numerical biomarkers. In this work, we propose the assessment and validation of a subset of such indices that is RTAP, D, and PA for the quantitative analysis of axonal remodeling in the uninjured motor network after stroke. Diffusion Spectrum Imaging (DSI) was performed on ten patients and ten controls at different time points and the indices were derived and exploited for tract-based quantitative analysis. Our results provide quantitative evidence on the eligibility of the derived indices as microstructural biomarkers.

## 1 Introduction

Connectivity remodeling after stroke has been reported in both injured [1] and uninjured hemispheres [2,3]. Generalized Fractional Anisotropy (GFA) had previously been successfully exploited to provide evidence of plasticity in the uninjured motor network in stroke patients with motor deficits. Recently, a robust mathematical formulation has been introduced for the closed-form analytical reconstruction of the diffusion signal from which new micro structural indices could be analytically derived. This is referred to as Mean Apparent Propagator (MAP)-MRI and 3D Simple Harmonic Oscillator Based Reconstruction and Estimation (3D-SHORE), respectively, depending on the reference frame. The corresponding MAP, also known in literature as Ensemble Average Propagator (EAP) [4], can then be profitably exploited for deriving information about the ensemble average values of pores' geometry and local diffusivity [4] and hold the potential for eligibility as the next generation of microstructural biomarkers. In particular, an estimation of the axons' cross-sectional area and diameter

can be derived analytically in white matter. In this work, we aimed at exploring whether the MAP-derived measures 1) could reveal contralesional structural changes along intracallosal connections after stroke; 2) correlate with the well established GFA index; and 3) jointly with clinical status allow to predict motor outcomes.

## 2 Materials and Methods

Ten stroke patients [6 males and 4 females (age:  $60.3 \pm 12.8$  years, mean  $\pm$  SD)] were enrolled in the study; the inclusion criteria, imaging protocol and post-processing were as in [2]. All patients underwent three DSI scans (TR/TE = 6600/138 msec, FOV =  $212 \times 212$  mm, 34 slices,  $2.2 \times 2.2 \times 3$  mm resolution, 258 gradient directions,  $b_{max} = 8000$  s/mm<sup>2</sup>) within one week (*tp1*), one month ( $\pm$  one week, *tp2*), and six months ( $\pm$  fifteen days, *tp3*) after stroke. Orientation distribution functions were reconstructed using the Diffusion Toolkit ([www.trackvis.org/dtk](http://www.trackvis.org/dtk)). Fiber-tracking was performed via a streamline algorithm ([www.cmtk.org](http://www.cmtk.org)). Patients benefited of clinical assessment (NIHSS: National Institute of Health Stroke Scale), with the motor part (NIHSS motor) derived from items 2 to 7 and 10 ([www.nihstrokescale.org/](http://www.nihstrokescale.org/)). Ten age and gender matched healthy controls were also included in the study (age:  $56.1 \pm 17.8$  years, mean  $\pm$  SD). Control group underwent two DSI scans one month apart (*tp1c* and *tp2c*). All subjects provided written informed consent and the Lausanne University Hospital review board approved the study protocol. To the best of our knowledge, this is the first attempt of using MAP-indices in patients, while *in-vivo* acquisition in healthy subjects were reported in [5].

### 2.1 Analytical Model for Signal Reconstruction

In this work, the orthonormal formulation of the 3D-SHORE model was chosen [6,7]. With respect to MAP, this formulation allows less degrees of freedom in the choice of the scale parameter but there is some evidence for improved capability in resolving complex structural micro-topologies [8]. The diffusion signal is modeled by using the Eigenfunctions of the SHORE as basis. After rotating the reference frame for diagonalizing the stiffness tensor, a separable solution can be obtained [4]

$$\begin{aligned} \Phi_{N_i}(\mathbf{A}, \mathbf{q}) &= \phi_{n_{x(i)}}(u_x, q_x) \phi_{n_{y(i)}}(u_y, q_y) \phi_{n_{z(i)}}(u_z, q_z) \\ \text{with } \begin{cases} \phi_n(u, q) = \frac{i^{-n}}{\sqrt{2^n n!}} e^{-2\pi^2 q^2 u^2} H_n(2\pi u q) \\ \mathbf{A} = \text{Diag}(u_x^2, u_y^2, u_z^2) \end{cases} \end{aligned} \quad (1)$$

where  $N_i = (n_{x(i)}, n_{y(i)}, n_{z(i)})$  is the basis order and  $H_n$  a Hermite polynomial. Diagonalization of the stiffness tensor is performed by tensor fitting  $\mathbf{A}'$  ( $\mathbf{A} = \mathbf{R}\mathbf{A}'\mathbf{R}^T$ ), where  $\mathbf{R}$  consists of the tensor Eigenvectors. Separability enables the anisotropic scaling of the basis functions along the coordinate axes making the 3D basis particularly suited to anisotropic data. The 3D-SHORE

model is expressed in spherical coordinates. Separability holds the radial and angular coordinates which prevents the independent scaling of the basis functions along the main coordinate axes. Following the formulation in [9], the basis functions  $\Phi_n(\mathbf{q}\mathbf{u})$  can be written as

$$\Phi_n(\mathbf{q}\mathbf{u}) = R_n(q)Y_n(\mathbf{u}) \quad (2)$$

where  $R_n(q)$  models the radial part of the signal and  $\{Y_n(\mathbf{u})\}$  are the real spherical harmonics of even order [10]. After a reordering of the terms, the signal model becomes

$$\begin{aligned} \mathbf{E}(\mathbf{q}\mathbf{u}) &= \sum_{l=0, \text{even}}^{N_{max}} \sum_{n=l}^{(N_{max}+l)/2} \sum_{m=-l}^l c_{nlm} \Phi_{nlm}(\mathbf{q}\mathbf{u}) \quad (3) \\ \Phi_{nlm}(\mathbf{q}\mathbf{u}) &= \left[ \frac{2(n-l)!}{\zeta^{3/2} \Gamma(n+3/2)} \right]^{1/2} \left( \frac{q^2}{\zeta} \right)^{l/2} \exp\left( \frac{-q^2}{2\zeta} \right) L_{n-l}^{l+1/2} \left( \frac{q^2}{\zeta} \right) Y_l^m(\mathbf{u}) \end{aligned}$$

where  $N_{max}$  is the maximal order in the truncated series and  $\Phi_{nlm}(\mathbf{q})$  is the orthonormal 3D-SHORE basis,  $\Gamma$  is the Gamma function and  $\zeta$  is an isotropic scaling parameter. The coefficients are determined by quadratic programming and positivity constraints are imposed to the MAP. The two formulations are equivalent for isotropic scaling.

Under such assumption, in this study we call MAP-based indices the measures derived from 3D-SHORE namely the Return to Axis Probability (RTAP) and Propagator anisotropy (PA). An estimate of the axon diameter (D) was inferred from RTAP as this provides an estimate of the exact statistical average of the cross-sectional area in white matter if some conditions are met [4] as  $D = \sqrt{4\pi / RTAP}$ . The MAP indices were assessed against GFA.

$$\begin{aligned} RTAP &= \sum_{l=0, \text{even}}^{N_{max}} \sum_{n=l}^{(N_{max}+l)/2} \sum_{m=-l}^l c_{nlm} \left[ \frac{\zeta^{1/2} 2^{l+3} \pi^2 \Gamma(l/2+1)^2 \Gamma(n+3/2)}{(n-l)! \Gamma(l+3/2)^2} \right]^{1/2} \times \\ &\quad \times {}_2F_1(l-n, l/2+1, l+3/2, 2) P_l(0) Y_l^m(\mathbf{u}^*) \\ PA &= \sqrt{1 - \frac{\sum_{l=0}^{N_{max}/2+1} c_{i00}^2}{\sum_{l=0, \text{even}}^{N_{max}} \sum_{n=l}^{(N_{max}+l)/2} \sum_{m=-l}^l c_{nlm}^2}} \quad (4) \end{aligned}$$

## 2.2 Tract-Based Quantitative Analysis

The primary motor area (M1), supplementary motor area (SMA), somatosensory cortex (SC) and thalamus (Thl) were considered in the analysis. GFA and MAP-indices were collected along intracallosal fiber bundles connecting those regions to the corpus callosum (CC) in the contralateral (non-lesioned) hemisphere. In particular, GFA, RTAP, D, and PA values were computed for each voxel and then averaged along each tract and among all tracts connecting the regions of interest to the CC.

### 2.3 Statistical Analysis

Reproducibility of mean GFA, RTAP, D, and PA values along motor tracts was assessed by evaluating statistical differences between  $tp1c$  and  $tp2c$  using a paired  $t$ -test ( $p > 0.05$ ) after a Kolmogorov-Smirnov normality test. Percentage absolute changes in mean values between time points were evaluated for each index on both groups as

$$\begin{aligned}
 \Delta_{tp12c}(m) &= |(m_{tp2c} - m_{tp1c})|/m_{tp1c} \\
 \Delta_{tp12}(m) &= |(m_{tp2} - m_{tp1})|/m_{tp1} \\
 \Delta_{tp23}(m) &= |(m_{tp3} - m_{tp2})|/m_{tp2} \\
 \Delta_{tp13}(m) &= |(m_{tp3} - m_{tp1})|/m_{tp1}
 \end{aligned} \tag{5}$$

where  $m$  denotes the mean value of the considered index along the fibers of a given connection, and the subscript  $c$  denotes the control group. Normality test (Kolmogorov-Smirnov) revealed that the values were normally distributed enabling the use of parametric statistics. Accordingly, the unpaired  $t$ -test with  $p < 0.05$  was performed to establish the significant differences between  $\Delta_{tp12c}(m)$  and  $\Delta_{tp12}(m)$ . With the purpose to further characterize the MAP-based indices, Spearman correlation with GFA was performed. In addition, for each patient, the  $z$ -score of the mean absolute changes of each index and connection with respect to the same measurement on the control group was calculated in order to highlight and visually render in an intuitive way the distance between each patient and the control group as well as individual changes over time. Finally, the predictive value of each metric was assessed by a linear regression model where the motor outcome at six months after stroke ( $tp3$ ) was the dependent variable and the mean values of each index for all the connections at  $tp1$ , age, stroke size, and NIHSS motor scores at  $tp1$  and  $tp2$  were the predictors. A backward selection process was used to select the optimal predictor model with  $p = 0.05$  as significance threshold.

## 3 Results and Discussions

*Reproducibility of index values in controls.* In controls, reproducibility of the mean GFA, RTAP, D and PA values was observed as confirmed by  $t$ -test which showed no statistical significant differences between  $tp1c$  and  $tp2c$  ( $p > 0.05$ ). The mean absolute GFA, RTAP, D, and PA changes calculated for all the motor connections between the two time points were:  $GFA : 0.0248 \pm 0.0074$ ,  $RTAP : 0.0290 \pm 0.0082$ ,  $D : 0.0205 \pm 0.0047$ ,  $PA : 0.0241 \pm 0.0072$  (mean  $\pm$  SEM). Among connections, the largest variability was recorded for SC.

*Comparison of absolute GFA, RTAP, D, and PA changes in patients and controls.* Figure 1 illustrates the mean absolute percent changes of the different indices for patients and controls. For each index, absolute changes between  $tp1$  and  $tp2$  in patients' connections were significantly different from the absolute

changes between the same regions in controls between  $tp1c$  and  $tp2c$  ( $0.01 \leq p \leq 0.05$ ). However, the thalamic intracallosal connection failed to reach significance in all conditions, and SC-CC did not reach significance for RTAP and D. As it is apparent from Figure 1, PA shows the highest sensitivity in differentiating the patients from the control group, outperforming GFA in the SMA-CC connection and having the same performance for the other considered ones. In particular, both are able to differentiate the groups for the M1 and SC intracallosal connections. RTAP and D also allow differentiating between the two groups for M1 and SMA, while they could not highlight differences for SC. However, RTAP and D provide a richer microstructural information with respect to GFA which only describes the level of anisotropy of restricted diffusion. In connections where RTAP and D are able to split patients and controls, MAP-based indices allow for a more accurate description of the microstructural changes in patients.

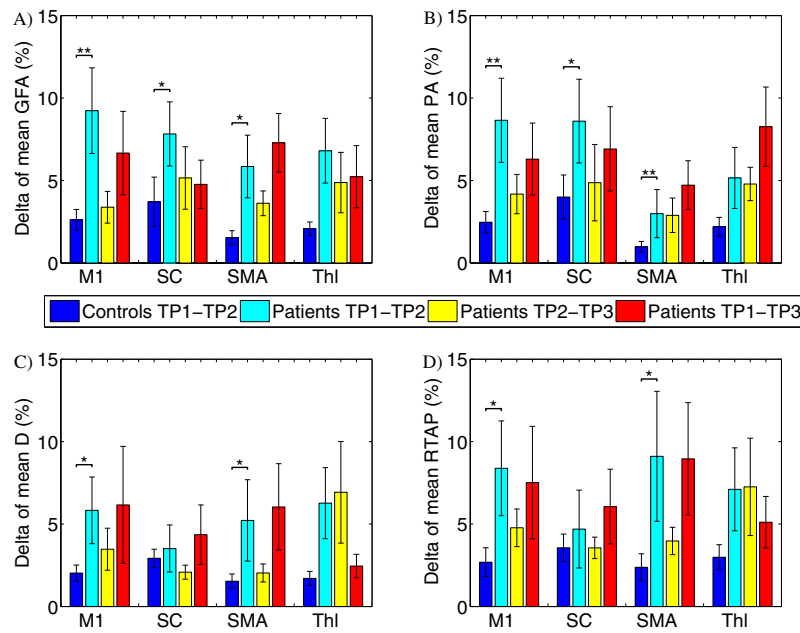


**Fig. 1.** Longitudinal changes in percent mean absolute values in controls and patients ( $*p < 0.05$ ,  $**p < 0.01$ ). (A) *GFA*; (B) *PA*; (C) *D*; (D) *RTAP*.

*Correlations of each absolute descriptor changes with GFA.* For both controls and patients, Spearman's correlation  $\rho$  showed a significant ( $p < 0.05$ ) monotonic relationship between the mean absolute changes of each MAP-based index and GFA changes. The overall correlation among all the intracallosal connections was assessed, showing the following results: 1) RTAP:  $\rho_{tp12c} = 0.48$ ,  $\rho_{tp12} = 0.74$ ,  $\rho_{tp23} = 0.38$ ,  $\rho_{tp13} = 0.65$ ; 2) D:  $\rho_{tp12c} = 0.43$ ,  $\rho_{tp12} = 0.76$ ,  $\rho_{tp23} = 0.37$ ,  $\rho_{tp13} = 0.40$ ; and 3) PA:  $\rho_{tp12c} = 0.51$ ,  $\rho_{tp12} = 0.74$ ,  $\rho_{tp23} = 0.40$ ,  $\rho_{tp13} = 0.64$ . In all cases results were significant with  $p < 0.05$ .

*Longitudinal changes in patients.* Figure 2 highlights the pattern of the longitudinal changes in the different connections for individual patients with respect

to the control group, that appeared to be patient-specific. The largest changes were observed in patients with the more severe motor deficit. The pattern is similar for the different indices providing evidence of the ability to capture the microstructural alterations due to white matter plasticity in the contralesional area. In particular, PA closely reproduces the pattern of GFA, while RTAP and D appear to be less sensitive especially for SC, coherently with the observation that for SC no significant difference between patients and controls could be detected by these two indices (see Figure 1). An increase in axon diameter is seen in patients over time. This could reveal axonal outgrowth and myelin increase due to plasticity as activated in the rehabilitation process [3], [11].

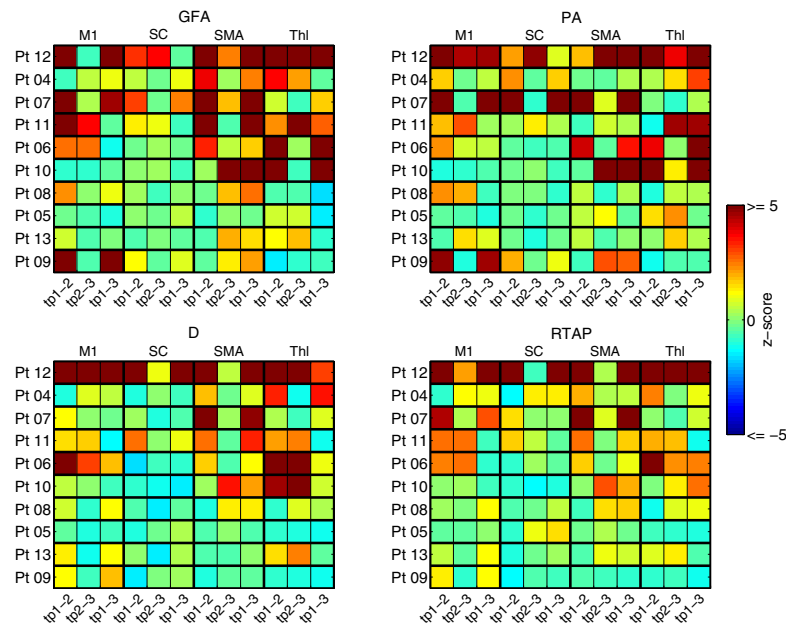


**Fig. 2.** Patients' individual profiles of mean absolute changes between  $tp1$  and  $tp2$  (first column),  $tp2$  and  $tp3$  (second column), and  $tp1$  and  $tp3$  (third column). Changes were compared to the corresponding controls' mean changes using  $z$ -scores. Patients are ordered according to the initial NIH Stroke Scale (NIHSS).

*Prediction of clinical outcomes in patients for each index.* In the patients' group, a linear regression model including only age and NIHSS at  $tp1$  and  $tp2$  gave low correlation as well as a model including only NIHSS at  $tp1$  and  $tp2$  ( $R^2 = 0.691$ ; adjusted  $R^2 = 0.652$ ). Conversely, for each index, the models including also its mean values across the different connections were able to predict the NIHSS at  $tp3$  with higher significance (Table 1). In particular, the best prediction model was obtained for D ( $R^2 = 0.998$ ; adjusted  $R^2 = 0.990$ ,  $p = 0.008$ ). The relative importance for each predictor of the different optimal models was evaluated with the Fisher test and reported in Supplementary Materials. However, all models led to high significance, with adjusted  $R^2 > 0.8$ , confirming the importance of GFA and MAP-based indices for an early prediction of the patient clinical outcome.

Moreover, although GFA and PA are both anisotropy indices, PA has a higher prediction significance pointing at a stronger reliability of this new descriptor.

**Table 1.** Performance of each prediction model

Index	Multiple $R^2$	Adjusted $R^2$	$p$
GFA	0.970	0.932	0.004
RTAP	0.919	0.818	0.026
D	0.998	0.990	0.008
PA	0.991	0.973	0.004

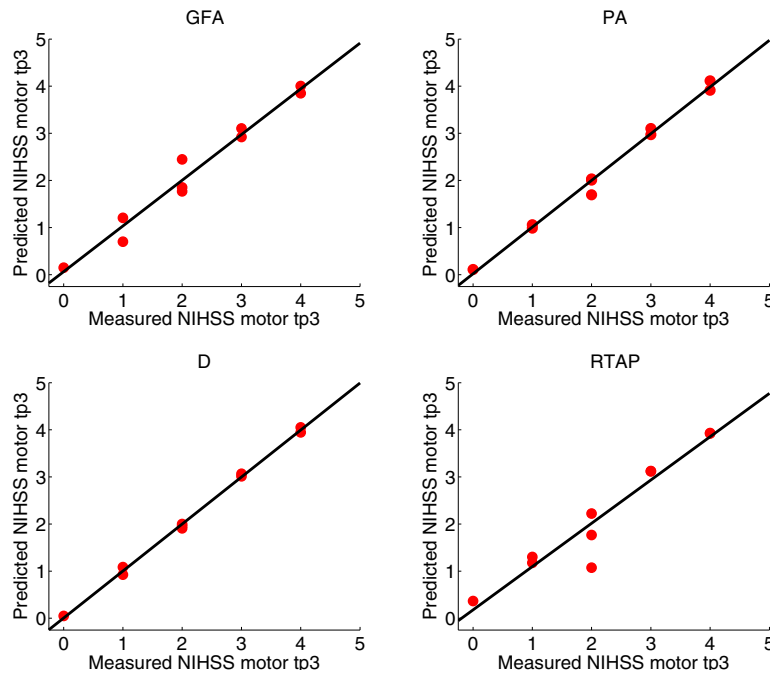


**Fig. 3.** Representation of the measured and predicted NIHSS at  $tp3$  using the models described above.

## 4 Conclusions

In this study, some evidence was provided on the suitability of the MAP-based indices RTAP, D, and PA as numerical biomarkers for stroke. Reproducibility was assessed by the test-retest method on the control group and longitudinal analysis on the patients group highlighted that contralesional structural changes after stroke could be well characterized and monitored by the newly proposed indices. The significant differences between controls and patients over multiple regions of interest lead the way to the application of RTAP, D, and PA as important descriptors for differentiating between the groups. Moreover, the performance of RTAP-, D-, and PA-based clinical regression models emphasized the suitability of these indices as early descriptors of patients' longitudinal changes and predictors of clinical outcomes.



## References

1. Sotak, C.: The role of diffusion tensor imaging in the evaluation of ischemic brain injury a review. *NMR in Biomedicine* 15(7-8), 561–569 (2002)
2. Granziera, C., Daducci, A., Meskaldji, D., Roche, A., Maeder, P., Michel, P., Hadjikhani, N., Sorensen, A., Frackowiak, R., Thiran, J., Meuli, R., Krueger, G.: A new early and automated mri-based predictor of motor improvement after stroke. *Neurology* 79, 39–46 (2012)
3. Lin, Y., Daducci, A., Meskaldji, D., Thiran, J., Michel, P., Meuli, R., Krueger, G., Menegaz, G., Granziera, C.: Quantitative analysis of myelin and axonal remodeling in the uninjured motor network after stroke. *Brain Connectivity* (2014)
4. Ozarslan, E., Koay, C., Shepherd, T., Komlosh, M., Irfanoglu, M., Pierpaoli, C., Basser, P.: Mean apparent propagator (map) mri: A novel diffusion imaging method for mapping tissue microstructure. *NeuroImage* 78, 16–32 (2013)
5. Zucchelli, M., Descoteaux, M., Menegaz, G.: Human brain tissue microstructure characterization using 3D-SHORE on the HCP data. In: *ISMRM, Toronto, Ontario, Canada* (2015)
6. Ozarslan, E., Koay, C., Shepherd, T., Blackband, S., Basser, P.: Simple harmonic oscillator based reconstruction and estimation for three-dimensional q-space mri. *Proc. Intl. Soc. Mag. Reson. Med.* 17, 1396 (2009c)
7. Merlet, S., Deriche, R.: Continuous diffusion signal, {EAP} and {ODF} estimation via compressive sensing in diffusion {MRI}. *Medical Image Analysis* 17(5), 556–572 (2013)
8. Fick, R., Zucchelli, M., Girard, G., Descoteaux, M., Menegaz, G., Deriche, R.: Using 3D-SHORE and MAP-MRI to Obtain Both Tractography and Microstructural Contrast from a Clinical DMRI Acquisition. In: *International Symposium on Biomedical Imaging: From Nano to Macro, Brooklyn, New York City, United States* (2015)
9. Cheng, J., Jiang, T., Deriche, R.: Theoretical Analysis and Practical Insights on EAP Estimation via a Unified HARDI Framework. In: *MICCAI Workshop on Computational Diffusion MRI (CDMRI), Toronto, Canada* (2011)
10. Descoteaux, M., Angelino, E., Fitzgibbons, S., Deriche, R.: Regularized, fast, and robust analytical q-ball imaging. *Magnetic Resonance in Medicine* 58(3), 497–510 (2007)
11. Ueno, Y., Chopp, M., Zhang, L., Buller, B., Liu, Z., Lehman, N., Liu, X., Zhang, Y., Roberts, C., Zhang, Z.: Axonal outgrowth and dendritic plasticity in the cortical peri-infarct area after experimental stroke. *Stroke* 43(8), 2221–2228 (2012)

# Multi-Tensor MAPMRI: How to Estimate Microstructural Information from Crossing Fibers

Mauro Zucchelli, Lorenza Brusini, C. Andrés Méndez, and Gloria Menegaz

**Abstract** Diffusion Magnetic Resonance Imaging (dMRI) is able to detect the properties of tissue microstructure underneath the voxel through the imaging of water molecules diffusion. Many reconstruction methods have been proposed to calculate the Orientation Distribution Function (ODF) from the diffusion signal in order to distinguish between coherent fiber bundles and crossing fibers. The diffusion signal was also used to infer other microstructural information such as the axon diameter, but most often in areas with coherent fiber direction such as the *corpus callosum*. In this work, we developed a reconstruction model called Multi-Tensor MAPMRI (MT-MAPMRI) that is an extension of the MAPMRI model which improves the performance of MAPMRI for crossing fibers. In particular, it provides (a) enhanced signal fitting; (b) improved ODFs; (c) a more accurate diameter estimation. The model was tested and validated on both simulated and in-vivo data.

## 1 Introduction

Diffusion MRI is able to extract information on the cerebral tissue in vivo. From the diffusion weighted (DW) signal, it is possible to calculate the ensemble average propagator (EAP) under the long diffusion time assumption. The diffusion signal  $E(\mathbf{q})$  depends on the pulse width  $\delta$ , the pulse separation time  $\Delta$  and the gradient strength  $G$ . Since the number of points that is possible to acquire with diffusion MRI in practice is limited, analytical reconstruction models represent a mean of extrapolating missing data in a controlled way. These are thus fitted to the signal enabling the estimation of the tissue physical properties based on analytical expressions. One of the first reconstruction models was the Diffusion tensor (DTI) [4] in which the signal was modeled as a single multivariate Gaussian function

---

M. Zucchelli (✉) • L. Brusini • C.A. Méndez • G. Menegaz  
University of Verona, Verona, Italy  
e-mail: [mauro.zucchelli@univr.it](mailto:mauro.zucchelli@univr.it)

(diffusion tensor). This model has been proved suitable for describing diffusion in unconstrained conditions and in the case of single fiber bundles. Many attempts have been made to expand the single tensor to a double or multi-tensor [13] estimation in order to characterize more complex fiber topologies, like crossings, which normally occur in the majority of the white matter [8]. Other reconstruction techniques try to fit more complex basis functions to the signal in order to be able to naturally fit crossing fibers. The 3D Simple Harmonic Oscillator Based Reconstruction and Estimation (SHORE) introduced in [10] fits the diffusion signal as a series of Hermite polynomials and spherical harmonics, leading to good results in the calculation of the Orientation Distribution Function (ODF). The model further evolved in the Mean Apparent Propagator (MAP) MRI [12] in which the spherical harmonics were replaced by a set of orthogonal 1D-SHORE functions. In addition to the ODF, other micro-structural descriptors were introduced, including the Return To the Axis Probability (RTAP), an index characterizing the pore mean cross sectional area, under certain conditions. Previously this feature was only calculated in single fibers voxels using compartmental models such as the one proposed in [3, 15] or using 3D-SHORE and MAPMRI as in [5, 6].

In this paper, we propose an improvement of MAPMRI based on a multi-tensor fitting which is able to improve signal fitting and the calculation of EAP features like the ODF and the RTAP for voxel containing multiple crossings fibers.

## 2 Materials and Methods

### 2.1 MAPMRI

The SHORE basis was originally defined in [10] and expresses the 1D diffusion signal as

$$\Phi_n(u, q) = \frac{i^{-n}}{\sqrt{2^n n!}} e^{-2\pi^2 u^2 q^2} H_n(2\pi uq) \quad (1)$$

where  $u$  is a scale factor and  $H$  is the Hermite polynomial of order  $n$ . MAPMRI is a 3D SHORE basis where signal reconstruction is performed in two steps: in the first, a Gaussian function (tensor) is fitted to the signal and the tensor eigenvectors are used to rotate the reference frame in order to have the axis aligned with principal diffusion directions. The eigenvalues are then used to calculate the scale parameters of the three SHORE bases  $u_x$ ,  $u_y$  and  $u_z$ .

Since the basis is separable in the new reference frame, MAPMRI basis can be expressed as a 3D basis

$$\Phi_{n_1, n_2, n_3}(\mathbf{u}, \mathbf{q}) = \Phi_{n_1}(u_x, q_x) \Phi_{n_2}(u_y, q_y) \Phi_{n_3}(u_z, q_z) \quad (2)$$

with independent radial orders  $n_1, n_2, n_3$ . The diffusion signal  $E(\mathbf{q})$  can then be modeled as

$$E(\mathbf{q}) = \sum_{N=0}^{N_{max}} \sum_{n_1, n_2, n_3} c_{n_1, n_2, n_3} \Phi_{n_1, n_2, n_3}(\mathbf{q}) \quad (3)$$

where  $c_{n_1, n_2, n_3}$  are the basis coefficients. The coefficients vector  $\mathbf{c}$  can be obtained using the standard least-squares fit or, alternatively, using quadratic programming in order to add positivity constraints in the EAP space as in [12].

MAPMRI provides very accurate signal fitting in the case of voxels containing bundles of fibers aligned in a single direction [5]. RTAP is calculated as the integral of the signal in the plane orthogonal to the main axes of the pore [12]. There is an intrinsic problem in identifying the principal direction of a fiber crossing. MAPMRI identifies it as the main axis of the tensor that is usually placed between the axes of the fibers. Selecting only the principal axis of one of each fiber would not solve the problem because the signal originating in the second fiber would anyway contribute to the integral. The only way to calculate this index accurately for crossing fibers is to split the signal contributions of each fiber, as is explained below.

## 2.2 Multi-Tensor MAPMRI

In order to overcome the limitations of MAPMRI the initial tensor fitting is replaced with the fitting of  $m$  axially symmetric tensor  $\mathbf{D}_i$ . With this model the diffusion signal can be expressed as

$$E(\mathbf{q}) = \sum_{i=1}^m f_i \exp(-4\pi^2 \tau \mathbf{q}^T \mathbf{D}_i \mathbf{q}) \quad (4)$$

Finding the volume fraction coefficients,  $f_i$ , along with the tensor parameters is a nonlinear optimization problem that can not be solved by ordinary least squares. In order to find the coefficients, we implemented a Monte Carlo Markov Chain optimization algorithm maximizing the Rician log-likelihood of the fitting [9]. From the diffusion tensors, it is possible to derive multiple MAPMRI bases  $\Phi^i$ , using the respective eigenvalues and the eigenvector of  $\mathbf{D}_i$ . MT-MAPMRI basis signal reconstruction can then be calculated as

$$E(\mathbf{q}) = \sum_{i=1}^m \sum_{N=0}^{N_{max}} \sum_{n_1, n_2, n_3} c_{n_1, n_2, n_3}^i \Phi_{n_1, n_2, n_3}^i(\mathbf{q}) \quad (5)$$

The coefficients set  $\mathbf{c}^i$  can be fitted at the same time using ordinary least squares or quadratic programming. It is then possible to calculate the EAP and its features, like the ODF and the RTAP, as the sum of the contributions of each component.

For example, in the case of RTAP, it is possible to calculate each  $RTAP_i$  using the set of coefficients  $\mathbf{c}^i$  for all the  $m$  components. The final RTAP for MT-MAPMRI will be equal to  $\sum_{i=1}^m RTAP_i$ . This is a sum, and not a weighted average because the relative volume fraction of each component is already embedded in the basis coefficients.

Therefore, fitting the multi-tensor correctly is absolutely crucial, since a poor fit will lead to an even worse fitting of the SHORE basis. In order to ensure the robustness of the approach we try to fit at the same time: one isotropic tensor, one axially-symmetric tensor, two axially-symmetric tensors and three axially-symmetric tensors meanwhile selecting the best model using Akaike information criterion [2]. In addition, if the tensor fraction  $f_i$  is less than 0.15 the relative tensor is not used for the SHORE fitting. In the case of voxels containing single bundles of fibers the MT-MAPMRI basis is equivalent to the classical MAPMRI basis using a single axially-symmetric tensor.

### 2.3 Simulated Data

RTAP allows inferring the underlying pore cross-sectional area accurately only under three conditions: (a) the compartment is homogeneous (e.g. the pore is composed only of cylinders with the same radius and orientation), (b) the pulse separation time  $\Delta$  is much larger than the pulse width  $\delta$ , and (c), there are enough points in the  $q$ -space to provide a good fitting of the bases. We will refer to these conditions as ideal conditions for what concerns this work.

In order to have homogeneous compartments with known ground truth we calculate the diffusion signal inside the cylindrical pore of given radius  $r_0$  as described in [11] as  $E^{cyl}(q_{\perp}, r_0) = (J_1(2\pi r_0 q_{\perp}) / (\pi r_0 q_{\perp}))^2$  where  $q_{\perp}$  is the plane perpendicular to the main cylinder axis and  $J_1$  is the Bessel function of the first kind.

The axis diffusivity  $E(q_{\parallel})$  is simulated as a 1D Gaussian function. The total 3D diffusivity can be calculated as  $E^{cyl}(\mathbf{q}, r_0) = E(q_{\perp}, r_0)E(q_{\parallel})$ . This equation holds true only if  $\Delta \gg \delta$  which is the necessary condition for testing MAPMRI and MT-MAPMRI RTAP. In these conditions, the RTAP represents the inverse of the cross sectional area of the pore, and the cylinder diameter can thus be estimated as  $2\sqrt{1/(RTAP \cdot \pi)}$ .

We simulated three different sets of cylinders with radii of 4, 6 and 8  $\mu\text{m}$ , and with crossing angles of 0 (coherent fibers), 45°, 60° and 90°. For each of the crossing angles, we changed the orientation of the crossing fibers in 11 different directions. Rician noise was then added to the voxels at a signal to noise ratio (SNR) equal to 20, with ten different instances per voxel. The final dataset was composed of 1320 voxels.

## 2.4 *In Vivo* Data

The Human Connectome Project (HCP) [14] data results from a three-shell diffusion weighted acquisition with 1.25 mm isotropic voxels in a  $145 \times 174 \times 145$  matrix. A total of 288 DW measurements were acquired in each voxel with 90 gradients per shell, respectively, with  $b$ -values 1000, 2000 and  $3000 \text{ s/mm}^2$  and 18 b0 images. Echo time and repetition time were respectively 78 ms, and 2.6 s, with pulse width  $\delta = 10.6 \text{ ms}$ , and pulse separation  $\Delta = 43.1 \text{ ms}$ .

## 3 Results

Cylindrical signal was simulated as is explained in Sect. 2.3, using the HCP gradient table. MAPMRI and MT-MAPMRI were fitted on the signal, the maximal radial order  $N_{max}$  was set to 6 for MAPMRI (50 coefficients) and to 4 for MT-MAPMRI (22 coefficients times the number of tensors), respectively. From the signal fitting, it was possible to calculate the ODF, the RTAP and the normalized mean square error (NMSE). The latter was calculated by reconstructing the cylinders signal on a 10-shell ground truth, with  $b_{max} = 10,000$ , in order to benchmark the interpolation performance of the basis in points different from the one used for the fitting. The RTAP was then used to estimate the cylinders diameter while from the ODF it was possible to extract the principal directions that were used for calculating the angular error (AE) with respect to the ground truth directions.

An example of ODF for a simulated voxel featuring a crossing of  $60^\circ$  is presented in Fig. 1. As can be seen MAPMRI ODF tends to underestimate the crossing angle, which is actually  $8^\circ$  below the ground truth value [6]. On the contrary MT-MAPMRI recovers the crossing angle correctly. Figure 2, top row, shows the ability of the two bases to estimate the cylinder diameter under the ideal conditions. Since the single tensor can not adapt to the topology of the fibers configuration, MAPMRI introduces an error in the estimation of the RTAP, leading to an overestimation of the

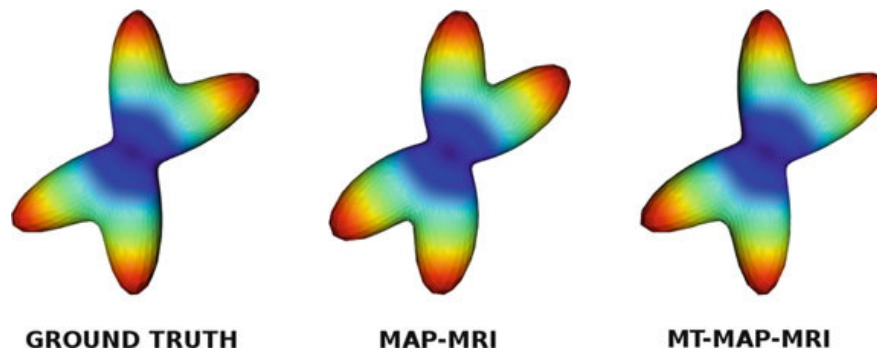


**Fig. 1** Ground truth ODF, MAPMRI ODF and MT-ODF for a simulated two tensors crossing of  $60^\circ$

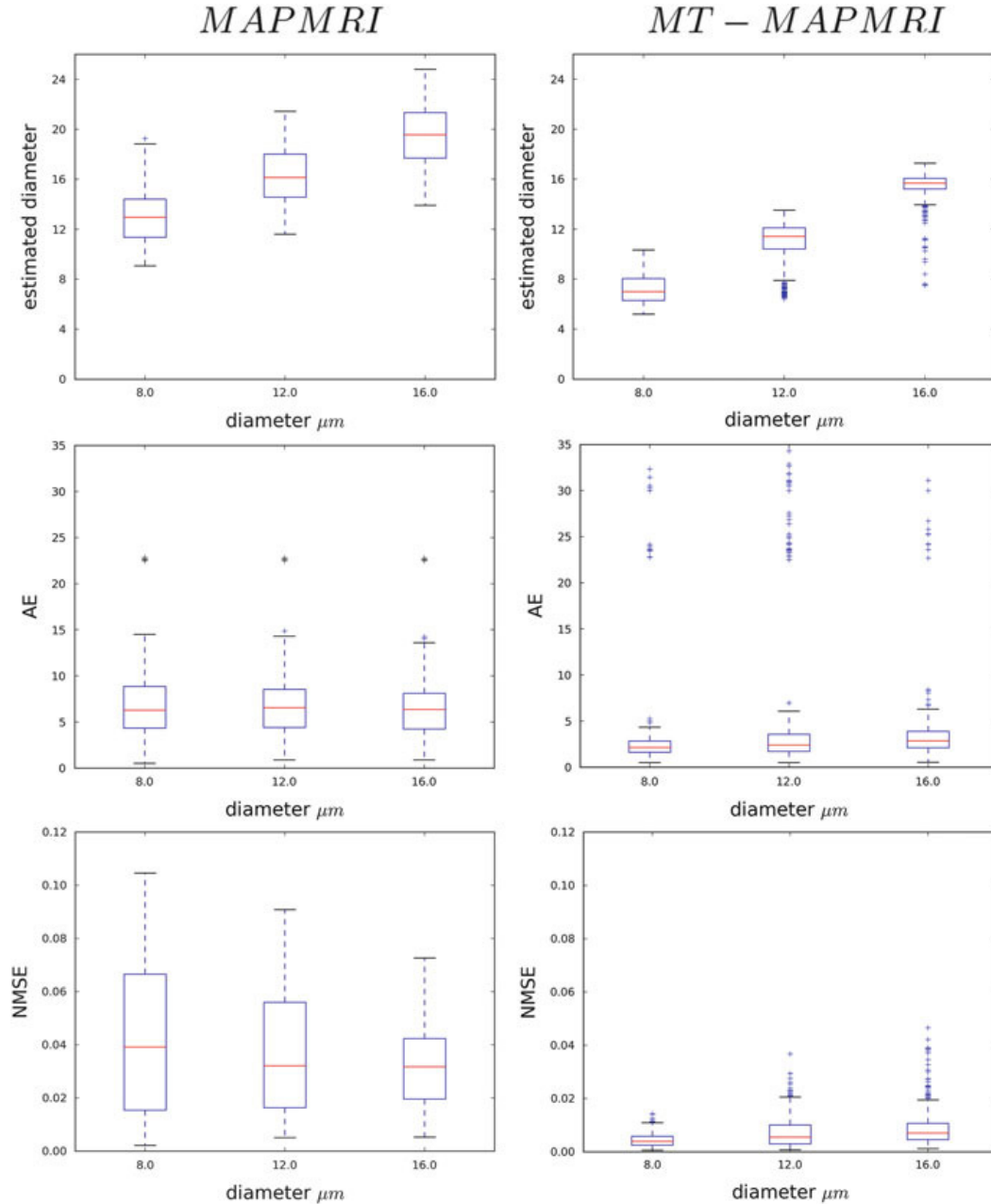


**Fig. 2** Estimated diameter (*top row*), angular error (*middle row*) and NMSE (*bottom row*) on pure cylinder voxels for MAPMRI (*left*) and MT-MAPMRI (*right*), grouped by the ground truth diameter

cylinders diameter. Instead, the multi-tensor of the MT-MAPMRI is able to detect the main diffusion directions and model the signal accordingly. In consequence, the diameter estimation is more accurate, outperforming MAPMRI. As stated in Sect. 2.1, MAPMRI tends to underestimate the crossing angles (Fig. 2, second row), while MT-MAPMRI is able to retrieve the orientation directions in a reliable way even for the majority of the  $45^\circ$  crossings. For the same reason the reconstruction

NMSE is lower for MT-MAPMRI than for MAPMRI. Although MT-MAPMRI is generally more robust than standard MAPMRI, with a narrower interquartile range, some outliers are still presents. These points represent voxels for which the initial multi-tensor fails to retrieve the correct fibers configuration, leading to a wrong MT-MAPMRI fitting.

Although it was possible to estimate the diameter under ideal conditions in these simulated voxels, a validation on in-vivo data is required. The real signal is the average of the signal contributions of all the water molecules trapped in the different compartments present in the voxel. Also, when we moving from the ideal condition  $\Delta \gg \delta$  to a more realistic  $\Delta \simeq \delta$  it is possible to observe an underestimation of the cylinder radius. The complete characterization of this behavior is beyond the scope of this paper. Figure 3 shows the values of the estimated mean diameter in a central coronal slice of HCP data for both MAPMRI and MT-MAPMRI. There are some little differences between the two techniques which are most probably due to the fact that in MT-MAPMRI the additional constraint of axially symmetric tensors is imposed for single fiber voxels, while MAPMRI uses classical DTI tensor. The corpus callosum (CC) presents an average apparent mean diameter of  $9.0 \mu\text{m}$  with both techniques (Fig. 4). The mean values in each section are higher than those reported in [1]. However, they are inline with those presented in [3]. This is due to different factors limiting the accuracy of the measure including partial volume effects. Fick et al. [5] were able to obtain a more accurate axon diameter estimation in CC but using a  $b_{max} = 10,000$  four shells acquisition, with 552 gradients.

In the areas of crossings like the corona radiata (CR) MAPMRI diameter values ( $14.0 \mu\text{m}$  on average) are higher than the one obtained in the CC, in agreement with the results of the simulations showing that MAPMRI is prone to apparent mean diameter overestimation in case of crossing fibers. MT-MAPMRI values, on the contrary, are lower ( $10.4 \mu\text{m}$ ) and closer to those obtained in CC. The histogram of

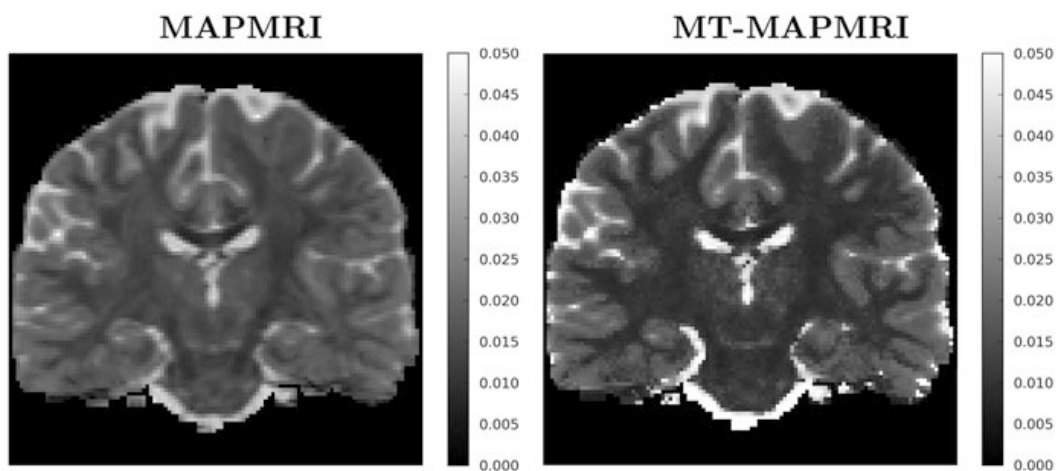


**Fig. 3** Estimated diameter in one coronal slice of HCP in vivo data. As it is possible to observe MAPMRI (*left*) apparent mean diameter is higher in regions with crossing fibers, while MT-MAPMRI (*right*) estimated diameter appears steadier across the white matter



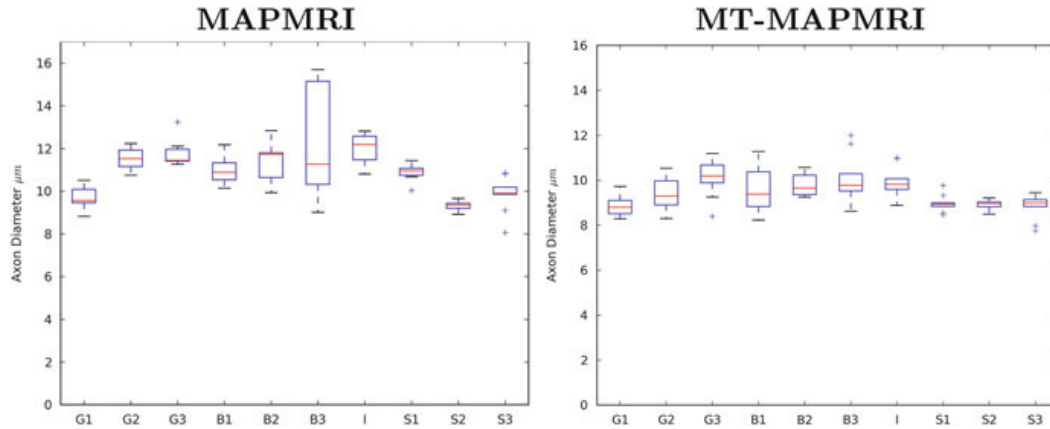


**Fig. 4** Estimated diameter in a corpus callosum ROI of HCP data

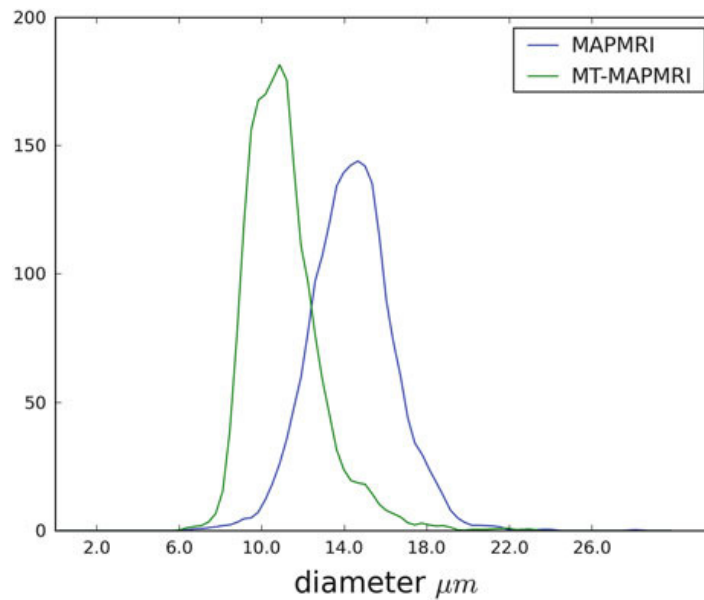


**Fig. 5** Profile of the histogram for the diameter estimation in white matter voxels for MAPMRI (blue) and MT-MAPMRI (green) for a slice of HCP brain

the white matter apparent mean diameter (Fig. 5) of MT-MAPMRI shows that there is a higher number of voxels with low diameter with respect to the same histogram for MAPMRI. This is due to the large amount of crossings present in brain white matter compared to pure single fiber voxels [8], highlighting the potential of MT-MAPMRI in detecting white matter structural features in the presence of complex fiber topologies.

## 4 Conclusions

The apparent mean diameter for in vivo data is an index that is limited by three factors: (a) the compartments inside the voxel are not homogeneous, (b) the long diffusion time hypothesis is not verified, (c) the gradient strength used for in vivo studies is not high enough for characterizing small compartments [7]. Despite these limitations this index holds the potential to describe anomalies and peculiarities of the different brain tissues in vivo, in both pathological and healthy subjects. MT-MAPMRI expands the MAPMRI reconstruction technique adding the possibility to align the basis on multiple tensors if the voxel presents a high likelihood to contain more than one fiber bundles. This led to a better estimation of ODF and apparent mean diameter for such voxels, in both simulations and in-vivo data. The principal drawback of the technique is the fact that the fitting of multiple tensors is a non-linear problem with no easy solution. It can give unstable results (especially in the presence of noise) and that requires a longer computation time with respect to the single tensor (three seconds per voxel on an Intel Core I7-3610QM, 2.3 GHz). Future work will include the research of an improved and faster multi-tensor implementation, besides the complete characterization of MT-MAPMRI performance on an extended set of data and with respect to other state-of-the-art methods such as constrained spherical deconvolution and 3D-SHORE.

**Acknowledgements** Data were provided by the Human Connectome Project, WU-Minn Consortium (Principal Investigators: David Van Essen and Kamil Ugurbil; 1U54MH091657) funded by the 16 NIH Institutes and Centers that support the NIH Blueprint for Neuroscience Research; and by the McDonnell Center for Systems Neuroscience at Washington University.

## References

1. Aboitiz, F., Scheibel, A.B., Fisher, R.S., Zaidel, E.: Fiber composition of the human corpus callosum. *Brain Res.* **598**(12), 143–153 (1992)
2. Akaike, H.: Information theory and an extension of the maximum likelihood principle. In: Parzen, E., Tanabe, K., Kitagawa, G. (eds.) *Selected Papers of Hirotugu Akaike*. Springer Series in Statistics, pp. 199–213. Springer, New York (1998)
3. Alexander, D.C., Hubbard, P.L., Hall, M.G., Moore, E.A., Ptito, M., Parker, G.J., Dyrby, T.B.: Orientationally invariant indices of axon diameter and density from diffusion MRI. *NeuroImage* **52**(4), 1374–1389 (2010)
4. Basser, P., Mattiello, J., LeBihan, D.: Estimation of the effective self diffusion tensor from the nmr spin echo. *J. Magn. Reson.* **103**, 247–254 (1994)
5. Fick, R.H., Wassermann, D., Sanguinetti, G., Deriche, R.: Laplacian-regularized MAP-MRI: improving axonal caliber estimation. In: *International Symposium on Biomedical Imaging: From Nano to Macro*, Brooklyn, New York (April 2015). <https://hal.inria.fr/hal-01140021>
6. Fick, R.H., Zucchelli, M., Girard, G., Descoteaux, M., Menegaz, G., Deriche, R.: Using 3D-SHORE and MAP-MRI to obtain both tractography and microstructural contrast from a clinical DMRI acquisition. In: *International Symposium on Biomedical Imaging: From Nano to Macro*, Brooklyn, New York (April 2015)

7. Huang, S., Nummenmaa, A., Witzel, T., Duval, T., Cohen-Adad, J., Wald, L., McNab, J.: The impact of gradient strength on in vivo diffusion {MRI} estimates of axon diameter. *NeuroImage* **106**, 464–472 (2015). <http://www.sciencedirect.com/science/article/pii/S1053811914010003>
8. Jeurissen, B., Leemans, A., Tournier, J.D., Jones, D.K., Sijbers, J.: Investigating the prevalence of complex fiber configurations in white matter tissue with diffusion magnetic resonance imaging. *Hum. Brain Mapp.* **34**(11), 2747–2766 (2013). <http://dx.doi.org/10.1002/hbm.22099>
9. Landman, B., Bazin, P.L., Prince, J.: Diffusion tensor estimation by maximizing rician likelihood. In: IEEE 11th International Conference on Computer Vision, 2007. ICCV 2007, pp. 1–8 (October 2007)
10. Ozarslan, E., Koay, C., Shepherd, T., Blackband, S., Basser, P.: Simple harmonic oscillator based estimation and reconstruction for three-dimensional q-space MRI. *Proc. Int. Soc. Magn. Reson. Med.* **17**, 1396 (2009)
11. Ozarslan, E., Koay, C., Basser, P.: Simple harmonic oscillator based reconstruction and estimation for one-dimensional q-space magnetic resonance (1d-shore). In: Andrews, T.D., Balan, R., Benedetto, J.J., Czaja, W., Okoudjou, K.A. (eds.) *Excursions in Harmonic Analysis. Applied and Numerical Harmonic Analysis*, vol. 2, pp. 373–399. Birkhauser, Boston (2013)
12. Ozarslan, E., Koay, C., Shepherd, T., Komlosh, M., Irfanoglu, M., Pierpaoli, C., Basser, P.: Mean apparent propagator (map) MRI: a novel diffusion imaging method for mapping tissue microstructure. *NeuroImage* **78**, 16–32 (2013)
13. Scherrer, B., Warfield, S.: Why multiple b-values are required for multi-tensor models. evaluation with a constrained log-euclidean model. In: 2010 IEEE International Symposium on Biomedical Imaging: From Nano to Macro, pp. 1389–1392 (April 2010)
14. Sotiropoulos, S.N., Jbabdi, S., Xu, J., Andersson, J.L., Moeller, S., Auerbach, E.J., Glasser, M.F., Hernandez, M., Sapiro, G., Jenkinson, M., Feinberg, D.A., Yacoub, E., Lenglet, C., Essen, D.C.V., Ugurbil, K., Behrens, T.E.: Advances in diffusion {MRI} acquisition and processing in the human connectome project. *NeuroImage* **80**, 125–143 (2013). <http://www.sciencedirect.com/science/article/pii/S105381191300551X>. Mapping the Connectome
15. Zhang, H., Hubbard, P.L., Parker, G.J., Alexander, D.C.: Axon diameter mapping in the presence of orientation dispersion with diffusion {MRI}. *NeuroImage* **56**(3), 1301–1315 (2011)

# SHORE-BASED BIOMARKERS ALLOW PATIENT VERSUS CONTROL CLASSIFICATION IN STROKE

S. Obertino<sup>1</sup>, L. Brusini<sup>1</sup>, I. Boscolo Galazzo<sup>2,3</sup>, M. Zucchelli<sup>1</sup>, C. Granziera<sup>4</sup>, M. Cristani<sup>1</sup>, G. Menegaz<sup>1</sup>

<sup>1</sup> Dept. of Computer Science, University of Verona, Italy

<sup>2</sup> Inst. of Nuclear Med., UCL, United Kingdom <sup>3</sup> Dept. of Neuroradiology, AOUI of Verona, Italy

<sup>4</sup> Dept. of Clinical Neuroscience, CHUV and University of Lausanne, Switzerland

## ABSTRACT

In diffusion MRI, numerical biomarkers are usually calculated for research and clinical purposes as Generalized Fractional Anisotropy (GFA). Recently, more eloquent indices allowing a more accurate description of tissue microstructure were derived from the SHORE model. Under certain experimental conditions, such indices express the morphological properties of the compartments where spins diffuse. Evidence of the suitability of such indices as biomarkers for stroke was provided in a previous study based on diffusion spectrum imaging (DSI) and focusing on the cortical motor loop. The goal of this work was to investigate the suitability of such indices for stratification, namely for distinguishing pathological from healthy subjects. To this end, two different paths were followed. First, the same approach used in the previous work for longitudinal analysis (statistics-based) was applied to detect inter-group variations. Then, a new approach based on the LASSO regressor was proposed. Results provided evidence of the suitability of the proposed indices for stratification purposes.

**Index Terms**— Diffusion MRI, Classification, Stroke, Tractography, 3D-SHORE

## 1. INTRODUCTION

Diffusion Weighted Imaging (DWI) studies highlighted connectivity remodeling after stroke in the uninjured hemispheres [1]. In particular, derived standard scalar measures as Generalized Fractional Anisotropy (GFA) has been successfully exploited to detect the plasticity process over time. In addition, the extension of previous analysis to the motor loops between cortical and subcortical regions provided additional evidence of this phenomenon [2]. Recently, a new generation of indices were derived from a closed-form analytical reconstruction of the diffusion signal referred as 3D Simple Harmonic Oscillator Based Reconstruction and Estimation (3D-SHORE) model [3]. Following the same approach, such indices were proven to be suitable as biomarkers of axonal remodelling after stroke [4] confirming their ability of detecting white matter structural changes in longitudinal studies.

In this work, we move a step further providing evidence of the suitability of the considered indices for stratification purposes, that is for distinguishing affected from healthy subjects, besides extending the set of features holding the potential for being additional biomarkers. Indeed, the possibility of automatic identifying lesions in a subject-vs-group approach would help disambiguating shady conditions where the lesion itself cannot be detected by visual inspection by the neuro-radiologist. To this end, first, an extended set of features were derived based on the probability density functions (pdfs) of the indices to be exploited for detecting statistically significant changes across groups (inter-group). Then, the Least Absolute Shrinkage and Selection Operator (LASSO) classifier was used for splitting pathological from healthy subjects.

## 2. METHODS

The processing pipeline consists of (i) signal and apparent propagator (EAP) reconstruction using the SHORE model; (ii) extraction of the microstructural indices along white matter fiber bundles connecting cortical-subcortical regions; (iii) feature extraction from the pdfs of the indices and, finally, (iv) both statistic and LASSO based analysis, as is detailed in the next sections.

### 2.1. Dataset

Ten patients (6 males) [age =  $56.1 \pm 17.8$ ] suffering from ischemic infraction affecting the motor cortex or subcortical structures were enrolled in the study. All patients underwent three Diffusion Spectrum Imaging (DSI) scans [TR/TE = 6600/138 msec, FoV =  $212 \times 212$  mm<sup>2</sup>, 34 slices,  $2.2 \times 2.2 \times 3$  mm<sup>3</sup> resolution, 258 diffusion directions,  $b$ -value = 8000 s/mm<sup>2</sup>,  $\sim 25$  min scan time] within one week (*tp1*), one month ( $\pm$  one week, *tp2*), and six months ( $\pm$  fifteen days, *tp3*) after stroke. Pre-processing was performed as in [1]. Ten age and gender matched healthy subjects [age =  $59.0 \pm 12.8$ ] were also recruited and underwent two DSI scans a month apart (*tp1c* and *tp2c*). All subjects provided written informed consent and the Lausanne University Hospital review board approved the study protocol.

## 2.2. SHORE Reconstruction Model

The orthonormalized SHORE model [5] was used for reconstructing the Mean Apparent Propagator (MAP) [3], which represents the probability density of the mean square displacement of spins across the spatial coordinates in the unit time and is related to the diffusion signal  $E(\mathbf{q})$  by the Fourier relation [6]. In the SHORE model the signal is approximated as

$$E(\mathbf{q}\mathbf{u}) = \sum_{l=0,even}^{N_{max}} \sum_{n=l}^{(N_{max}+l)/2} \sum_{m=-l}^l c_{nlm} \Phi_{nlm}(\mathbf{q}\mathbf{u}) \quad (1)$$

where  $N_{max}$  is the maximal order of the functions in the truncated series and  $\Phi_{nlm}(\mathbf{q})$  is the orthonormal SHORE basis. This family of functions is defined as

$$\Phi_{nlm}(\mathbf{q}\mathbf{u}) = \left[ \frac{2(n-l)!}{\zeta^{3/2} \Gamma(n+3/2)} \right]^{1/2} \left( \frac{q^2}{\zeta} \right)^{l/2} \exp\left( \frac{-q^2}{2\zeta} \right) L_{n-l}^{l+1/2} \left( \frac{q^2}{\zeta} \right) Y_l^m(\mathbf{u}) \quad (2)$$

where  $\Gamma$  is the Gamma function,  $\zeta = \frac{1}{8\pi^2\tau D}$  is the scaling parameter [ $\tau$ : diffusion time;  $D$ : diffusivity]. In the implementation,  $\zeta$  was derived forcing the zero order term  $\Phi_{000}$  to be the DTI-derived Gaussian function.

Several indices related to the microstructural properties can be derived from MAP, which allow the estimation of pores' geometry and local diffusivity properties under specific assumptions [3]. In particular, the Return To the Axis Probability (RTAP), the Propagator Anisotropy (PA), the Orientation Distribution Function (ODF) and the well-known GFA were derived as in [4] and analyzed. Among these, the ODF is necessary for performing tractography since it represents the mean square displacement probability of spins across spatial directions and allows identifying the principal diffusion direction. It is derived by integrating the EAP along the radial dimension. Interestingly, RTAP represents the reciprocal of the mean cross-sectional area of the pore [3] such that an estimation of the axonal radius ( $R$ ) can be inferred from its value as  $R = \sqrt{\pi/RTAP}$ .

## 2.3. Tract-based Analysis

The ODFs were reconstructed using the Diffusion Toolkit<sup>1</sup> and fiber-tracking was performed via a streamline algorithm<sup>2</sup>. Binary masks representing fiber connections between specific Regions Of Interest (ROI) were derived and values for each index were collected along each fiber tract. The pdf was derived for each index and the features chosen for describing it were calculated. In particular, the mean, variance, skewness, and kurtosis ( $m, v, s, k$ , respectively) were considered. Moreover, the distances between the pdfs at different time-points were characterized by three measures: Mean Standard

<sup>1</sup>www.trackvis.org/dtk

<sup>2</sup>www.cmtk.org

Error (MSE), Kullback-Leibler Divergence (KLD), and Hausdorff distance (H). These measures were introduced as they can be directly derived from the pdfs at different time-points and be considered as direct measures of longitudinal changes over time. A subset of connections between cortical and sub-cortical regions were selected from three major motor networks (Fig. 1): a) the sensory-motor sub-loop [primary motor cortex (M1), putamen (Put), globus pallidus (GPi), Thalamus (Thal)], b) the premotor subloop [premotor cortex (PM), caudate nucleus (Cau), Put, GPi, Thal] c) the supplementary motor cortex (SMA) sub-loop [SMA, Put, Cau, Thal, GPi].

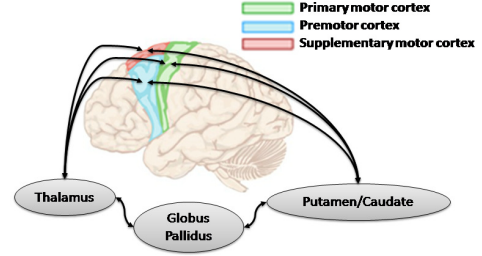


Fig. 1: Cortical-Subcortical motor networks.

## 2.4. Statistical Analysis

For each feature, that is for each histogram descriptor, the reproducibility of the measurement along cortico-subcortical tracts was assessed by evaluating in the control group the percentage absolute change between time-points as

$$\Delta_{tp12c,i} = \frac{|F_{tp1c,i} - F_{tp2c,i}|}{F_{tp1c,i}} \quad (3)$$

where  $F$  denotes the feature, that is  $F = \{m, v, s, k\}$ ,  $i$  runs over the indices, that is  $i = \{GFA, RTAP, R, PA\}$ , and subscript  $c$  denotes the control group. In addition, the percentage absolute changes between patients' time-points were also calculated as

$$\Delta_{tp12,i} = \frac{|F_{tp1,i} - F_{tp2,i}|}{F_{tp1,i}} \quad (4)$$

$$\Delta_{tp13,i} = \frac{|F_{tp1,i} - F_{tp3,i}|}{F_{tp1,i}} \quad (5)$$

As the normality test (Kolmogorov-Smirnov) to the whole set of feature changes extracted from both groups of participants revealed that the values were normally distributed, the use of parametric statistics was enabled. Accordingly, the unpaired  $t$ -test was used to detect significant differences in the feature values across groups ( $p < 0.05$ ). In particular,  $\Delta_{tp12c,i}$  was compared to  $\Delta_{tp12,i}$  and  $\Delta_{tp12c,i}$  to  $\Delta_{tp13,i}$ . Moreover, for both groups the distances between the pdfs of each index (GFA, RTAP, R, PA) at different time-points were also considered. Since only one distance per each couple of histograms

and per connection can be calculated, all the connections were considered jointly resulting in  $N_s \times N_c$  measurements,  $N_s=10$  and  $N_c=11$  being the number of subjects in each group and the number of connections, respectively. The sets of distance measures obtained from the control and the patient groups were compared using the unpaired  $t$ -test ( $p < 0.05$ ). Noteworthy, two sets of distances are available for patients to be compared to that of controls.

## 2.5. Classification Model

In order to automatically separate patients from controls, a classification approach combining a training and testing pools was applied. These datasets were created using a cross-validation process leave- $N$ -out (where  $N = 1:5$ ), while LASSO has been used to model the classifier [7]. It derives the linear combination of connections for all features and distances of each index, estimating the weight vector  $w$  by minimizing the standard least square error function:

$$E(w) = \sum_{m=1}^N (y_m - w^T x_m)^2, \quad (6)$$

where  $y_m$  is a binary identifier of each class, and  $x_m$  represents the vector with variations value between  $tp1$  and  $tp2$  of connections (independent variable). The vector  $w$  was used to classify the test pool and to extract a robust measure of accuracy for each feature and distance.

## 3. RESULTS & DISCUSSION

### 3.1. Statistical Analysis

In the control group, the longitudinal percentage absolute change of all features for each index is always under 17% (worst case:  $16.6 \pm 13.5$  [%] for GFA  $k$ ), as shown in the first bar column in Fig. 2. This points at a good reproducibility

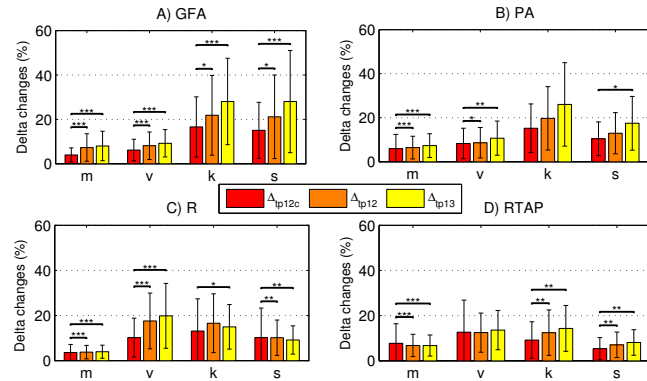


**Fig. 2:** Longitudinal features changes in percent absolute values in controls and patients ( $*p < 0.05$ ,  $**p < 0.01$ ,  $***p < 0.001$ ).

of the whole set of extended features. In particular, for all indices, mean has always an higher reproducibility (worst case:  $7.8 \pm 8.6$  [%] for RTAP) in agreement with previous studies [1, 8, 2, 4]. Skewness and kurtosis presented a large variability over time, except for RTAP in which these two features have lower percentage absolute change ( $< 10\%$ ). Moreover, Fig. 2 also reports the longitudinal changes in the patient group for both short ( $tp12$ ) and long ( $tp13$ ) term changes, along with the results of the statistical comparison with control group. For all indices, mean is the feature with the highest statistical significant difference between groups ( $p < 0.001$ ) in both longitudinal comparisons. Variance shows statistical significance in all indices except for RTAP. Kurtosis detects significant differences in both longitudinal terms in GFA and RTAP, it is present in long term in R, and absent in PA. Skewness exhibits significance in both longitudinal short and long term of GFA, R and RTAP, while it has statistical significance only in long term for PA. GFA and PA show an overall match in terms of longitudinal changes for all the features, confirming the similarity of their nature as indices of anisotropy.

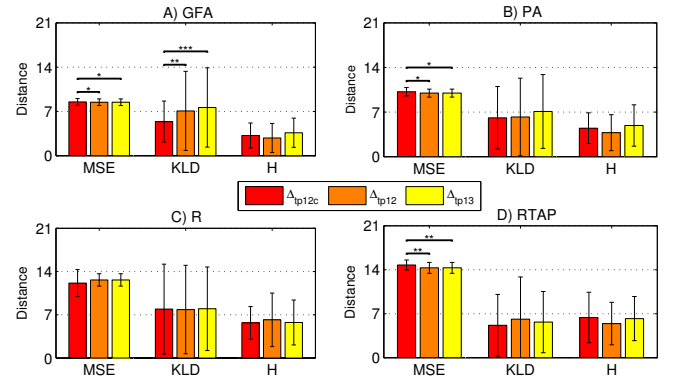


**Fig. 3:** Probability distribution function distances in controls and patients ( $*p < 0.05$ ,  $**p < 0.01$ ,  $***p < 0.001$ ).

Distances' values for each index are reported in Fig. 3 applying the same scale for visualization purposes despite their different order of magnitude (MSE and H:  $e-03$ , KLD:  $e-02$ ). For both patients and controls, MSE shows the lowest inter-subject variability, with consistent results among the different indices. Moreover, a significant difference between groups is detected by MSE both for  $\Delta_{tp12c,i}$  vs  $\Delta_{tp12,i}$  and  $\Delta_{tp12c,i}$  vs  $\Delta_{tp13,i}$  in all indices except for R. GFA presents statistically significant variations in KLD as well, for both patients vs controls comparisons.

### 3.2. Classification Analysis

Classification models based on both feature and distance variables are reported for all indices in Fig. 4 as curves of performance in terms of accuracy [0:1] across the different cross-validation levels. PA reaches the best accuracy with H (best

case: leave-2-out = 0.95), in addition H shows the highest level of accuracy also for GFA (best case: leave-4-out = 0.79). R reaches the best accuracy with both variance and H (best case: leave-1-out = 0.7). Conversely, RTAP exhibits different trends in comparison to the other indices, in particular the best accuracy is obtained with MSE (best case: leave-2-out = 0.7). This result is in agreement with the statistical analysis findings (Fig. 3), further confirming the ability of MSE in differentiating patients from healthy subjects.

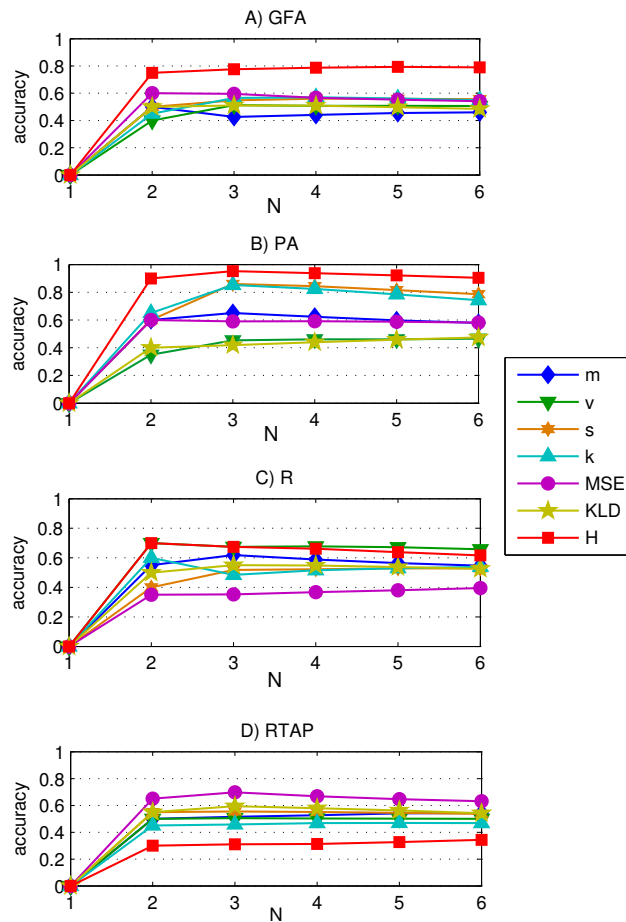


Fig. 4: Leave-N-out method cross-validation accuracy.

#### 4. CONCLUSIONS

In this work, the SHORE-derived indices and related set of features were assessed on cortico-subcortical connections. Despite having considered motor connections with deep brain structures, the statistical analysis confirmed an overall good reproducibility of the new indices, in agreement with previous findings on cortical motor networks. Moreover, statistically significant differences between patients and controls were detected, not only for the classical mean feature but also

for the extended set of features which demonstrated their potential for being considered additional biomarkers. The complementary classification method was successfully exploited, revealing the prediction power of atypically features like Hausdorff distance in PA. In conclusion, the proposed analysis strategies suggest that a combination of features can be used to model a classifier aiming at differentiating pathological from physiological patterns. Future works will be focused on a feature selection procedure across the different possibilities for finding the optimal combination of variables (in terms of features and distances) and indices in order to optimize the classifier model.

#### 5. REFERENCES

- [1] C. Granziera et al, "A new early and automated MRI-based predictor of motor improvement after stroke," *Neurology*, vol. 79, no. 1, pp. 39–46, 2012.
- [2] S. Obertino et al, "Tract-based assessment of the subcortical motor network plasticity after stroke," *Processings of International Society for Magnetic Resonance in Medicine*, vol. 22, pp. 4764, 2015.
- [3] E. Ozarslan et al, "Mean apparent propagator (MAP) MRI: A novel diffusion imaging method for mapping tissue microstructure," *NeuroImage*, vol. 78, pp. 16 – 32, 2013.
- [4] L. Brusini et al, "Assessment of Mean Apparent Propagator-based indices as biomarkers of axonal remodeling after stroke," *Medical Image Computing and Computer-Assisted Intervention - MICCAI 2015*, vol. 9349, pp. 199–206, 2015.
- [5] E. Ozarslan et al, "Simple harmonic oscillator based reconstruction and estimation for three-dimensional q-space MRI," *Processings of International Society for Magnetic Resonance in Medicine*, vol. 17, pp. 1396, 2009.
- [6] E. Stejskal et al, "Spin diffusion measurements: Spin echoes in the presence of a time-dependent field gradient," *Journal of Chemical Physics*, vol. 42, no. 1, pp. 288–292, 1965.
- [7] R. Tibshirani et al, "Regression shrinkage and selection via the lasso: a retrospective," *Journal of the Royal Statistical Society: Series B (Statistical Methodology)*, vol. 73, no. 3, pp. 273 – 282, 2011.
- [8] Y. Lin et al, "Quantitative Analysis of Myelin and Axonal Remodeling in the Uninjured Motor Network After Stroke," *Brain Connectivity*, vol. 5, no. 7, pp. 401–412, 2015.



# What lies beneath? Diffusion EAP-based study of brain tissue microstructure

Mauro Zucchelli<sup>a,\*</sup>, Lorenza Brusini<sup>a</sup>, C. Andrés Méndez<sup>a</sup>, Alessandro Daducci<sup>c</sup>,  
Cristina Granziera<sup>b</sup>, Gloria Menegaz<sup>a</sup>

<sup>a</sup> Department of Computer Science, University of Verona, Verona, Italy

<sup>b</sup> Department of Clinical Neurosciences, CHUV and University of Lausanne, Lausanne, Switzerland

<sup>c</sup> Swiss Federal Institute of Technology (EPFL) Lausanne, Lausanne, Switzerland

## ARTICLE INFO

### Article history:

Received 28 November 2014

Revised 22 March 2016

Accepted 24 March 2016

Available online 1 April 2016

### Keywords:

Diffusion MRI

NODDI

3D-SHORE

DSI

EAP

Microstructure

## ABSTRACT

Diffusion weighted magnetic resonance signals convey information about tissue microstructure and cytoarchitecture. In the last years, many models have been proposed for recovering the diffusion signal and extracting information to constitute new families of numerical indices. Two main categories of reconstruction models can be identified in diffusion magnetic resonance imaging (DMRI): ensemble average propagator (EAP) models and compartmental models. From both, descriptors can be derived for elucidating the underlying microstructural architecture. While compartmental models indices directly quantify the fraction of different cell compartments in each voxel, EAP-derived indices are only a derivative measure and the effect of the different microstructural configurations on the indices is still unclear. In this paper, we analyze three EAP indices calculated using the 3D Simple Harmonic Oscillator based Reconstruction and Estimation (3D-SHORE) model and estimate their changes with respect to the principal microstructural configurations. We take advantage of the state of the art simulations to quantify the variations of the indices with the simulation parameters. Analysis of *in-vivo* data correlates the EAP indices with the microstructural parameters obtained from the Neurite Orientation Dispersion and Density Imaging (NODDI) model as a pseudo ground truth for brain data. Results show that the EAP derived indices convey information on the tissue microstructure and that their combined values directly reflect the configuration of the different compartments in each voxel.

© 2016 Elsevier B.V. All rights reserved.

## 1. Introduction

Diffusion MRI is a non-invasive imaging method that is able to provide information *in-vivo* on the cerebral tissue microstructure. The EAP, indicating the likelihood for a particles to undergo a net displacement  $\mathbf{r}$  in the unit time, can be recovered from the diffusion weighted signal attenuation  $E(\mathbf{q})$  under the narrow pulse assumption (Stejskal and Tanner, 1965) from the Fourier relationship

$$P(\mathbf{r}) = \int_{\mathbf{q} \in \mathbb{R}^3} E(\mathbf{q}) e^{2\pi \mathbf{q} \cdot \mathbf{r}} d\mathbf{q} \quad (1)$$

where  $P(\mathbf{r})$  is the EAP,  $\mathbf{q} = \mathbf{q}\mathbf{u}$  is the sampling position, with  $\mathbf{u}$  unit vector of the reciprocal space, or  $\mathbf{q}$ -space, and  $E(\mathbf{q}) = E(\mathbf{q})/E(0)$  is the ratio between the value of the signal at  $\mathbf{q}$  and its value at  $\mathbf{q} = 0$ .

The vector  $\mathbf{q}$  depends on the gyromagnetic ratio  $\gamma$ , the diffusion gradient  $\mathbf{G}$  and the gradient duration  $\delta$  according to  $\mathbf{q} = \gamma \delta \mathbf{G} / (2\pi)$ . The norm of  $\mathbf{q}$ ,  $|\mathbf{q}| = q$  is related to the so-called *b-value* through  $\delta$  and the diffusion pulse separation time  $\Delta$  as  $b = 4\pi^2 q^2 \tau$  with  $\tau = \Delta - \delta/3$ .

Last years have witnessed a proliferation of modeling methods aiming at inferring microstructural features from the diffusion signal. Overall, two main approaches can be identified: EAP models and compartmental models. EAP models aim at recovering the probability density function of the water molecules displacement  $P(\mathbf{r})$ , while compartmental models ground on the representation of the diffusion signal as the sum of the contributions originating from a set of pre-defined biophysical models of the tissues. These categorization of reconstruction models are not mutually exclusive and several hybrid models have been proposed in the literature (Tuch et al., 2002; Scherrer et al., 2015). From both families of models, numerical descriptors expressing different features of the underlying structural architecture and thus holding the potential for being the next generation of microstructural biomarkers can be inferred.

\* Corresponding author. Tel.: +393477838267.

E-mail address: [mauro.zucchelli@univr.it](mailto:mauro.zucchelli@univr.it) (M. Zucchelli).



The most widely used EAP model is the Diffusion Tensor Imaging (DTI) (Basser et al., 1994). DTI models the EAP as a single multivariate Gaussian function called diffusion tensor. Although this model has been proved to be suitable for describing weakly constrained diffusion (extracellular, cerebrospinal fluid) and simple white matter topologies (single dominant diffusion direction, as in the corpus callosum), it cannot cope with complex architectures like fiber crossing, fanning and kissing, neither with the non-Gaussianity of the diffusion process inside a restricted medium such as the white matter (WM) (Santis et al., 2011). In Diffusion Spectrum Imaging (DSI) (Wedeen et al., 2005) the dense sampling of  $\mathbf{q}$ -space on a Cartesian grid including high b-values allowed to overcome such a limitation improving the accuracy in the detection of the WM configurations. However, even though such a model-free reconstruction is quite appealing also due to its intrinsic simplicity (the EAP is recovered by taking the discrete Fast Fourier Transform (FFT) of the signal, eventually using a smoothing window for avoiding spectral leakage), the long acquisition time seriously limits its applicability in clinics.

Among the more widespread EAP models proposed so far, one of the most accurate is the Simple Harmonic Oscillator Based Reconstruction and Estimation (SHORE), first introduced in Ozarslan et al. (2009). In the original version, called 3D-SHORE, the same scaling parameter was used in all directions (isotropic scaling). A minor change to the 3D-SHORE model was introduced in Cheng et al. (2011) and in Merlet and Deriche (2013) where the orthonormality property of the basis was imposed. 3D-SHORE showed good performance in detecting multiple diffusion directions and EAP indices (Merlet and Deriche, 2013; Zucchelli et al., 2015; Fick et al., 2015b). The isotropic scaling constraint was removed in Ozarslan et al. (2013) where a tensorial scale parameter was introduced allowing for a separable solution in the Cartesian space and leading to the so-called Mean Apparent Propagator (MAP) MRI model. Both 3D-SHORE and MAP-MRI are among the most promising EAP models for the characterization of tissue microstructure, as recently highlighted at the SPARC-dMRI contest (Ning et al., 2015). Among the other EAP models, it is worth mentioning the Spherical Polar Fourier Imaging (SPFI) (Assemlal et al., 2009; Cheng et al., 2010), exploiting Laguerre polynomials and Spherical Harmonics (SH) for modeling the radial and the angular parts of the diffusion signal, respectively, and the Diffusion Propagator Imaging (DPI) (Descoteaux et al., 2011) where  $E(\mathbf{q})$  was obtained by solving the 3D Laplace equation. Finally, the Bessel Fourier Orientation Reconstruction (BFOR) (Hosseini et al., 2013) model was derived as the solution of the heat equation that can be seen as a generalization of the Laplace equation. All these models provide close approximations of the diffusion signal and allow deriving important EAP features such as the Orientation Distribution Function (ODF) in a reliable manner. From EAP models, it is also possible to derive microstructure related indices, namely the Return To the Origin Probability (RTOP), the Return To the Axis Probability (RTAP), and the Return To the Plane Probability (RTPP) (Ozarslan et al., 2013). These indices reflect the degree of restriction of the water molecules in the voxel, which is directly linked to the underlying pore shape. However, a complete characterization of the behavior of these indices in regard to microstructural variations is still lacking in the literature.

Compartmental models ground on the assumption that the diffusion signal can be represented as a mixture of components each resulting from spin motion in geometrically constrained compartments having different biophysical characteristics (Latour et al., 1994; Stanisz et al., 1997; Pfeuffer et al., 1998; Mulkern et al., 1999). In the most general form, compartments correspond to glial cells, axons and extracellular space, respectively. In axon compartments diffusion is *restricted*, where restriction is due to geometry. In particular, restriction is assumed to be anisotropic in white mat-

ter tracts. Then, diffusion is *hindered* in extracellular space and glial cells, where the EAP is assumed to be Gaussian (Assaf et al., 2004). Among compartmental models a well known example is the Ball and Sticks (Behrens et al., 2003) in which the white matter axons were modeled as zero-radius cylinders (*sticks*) and the extracellular compartment as isotropic Gaussian (*ball*). Assaf and Basser (2005) proposed the Composite Hindered and Restricted Model (CHARMED) which represented the intracellular compartment as a cylinder with a given radius, while diffusion in the extracellular compartment was described by a diffusion tensor. Alexander et al. (2010) improved CHARMED by adding an extra compartment to model the cerebrospinal fluid (CSF) as an isotropic Gaussian function with constant diffusivity. Several studies showed that white matter fibers are generally not coherently oriented (Jones, 2003; Koay et al., 2008). Zhang et al. (2011) further improved compartmental models allowing the cylinders of the intracellular compartment to be dispersed according to the Watson distribution on the sphere. A simplified version of this model, called the NODDI was proposed in Zhang et al. (2012). NODDI principal innovation was the replacement of the cylinder with sticks for the intracellular compartment. The NODDI model has been extensively tested on different datasets (Zhang et al., 2012) taking the classical DTI measures, like fractional anisotropy (FA) and mean diffusivity (MD), as benchmarks. From NODDI indices it is possible to obtain information on the tissue intracellular volume fraction, the isotropic volume fraction and the orientation dispersion in the voxel.

The aim of this study is to characterize how EAP derived indices change in different tissue microstructure configurations. This is done via a systematic comparison between RTOP, RTAP, and RTPP with (i) axon diameter, (ii) intracellular volume fraction, (iii) isotropic volume fraction, and (iv) axon orientation dispersion in both simulated and *in-vivo* data. The use of simulated data enables the benchmarking of the variation of the indices as a function of the model parameters and provides a guideline for the interpretation of the results on *in-vivo* data in both healthy and pathological conditions. In this study we consider a non-clinical DSI acquisition with 257 diffusion directions, but 3D-SHORE and other EAP models could be employed also on multi-shell data with only 60 gradients (Fick et al., 2015b) that makes the calculation of the EAP indices more suitable for clinical studies.

This paper is organized as follows: Section 2 illustrates the main features of the 3D-SHORE model, highlighting the differences from the previous ones, revisits the NODDI model and describes the simulated and *in-vivo* data. Section 3 illustrates and discusses the results and Section 4 derives conclusions.

## 2. Materials and methods

### 2.1. The 3D-SHORE model

Functional bases decompose the diffusion signal  $E(\mathbf{q})$  as a linear combination of basis functions  $\Phi(\mathbf{q}\mathbf{u})$

$$E(\mathbf{q}) = \sum_{n=0}^N c_n \Phi_n(\mathbf{q}\mathbf{u}) \quad (2)$$

Thanks to the linearity of the representation, the EAP is recovered by applying the Fourier operator to (2). Accordingly, the EAP results from the linear combination of the dual basis functions  $\Psi(\mathbf{r}\mathbf{u})$

$$\begin{aligned} P(\mathbf{r}) &= \mathcal{F}\{E(\mathbf{q})\} = \mathcal{F}\left\{\sum_{n=0}^N c_n \Phi_n(\mathbf{q}\mathbf{u})\right\} \\ &= \sum_{n=0}^N c_n \mathcal{F}\{\Phi_n(\mathbf{q}\mathbf{u})\} = \sum_{n=0}^N c_n \Psi_n(\mathbf{r}\mathbf{u}) \end{aligned} \quad (3)$$

where  $\Psi_n(\mathbf{r})$  is the Fourier transform of the basis function  $\Phi_n(\mathbf{q})$ . As it is the case for SPFI, DPI and BFOR, the basis is separable in both the radial and the angular coordinates. In particular, while these methods differ in the choice of the radial part, all rely on SH for expressing the angular dependence. According to Cheng et al. (2011), the basis functions  $\Phi_n(\mathbf{q})$  can be written as

$$\Phi_n(q\mathbf{u}) = R_n(q)Y_n(\mathbf{u}) \quad (4)$$

where  $R_n(q)$  models the radial part of the signal and  $\{Y_n(\mathbf{u})\}$  are the real SH of even degree as in Descoteaux et al. (2007).

In this work, the orthonormal formulation of the 3D-SHORE model was chosen (Merlet and Deriche, 2013)

$$\begin{aligned} \mathbf{E}(q\mathbf{u}) &= \sum_{l=0, \text{even}}^{N_{\max}} \sum_{n=l}^{(N_{\max}+1)/2} \sum_{m=-l}^l c_{nlm} \Phi_{nlm}(q\mathbf{u}) \\ \Phi_{nlm}(q\mathbf{u}) &= \left[ \frac{2(n-l)!}{\zeta^{3/2} \Gamma(n+3/2)} \right]^{1/2} \left( \frac{q^2}{\zeta} \right)^{l/2} \\ &\quad \exp\left( \frac{-q^2}{2\zeta} \right) L_{n-l}^{l+1/2} \left( \frac{q^2}{\zeta} \right) Y_l^m(\mathbf{u}) \end{aligned} \quad (5)$$

where  $\Phi_{nlm}(\mathbf{q})$  is the orthonormal 3D-SHORE basis,  $N_{\max}$  is the maximal order of the functions in the truncated series,  $\Gamma$  is the Gamma function and  $\zeta$  is a scaling parameter.

It could be useful to point out that the ordering of the basis functions presented here is the same as in Eq. 58 in Ozarslan et al. (2013), after the reworking implied by the use of Merlet and Deriche (2013) basis (see Appendix A). In particular, the first  $N_{\max}/2 + 1$  components of the basis are isotropic ( $l = 0$  and  $m = 0$ ). The scale factor  $\zeta$  was derived by forcing the zero order term  $\Phi_{000}$  to be the DTI-derived Gaussian function  $\exp(-4\pi^2 \tau q^2 D)$  leading to  $\zeta = \frac{1}{8\pi^2 \tau D}$  as in Merlet and Deriche (2013). Accordingly, the scale factor depends on two parameters: the diffusion time  $\tau$  and the diffusivity  $D$ . In the 3D-SHORE model  $D$  is assumed to be constant across the angular directions, which corresponds to isotropic diffusion, and is calculated as the diffusion tensor derived mean diffusivity. We are aware of the fact that such an assumption is not suitable where diffusion is either restricted or hindered as it is the case in WM and, to a lesser extent, in GM (Ozarslan et al., 2013). This constraint cannot easily be removed because the radial term of the 3D-SHORE model is not separable since it only depends on the norm of the reciprocal vector. Angular dependency is recovered by SH. In case of high anisotropy this limits the accuracy of the signal representation. Nevertheless, the 3D-SHORE model provides competitive performance in terms of both signal reconstruction error and estimation of main fiber directions (Fick et al., 2015b; Ning et al., 2015). The closed form expression for the EAP is obtained by solving Eq. 4

$$P(\mathbf{r}\mathbf{u}) = \sum_{l=0, \text{even}}^{N_{\max}} \sum_{n=l}^{(N_{\max}+1)/2} \sum_{m=-l}^l c_{nlm} \Psi_{nlm}(\mathbf{r}\mathbf{u}) \quad (6)$$

$$\begin{aligned} \Psi_{nlm} &= (-1)^{n-l/2} \left[ \frac{2(4\pi^2 \zeta)^{3/2} (n-l)!}{\Gamma(n+3/2)} \right]^{1/2} \\ &\quad \times (4\pi^2 \zeta r^2)^{l/2} \exp(-2\pi^2 \zeta r^2) L_{n-l}^{l+1/2} (4\pi^2 \zeta r^2) Y_l^m(\mathbf{u}) \end{aligned} \quad (7)$$

One of the main advantages of 3D-SHORE is that the coefficients  $c_{nlm}$  are the same for the signal and the EAP, which is extremely important from the computational point of view.

### 2.1.1. 3D-SHORE indices

The three EAP indices proposed in Ozarslan et al. (2013), the RTOP, RTAP, and RTPP are linked to the underlying mean pore ge-

ometry irrespectively of the pore shape. These indices can be calculated in a dual manner, either from the signal or from the EAP

$$RTOP = \int_{\mathbb{R}^3} E(\mathbf{q}) d^3 \mathbf{q} = P(\mathbf{0}) \quad (8)$$

$$RTAP = \int_{\mathbb{R}^2} E(\mathbf{q}_{\perp}) d^2 \mathbf{q}_{\perp} = \int_{\mathbb{R}} P(\tilde{r}_{\parallel}) dr \quad (9)$$

$$RTPP = \int_{\mathbb{R}} E(\tilde{q}_{\parallel}) dq = \int_{\mathbb{R}^2} P(\mathbf{r}_{\perp}) d^2 \mathbf{r}_{\perp} \quad (10)$$

RTOP is calculated as the volume integral of the signal or, alternately, following the properties of the Fourier transform, as the EAP in zero. Similarly, RTAP can be obtained either as the integral of the signal in the plane passing through the origin and perpendicular to the main diffusion direction,  $\mathbf{q}_{\perp}$ , or as the integral of the EAP along the main diffusion direction  $\tilde{r}_{\parallel}$ . Finally, RTPP can be obtained as the integral of the signal along the main diffusion direction or as the integral of the EAP over the plane passing through the origin and perpendicular to the main diffusion direction.

Under long diffusion time and narrow pulse assumptions ( $\Delta \gg \delta$ ,  $\delta \sim 0$ ) these indices are respectively related to the apparent mean volume  $\langle V \rangle$ , apparent mean cross sectional area  $\langle A \rangle$ , and apparent mean length  $\langle L \rangle$  of the pores inside the voxel as follow:

$$RTOP = \frac{1}{\langle V \rangle} \quad (11)$$

$$RTAP = \frac{1}{\langle A \rangle} \quad (12)$$

$$RTPP = \frac{1}{\langle L \rangle} \quad (13)$$

Several attempts have been made in order to estimate the axon diameter using the relationship between RTAP and  $\langle A \rangle$  (Fick et al., 2015b; 2015a). Results shows that when diffusion is restricted within cylindrical pores,  $\Delta \gg \delta$ , and  $\delta \approx 0$ , it is actually possible to retrieve the cylinder diameter in simulated data. Unfortunately, it is impossible to acquire data satisfying such a constraint *in-vivo* with the current MRI technology, at the  $b$ -values that are required to detect the signal decay in cylinders with small diameter. Moreover the brain tissue is not composed purely by coherently oriented axons, and the diffusion signal is influenced also by extracellular water and dispersion in the axons direction which both contribute to the RTAP and, therefore, the axon diameter estimation.

The RTOP, RTAP and RTPP expressions resulting from the 3D-SHORE model after replacing Eq. 8 in Eq. 10 are as follows:

$$RTOP = \sum_{n=0}^{N_{\max}/2} c_{n00} (-1)^n \left[ \frac{4\pi^2 \zeta^{3/2} (n)!}{\Gamma(n+3/2)} \right]^{1/2} L_n^{1/2}(0) \quad (14)$$

$$\begin{aligned} RTAP &= \sum_{l=0, \text{even}}^{N_{\max}} \sum_{n=l}^{(N_{\max}+1)/2} \sum_{m=-l}^l c_{nlm} \left[ \frac{\zeta^{1/2} 2^{l+3} \pi^2 \Gamma(l/2+1)^2 \Gamma(n+3/2)}{(n-l)! \Gamma(l+3/2)^2} \right]^{1/2} \times \\ &\quad \times {}_2F_1(l-n, l/2+1, l+3/2, 2) P_l(0) Y_l^m(\tilde{u}_{\parallel}) \end{aligned} \quad (15)$$

$$\begin{aligned} RTPP &= \sum_{l=0, \text{even}}^{N_{\max}} \sum_{n=l}^{(N_{\max}+1)/2} \sum_{m=-l}^l c_{nlm} \left[ \frac{\Gamma(l/2+1/2)^2 \Gamma(n+3/2) 2^l}{\zeta^{1/2} (n-l)! \Gamma(l+3/2)^2} \right]^{1/2} \\ &\quad \times {}_2F_1(l-n, l/2+1/2, l+3/2, 2) Y_l^m(\tilde{u}_{\parallel}) \end{aligned} \quad (16)$$

where  $P_l(0)$  is the  $l$ -degree Legendre polynomial at zero and  $\tilde{u}_{\parallel}$  the main diffusion direction as detected by the initial diffusion

tensor estimation. The derivation of the indices is illustrated in Appendix B.

Another possibility for calculating  $\bar{u}_{\parallel}$  is to consider the maximal peak of the ODF as the principal direction. While these methods perform equally well in case of single diffusion direction, they lead to different results in case of crossings. In particular, in crossings of two fibers with an angle less than 90 degrees, the tensor principal direction will be likely placed midway, leading to an underestimation of the ground truth RTAP and RTPP, while the ODF peaks will be aligned with the two fibers, respectively. Although using the ODF we could calculate two different indices, one for each peak, these will not be the same as the ground truth RTAP and RTPP of the two fibers, because the integrals cannot separate the mixed contribution of the two compartments. A complete characterization of this phenomenon is beyond the scope of this paper. In this work we choose to use the diffusion tensor to detect the principal direction, following the same approach as in Ozarslan et al. (2013), where the RTAP and RTPP were initially introduced for MAPMRI.

## 2.2. NODDI biomarkers

In the NODDI model the diffusion signal  $E$  is represented as the sum of the contributions from the intracellular ( $E_{ic}$ ), the extracellular ( $E_{ec}$ ) and the isotropic ( $E_{iso}$ ) compartments (Zhang et al., 2012). Accordingly, the full normalized signal can be written as

$$E = (1 - v_{iso}) (v_{ic}^0 E_{ic} + (1 - v_{ic}^0) E_{ec}) + v_{iso} E_{iso} \quad (17)$$

where  $v_{ic}^0$  and  $v_{iso}$  are respectively the initial estimates of the intracellular and the isotropic volume fractions, respectively. The extracellular volume fraction is then obtained as  $(1 - v_{ic}^0)$ . The model does not guarantee that the three volume fractions sum up to one and this happens to generate an odd behavior of the indices that require a post-processing for use. In particular, fitting in voxels where isotropic diffusion dominates, corresponding to high  $v_{iso}$ , results in the divergence of the unconstrained  $v_{ic}^0$  that takes values that are clearly out of range. In order to overcome this limitation, the intracellular volume fraction has to be corrected *a-posteriori* as follows

$$v_{ic} = v_{ic}^0 (1 - v_{iso}) \quad (18)$$

This normalization is derived from Eq. 17 where the estimated  $v_{ic}^0$  is multiplied by  $(1 - v_{iso})$ . The model also provides an additional parameter that accounts for the orientation dispersion of the fibers within the voxels. Jointly with  $v_{ic}$ , this allows disambiguating regions of pseudo-isotropic diffusion, as gray matter (GM), from crossing fibers, where high  $v_{ic}$  corresponds to high dispersion indices. This is a clear advantage over classical DTI indices like FA that takes low values in both cases. Orientation dispersion is modelled using a Watson distribution (Zhang et al., 2011) of sticks representing WM fibers

$$f(\mathbf{u}) = M \left( \frac{1}{2}, \frac{3}{2}, \kappa \right)^{-1} \exp^{\kappa(\boldsymbol{\mu} \cdot \mathbf{u})^2} \quad (19)$$

where  $\boldsymbol{\mu}$  is the principal direction of the sticks population,  $M$  is the confluent hypergeometric function and  $\kappa$  is a concentration parameter measuring the extent of the orientation dispersion around  $\boldsymbol{\mu}$ . From  $\kappa$ , the Orientation Dispersion Index  $ODI$  (Zhang et al., 2012) is calculated as

$$ODI = \frac{2}{\pi} \arctan \left( \frac{1}{\kappa} \right) \quad (20)$$

ODI is lower in voxels with highly coherent stick orientations (single fiber white matter areas, like the corpus callosum) and larger where a principal orientation direction cannot be identified (crossing, kissing, GM, CSF).

## 2.3. Datasets

### 2.3.1. Simulated data

We simulate the diffusion signal in the three compartments model proposed in Zhang et al. (2011), in which the total signal  $E(\mathbf{q})$  can be calculated as

$$E(\mathbf{q}) = v_{ic} E_{ic}(\mathbf{q}) + v_{ec} E_{ec}(\mathbf{q}) + v_{iso} E_{iso}(\mathbf{q}) \quad (21)$$

with  $v_{ic} + v_{ec} + v_{iso} = 1$ . The intracellular signal results from a set of impermeable cylinders, in which the main cylinders axis are dispersed around a global direction  $\boldsymbol{\mu}$ , following the Kent distribution on the sphere [19].

In order to model the diffusivity inside each cylinder, taking into account also the diffusion time, we use the Multiple Correlation Function (MCF) approach proposed in Özarslan et al. (2009) after adapting it for single pulse spin echo. Within the MCF framework it is possible to simulate the diffusion in the plane perpendicular to the main cylinder axis  $E_{ic}(\mathbf{q}_{\perp})$  as a function of the cylinder diameter, the pulse separation time  $\Delta$ , the pulse duration  $\delta$ , the gradient strength  $G$  and the bulk diffusivity coefficient  $D_0$ . The diffusion along the cylinder main axis  $E_{ic}(\bar{q}_{\parallel})$  is assumed to be Gaussian with diffusion  $D_0$ . The total intracellular signal can then be obtained by the product of the two contributions as  $E_{ic}(\mathbf{q}) = E_{ic}(\mathbf{q}_{\perp}) E_{ic}(\bar{q}_{\parallel})$ .

The Kent distribution represents the analogous of the 2D multivariate Gaussian function on the sphere. The probability density function  $\rho$  given an unit vector  $\mathbf{u}$  is defined as

$$\rho(\mathbf{u} | \beta, \kappa, \boldsymbol{\mu}) = \frac{1}{c(\kappa, \beta)} \exp\{\kappa \boldsymbol{\mu} \cdot \mathbf{u} + \beta[(\boldsymbol{\gamma}_1 \cdot \mathbf{u})^2 - (\boldsymbol{\gamma}_2 \cdot \mathbf{u})^2]\} \quad (22)$$

where  $\boldsymbol{\gamma}_1, \boldsymbol{\gamma}_2$  are the two orthogonal directions of elliptical dispersion centered in  $\boldsymbol{\mu}$  and

$$c(\kappa, \beta) = 2\pi \sum_{j=0}^{\infty} \frac{\Gamma(j + \frac{1}{2})}{\Gamma(j + 1)} \beta^{2j} \left( \frac{1}{2} \kappa \right)^{-2j - \frac{1}{2}} I_{2j + \frac{1}{2}}(\kappa) \quad (23)$$

with  $I_j(\kappa)$  the modified Bessel function. The parameter  $\kappa$  controls the concentration of the orientation and corresponds to the standard deviation of the Gaussian function, and the parameter  $\beta$  controls the ellipticity (Koay et al., 2008) of the directions ( $\beta = 0$  isotropic dispersion around  $\boldsymbol{\mu}$ ). As in Zhang et al. (2012) it is possible to derive the ODI from  $\kappa$  using Eq. 20.

In order to simulate the orientation dispersion we sample a certain number of directions  $N_{dir}$  from the Kent distribution such that the global intracellular signal can be calculated as

$$E_{ic}(q | \boldsymbol{\mu}) = \frac{1}{N_{dir}} \sum_{j=0}^{N_{dir}} E_{ic}(q | \mathbf{u}_j) \quad (24)$$

where  $\mathbf{u}_j$  identifies the direction sampled from the Kent distribution centered on  $\boldsymbol{\mu}$ .

The extracellular signal is simulated as proposed by Zhang et al. (2011), as a Gaussian function:

$$E_{ec}(\mathbf{q}) = \exp(-4\pi^2(\Delta - \delta/3)\mathbf{q}^T D_{ec}(v_{ec}, \boldsymbol{\mu})\mathbf{q}) \quad (25)$$

with the axially symmetric tensor  $D_{ec}$  calculated using the following tortuosity model:

$$D_{ec}(v_{ec}, \boldsymbol{\mu}) = \frac{1}{N_{dir}} \sum_{j=0}^{N_{dir}} (D_0 - d_{\perp}) \mathbf{u}_j^T \mathbf{u}_j + d_{\perp} \mathbf{I} \quad (26)$$

where  $d_{\perp} = D_0 v_{ec}$ , and  $\mathbf{I}$  is the  $3 \times 3$  identity matrix.

The isotropic term  $v_{iso}$  is designed to model the cerebrospinal fluid and is represented as an isotropic Gaussian function:

$$E_{iso}(\mathbf{q}) = \exp(-4\pi^2(\Delta - \delta/3)3e^{-03} \|\mathbf{q}\|^2) \quad (27)$$

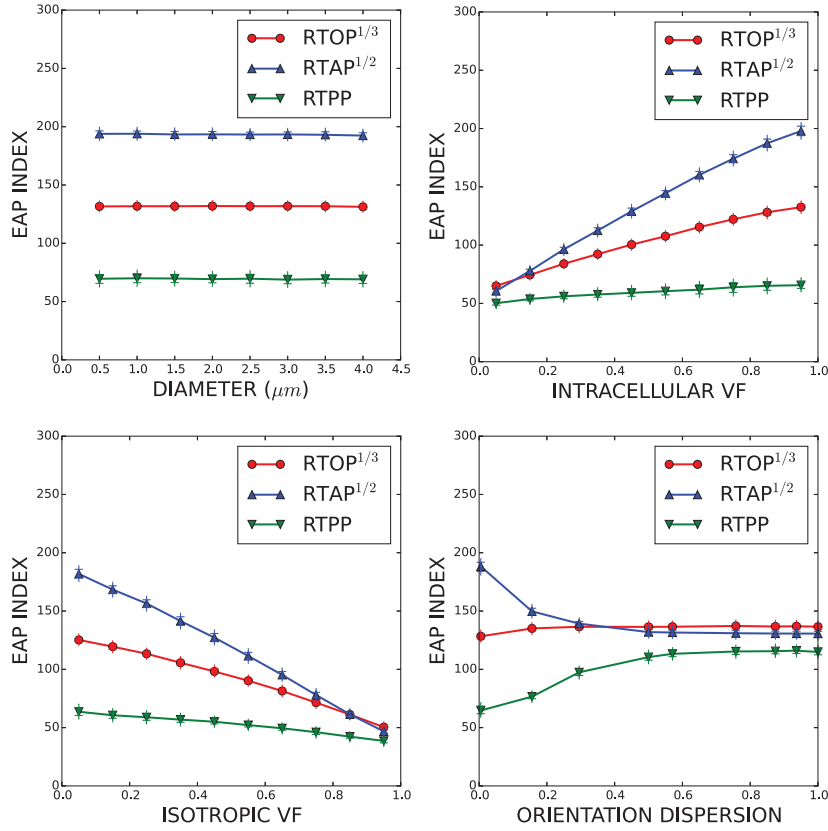


**Fig. 1.** Variation of RTOP, RTAP, and RTPP with respect to microstructural parameters: *top left* cylinders diameter, *top right* intracellular volume fraction, *bottom left* isotropic volume fraction, *bottom right* orientation dispersion. Bold symbols (triangles and circle) represent the median of the indices, while the crosses represent the interquartile range.

with  $3 \cdot 10^{-03} \text{mm}^2/\text{s}$  the water diffusivity coefficient at 37 Celsius degrees.

In order to disambiguate the effect of the compartments on the EAP derived indices, a single simulation with predefined parameters (reference simulation) was fixed and only one parameter at a time was changed. The reference simulation parameters were:  $v_{ic} = 0.85$ , cylinder diameter  $1 \mu\text{m}$ ,  $\kappa = 128$ ,  $v_{ec} = 0.15$ ,  $D_0 = 1.7 \cdot 10^{-3} \text{mm}^2/\text{s}$ , and  $v_{iso} = 0$ . Intracellular volume fraction was changed between  $v_{ic} = 0.05$  and  $v_{ic} = 0.95$  (step=0.05), keeping  $v_{iso} = 0$ . Cylinder diameter was varied from  $0.5 \mu\text{m}$  to  $4 \mu\text{m}$  (step=0.5  $\mu\text{m}$ ). The isotropic volume fraction was changed between  $v_{iso} = 0.05$  and  $v_{iso} = 0.95$  (step=0.05), while keeping  $v_{ic} = 0.85 \cdot v_{iso}$ , and  $v_{ec} = 0.15 \cdot v_{iso}$ . The concentration parameter ranged from 128, corresponding to very high concentration, to zero, corresponding to completely dispersed cylinders:  $\kappa = [128, 4, 2, 1, 0.8, 0.4, 0.2, 0.1, 0]$ .

All simulations were performed changing the main orientation  $\mu$  in 11 different directions and for each orientation and combination of parameters 30 instances of Rician noise with signal to noise ratio  $\text{SNR} = 20$  were used, for a total of 330 voxels for each parameter set. The number of samples of the Kent distribution was set to 30 for all the simulations with  $\kappa = 128$ , while  $N_{dir} = 1000$  was used for the simulation with the varying  $\kappa$ . For these simulations, we used the DSI sampling scheme,  $\Delta$ , and  $\delta$  used for the *in-vivo* data.

### 2.3.2. Data acquisition and processing

One healthy subject and one stroke patient underwent a DSI acquisition using the following protocol: TR/TE= 6000/136 ms, FoV=  $212 \times 212 \text{mm}^2$ , 34 slices,  $2.2 \times 2.2 \times 3 \text{mm}^3$  resolution, 257 diffusion directions, b-max=8000  $\text{s}/\text{mm}^2$ ,  $\Delta = 32.2 \text{ms}$ ,  $\delta = 27.7 \text{ms}$ ,

scan time: 25.8 min. A 3T (Magnetom Trio a Tim System, Siemens, Erlangen, Germany) using a 32-channels head matrix coil was used for the acquisitions reported in Granziera and et al. (2012). For the healthy subject, the DSI acquisition was repeated after one month. In this work we will refer to the first acquisition as time point one (TP1) and the second acquisition as time point two (TP2).

High-resolution MPRAGE images (TR/TE = 2300/3 ms, voxel =  $1 \times 1 \times 1.2 \text{mm}^3$ , FoV =  $256 \times 240 \text{mm}^2$ , scan time: 6.13 min) and T2 weighted images (TR/TE = 3000/84 ms, voxel =  $0.5 \times 0.5 \times 3 \text{mm}^3$ , scan time: 2.4 min) were acquired for anatomico-pathological reference. Total scan time was 34 min. Both subjects provided informed consent before the acquisition and the Lausanne University Hospital review board approved the study protocol. Segmentation of high-resolution MPRAGE images into the grey matter and white matter was performed using Freesurfer (<http://freesurfer.net/>). The masks were manually corrected to ensure a correct representation of the tissues. WM and GM masks were used for extracting the microstructural indices in the corresponding tissues for the healthy subject.

### 2.4. Data analysis

3D-SHORE indices were analyzed with respect to microstructural changes on both synthetic and *in-vivo* data. While in synthetic data the ground truth microstructure is known, the lack of a ground truth impedes the direct assessment of the 3D-SHORE-based indices *in-vivo*. Accordingly, a shortcut was followed, consisting in comparing the results with NODDI microstructural indices. Although NODDI compartments are not guaranteed to correspond to the real underlying tissues microstructure it is a well established model which could give an insight of the tissues composition. The

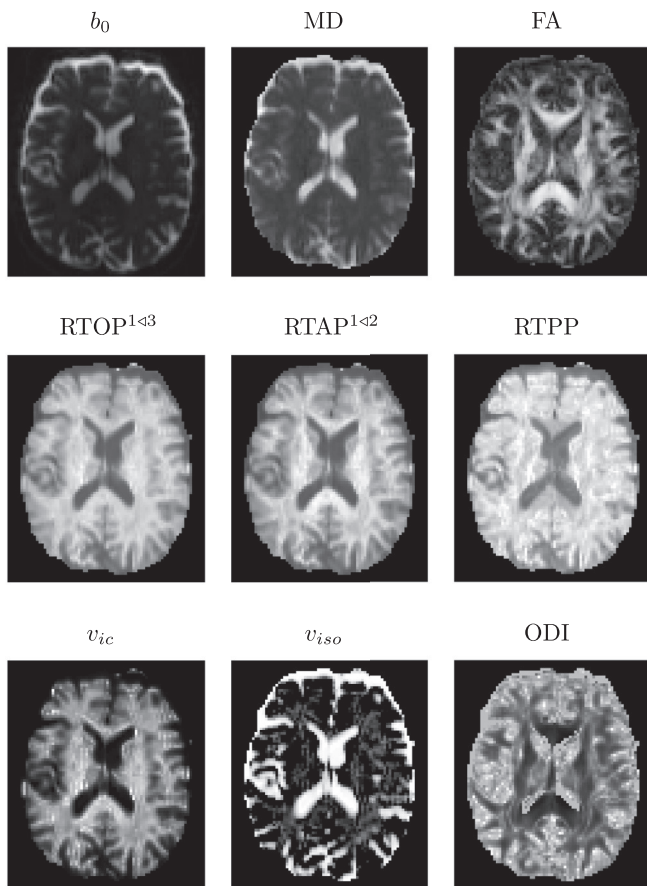


**Fig. 2.** Results of the indices for one healthy subject. First row: signal at  $b$ -value =  $0\text{s/mm}^2$ , fractional anisotropy (FA), mean diffusivity (MD); Second row: scalar 3D-SHORE indices RTOP, RTAP, and RTPP; Third row NODDI indices intracellular volume fraction  $v_{ic}$ , isotropic volume fraction  $v_{iso}$ , orientation dispersion index (ODI).

precision of the indices was assessed through a test-retest procedure. The control subject went through two successive scans one month apart and the distributions of the indices at the two time-points were extracted and compared. The results on simulated data were used for guiding the interpretation of the measurements performed *in-vivo*, based on the assumption that the trends observed on synthetic data in voxels simulating WM and GM provide an indication of the plausibility of results on the DSI data. A maximal radial order of  $N_{max} = 8$  was used for 3D-SHORE leading to 95 coefficients. This parameter was obtained evaluating the NMSE of simulated voxels using different radial orders, with  $SNR = 20$ , with respect to the ground truth. The RTOP, RTAP, and RTPP were calculated as described in Section 2. All the computations for 3D-SHORE were performed using the Dipy software library 3D-SHORE implementation (<http://dipy.org>). NODDI was fitted using the standard parameters using Matlab (The Mathworks) NODDI toolbox (<http://mig.cs.ucl.ac.uk/index.php?n=Tutorial.NODDIatlab>). As mentioned before,  $v_{ic}$  was subsequently modulated as in Eq. 18.

### 3. Results and discussion

#### 3.1. Simulated data

Fig. 1 summarizes the values of RTOP, RTAP, and RTPP while changing the microstructural parameters as explained in Section 2.3.1. In order to keep the same units ( $1/\text{mm}$ ) for all the indices the cube root of RTOP and the square root of RTAP were calculated as in Ozarslan et al. (2013). Although the EAP indices RTOP and RTAP at long diffusion time are respectively sensitive

to the pore volume and cross sectional area, changing the cylinders diameter (Fig. 1, top left) does not have any effect on the 3D-SHORE derived indices when the DSI acquisition scheme is used. This could be due to the fact that the signal component perpendicular to the main diffusion direction  $E_{ic}(\mathbf{q}_{\perp})$  for the range of considered diameters [ $0.5\text{--}4.0\ \mu\text{m}$ ] is close to one and features a very low decay, even at  $b$ -value  $8000\ \text{s/mm}^2$ . This results shed new light on previous studies that used RTAP as an estimator of the apparent mean axon diameter *in-vivo* (Fick et al., 2015a; Brusini et al., 2015). Since RTAP is calculated as the integral of the signal in the perpendicular plane with respect to the main diffusion direction, RTAP values remain substantially constant in the diameter-changing simulation. This particular diameter range was chosen according on the recent results reported for human WM and based on histology (Liewald et al., 2014).

In simulated data the 3D-SHORE derived indices decrease with the decreasing of the intracellular volume fraction. This was observed both when the extracellular volume fraction was increased (Fig. 1, top right), and when the isotropic volume fraction was increased (Fig. 1, bottom left). Although the diffusivity coefficient is different for 100% isotropic compartment voxel and 100% extracellular compartment voxel, all the indices take similar values in both cases. This is most probably due to errors in the fitting caused by the fast signal decay of CSF-like isotropic signal as well as to the presence of noise. 3D-SHORE with radial order set to 8 was preferred for its ability to model highly anisotropic voxels (pure white matter), as in the reference simulation. In case of voxels with either low intracellular volume fraction, or high isotropic volume fraction a lower radial order should be preferred, in particular at low SNR.

Fig. 1 (bottom right) shows the variation of 3D-SHORE indices while varying the orientation dispersion. While RTOP is insensitive to ODI variations, RTAP and RTPP show a complementary trend, that is RTAP decreases and RTPP increases at increasing ODI. This allows disambiguating the effect of intracellular volume fraction and ODI on RTAP variations being the changes of RTPP of the same sign as RTAP for decreasing intracellular VF (RTPP decreases as well) and of opposite sign for increasing ODI (RTPP increases). This is important because it allows disambiguating whether an observed change in tissue RTAP is most probably due to an increase of dispersion of WM fiber directionality or to partial volume effects (i.e., decrease in the WM volume fraction). This moves a step forward in the interpretation of the link between 3D-SHORE-based indices and the microstructural properties as recorded *in-vivo*, providing further evidence of their suitability as numerical biomarkers. With an orientation dispersion above 0.5 all the EAP indices reach a plateau. This can be explained by the fact that with such a dispersed distribution the cylinders orientation already covered almost the entire hemisphere of possible directions. Further increasing the dispersion of the cylinders does not change significantly the range of directions in the simulations, thus the values of the indices do not change further. RTOP geometrical meaning directly correlates with the volume of the pore  $\langle V \rangle$  in  $\Delta \gg \delta$  and  $\delta \approx 0$  conditions. Since the volume can be viewed as the product of the cross sectional area times the length of the pore we can expect that the RTOP value strongly depends of RTAP and RTPP values. This holds true also in our simulations, even if  $\Delta$  and  $\delta$  do not satisfy the long diffusion time and narrow pulse assumptions. For example when RTAP decreases and RTPP increases, RTOP value remains approximately constant (see Fig. 1, bottom left).

#### 3.2. DSI data

*In-vivo* tissue microstructure characterization is not possible without histology. However, compartmental models provide an estimation of the microstructural parameters in living tissues. In

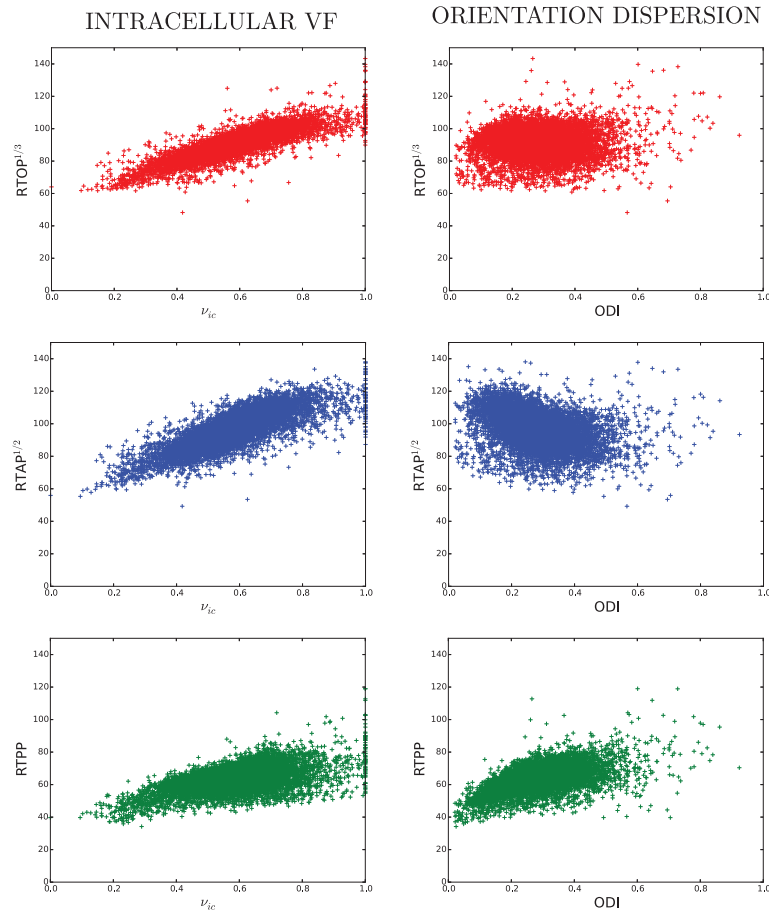


**Fig. 3.** Scatterplots of NODDI  $v_{ic}$  (left) and ODI (right) versus 3D-SHORE RTOP (top), RTAP (middle), and RTPP (bottom) obtained from a subsample of the WM voxels.

our simulation we observed that EAP indices are sensitive to intracellular volume fraction ( $v_{ic}$ ), isotropic volume fraction ( $v_{iso}$ ), and orientation dispersion variations. We compared RTOP, RTAP, and RTPP with NODDI estimated compartmental parameters as a pseudo ground truth for the DSI data, using the simulation results as a benchmark. Fig. 2 shows (i) the  $b_0$  image and the traditional DTI-derived indices, MD and FA as reference (first row); (ii) the 3D-SHORE derived RTOP, RTAP, RTPP (second row); (iii) the NODDI  $v_{ic}$ ,  $v_{iso}$ , and ODI (third row).

In agreement with the results described in Ozarslan et al. (2013), for the formalin fixed marmoset brain, RTPP shows low contrast between GM and WM, since the diffusion is not restricted along the main diffusion direction, while it presents higher values in crossing regions. RTAP values are higher in regions of highly coherent WM, like the corpus callosum (CC), and presents higher contrast than RTPP at the WM-GM boundary. Coherently with what observed on simulated data, in presence of fiber crossings the RTAP is lower than in regions where only one fiber bundle is present (low orientation dispersion). RTOP contrast is very similar to RTAP, but presents lower contrast between crossing and single fibers regions with respect to the RTAP. These results are in agreement with the simulation results in Fig. 1.

With regards to NODDI maps, the resulting indices for our data are coherent with the results presented in Zhang et al. (2012):  $v_{ic}$  is higher for white matter voxels (high FA),  $v_{iso}$  is equal to one in CSF regions (high MD), and ODI presents an opposite contrast with respect to FA.

Fig. 3 shows NODDI  $v_{ic}$  and ODI versus RTOP, RTAP, and RTPP in WM. In this case we omitted  $v_{iso}$  because its values were extremely low ( $< 0.1$ ) and non-informative. As in the simulations, a

**Table 1**

Spearman correlation coefficients  $\rho$  for WM and GM between EAP indices and NODDI microstructural indices for the healthy subject. The maximum p-value among all the results presented in the table is  $1 \cdot 10^{-20}$ .

	WM	GM
$v_{ic}$ vs RTOP	0.87	0.82
$v_{ic}$ vs RTAP	0.82	0.82
$v_{ic}$ vs RTPP	0.48	0.79
$v_{iso}$ vs RTOP	0.06	-0.24
$v_{iso}$ vs RTAP	0.06	-0.27
$v_{iso}$ vs RTPP	-0.14	-0.45
ODI vs RTOP	-0.05	-0.22
ODI vs RTAP	-0.43	-0.34
ODI vs RTPP	0.55	0.09

positive correlation can be observed between NODDI  $v_{ic}$  and RTOP, RTAP, and RTPP, as well as between NODDI ODI and RTPP, while a negative correlation links NODDI ODI and RTAP.

In order to quantify these relationships we calculated the Spearman correlation coefficient ( $\rho$ ) for all the indices in WM and GM. Results are summarized in Table 1. Spearman  $\rho$  assesses if between two variables there is a monotonic relationship. We considered this index to be more appropriate to our case with respect to others (e.g., Pearson's  $r$ ) because the relation between the EAP indices and the ODI was non-linear in our simulations. Results revealed high correlation of  $v_{ic}$  with both RTOP and RTAP ( $\rho > 0.8$

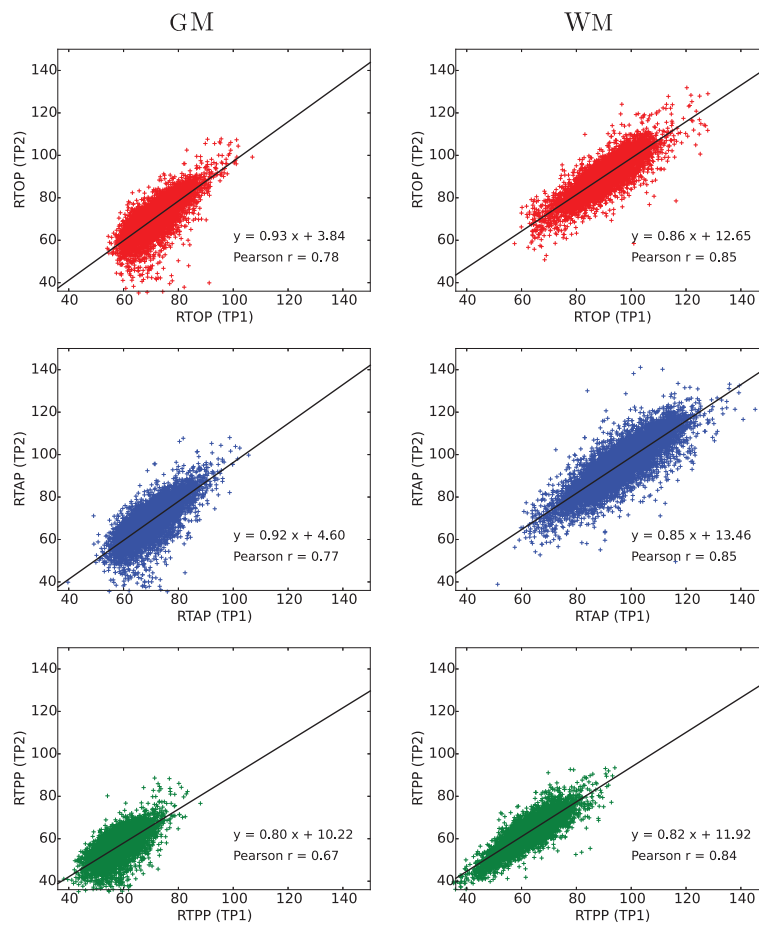


**Fig. 4.** Test-retest plots for the EAP indices RTOP (top), RTAP (center), and RTPP (bottom) for GM (left column) and WM (right column). The interpolating line is shown in black and its equation is reported jointly with the Pearson correlation coefficients,  $r$  ( $p$ -values  $< 0.05$ ). (For interpretation of the references to colour in this figure legend, the reader is referred to the web version of this article.)

) and a weaker correlation with RTPP ( $\rho \sim 0.5$ ) in WM. In GM all the correlation coefficients are slightly lower with the exception of RTPP. The correlation coefficient is very low between  $v_{iso}$  and 3D-SHORE indices in white matter ( $\rho < 0.2$ ) and presents weak negative values for GM ( $|\rho| < 0.5$ ).

As it was the case in simulations, the correlation coefficient between ODI and RTOP is close to zero. On the contrary, the correlation coefficient between ODI and RTAP is negative ( $\rho = -0.43$ ) while it is positive between ODI and RTPP ( $\rho = 0.55$ ) for WM in agreement with the trend highlighted in Fig. 1. In GM all the ODI  $\rho$  values are very low ( $|\rho| < 0.35$ ). All the  $p$ -values for both WM and GM are close to zero, with a maximum  $p$ -value of  $1 \cdot 10^{-20}$ , thus all the indices are significantly correlated. Although NODDI was extensively validated (Zhang et al., 2012), it does not represent the real ground truth for our data. In particular, NODDI  $v_{ic}$  is correlated with ODI *in-vivo* (Zhang et al., 2012), and while this can be actually true in WM, it makes difficult the disambiguation of tissue microstructural changes. Of particular interest is the case crossing areas, where  $v_{ic}$  decreases and ODI increases. The increase of RTPP jointly with the reduction of RTAP suggest that only the orientation dispersion increases in crossing area, while intracellular volume fraction remains constant. This provides a more anatomically plausible characterization of the microstructure and provides information that goes beyond what can be inferred from the NODDI model.

EAP indices stability was measured via a test-retest procedure. The corresponding plots are provided in Fig. 4 for WM and GM. Pearson correlation coefficients  $r$  between the two time points (TP1

and TP2) for all the indices are above 0.8 in WM, and above 0.65 in GM. The lower values observed in GM could be due to the prominence of partial volume effects.

In order to assess the sensitivity of the considered indices in detecting microstructural properties, probability density functions as approximated by the histograms were extracted and compared in GM and WM in two time points, as illustrated in Fig. 5. In the figure, the red-magenta line represents GM and the blue-cyan line the WM. The 3D-SHORE-derived indices allow to clearly distinguish between WM and GM (in particular RTOP and RTAP), as it is also the case for  $v_{ic}$  and ODI;  $v_{iso}$  tends to shrink to values at the extremes of the available range being close to zero in the majority of the WM and GM voxels. The histograms for all the indices at the two time points present comparable distributions, which provides some evidence of the reliability for the indices as biomarker candidates for *in-vivo* data. A comprehensive analysis in this respect can be found in Brusini et al. (2015).

Preliminary results on stroke data revealed that the 3D-SHORE-based indices hold potential for characterizing pathology-induced microstructural changes. As an illustration Fig. 6 shows the corresponding maps for one patient affected by stroke, that was acquired one week after the onset of the pathology using the acquisition protocol described in Section 2.3.2. The stroke lesion appears hyperintense in  $b_0$ , while MD and FA show reduced contrast. All the EAP indices appear brighter, which supports the hypothesis of an augmented restriction of diffusion in the lesion area. This is also confirmed by NODDI  $v_{ic}$  which saturates in the majority of the voxels in the lesion. ODI values are higher than in the contralateral

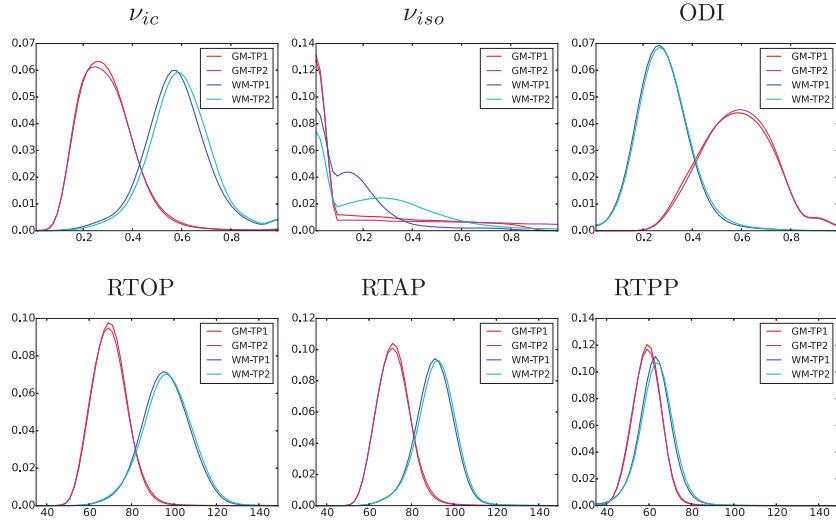


**Fig. 5.** Normalized histograms of NODDI indices ( $v_{ic}$ ,  $v_{iso}$ , ODI) and 3D-SHORE indices (RTOP, RTAP, RTPP) in GM (red-magenta) and WM (blue-cyan) for one healthy subject acquired at two different time points. (For interpretation of the references to colour in this figure legend, the reader is referred to the web version of this article.)

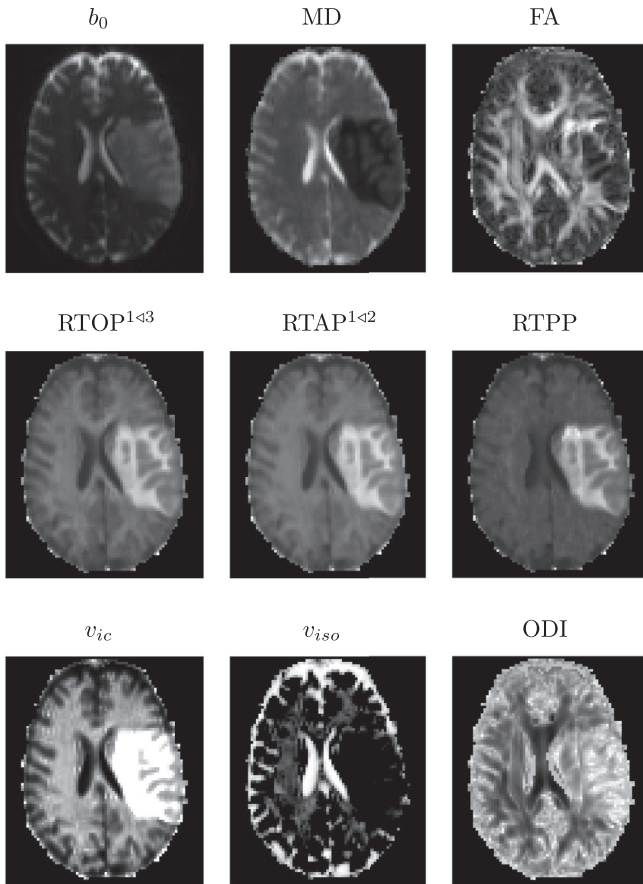


**Fig. 6.** Results of the indices for one ischemic stroke patient. First row: signal at b-value = 0 s/mm<sup>2</sup>. FA, MD; Second row: scalar 3D-SHORE indices RTOP, RTAP and RTPP; Third row NODDI indices.

part, which is in agreement with the FA reduction. White matter areas inside the lesion are still partially visible in FA, RTOP, RTAP, and RTPP. On the contrary, the contrast between GM and WM in the lesion is reduced in all the NODDI indices.

#### 4. Conclusions

In this paper we illustrate the effect that tissue microstructural variations have on 3D-SHORE-derived EAP indices: RTOP, RTAP, and RTPP. Although RTOP and RTAP are correlated with pore shape descriptors under long diffusion time and narrow pulse assumptions, we were not able to see any variation in these indices while changing the cylinder diameter. Instead, we found that EAP indices values variations are related to changes in the intracellular volume fraction and orientation dispersion of the axons. These results were confirmed *in-vivo* by comparing the 3D-SHORE indices with NODDI derived microstructural parameters. Results on stroke patient suggest the suitability of the EAP indices for characterizing pathologically-induced microstructural changes in brain tissues.

In this work, we focused on 3D-SHORE derived indices. The comparison with other EAP models including MAPMRI and also DTI was out of the scope of the paper and is currently under investigation. Future work will also include the study of the effects of different models of orientation dispersion and fiber crossings on the EAP indices, as well as the use of the indices for tissue classification.

#### Appendix A. Ordering of the 3D-SHORE bases

The signal reconstruction equation for Ozarslan et al. (2013), basis  $\Phi^O$  is:

$$S(\mathbf{q}) = \sum_{N=0}^{N_{\max}^O} \sum_{(j,l)} \sum_{m=-l}^l c_{jlm} \Phi^O(\mathbf{q}) \quad (\text{A.1})$$

Where  $j \geq 1$ ,  $l \geq 0$  with the constrain  $2j + l = N + 2$ . In Merlet and Deriche (2013), 3D-SHORE basis  $\Phi^M$ , the terms of the summation used were different:

$$S(\mathbf{q}) = \sum_{n=0}^{N_{\max}^M} \sum_{l=0}^n \sum_{m=-l}^l c_{jlm} \Phi^M(\mathbf{q}) \quad (\text{A.2})$$

In this notation  $N_{\max}^O$  is equal to two times  $N_{\max}^M$ , used in Merlet and Deriche (2013). If the signal is symmetric, the odd terms for both  $N$  and  $l$  vanished with both bases. The two basis are equivalent, but the ordering of the basis functions are different. For example, considering  $N_{\max}^M = 2$  (corresponding to  $N_{\max}^O = 4$ ) for Merlet and Deriche (2013) 3D-SHORE basis the Laguerre polynomial term in the basis  $L_{n-l}^{l+0.5}$  consist of 4 elements:



$$\begin{aligned} n = 0 \rightarrow l = 0 &\Rightarrow L_0^{0.5} \\ n = 1 \rightarrow l = 0 &\Rightarrow L_1^{0.5} \\ n = 2 \rightarrow l = 0 &\Rightarrow L_2^{0.5} \\ n = 2 \rightarrow l = 2 &\Rightarrow L_0^{2.5} \end{aligned}$$

In Ozarslan et al. (2013), notation, the Laguerre polynomial are calculated as  $L_{j-1}^{l+0.5}$  and corresponds to 6 elements:

$$\begin{aligned} N = 0 \rightarrow (j = 1, l = 0) &\Rightarrow L_0^{0.5} \\ N = 2 \rightarrow (j = 2, l = 0) &\Rightarrow L_1^{0.5} \\ N = 2 \rightarrow (j = 1, l = 2) &\Rightarrow L_0^{2.5} \\ N = 4 \rightarrow (j = 3, l = 0) &\Rightarrow L_2^{0.5} \\ N = 4 \rightarrow (j = 2, l = 2) &\Rightarrow L_1^{2.5} \\ N = 4 \rightarrow (j = 1, l = 4) &\Rightarrow L_0^{4.5} \end{aligned}$$

which include two more terms with respect to Merlet and Deriche (2013) notation.

In this paper, in order to have the proper 3D-SHORE basis, the summation order for Merlet and Deriche (2013) basis  $\Phi^M$  has been corrected in

$$\sum_{l=0, \text{even}}^{N_{\max}} \sum_{n=l}^{(N_{\max}+l)/2} \sum_{m=-l}^l c_{nlm} \Phi^M(\mathbf{q}) \quad (\text{A.3})$$

With  $N_{\max}$  the same as Ozarslan et al. (2013). For  $N_{\max} = 4$  the Laguerre polynomials of the corrected 3D-SHORE basis are  $l = 0 \rightarrow n = 0 \Rightarrow L_0^{0.5}$

$$\begin{aligned} l = 0 \rightarrow n = 1 &\Rightarrow L_0^{1.5} \\ l = 0 \rightarrow n = 2 &\Rightarrow L_0^{2.5} \\ l = 2 \rightarrow n = 2 &\Rightarrow L_0^{2.5} \\ l = 2 \rightarrow n = 3 &\Rightarrow L_1^{2.5} \\ l = 4 \rightarrow n = 4 &\Rightarrow L_0^{4.5} \end{aligned}$$

which are exactly the same as the one calculated for  $\Phi^O$ .

## Appendix B. EAP indices derivation for 3D-SHORE

In this section we provide the analytic derivation of EAP indices for 3D-SHORE basis.

### B1. 3D-SHORE RTOP

By definition (Eq. 8) RTOP can be written as:

$$\text{RTOP} = \int_{\mathbb{R}^3} E(\mathbf{q}) d^3 \mathbf{q} = P(0) \quad (\text{B.1})$$

If we consider the EAP formula (Eq. 6), its value in zero can be calculated as:

$$P(\mathbf{0}\mathbf{u}) = \sum_{l=0, \text{even}}^{N_{\max}} \sum_{n=l}^{(N_{\max}+l)/2} \sum_{m=-l}^l c_{nlm} \Psi_{nlm}(\mathbf{0}\mathbf{u}) \quad (\text{B.2})$$

$$\begin{aligned} \Psi_{nlm}(\mathbf{0}\mathbf{u}) &= (-1)^{n-l/2} \left[ \frac{2(4\pi^2 \zeta)^{3/2} (n-l)!}{\Gamma(n+3/2)} \right]^{1/2} \\ &\times (0)^{l/2} \exp(0) L_{n-l}^{l+1/2}(0) Y_l^m(\mathbf{u}) \end{aligned} \quad (\text{B.3})$$

Analyzing the term  $(0)^{l/2} \exp(0) L_{n-l}^{l+1/2}(0)$  we note the radial function vanish every time when  $l \neq 0$  for  $r = 0$ . The global formula can thus be rewritten as:

$$P(\mathbf{0}\mathbf{u}) = \sum_{n=0}^{N_{\max}/2} c_{n00} \Psi_{n00}(\mathbf{0}\mathbf{u}) \quad (\text{B.4})$$

$$\Psi_{n00}(\mathbf{0}\mathbf{u}) = (-1)^n \left[ \frac{2(4\pi^2 \zeta)^{3/2} n!}{\Gamma(n+3/2)} \right]^{1/2} L_n^{1/2}(0) Y_0^0(\mathbf{u}) \quad (\text{B.5})$$

The spherical harmonic of order  $[l = 0, m = 0]$  is the constant harmonic and its value is equal to  $\frac{1}{\sqrt{4\pi}}$ .  $Y_0^0(\mathbf{u})$  can then be replaced

and the final formula become:

$$\begin{aligned} P(\mathbf{0}\mathbf{u}) &= \frac{1}{\sqrt{4\pi}} \sum_{n=0}^{N_{\max}/2} c_{n00} k_{n0} L_n^{1/2}(0) \\ &= \frac{1}{\sqrt{4\pi}} \sum_{n=0}^{N_{\max}/2} c_{n00} (-1)^n \left[ \frac{16\pi^3 \zeta^{3/2} (n)!}{\Gamma(n+3/2)} \right]^{1/2} L_n^{1/2}(0) \\ &= \sum_{n=0}^{N_{\max}/2} c_{n00} (-1)^n \left[ \frac{4\pi^2 \zeta^{3/2} (n)!}{\Gamma(n+3/2)} \right]^{1/2} L_n^{1/2}(0) \end{aligned} \quad (\text{B.6})$$

### B2. 3D-SHORE RTAP

By definition (Eq. 9) RTAP can be written as:

$$\begin{aligned} \text{RTAP} &= \int_{\mathbb{R}^2} E(\mathbf{q}_{\perp}) d^2 \mathbf{q}_{\perp} \\ &= \int_{\mathbb{R}^2} \sum_{l=0, \text{even}}^{N_{\max}} \sum_{n=l}^{(N_{\max}+l)/2} \sum_{m=-l}^l c_{nlm} \Phi(\mathbf{q}_{\perp}) d\mathbf{q}_{\perp} \\ &= \sum_{l=0, \text{even}}^{N_{\max}} \sum_{n=l}^{(N_{\max}+l)/2} \sum_{m=-l}^l c_{nlm} \int_{\mathbb{R}^2} \Phi_{nlm}(\mathbf{q}_{\perp}) d\mathbf{q}_{\perp} \end{aligned} \quad (\text{B.7})$$

We can subdivide 3D-SHORE basis  $\Phi$  (Eq. 5) in three parts: the constant term  $K_{nl}$ , the radial term  $R_{nl}(q)$ , and the angular term  $Y_l^m(\mathbf{u})$ . With

$$\begin{aligned} K_{nl} &= \left[ \frac{2(n-l)!}{\zeta^{3/2} \Gamma(n+3/2)} \right]^{1/2} \\ R_{nl}(q) &= \left( \frac{q^2}{\zeta} \right)^{l/2} \exp\left( \frac{-q^2}{2\zeta} \right) L_{n-l}^{l+1/2}\left( \frac{q^2}{\zeta} \right) \end{aligned} \quad (\text{B.8})$$

3D-SHORE basis after these substitutions become:

$$\Phi_{nlm}(\mathbf{q}\mathbf{u}) = K_{nl} R_{nl}(q) Y_l^m(\mathbf{u}) \quad (\text{B.9})$$

We can solve the angular part of the integral of the basis function using the Funk-Hecke Theorem (Descoteaux et al., 2007):

$$\begin{aligned} \int_{\mathbb{R}^2} \Phi_{nlm}(\mathbf{q}_{\perp}) d\mathbf{q}_{\perp} &= \int_{\mathbb{R}^2} K_{nl} R_{nl}(q) Y_l^m(\mathbf{u}_{\perp}) d\mathbf{q}_{\perp} \\ &= K_{nl} \int_0^{\infty} R_{nl}(q) q dq \int_{\mathbb{R}} Y_l^m(\mathbf{u}_{\perp}) d\mathbf{u}_{\perp} \\ &= K_{nl} \int_0^{\infty} R_{nl}(q) q dq \int_{|\mathbf{w}|=1} \delta(\vec{u}_{\parallel}^T \mathbf{w}) Y_l^m(\mathbf{w}) d\mathbf{w} \\ &= K_{nl} \int_0^{\infty} R_{nl}(q) q dq 2\pi P_l(0) Y_l^m(\vec{u}_{\parallel}) \end{aligned} \quad (\text{B.10})$$

With  $\vec{u}_{\parallel}$  the vector pointing in the direction perpendicular to the perpendicular plane  $\mathbf{u}_{\perp}$ . For what concern the radial integral it can be solve applying the following identity (Jeffrey, Zwillingier, 2007):

$$\begin{aligned} \int_0^{\infty} (t)^{\beta} \exp(-st) L_{\eta}^{\alpha}(t) dt \\ = \frac{\Gamma(\beta+1) \Gamma(\alpha+\eta+1)}{\eta! \Gamma(\alpha+1)} s^{-\beta-1} {}_2F_1(-\eta, \beta+1, \alpha+1, 1/s) \end{aligned} \quad (\text{B.11})$$

Using B.11 we obtain

$$\begin{aligned} \int_0^{\infty} R_{nl}(q) q dq &= \int_0^{\infty} \left( \frac{q^2}{\zeta} \right)^{l/2} \exp\left( \frac{-q^2}{2\zeta} \right) L_{n-l}^{l+1/2}\left( \frac{q^2}{\zeta} \right) q dq \\ &= \frac{\zeta}{2} \int_0^{\infty} \left( \frac{q^2}{\zeta} \right)^{l/2} \exp\left( \frac{-q^2}{2\zeta} \right) L_{n-l}^{l+1/2}\left( \frac{q^2}{\zeta} \right) \frac{2q}{\zeta} dq \end{aligned}$$

$$\begin{aligned}
&= \frac{\zeta}{2} \int_0^\infty (t)^{l/2} \exp(-t/2) L_{n-l}^{l+1/2}(t) dt \\
&= \frac{\zeta}{2} \frac{\Gamma(l/2+1/2)\Gamma(n+3/2)}{(n-l)!\Gamma(l+3/2)} 2^{l/2+1} {}_2F_1(l-n, l/2+1, \\
&\quad l+3/2, 2) \quad (B.12)
\end{aligned}$$

The final RTAP equation can then be calculated as

$$\begin{aligned}
RTAP &= \sum_{l=0, \text{ even}}^{N_{\max}} \sum_{n=l}^{(N_{\max}+l)/2} \sum_{m=-l}^l c_{nlm} K_{nl} \frac{\zeta}{2} \frac{\Gamma(l/2+1/2)\Gamma(n+3/2)}{(n-l)!\Gamma(l+3/2)} 2^{l/2+1} \\
&\quad \times {}_2F_1(l-n, l/2+1, l+3/2, 2) 2\pi P_l(0) Y_l^m(\bar{u}_{\parallel}) \\
&= \sum_{l=0, \text{ even}}^{N_{\max}} \sum_{n=l}^{(N_{\max}+l)/2} \sum_{m=-l}^l c_{nlm} \left[ \frac{\zeta^{1/2} 2^{l+3} \pi^2 \Gamma(l/2+1/2)^2 \Gamma(n+3/2)}{(n-l)!\Gamma(l+3/2)^2} \right]^{1/2} \\
&\quad \times {}_2F_1(l-n, l/2+1, l+3/2, 2) P_l(0) Y_l^m(\bar{u}_{\parallel}) \quad (B.13)
\end{aligned}$$

where

$$P_l(0) = (-1)^{l/2} \frac{1 \cdot 3 \cdot 5 \cdots (l-1)}{2 \cdot 4 \cdots (l)} \quad (B.14)$$

with  $l$  even.

### B3. 3D-SHORE RTPP

By definition (Eq. 10) RTPP can be written as:

$$\begin{aligned}
RTPP &= \int_{\mathbb{R}} E(\bar{q}_{\parallel}) d\bar{q}_{\parallel} \\
&= \int_{\mathbb{R}} \sum_{l=0, \text{ even}}^{N_{\max}} \sum_{n=l}^{(N_{\max}+l)/2} \sum_{m=-l}^l c_{nlm} \Phi(\bar{q}_{\parallel}) d\bar{q}_{\parallel} \\
&= \sum_{l=0, \text{ even}}^{N_{\max}} \sum_{n=l}^{(N_{\max}+l)/2} \sum_{m=-l}^l c_{nlm} \int_{\mathbb{R}} \Phi_{nlm}(\bar{q}_{\parallel}) d\bar{q}_{\parallel} \quad (B.15)
\end{aligned}$$

As in the case of RTAP the integral of the basis can be rewritten as

$$\begin{aligned}
\int_{\mathbb{R}} \Phi_{nlm}(\mathbf{q}_{\parallel}) d\mathbf{q}_{\parallel} &= \int_{\mathbb{R}} K_{nl} R_{nl}(q) Y_l^m(\bar{u}_{\parallel}) d\mathbf{q}_{\parallel} \\
&= K_{nl} \int_0^\infty R_{nl}(q) dq Y_l^m(\bar{u}_{\parallel}) \\
&= K_{nl} \int_0^\infty \left(\frac{q^2}{\zeta}\right)^{l/2} \exp\left(\frac{-q^2}{2\zeta}\right) L_{n-l}^{l+1/2}\left(\frac{q^2}{\zeta}\right) dq Y_l^m(\bar{u}_{\parallel}) \quad (B.16)
\end{aligned}$$

This integral can be solved applying Eq. B.11 and the RTPP can be written as:

$$\begin{aligned}
RTPP &= \sum_{l=0, \text{ even}}^{N_{\max}} \sum_{n=l}^{(N_{\max}+l)/2} \sum_{m=-l}^l c_{nlm} K_{nl} \frac{\zeta^{1/2}}{2} \frac{\Gamma(l/2+1/2)\Gamma(n+3/2)}{(n-l)!\Gamma(l+3/2)} 2^{l/2+1/2} \\
&\quad \times {}_2F_1(l-n, l/2+1/2, l+3/2, 2) Y_l^m(\bar{u}_{\parallel}) \\
&= \sum_{l=0, \text{ even}}^{N_{\max}} \sum_{n=l}^{(N_{\max}+l)/2} \sum_{m=-l}^l c_{nlm} \left[ \frac{\Gamma(l/2+1/2)^2 \Gamma(n+3/2) 2^l}{\zeta^{1/2} (n-l)!\Gamma(l+3/2)^2} \right]^{1/2} \\
&\quad \times {}_2F_1(l-n, l/2+1/2, l+3/2, 2) Y_l^m(\bar{u}_{\parallel}) \quad (B.17)
\end{aligned}$$

## Appendix C. Multiple correlation function for cylindrical pore

Multiple Correlation Function (MCF) is a powerful mathematical framework to calculate the analytic expression of the diffusion signal in predefined compartment shapes as cylinders and spheres

**Table C.2**

The first ten roots of the  $m$ th order Bessel function.

Position	$\alpha$	$m$	$k$
1th	0	0	0
2th	1.8411	1	0
3th	3.0542	2	0
4th	3.8317	0	1
5th	4.2011	3	0
6th	5.3175	4	0
7th	5.3314	1	1
8th	6.4156	5	0
9th	6.7061	2	1
10th	7.0155	0	2

(Grebekov, 2008; Özarslan et al., 2009). The main idea is to represent the temporal effects of the gradients as matrices exponentials. The elements of these matrices depends on the geometry of the pore.

The MCF for single PGF is based on the calculation of two matrices the square diagonal matrix  $\Lambda$  and the square matrix  $\mathbf{A}$ . These matrices are theoretically infinite and their values are ordered according to the roots of the zeros of the derivative of the  $m$ th order Bessel function,  $\alpha_{mk}$ :

$$J'_m(\alpha_{mk}) = 0 \quad (m = 0, 1, 2, 3, 4, \dots) \quad (C.1)$$

where  $k$  indicates the  $k$ th root of the  $m$ th order Bessel function, (including the zero). These are ordered in ascending order according to their values. In Table C.2 we present the first ten  $\alpha$  and the corresponding indices. The matrix  $\Lambda$  can be calculated using the Bessel roots as follows:

$$\Lambda_{km, k'm'} = \delta_{kk'} \delta_{mm'} \frac{\alpha_{km}^2 D_0}{r_0^2} \quad (C.2)$$

where  $D_0$  is the initial diffusivity,  $\delta_{xx'}$  is a function that is one if  $x = x'$  and zero otherwise, and  $r_0$  is the cylinder radius. In order to calculate the matrix  $\mathbf{A}$  first is useful to define  $B_{km}$  as

$$B_{km} = \begin{cases} 1 & \text{if } k = m = 0 \\ \frac{\alpha_{km}}{(\alpha_{km}^2 - m^2)^{1/2}} & \text{otherwise.} \end{cases} \quad (C.3)$$

From  $B_{km}$  it is possible to calculate the matrix  $\mathbf{A}$  as:

$$\begin{aligned}
\mathbf{A}_{km, k'm'} &= r_0 \delta_{m, m' \pm 1} (1 + \delta_{m,0} + \delta_{m',0})^{1/2} \\
&\quad \times B_{km} B_{k'm'} \frac{\alpha_{km}^2 + \alpha_{k'm'}^2 - 2 m m'}{(\alpha_{km}^2 - \alpha_{k'm'}^2)^2} \quad (C.4)
\end{aligned}$$

These matrices are designed to be infinite dimensional, so for practical reason they are truncated up to the 30th Bessel root. This number is empirically set to the point when your simulated signal does not change any more even if you double the number of  $\alpha$ .

The final step is to calculate the signal in the plane perpendicular to the cylinder main axis,  $E(q_{\perp})$ , as

$$E(q_{\perp}) = \langle 0 | e^{-\Lambda \delta + i 2\pi q \cdot \mathbf{A}^\dagger} e^{-\Lambda(\Delta - \delta)} e^{-\Lambda \delta - i 2\pi q \cdot \mathbf{A}^\dagger} | 0 \rangle \quad (C.5)$$


Where  $q = \frac{C\delta\gamma}{2\pi}$  is a point in the direction perpendicular to the cylinder axis,  $\langle 0 | \mathbf{M} | 0 \rangle$  is the so-called bra-ket notation and indicates the element [0,0] of the matrix  $\mathbf{M}$ .  $\Delta$ ,  $\delta$ , and  $\gamma$  are respectively the pulse separation time, the pulse duration time, and proton gyromagnetic ratio.

## References

- Alexander, D.C., Hubbard, P.L., Hall, M.G., Moore, E.A., Ptito, M., Parker, G.J., Dyrbj, T.B., 2010. Orientationally invariant indices of axon diameter and density from diffusion MRI. *NeuroImage* 52 (4), 1374–1389.

- Assaf, Y., Basser, P.J., 2005. Composite hindered and restricted model of diffusion (charmed) {MR} imaging of the human brain. *NeuroImage* 27 (1), 48–58. <http://dx.doi.org/10.1016/j.neuroimage.2005.03.042>.
- Assaf, Y., Freidlin, R.Z., Rohde, G.K., Basser, P.J., 2004. New modeling and experimental framework to characterize hindered and restricted water diffusion in brain white matter. *Magn. Reson. Med.* 52 (5), 965–978.
- Assemlal, H.-E., Tschumperl, D., Brun, L., 2009. Efficient and robust computation of {PDF} features on diffusion {MR} signal. *Med. Image Anal.* 13 (5), 715–729.
- Basser, P., Mattiello, J., LeBihan, D., 1994. Estimation of the effective self diffusion tensor from the NMR spin echo. *J. Magn. Reson.* 103, 247–254.
- Behrens, T.E.J., Woolrich, M.W., Jenkinson, M., Johansen-Berg, H., Nunes, R.G., Clare, S., Matthews, P.M., Brady, J.M., Smith, S.M., 2003. Characterization and propagation of uncertainty in diffusion-weighted MR imaging. *Magn. Reson. Med.* 50 (5), 1077–1088.
- Brusini, L., Obertino, S., Zucchelli, M., Galazzo, I., Krueger, G., Granziera, C., Menegaz, G., 2015. Assessment of mean apparent propagator-based indices as biomarkers of axonal remodeling after stroke. In: Navab, N., Hornegger, J., Wells, W., Frangi, A. (Eds.), *Medical Image Computing and Computer-Assisted Intervention MICCAI 2015*. In: *Lecture Notes in Computer Science*, 9349. Springer International Publishing, pp. 199–206. doi:10.1007/978-3-319-24553-9\_25.
- Cheng, J., Ghosh, A., Jiang, T., Deriche, R., 2010. Model-free and analytical EAP reconstruction via spherical polar Fourier diffusion MRI. In: *Medical Image Computing and Computer-Assisted Intervention—MICCAI*. Springer Berlin Heidelberg, pp. 590–597.
- Cheng, J., Jiang, T., Deriche, R., 2011. Theoretical Analysis and Practical Insights on EAP Estimation via a Unified HARDI Framework. In: *MICCAI Workshop on Computational Diffusion MRI (CDMRI)*.
- Descoteaux, M., Angelino, E., Fitzgibbons, S., Deriche, R., 2007. Regularized, fast, and robust analytical q-ball imaging. *Magn. Reson. Med.* 58 (3), 497–510. doi:10.1002/mrm.21277.
- Descoteaux, M., Deriche, R., Bihan, D.L., Mangin, J.-F., Poupon, C., 2011. Multiple q-shell diffusion propagator imaging. *Med. Image Anal.* 15 (4), 603–621. <http://dx.doi.org/10.1016/j.media.2010.07.001>. Special section on {IPMI} 2009.
- Fick, R.H., Wassermann, D., Sanguinetti, G., Deriche, R., 2015. Laplacian-Regularized MAP-MRI: Improving Axonal Caliber Estimation. *International Symposium on BIOMEDICAL IMAGING: From Nano to Macro*. Brooklyn, New York City, United States.
- Fick, R.H., Zucchelli, M., Girard, G., Descoteaux, M., Menegaz, G., Deriche, R., 2015. Using 3D-SHORE and MAP-MRI to Obtain Both Tractography and Microstructural Contrast from a Clinical DMRI Acquisition. In: *International Symposium on BIOMEDICAL IMAGING: From Nano to Macro*. Brooklyn, New York City, United States.
- Jeffrey, A., Zwillinger, D., 2007. *Table of Integrals, Series, and Products (Seventh Edition)*. Academic Press.
- Granziera, C., Daducci, A., Meskaldji, D.E., Roche, A., Maeder, P., Michel, P., Hadjikhani, N., Sorensen, A.G., Frackowiak, R.S., Thiran, J., et al., 2012. A new early and automated MRI-based predictor of motor improvement after stroke. *NeuroImage* 79 (1), 39–46.
- Grebenkov, D.S., 2008. Analytical solution for restricted diffusion in circular and spherical layers under inhomogeneous magnetic fields. *J. Chem. Phys.* 128 (13). <http://dx.doi.org/10.1063/1.2841367>.
- Hosseini, A.P., Chung, M.K., Wu, Y.-C., Alexander, A.L., 2013. Bessel Fourier orientation reconstruction (BFOR): an analytical diffusion propagator reconstruction for hybrid diffusion imaging and computation of q-space indices. *NeuroImage* 64 (0), 650–670. <http://dx.doi.org/10.1016/j.neuroimage.2012.08.072>.
- Jones, D.K., 2003. Determining and visualizing uncertainty in estimates of fiber orientation from diffusion tensor MRI. *Magn. Reson. Med.* 49 (1), 7–12. doi:10.1002/mrm.10331.
- Kent, J.T., 1982. The fisher-bingham distribution on the sphere. *J. R. Stat. Soc. Ser. B (Methodological)* 44 (1), 71–80.
- Koay, C.G., Nevo, U., Chang, L.-C., Pierpaoli, C., Basser, P., 2008. The elliptical cone of uncertainty and its normalized measures in diffusion tensor imaging. *Med. Imaging IEEE Trans.* 27 (6), 834–846. doi:10.1109/TMI.2008.915663.
- Latour, L.L., Svoboda, K., Mitra, P.P., Sotak, C.H., 1994. Time-dependent diffusion of water in a biological model system. *Proc. Natl. Acad. Sci.* 91 (4), 1229–1233. doi:10.1073/pnas.91.4.1229.
- Liewald, D., Miller, R., Logothetis, N., Wagner, H.-J., Schz, A., 2014. Distribution of axon diameters in cortical white matter: an electron-microscopic study on three human brains and a macaque. *Biol. Cybern.* 108 (5), 541–557. doi:10.1007/s00422-014-0626-2.
- Merlet, S.L., Deriche, R., 2013. Continuous diffusion signal, {EAP} and {ODF} estimation via compressive sensing in diffusion {MRI}. *Med. Image Anal.* 17 (5), 556–572.
- Mulkern, R.V., Gudbjartsson, H., Westin, C.-F., Zengingonul, H.P., Gartner, W., Guttman, C.R.G., Robertson, R.L., Kyriakos, W., Schwartz, R., Holtzman, D., Jolesz, F.A., Maier, S.E., 1999. Multi-component apparent diffusion coefficients in human brain. *NMR Biomed.* 12 (1), 51–62. doi:10.1002/(SICI)1099-1492(199902)12:1<51::AID-NBM546>3.0.CO;2-E.
- Ning, L., Laun, F., Gur, Y., DiBella, E.V., Deslauriers-Gauthier, S., Megherbi, T., Ghosh, A., Zucchelli, M., Menegaz, G., Fick, R., St-Jean, S., Paquette, M., Aranda, R., Descoteaux, M., Deriche, R., O'Donnell, L., Rath, Y., 2015. Sparse reconstruction challenge for diffusion MRI: Validation on a physical phantom to determine which acquisition scheme and analysis method to use? *Med. Image Anal.* <http://dx.doi.org/10.1016/j.media.2015.10.012>.
- Ozarslan, E., Koay, C., Shepherd, T., Blackband, S., Basser, P., 2009. Simple harmonic oscillator based estimation and reconstruction for three-dimensional q-space MRI. *Proc. Intl. Soc. Mag. Reson. Med.* 17, 1396.
- Ozarslan, E., Koay, C.G., Shepherd, T.M., Komlos, M.E., rfanolu, M.O., Pierpaoli, C., Basser, P.J., 2013. Mean apparent propagator (map) MRI: a novel diffusion imaging method for mapping tissue microstructure. *NeuroImage* 78 (0), 16–32.
- Özarslan, E., Shemesh, N., Basser, P.J., 2009. A general framework to quantify the effect of restricted diffusion on the NMR signal with applications to double pulsed field gradient NMR experiments. *J. Chem. Phys.* 130 (10). <http://dx.doi.org/10.1063/1.3082078>.
- Pfeuffer, J., Dreher, W., Sykova, E., Leibfritz, D., 1998. Water signal attenuation in diffusion-weighted 1h {NMR} experiments during cerebral ischemia: influence of intracellular restrictions, extracellular tortuosity, and exchange. *Magn. Reson. Imaging* 16 (9), 1023–1032. [http://dx.doi.org/10.1016/S0730-725X\(98\)00107-6](http://dx.doi.org/10.1016/S0730-725X(98)00107-6).
- Santis, S.D., Gabrielli, A., Palombo, M., Maraviglia, B., Capuani, S., 2011. Non-gaussian diffusion imaging: a brief practical review. *Magn. Reson. Imaging* 29 (10), 1410–1416. <http://dx.doi.org/10.1016/j.mri.2011.04.006>. Proceedings of the International School on Magnetic Resonance and Brain Function.
- Scherrer, B., Schwartzman, A., Taquet, M., Sahin, M., Prabhu, S.P., Warfield, S.K., 2015. Characterizing brain tissue by assessment of the distribution of anisotropic microstructural environments in diffusion-compartment imaging (diamond). *Magn. Reson. Med.* doi:10.1002/mrm.25912.n/a-n/a.
- Stanisz, G.J., Wright, G.A., Henkelman, R.M., Szafer, A., 1997. An analytical model of restricted diffusion in bovine optic nerve. *Magn. Reson. Med.* 37 (1), 103–111. doi:10.1002/mrm.1910370115.
- Stejskal, E., Tanner, J., 1965. Spin diffusion measurements: spin echoes in the presence of a time-dependent field gradient. *J. Chem. Phys.* 42 (1), 288–292.
- Tuch, D.S., Reese, T.G., Wiegell, M.R., Makris, N., Belliveau, J.W., Wedeen, V.J., 2002. High angular resolution diffusion imaging reveals intravoxel white matter fiber heterogeneity. *Magn. Reson. Med.* 48 (4), 577–582. doi:10.1002/mrm.10268.
- Wedeen, V.J., Hagmann, P., Tseng, W.-Y. I., Reese, T.G., Weisskoff, R.M., 2005. Mapping complex tissue architecture with diffusion spectrum magnetic resonance imaging. *Magn. Reson. Med.* 54 (6), 1377–1386. doi:10.1002/mrm.20642.
- Zhang, H., Hubbard, P.L., Parker, G.J., Alexander, D.C., 2011. Axon diameter mapping in the presence of orientation dispersion with diffusion {MRI}. *NeuroImage* 56 (3), 1301–1315. <http://dx.doi.org/10.1016/j.neuroimage.2011.01.084>.
- Zhang, H., T., S., Wheeler-Kingshott, C., Alexander, D., 2012. NODDI: Practical in vivo neurite orientation dispersion and density imaging of the human brain. *NeuroImage* 61 (4), 1000–1016.
- Zucchelli, M., Descoteaux, M., Menegaz, G., 2015. Human brain tissue microstructure characterization using 3D-SHORE on the HCP data. *Proc. Intl. Soc. Mag. Reson. Med.* 23, 3040.

# Ensemble average propagator-based detection of microstructural alterations after stroke

Lorenza Brusini<sup>1</sup>  · Silvia Obertino<sup>1</sup> · Ilaria Boscolo Galazzo<sup>2,3</sup> · Mauro Zucchelli<sup>1</sup> · Gunnar Krueger<sup>4</sup> · Cristina Granziera<sup>5</sup> · Gloria Menegaz<sup>1</sup>

Received: 1 February 2016 / Accepted: 2 June 2016 / Published online: 1 July 2016  
© CARS 2016

## Abstract

**Purpose** New analytical reconstruction techniques of diffusion weighted signal have been proposed. A previous work evidenced the exploitability of some indices derived from the simple harmonic oscillator-based reconstruction and estimation (3D-SHORE) model as numerical biomarkers of neural plasticity after stroke. Here, the analysis is extended to two additional indices: return to the plane/origin (RTPP/RTOP) probabilities. Moreover, several motor networks were introduced and the results were analyzed at different time scales. **Methods** Ten patients underwent three diffusion spectrum imaging (DSI) scans [1 week (*tp1*), 1 month (*tp2*) and 6 months (*tp3*) after stroke]. Ten matched controls underwent two DSI scans 1 month apart. 3D-SHORE was used for reconstructing the signal and the microstructural indices were derived. Tract-based analysis was performed along motor cortical, subcortical and transcallosal networks in the contralesional area.

**Results** The optimal intra-class correlation coefficient (ICC) was obtained in the subcortical loop for propagator anisotropy

(ICC = 0.96), followed by generalized fractional anisotropy (ICC = 0.94). The new indices reached the highest stability in the transcallosal network and performed well in the cortical and subcortical networks with the exception of RTOP in the cortical loop (ICC = 0.59). They allowed discriminating patients from controls at the majority of the timescales. Finally, the regression model using indices calculated along the subcortical loop at *tp1* resulted in the best prediction of clinical outcome.

**Conclusions** The whole set of microstructural indices provide measurements featuring high precision. The new indices allow discriminating patients from controls in all networks, except for RTPP in the cortical loop. Moreover, the 3D-SHORE indices in subcortical connections constitute a good regression model for predicting the clinical outcome at 6 months, supporting their suitability as numerical biomarkers for neuronal plasticity after stroke.

**Keywords** Stroke · 3D-SHORE · GFA · Biomarker

**Electronic supplementary material** The online version of this article (doi:10.1007/s11548-016-1442-z) contains supplementary material, which is available to authorized users.

✉ Lorenza Brusini  
lorenza.brusini@univr.it

<sup>1</sup> Department of Computer Science, University of Verona, Verona, Italy

<sup>2</sup> Institute of Nuclear Medicine, University College of London, London, UK

<sup>3</sup> Department of Neuroradiology, University Hospital Verona, Verona, Italy

<sup>4</sup> Siemens Healthcare USA, Boston, MA, USA

<sup>5</sup> Department of Clinical Neuroscience, CHUV and University of Lausanne, Lausanne, Switzerland

## Introduction

Stroke is the second most common cause of morbidity worldwide and is the leading cause of acquired disability [1]. Following initial damage, stroke patients can recover to some extent, partially due to the resolution of edema and possibly because of structural and functional modifications in surviving brain tissue. In particular, several experimental studies on both animal models and patients showed that this spontaneous recovery mainly depends on brain plastic reorganization of the infarct and peri-infarct areas [2, 3].

Important insights into the underlying remodeling and reorganization processes of functional recovery can nowadays be derived in human patients via advanced neuroimag-

ing methods and brain mapping [4]. In addition, the recent developments in connectivity analyses from multiple magnetic resonance imaging (MRI) data have provided new details about the network pathophysiology and stroke recovery, although the role of the non-injured hemisphere in this process is still controversial. At functional level, positron emission tomography (PET) and subsequently functional MRI (fMRI) studies have evidenced task-related brain activations in both lesional and contralateral hemispheres, which were highly dependent on the degree of brain damage [5,6]. In particular, Ward et al. [7] investigated a series of patients who went through a good recovery after stroke and suggested that the recruitment of other contralateral motor-related networks would have subserved the recovery and played an essential role for compensation of the impaired functions. At structural level, diffusion imaging (dMRI) has recently generated considerable interest due to its ability to disclose early pathophysiological changes in acute stroke, both in terms of structural changes of fiber tracts and microstructural properties of the tissues. Several studies demonstrated structural remodeling in ipsilateral and contralesional corticospinal tracts [8] and changes in the number of neural pathways in areas both ipsilateral and contralateral to the stroke [9], especially for the specific fiber trajectories connecting cortical regions in both hemispheres [10]. In addition, dMRI studies performed in well-recovered stroke patients revealed increased fractional anisotropy (FA) in both ipsi- and contralesional corticospinal tracts in comparison with controls, and that tracts' FA asymmetries in the contralateral corticospinal tract may play a role in motor recovery after unilateral stroke [11].

Current literature works suggest that dMRI may be one of the most sensitive neuroimaging biomarkers of vascular damage in stroke patients [12]. Among the different variants currently available, diffusion spectrum imaging (DSI) is a particular technique that is sensitive to intra-voxel heterogeneities in diffusion directions caused by crossing fiber tracts and thus allows more accurate mapping of axonal trajectories than other diffusion imaging approaches [13]. Generalized fractional anisotropy (GFA), as measured from DSI data, had been previously successfully exploited to provide evidence of plasticity in the uninjured motor networks in stroke patients [14,15]. Although anisotropy is the most widely studied diffusion index, there is a growing interest in investigating white matter (WM) microstructural properties and changes by analyzing different diffusion indices. To this end, the application of a recently proposed new analytical reconstruction model referred to as simple harmonic oscillator-based reconstruction and estimation (3D-SHORE) [16] can provide a more complete set of new generation indices describing different microstructural properties. In [17], the 3D-SHORE model was introduced and some microstructural indices were derived and analyzed. In par-

ticular, propagator anisotropy (PA) and return to the axis probability (RTAP) were considered. These indices are of particular interest as the first provides a measure of the ensemble average propagator (EAP) directional predominance and highly correlates with GFA [18], while the second provides an estimation of the axon's cross-sectional area and thus of the axon's diameter. Even though many factors affect the accuracy of such an estimation, including acquisition parameters such as diffusion time, diffusion gradient duration, gradient strength, partial volume effects due to limited resolution and, last but not least, the presence of crossing fibers, this measure is of particular interest because it naturally maps to a very clear property of WM. Following the same line, in this paper other two indices were considered: return to the origin probability (RTOP) and return to the plane probability (RTPP) [18]. In addition, the scope of the study was widened by including the transcallosal circuit and the subcortical motor loops as well as multiple temporal scales from injury.

## Materials and methods

The same cohort of patients and controls as in [17] was considered. Ten stroke patients [6 males, age  $60.3 \pm 12.3$  years, mean  $\pm$  standard deviation (SD)] underwent three acquisitions within 1 week (*tp1*), 1 month ( $\pm 1$  week, *tp2*) and 6 months ( $\pm 15$  days, *tp3*) after the injury, respectively. Ten age- and gender-matched controls were scanned twice 1 month apart (*tp1c* and *tp2c*). The same imaging protocol was used: DSI (TR/TE = 6600/138 ms, FOV =  $212 \times 212$  mm<sup>2</sup>, 34 slices,  $2.2 \times 2.2 \times 3$  mm<sup>3</sup> resolution, 258 gradient directions,  $b_{\max} = 8000$  s/mm<sup>2</sup>, scan time = 25.8 min), high-resolution 3D T1-weighted imaging (TR/TE = 2300/3 ms, FOV =  $256 \times 240$  mm<sup>2</sup>, 160 slices,  $1 \times 1 \times 1.2$  mm resolution, scan time = 6.13 min) using a 3T Siemens scanner (Trio, Siemens, Erlangen, Germany) equipped with a 32-channel head coil. Out of clinical assessment, the motor part of the NIHSS scale (NIHSS motor) was retained and used for modeling purposes as well as stroke volume and patients' age. All subjects provided written informed consent prior to imaging and the Lausanne University Hospital review board approved the study protocol, which has been performed in agreement with the Declaration of Helsinki.

## Microstructural indices

The 3D-SHORE model approximates the diffusion signal  $E(q\mathbf{u})$  as a linear combination of functions  $\Phi_{nlm}(q\mathbf{u})$  that are the solutions to the three-dimensional quantum mechanical harmonic oscillator

$$\mathbf{E}(q\mathbf{u}) = \sum_{l=0, \text{even}}^{N_{\max}} \sum_{n=l}^{(N_{\max}+l)/2} \sum_{m=-l}^l c_{nlm} \Phi_{nlm}(q\mathbf{u}) \quad (1)$$

$$\Phi_{nlm}(q\mathbf{u}) = \left[ \frac{2(n-l)!}{\zeta^{3/2} \Gamma(n+3/2)} \right]^{1/2} \times \left( \frac{q^2}{\zeta} \right)^{l/2} \exp\left( \frac{-q^2}{2\zeta} \right) L_{n-l}^{l+1/2} \left( \frac{q^2}{\zeta} \right) Y_l^m(\mathbf{u})$$

where  $N_{\max}$  is the maximal order in the truncated series,  $\zeta$  is an isotropic scaling parameter,  $\Gamma$  is the Gamma function,  $L$  is the Laguerre polynomial and  $Y$  are the real symmetric spherical harmonics. The coefficients  $c_{nlm}$  are determined by quadratic programming and positivity constraints are imposed to the EAP [18]. The corresponding EAP is recovered by Fourier transformation

$$P(r\mathbf{u}) = \sum_{l=0, \text{even}}^{N_{\max}} \sum_{n=l}^{(N_{\max}+l)/2} \sum_{m=-l}^l c_{nlm} \Psi_{nlm}(r\mathbf{u}) \quad (2)$$

where, due to the linearity of the transform operator, the coefficients  $c_{nlm}$  are the same as in Eq. (1) and  $\Psi_{nlm}(r\mathbf{u})$  is the Fourier transform of  $\Phi_{nlm}(q\mathbf{u})$

$$\Psi_{nlm}(r\mathbf{u}) = (-1)^{n-l/2} \left[ \frac{2(4\pi^2\zeta)^{3/2}(n-l)!}{\Gamma(n+3/2)} \right]^{1/2} \left( 4\pi^2\zeta r^2 \right)^{l/2} \times \exp\left( 4\pi^2\zeta r^2 \right) L_{n-l}^{l+1/2} \left( 4\pi^2\zeta r^2 \right) Y_l^m(\mathbf{u}) \quad (3)$$

The RTOP, RTAP and RTPP indices can then be derived from the EAP as follows [18]

$$\text{RTOP} = P(\mathbf{0}) = \sum_{n=0}^{N_{\max}/2} c_{n00} (-1)^n \times \left[ \frac{16\pi\zeta^{\frac{3}{2}} \Gamma(n+3/2)}{n!} \right]^{1/2} \quad (4)$$

$$\begin{aligned} \text{RTAP} &= \int_{\mathbb{R}} P(\mathbf{u}_{\parallel}) d\mathbf{r} \\ &= \sum_{l=0, \text{even}}^{N_{\max}} \sum_{n=l}^{(N_{\max}+l)/2} \sum_{m=-l}^l c_{nlm} \\ &\times \left[ \frac{\zeta^{1/2} 2^{l+3} \pi^2 \Gamma(l/2+1)^2 \Gamma(n+3/2)}{(n-l)! \Gamma(l+3/2)^2} \right]^{1/2} \\ &\times {}_2F_1(l-n, l/2+1, l+3/2, 2) P_l(0) Y_l^m(\mathbf{u}_{\parallel}) \end{aligned} \quad (5)$$

$$\begin{aligned} \text{RTPP} &= \int_{\mathbb{R}^2} P(\mathbf{r}_{\perp}) d^2\mathbf{r}_{\perp} \\ &= \sum_{l=0, \text{even}}^{N_{\max}} \sum_{n=l}^{(N_{\max}+l)/2} \sum_{m=-l}^l c_{nlm} \end{aligned}$$

$$\begin{aligned} &\times \left[ \frac{\Gamma(l/2+1/2)^2 \Gamma(n+3/2) 2^l}{\zeta^{1/2} (n-l)! \Gamma(l+3/2)^2} \right]^{1/2} \\ &\times {}_2F_1(l-n, l/2+1/2, l+3/2, 2) Y_l^m(\mathbf{u}_{\parallel}) \end{aligned} \quad (6)$$

where  $\mathbf{u}_{\parallel}$  is the main diffusion direction,  ${}_2F_1$  is the Gaussian hypergeometric function,  $P_l(0)$  is the  $l$ -degree Legendre polynomial in zero,  $\mathbf{r}_{\perp}$  is the plane passing through the origin and perpendicular to the main diffusion direction.

RTOP, RTAP and RTPP represent the probabilities of zero absolute net displacement, zero net displacement in the plane perpendicular to the main diffusion direction and zero net displacement in the main diffusion direction, respectively. More in details, Ozarslan et al. [18] proved the equivalence between RTOP, RTAP and RTPP and the reciprocal of the ensemble average of the pores' geometrical properties under the long diffusion time and narrow pulse separation assumptions. In particular, the estimation of the apparent mean axon's radius can be obtained as  $R = \sqrt{1/\pi \text{RTAP}}$  under the assumption of cylindrical pore. Finally, PA represents a measure of the anisotropy of the EAP and is defined as

$$PA = \sqrt{1 - \frac{\sum_{l=0}^{N_{\max}/2+1} c_{l00}^2}{\sum_{l=0, \text{even}}^{N_{\max}} \sum_{n=l}^{(N_{\max}+l)/2} \sum_{m=-l}^l c_{nlm}^2}} \quad (7)$$

Due to the fact that the apparent geometric features are obtained as ensemble averages, they map exactly to pores' properties only if a single type of pore with fixed shape and orientation is present in the voxel (e.g., only impermeable cylinders aligned in the same direction) [19]. The analysis of the robustness of the indices at changing acquisition parameters was out of the scope of this paper. It is well recognized in the literature that the pulse separation, pulse width and gradient strength impact on the estimated parameters [21–23] and a complete characterization in this respect is required for assessing the sensitivity of the indices to such changes and, in consequence, their suitability as biomarkers. However, this work provides evidence in support of their precision and their ability of capturing stroke induced microstructural changes, which are among the set of features that are required in this respect [24], marking a step in that direction. Although the assumptions on the diffusion time and gradient duration in general are not satisfied for in-vivo data, it is still possible to estimate the geometrical features of interest. In this manuscript, we refer to the estimated quantities using the prefix *apparent* (e.g., apparent mean diameter) to distinguish them from the real measures.

### Tract-based analysis

For each subject, dMRI images were processed using the Diffusion Toolkit (CMTK; [www.cmtk.org](http://www.cmtk.org)) in order to derive the orientation distribution functions (ODFs) needed for fiber

tracking, subsequently performed via a streamline-based algorithm. Individual high-resolution T1-weighted images were segmented using Freesurfer (<http://www.surfer.nmr.mgh.harvard.edu>) and further subdivided into a subject-specific 84-region atlas through a brain parcellation procedure. More in details, the Desikan–Killany atlas for cortical parcellation (32 regions per hemisphere) and the automated subcortical segmentation (20 regions) provided by Freesurfer were used. The parcellation mask was then created with an in-house Matlab script. A linear (affine) image registration to the diffusion space ( $b_0$  volume) was performed using FSL FLIRT ([www.fmrib.ox.ac.uk/fsl](http://www.fmrib.ox.ac.uk/fsl)) in order to back-project the subject-specific atlas from anatomical to diffusion space. A series of networks involved in different motor skills were identified in collaboration with the neurologists. These networks were practically created by selecting the respective regions of interest (ROIs) from the whole set of regions derived from the automatic brain parcellation and all the subsequent analysis were performed on these networks in order to study the specific contralateral motor mechanisms. The considered cortical and subcortical ROIs include the primary motor area (M1), supplementary motor area (SMA), somatosensory cortex (SC) and premotor area (PM), thalamus (Thl), caudatus (Cau), putamen (Put) and globus pallidus (GPi). In particular, the following ensembles of tracts were considered: (1) the set of connections between each region cited above in the contralesional area and the *corpus callosum* (Fig. 1a) that we call here transcallosal circuit (CC); (2) the ensemble of connections linking the cortical regions that we define cortical loop (CORT) (Fig. 1b); (3) the ensemble of connections linking subcortical regions called subcortical loop (SUBCORT) (Fig. 1c). The latter has been further investigated, identifying its five main sub-networks, in order to provide a more detailed description of the SUBCORT motor pathways: (a) M1 loop (Fig. 1d), (b) SMA1 loop (Fig. 1e), (c) SMA2 loop (Fig. 1f), (d) PM1 loop (Fig. 1g), (e) PM2 loop (Fig. 1h).

The six 3D-SHORE indices (GFA, PA, RTAP, R, RTOP, RTPP) were collected along the different pairs of ROI links shaping each of the aforementioned networks. To this end, an in-house software was used to extract the mean of values along each fiber connecting two specific ROIs. After that, the mean of fibers' values was calculated for each fiber bundle to obtain a value for each index and each particular connection of the considered networks.

## Statistical analysis

### Precision of the measurements

In order to demonstrate the longitudinal stability of the different 3D-SHORE indices, a repeatability analysis was performed on the test–retest data from the control group.

First, for each index and each network the degree of correlation as assessed by the square of the Pearson's correlation coefficient ( $r^2$ ) was calculated between  $tp1c$  and  $tp2c$  data. Second, the Bland–Altman plot was derived for illustrating the variations of the differences between paired data for each of the main networks, together with the percent coefficient of variation (CV%), and the intra-class correlation coefficient (ICC). More in details, the ICC estimates the reliability of the measurements by comparing the within-subject (WS) to the between-subject (BS) variability:

$$ICC = \frac{BSMSS - WSMSS}{BSMSS + WSMSS} \quad (8)$$

where MSS represents the mean sum of squares and is calculated for the WS and the BS as follows:

$$WSMSS = \frac{\sum_{i=1}^N \sum_{k=1}^2 (m_{ik} - \bar{m}_i)^2}{N} \quad (9)$$

$$BSMSS = \frac{\sum_{i=1}^N 2(\bar{m}_i - \bar{m})^2}{N - 1} \quad (10)$$

where  $N$  is the number of subjects,  $m_{ik}$  is the value of the  $k$ th measurement session for subject  $i$ ,  $\bar{m}_i$  is the mean of the measurements for subject  $i$  across all sessions and  $\bar{m}$  the overall mean across all subjects and sessions. The ICC values were interpreted as follows:  $>0.75$  as excellent,  $0.40$ – $0.75$  as fair to good and  $<0.40$  as poor [20].

### Comparison of absolute GFA, PA, R, RTAP, RTOP and RTPP changes in patients and controls

After the stability analysis, on both groups the percentage absolute changes in mean values between time points were calculated for each index and each network as:

$$\Delta_{tp12c}(m) = |(m_{tp2c} - m_{tp1c})|/m_{tp1c} \quad (11)$$

$$\Delta_{tp12}(m) = |(m_{tp2} - m_{tp1})|/m_{tp1}$$

$$\Delta_{tp23}(m) = |(m_{tp3} - m_{tp2})|/m_{tp2}$$

$$\Delta_{tp13}(m) = |(m_{tp3} - m_{tp1})|/m_{tp1}$$

where  $m$  denotes the mean value of the considered index along the fibers of a given connection and loop, and the subscript  $c$  denotes the control group. Since Kolmogorov–Smirnov normality test informed about the normal distribution of the percentage values, unpaired  $t$ -test (corrected for multiple comparisons with a false discovery rate of 0.05) was performed to detect significant differences between  $\Delta_{tp12c}(m)$  and  $\Delta_{tp12}(m)$ ,  $\Delta_{tp12c}(m)$  and  $\Delta_{tp23}(m)$ , and  $\Delta_{tp12c}(m)$  and  $\Delta_{tp13}(m)$ .

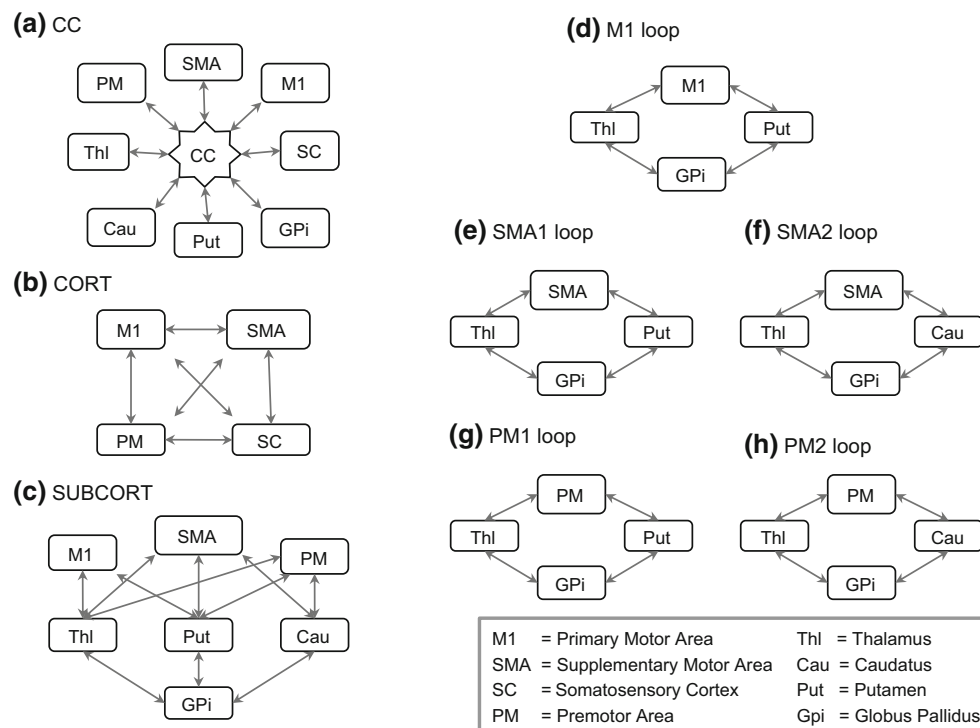


**Fig. 1** Schematic representation of the transcallosal (CC), cortical (CORT) and subcortical (SUBCORT) networks. The five sub-networks of this latter circuit are also reported on the *right panel (d–h)*

### Predictive model

In order to assess the predictive power of the 3D-SHORE indices, different linear regression models were considered for prediction of the motor outcome at 6 months after stroke (NIHSS at *tp3*). First, a linear regression model including only age, stroke size, and NIHSS motor scores at *tp1* as predictors was calculated. Then, for each of the three main networks, the mean value of each index along the connections of the set at *tp1* was calculated and included as predictor together with age, stroke size and NIHSS motor scores at *tp1*. Moreover, a predictive model was derived for each index separately using its  $\Delta_{tp12}$  values and including all the networks shown in Fig. 1 and NIHSS at *tp1*. The optimal model was identified by a backward selection process (significance threshold:  $p = 0.05$ ).

## Results

### Precision of the measurements

The repeatability of the measurements was assessed on the three main networks using the Bland–Altman plots.

The Bland–Altman plots comparing the mean index values across the CC connections for *tp1c* and *tp2c* are reported

in Fig. 2. The corresponding correlation scatter plots are provided in the Supplementary Materials. As shown in Table 1, a strong correlation between *tp1c* and *tp2c* was detected for all the indices. The best degree of association was achieved for GFA ( $r^2 = 0.85$ ,  $p < 0.05$ ), followed by PA ( $r^2 = 0.83$ ,  $p < 0.05$ ) while R showed the lowest correlation value ( $r^2 = 0.78$ ,  $p < 0.05$ ). High ICC values, close to unity, were found in all cases, with GFA and R showing also the highest and lowest ICC values (0.92 and 0.88), respectively. Regarding the relative variability expressed by the CV index, RTPP resulted the index with the best performance and lowest value, below 3%. In all cases, the Bland–Altman plots showed a mean difference close to zero (except for RTOP, due to the values' range for this index) with a limited spread of values.

The Bland–Altman plots for the CORT and SUBCORT loops are reported in Figs. 3 and 4, respectively, while the corresponding repeatability indices are given in Table 1. For the CORT network, the correlation plots evidenced a positive association between time points for all the indices (Supplementary Materials), with the highest correlation obtained for RTOP ( $r^2 = 0.82$ ,  $p < 0.05$ ), while RTPP showed a poor degree of correlation between values along time. RTOP and RTPP also displayed, respectively, the highest and lowest agreement in terms of ICC values between repeated measures in the test–retest procedure (0.91 and 0.59, respectively). For



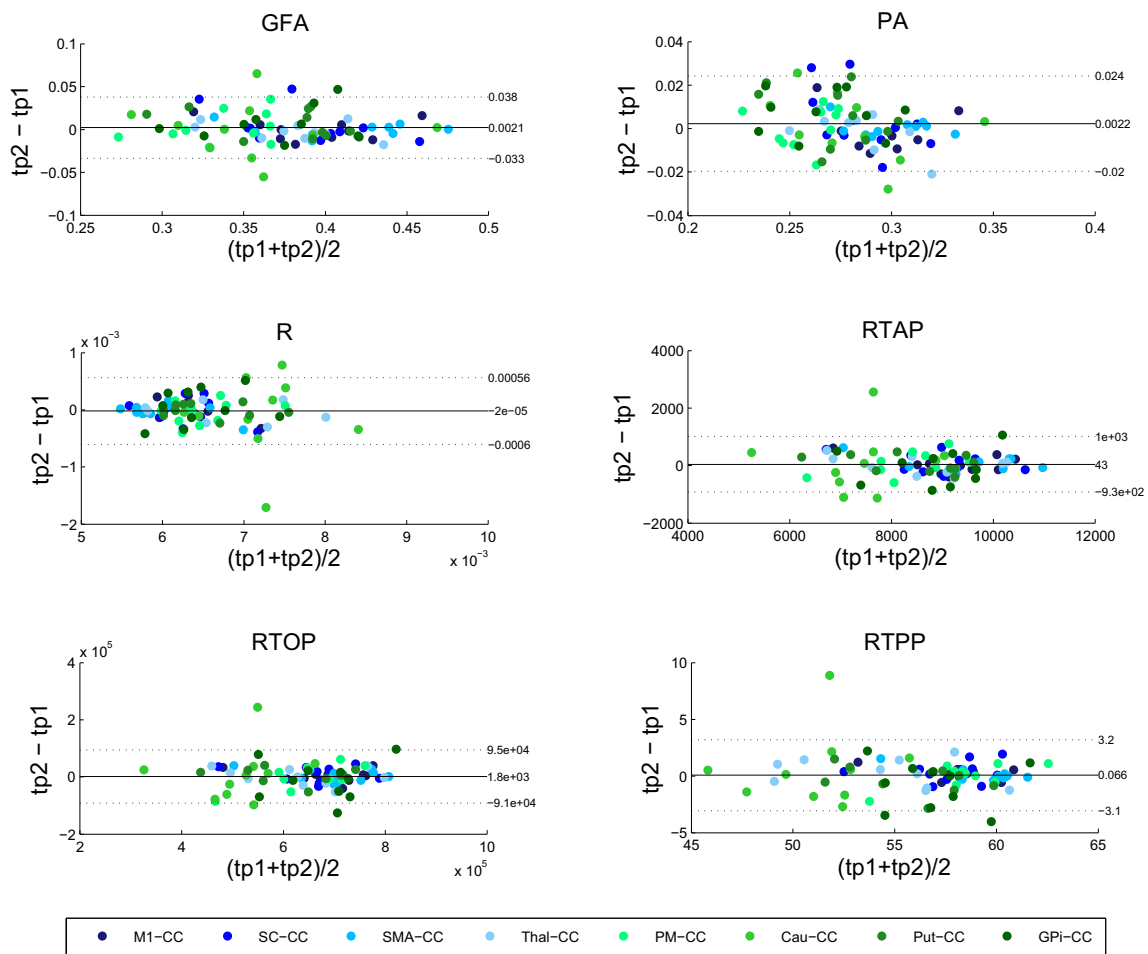


**Fig. 2** Bland Altman plot for each index in the transcalsal (CC) network. The *solid line* represent the mean value, while the *dashed lines* represent the  $\pm 1.96$  SD values, respectively

all the indices, the CV values between the repeated measures were well below 6%. Also in this network, the Bland–Altman plots confirmed a good reproducibility for all the indices, with a limited spread of the values around the mean (close to zero) and almost entirely within  $\pm 1.96$  SD.

For SUBCORT, PA showed the highest temporal stability both in terms of correlation and ICC ( $r^2 = 0.90$ ,  $p < 0.05$ ; ICC = 0.96). Differently from the other two sets of connections, RTTP and RTOP showed, respectively, the lowest correlation and repeatability values relatively to the other indices (RTTP  $r^2 = 0.73$ ,  $p < 0.05$ ; RTOP ICC = 0.85). RTOP also showed a larger CV value in comparison with the other networks (11%). The good reproducibility of the indices for this loop was further confirmed by the Bland–Altman plots, with almost all the values concentrated within the agreement limits for all the indices.

Overall, all the microstructural indices resulted to be stable across acquisition sessions guaranteeing precise measurements.

### Comparison of absolute GFA, PA, R, RTAP, RTOP, and RTPP changes in patients and controls

The mean absolute percent changes for  $\Delta_{tp12c}$ ,  $\Delta_{tp12}$ ,  $\Delta_{tp23}$  and  $\Delta_{tp13}$  for each index and for each of the main networks are reported in Fig. 5. Regarding the CC network, a significant difference was reached in all the comparisons between temporal changes. In particular, a marked statistically significant difference was detected in all the indices, except R, between the pairs  $\{\Delta_{tp12c}, \Delta_{tp12}\}$  and  $\{\Delta_{tp12c}, \Delta_{tp13}\}$  with the same range of  $p$  values ( $0.001 < p \leq 0.01$ , corrected) while  $\Delta_{tp23}$  appeared to be less different from the control variations in this loop. Regarding the CORT network, this failed to show statistically significant differences for RTTP at all time scales as well as for the pair  $\{\Delta_{tp12c}, \Delta_{tp23}\}$  in all the considered indices. In the other cases, the differences with the control group appeared to be equally or less strongly significant in comparison with the other two networks at all the time scales. Finally, the

**Table 1** Repeatability performance in terms of correlation coefficient ( $r^2$ ), intra-class correlation coefficient (ICC) and coefficient of variation (CV%) for all the indices for each set of connections

Network	Index	$r^2$	ICC	CV %
CC	GFA	0.85	0.92	4.8
	PA	0.83	0.90	4.0
	R	0.78	0.88	4.6
	RTAP	0.84	0.91	5.7
	RTOP	0.81	0.90	7.4
	RTPP	0.82	0.90	2.8
CORT	GFA	0.80	0.89	5.2
	PA	0.68	0.82	5.2
	R	0.49	0.69	5.3
	RTAP	0.79	0.89	5.1
	RTOP	0.82	0.91	5.6
	RTPP	0.35	0.59	4.9
SUBCORT	GFA	0.88	0.94	5.0
	PA	0.90	0.96	4.7
	R	0.82	0.91	3.1
	RTAP	0.77	0.88	6.2
	RTOP	0.76	0.85	11.0
	RTPP	0.73	0.88	3.1

In all the networks, correlation values were statistically significant ( $p < 0.05$ )

SUBCORT network presents the same results as for the CC connections for GFA and PA. A higher significance than for the CC network could be observed for R and RTAP for the comparison between  $\Delta_{tp12c}$  and  $\Delta_{tp12}$ , while a lower significance is shown for the comparison between the pairs  $\{\Delta_{tp12c}, \Delta_{tp12}\}$  and  $\{\Delta_{tp12c}, \Delta_{tp23}\}$  in RTTP. Moreover, RTOP had no significant differences for the pair  $\{\Delta_{tp12c}, \Delta_{tp23}\}$ .

RTTP results revealed that this index has lower percentage absolute changes over time in comparison with the other indices, both for controls and patients, while RTOP trends in all the networks are in line with those of RTAP.

Overall, mean absolute changes of the set of microstructural indices along the CORT network resulted less effective in discriminating patient and control groups. We thus decided to investigate further the role of the SUBCORT network by considering the five SUBCORT loops that are illustrated in Fig. 1. This allows a finer granularity in the analysis while still keeping the loop as the basic structural element. Noteworthy, splitting the CC network in its basic constituents would have brought to the level of single connections between each region and the *corpus callosum*. We consider this to be the next level of analysis and leave it for future investigation.

Splitting the SUBCORT network to the set of five sub-network components (Figs. 1d–h, 6) highlighted the leading

role of the M1 loop since it allowed discriminating the two groups at all time scales for GFA, PA and R ( $p < 0.05$ , corrected). On the other end, the PM2 sub-network had a less prominent role detecting significant differences only at longer time scales using PA and RTAP as shown in Fig. 6.

Focusing on the indices, GFA was highlighted as the index reaching the highest significant differences for all the three temporal conditions and all the sub-networks. Furthermore, R showed a good ability to differentiate controls from patients in all loops, followed by PA and, to a lesser extent, RTAP. Finally, RTOP and RTTP changes failed to reach significance in all conditions, namely for all sub-networks and temporal scales. However, a positive trend could be observed in the absolute percent change  $\Delta_{tp13}$  between  $tp1$  and  $tp3$  in patients, which indicates a change in the absolute value of the corresponding index. Even though such changes did not reach statistical significance, they witness the ability of RTOP and RTTP indices of capturing microstructural remodeling in patients. It could be useful to highlight that the method used for correction for multiple comparisons strongly influences the results. A clear indication does not emerge from the literature in this respect so far and this aspect deserves further investigation.

## Predictive model

Two families of predictive models were considered: the first targeting the identification of the networks playing a dominant role in the prediction of the clinical outcomes at  $tp3$  and the second aiming at disambiguating the role of a specific index in the same predictive task by gathering the different circuits.

In the patients cohort, a linear regression model including only age, stroke size and NIHSS at  $tp1$  has shown to predict the NIHSS outcome at  $tp3$  with low correlation ( $R^2 = 0.546$ ; adjusted  $R^2 = 0.489$ ;  $p = 0.772$ ). The R index was not considered because of its dependence on RTAP [17]. Conversely, the construction of a predictive model for each of the three networks including all together the corresponding  $tp1$  values of GFA, PA, RTAP, RTOP and RTTP, increased the prediction capability, except for the CORT loop, as shown in Fig. 7 ( $R^2 = 0.558$ ; adjusted  $R^2 = 0.431$ ;  $p = 0.057$ ). Notably, the best results were obtained in the SUBCORT set ( $R^2 = 0.997$ ; adjusted  $R^2 = 0.988$ ;  $p = 0.009$ ), even though the regression model for the CC network proved to have a high correlation as well ( $R^2 = 0.994$ ; adjusted  $R^2 = 0.973$ ;  $p = 0.021$ ). Moreover, all the prediction models retain RTOP as a significant predictor while GFA was the only one rejected in the model composed by SUBCORT connections.

When the 3D-SHORE indices were considered separately, the advantage of taking into account RTOP to determine a

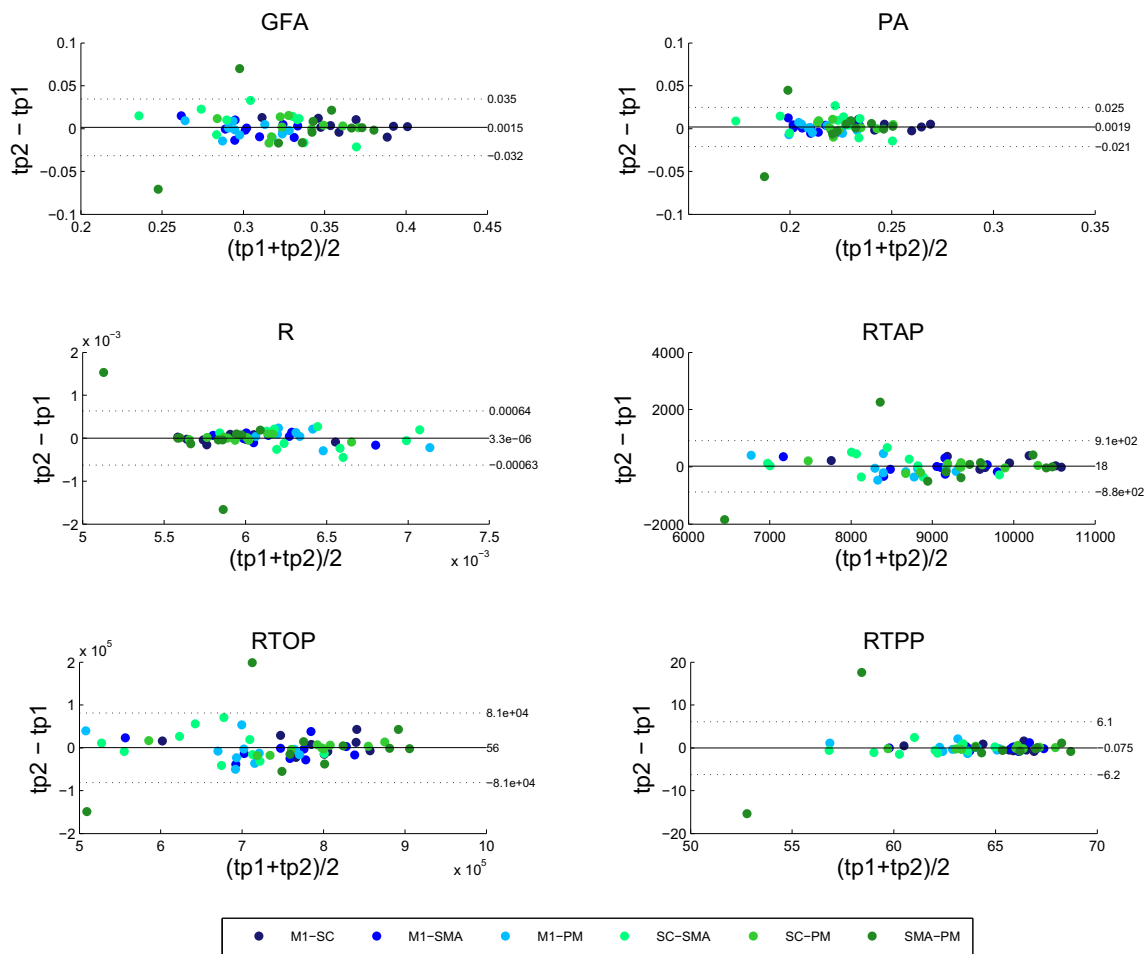


**Fig. 3** Bland–Altman plot for each index in the cortical (CORT) network. The *solid line* represents the mean value, while the *dashed lines* represent the  $\pm 1.96$  SD values, respectively

good prediction of clinical outcome was further confirmed as shown in Fig. 8. Indeed, the predictive model for this index showed the highest correlation value ( $R^2 = 0.998$ ; adjusted  $R^2 = 0.983$ ;  $p = 0.096$ ). The models using GFA ( $R^2 = 0.992$ ; adjusted  $R^2 = 0.976$ ;  $p = 0.003$ ), RTPP ( $R^2 = 0.956$ ; adjusted  $R^2 = 0.802$ ;  $p = 0.146$ ), and PA ( $R^2 = 0.861$ ; adjusted  $R^2 = 0.688$ ;  $p = 0.073$ ) also showed a good correlation and prediction power. Conversely, no meaningful prediction models could be derived for RTAP using these sets of connections.

For all the different optimal models, the relative importance of each predictor was evaluated by the Fisher test and the results are reported in the Supplementary Materials.

## Discussion

This longitudinal study on motor stroke patients demonstrates the suitability of 3D-SHORE indices for charac-

terizing the contralesional structural changes of the main motor pathways. In particular, our findings suggest that the complete microstructural characterization provided by these indices over the contralateral white matter connections can enable a more detailed knowledge of axonal remodeling after stroke, confirming and extending recent studies based on anisotropy measures [14, 15] and on a different and less extended set microstructural indices [17].

The potential of 3D-SHORE derived indices as new markers of disease-induced changes has been further demonstrated by the test–retest study on healthy volunteers which proved the high stability of all these indices over time. Finally, our results stress the indication that the different 3D-SHORE measures within 1 week from the insult, combined with clinical status in the acute phase, can predict the motor outcome at 6 months after stroke with strong correlation.

While previous studies focused on the plastic changes considering individually the contralateral intrahemispheric and

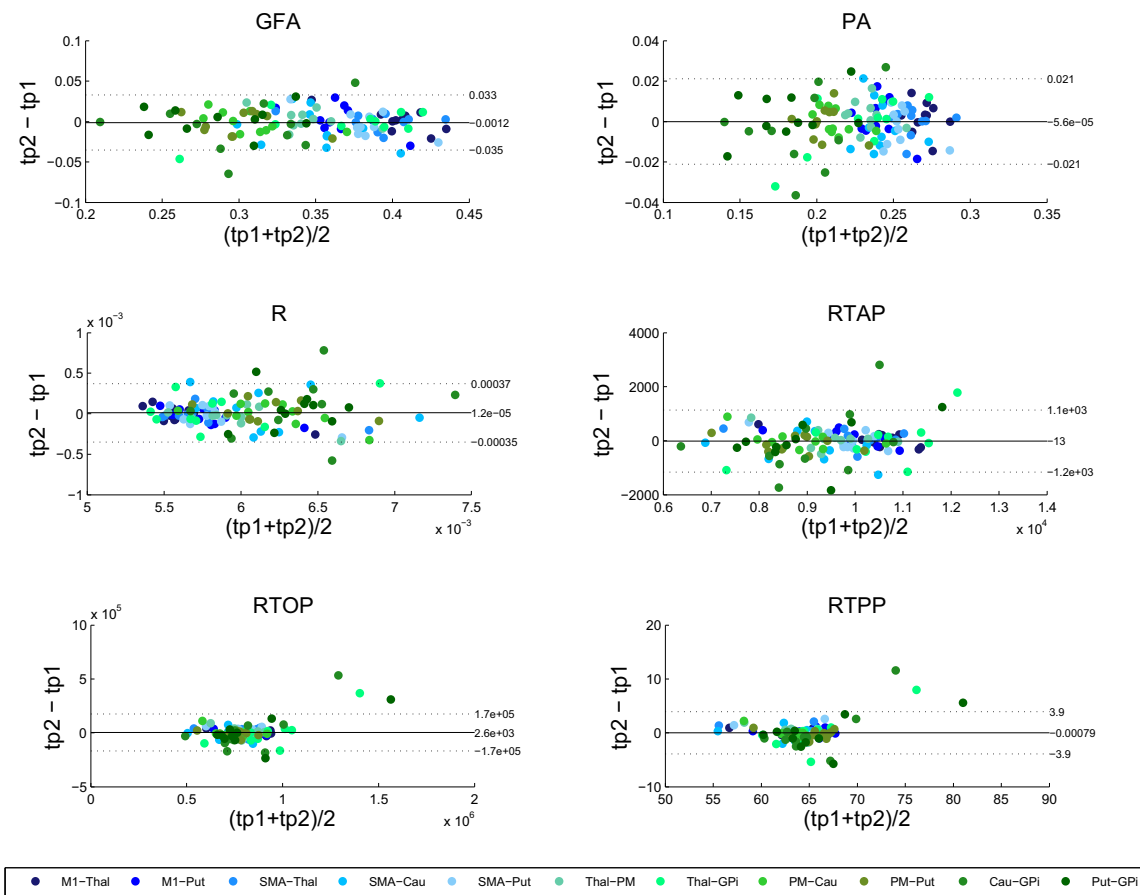


**Fig. 4** Bland–Altman plot for each index in the subcortical (SUBCORT) network. The *solid line* represents the mean value, while the *dashed lines* represent the  $\pm 1.96$  SD values, respectively

interhemispheric motor connections [6, 10, 14], here the concept of network has been introduced and fully investigated. Acute ischemic strokes can indeed disrupt the nodes and edges of the circuits and lead to time- and recovery-dependent changes in the specific structural network characteristics [25]. Thus, studying different CORT and SUBCORT circuits we could identify which are more involved in the recovery process and which allow to more clearly discriminate acute stroke patients from controls. Our findings demonstrate the detection of microstructural changes in all the considered networks. More in details, the changes in all the indices of the CC and SUBCORT network loops, which differ substantially between patients and healthy subjects, put forth the important role played by these two interacting networks which have been largely neglected for a long time. Our results about the CC network are in line with previous findings from functional imaging and electrophysiological studies applying transcranial magnetic stimulation (TMS) that have suggested a critical importance of interhemispheric connections for stroke recovery [26].

Regarding the different indices, GFA and PA appeared to be the most sensitive to longitudinal changes in stroke patients and the most specific in discriminating patients from controls for all the loops. The remodeling of the contralesional white matter in post-stroke functional improvement was reported in many studies [6, 9, 11, 27] and specified as possibly caused by axonal sprouting, axonal outgrowth, dendritic plasticity or new connections [28, 29]. The new indices, in particular RTAP, RTOP and RTPP, help us to disentangle the different sources of the contralesional compensation. More in details, GFA permits to only enhance differences in the diffusivity while RTAP, RTOP and RTPP can specify the changes in the axonal structures.

In terms of longitudinal stability and repeatability, the statistical measures applied to the test–retest data from the control group confirmed strong and significant correlations between time points for all the indices and sets of connections, with higher and consistent values for the interhemispheric connections and SUBCORT loop. The ICC

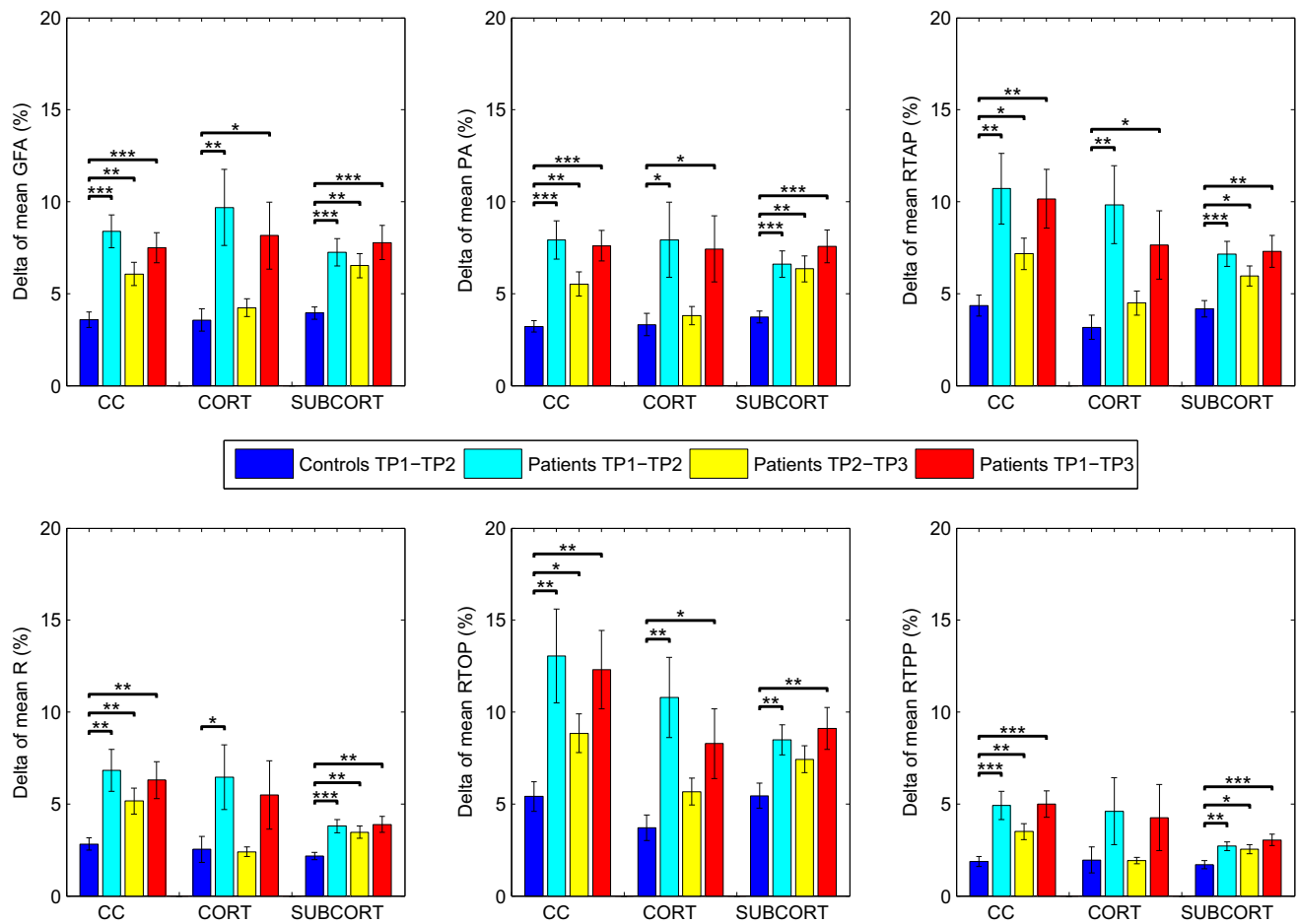


**Fig. 5** Longitudinal changes in percent mean absolute values in controls and patients for each index in transcallosal (CC), cortical (CORT) and subcortical (SUBCORT) networks (\* $p < 0.05$ ; \*\* $p < 0.01$ ; \*\*\* $p < 0.001$ )

values for these two circuits demonstrated excellent agreement for all the indices, while those for the CORT network resulted to be slightly inferior for R and RTOP, although still excellent for the remaining four indices. Finally, the Bland–Altman plots further elucidated a strong repeatability of the indices in test–retest trials showing narrow limits of agreement and small mean differences between the two repetitions. Overall, the CC and SUBCORT connections appeared to be the most stable and reproducible networks for all the indices, suggesting their importance as circuits to take into consideration for assessing patients' changes over time.

Regarding the prediction power of these indices, the predictive models introduced in this study further demonstrated how 3D-SHORE measures calculated over specific circuits, in combination with clinical and functional status, can provide a powerful and easy-to-use tool to evaluate acute stroke patients and predict their motor recovery. In particular, two types of models have been presented. First, a predictive

model for each of the three main networks have been derived, considering all the indices' values at  $tp1$  together. Again, the interhemispheric (CC) circuit and the SUBCORT loop highlighted the beyond suspicious importance of taking into account these brain circuits. For these models, the inclusion of RTOP as predictor in all the regressions, instead of the conventional GFA, evidenced the role played by the 3D-SHORE indices in the creation of an effective prediction model. Second, we defined a predictive model for each index, considering all together the circuits as predictors. However, different from our previous work [17] in which we focused on a subset of these 3D-SHORE indices, along with several clinical scales including NIHSS at  $tp2$ , here we considered the mean absolute changes rather than the individual values at  $tp1$  and only included the clinical variables at  $tp1$  demonstrating that early changes can provide a good prediction of the clinical outcome. While GFA results further confirmed previous findings in the literature about its strong prediction power [14,15], RTOP and RTPP results

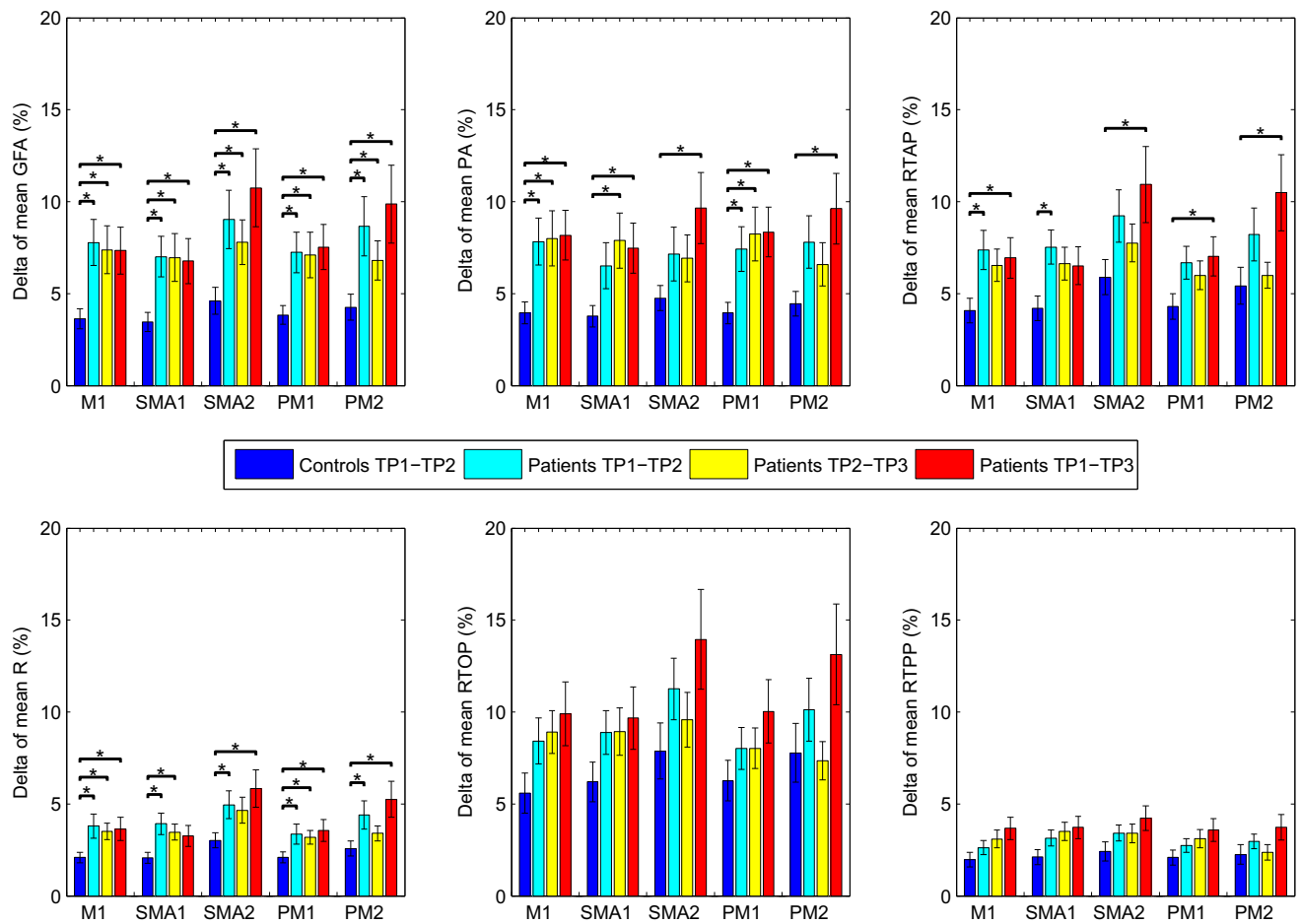


**Fig. 6** Longitudinal changes in percent mean absolute values in controls and patients for each index in the five sub-networks (\* $p < 0.05$ , \*\* $p < 0.01$ , \*\*\* $p < 0.001$ )

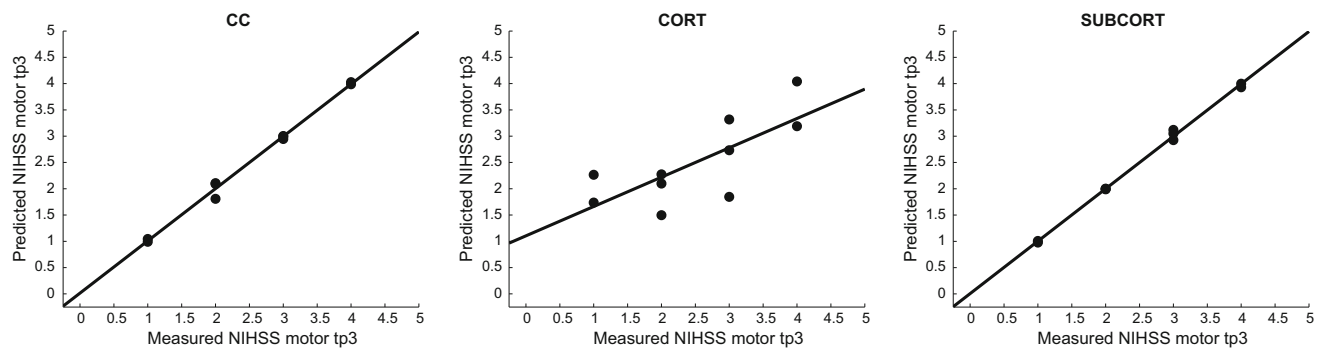


**Fig. 7** Representation of the measured and predicted NIHSS at  $tp3$  using the models described above

are novel and permit an improved prediction, especially in the case of RTOP, in comparison with the conventional models including only clinical variables and/or GFA measures. Future studies will be performed to broaden both the inclu-

sion criteria and the number of patients, in order to fully validate these promising findings for a wider clinical use and for a better planning of the rehabilitation processes in stroke patients.

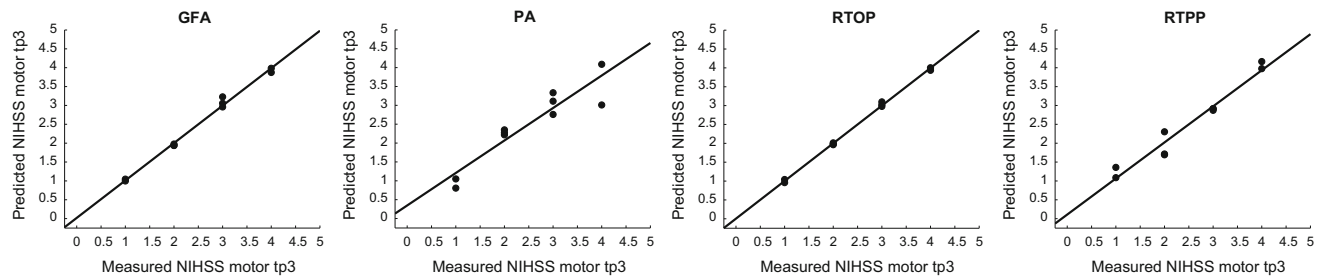


**Fig. 8** Representation of the measured and predicted NIHSS at *tp3* for each index

## Conclusions

The 3D-SHORE indices convey information regarding the cerebral microstructure which are different from one to each other. This makes possible a more thorough characterization of the type of microscopic differences that arise between healthy and diseased subjects and opens the way for an accurate automatic discrimination. The reproducibility of the indices as evidenced by the repeatability analyses, the accuracy in the estimation of microstructural features and the capability to predict the clinical outcome provide elements in favor of the suitability of the 3D-SHORE indices as numerical biomarkers for cerebral stroke recovery. This study emphasizes the importance of having more information than standard clinical variables to predict the clinical outcome at 6 months after the onset of a stroke as early as the first week of affection of the injury. Moreover, in addition to confirming the importance of the remodeling of interhemispheric connections in the recovery of the motor deficit, it reveals the unsuspected importance of the role of subcortical regions. The results also emphasize the importance of using networks' information rather than the single connections considered one by one, possibly highlighting the highly cooperative behavior of the brain. Overall, the 3D-SHORE indices could be a support for clinical activity and in particular for the prognosis phase as suggested by the timely prediction of the clinical outcome at 6 months after only 1 week from the injury.

### Compliance with ethical standards

**Conflict of interest** None.

**Informed consent** This article does not contain any studies with animals performed by any of the authors.

## References

- Donnan GA, Fisher M, Macleod M, Davis SM (2008) Stroke. *Lancet* 371:1612–1623
- Dijkhuizen RM, Nicolay K (2003) Magnetic resonance imaging in experimental models of brain disorders. *J Cereb Blood Flow Metab* 23(12):1383–1402
- Mountz JM, Liu HG, Deutsch G (2003) Neuroimaging in cerebrovascular disorders: measurement of cerebral physiology after stroke and assessment of stroke recovery. *Semin Nucl Med* 33(1):56–76
- Rehme AK, Grefkes C (2013) Cerebral network disorders after stroke: evidence from imaging-based connectivity analyses of active and resting brain states in humans. *J Physiol* 591(Pt 1):17–31
- Weiller C, Chollet F, Friston KJ, Wise RJ, Frackowiak RS (1992) Functional reorganization of the brain in recovery from striatocapsular infarction in man. *Ann Neurol* 31:463–472
- Riecker A, Groschel K, Ackermann H, Schnaudigel S, Kassubek J, Kastrup A (2010) The role of the unaffected hemisphere in motor recovery after stroke. *Hum Brain Mapp* 31:1017–1029
- Ward NS, Brown MM, Thompson AJ, Frackowiak RS (2003) Neural correlates of motor recovery after stroke: a longitudinal fMRI study. *Brain* 126:2476–2496
- Buffon F, Molko N, Herv D, Porcher R, Denghien I, Pappata S, Le Bihan D, Bousser MG, Chabriat H (2005) Longitudinal diffusion changes in cerebral hemispheres after MCA infarcts. *J Cereb Blood Flow Metab* 25:641–650
- Gerloff C, Bushara K, Sailer A, Wassermann EM, Chen R, Matsuo T, Waldvogel D, Wittenberg GF, Ishii K, Cohen LG, Hallett M (2006) Multimodal imaging of brain reorganization in motor areas of the contralesional hemisphere of well recovered patients after capsular stroke. *Brain* 129(Pt 3):791–808
- Crofts JJ, Higham DJ, Bosnell R, Jbabdi S, Matthews PM, Behrens TE, Johansen-Berg H (2011) Network analysis detects changes in the contralesional hemisphere following stroke. *Neuroimage* 54(1):161–169
- Schaechter JD, Fricker ZP, Perdue KL, Helmer KG, Vangel MG, Greve DN, Makris N (2009) Microstructural status of ipsilesional and contralesional corticospinal tract correlates with motor skill in chronic stroke patients. *Hum Brain Mapp* 30(11):3461–3474
- Moseley M, Cohen Y, Mintorovitch J, Chileuit L, Shimizu H, Kucharczyk J, Wendland M, Weinstein P (1990b) Early detection of regional cerebral ischemia in cats: comparison of diffusion and T2-weighted MRI and spectroscopy. *Magn Reson Med* 14:330–346
- Wedeen VJ, Hagmann P, Tseng WY, Reese TG, Weisskoff RM (2005) Mapping complex tissue architecture with diffusion spectrum magnetic resonance imaging. *Magn Reson Med* 54(6):1377–1386
- Granziera C, Daducci A, Meskaldji DE, Roche A, Maeder P, Michel P, Hadjikhani N, Sorensen AG, Frackowiak RS, Thiran JP, Meuli R, Krueger G (2012) A new early and automated MRI-based predictor of motor improvement after stroke. *Neurology* 79(1):39–46
- Lin Y, Daducci A, Meskaldji D, Thiran J, Michel P, Meuli R, Krueger G, Menegaz G, Granziera C (2015) Quantitative analysis

- of myelin and axonal remodeling in the uninjured motor network after stroke. *Brain Connect* 5(7):401–412
16. Özarslan E, Koay C, Shepherd T, Blackband S, Basser P (2009c) Simple harmonic oscillator based reconstruction and estimation for three-dimensional q-space MRI. *Proc Intl Soc Mag Reson Med* 17:1396
  17. Brusini L, Obertino S, Zucchelli M, Boscolo Galazzo I, Krueger G, Granziera C, Menegaz G (2015) Assessment of mean apparent propagator-based indices as biomarkers of axonal remodeling after stroke. *MICCAI* 9349:199–206
  18. Özarslan E, Koay C, Shepherd T, Komlosh M, İrfanoğlu M, Pierpaoli C, Basser P (2013) Mean apparent propagator (MAP) MRI: a novel diffusion imaging method for mapping tissue microstructure. *NeuroImage* 78:16–32
  19. Zucchelli M, Brusini L, Mendez CA, Daducci A, Granziera C, Menegaz G (2016) What lies beneath? Diffusion EAP-based study of brain tissue microstructure. *Med Image Anal* 32:145–156
  20. Fleiss JL (1981) *Methods for rates and proportions*, 2nd edn. Wiley, New York
  21. Bar-Shir A, Avram L, Özarslan E, Basser PJ, Cohen Y (2008) The effect of the diffusion time and pulse gradient duration ratio on the diffraction pattern and the structural information estimated from q-space diffusion MR: experiments and simulations. *J Magn Reson* 194:230–236
  22. Avram L, Özarslan E, Assaf Y, Bar-Shir A, Cohen Y, Basser PJ (2008) Three-dimensional water diffusion in impermeable cylindrical tubes: theory versus experiments. *NMR Biomed* 21:888–898
  23. Huang SY, Nummenmaa A, Witzel T, Duval T, Cohen-Adad J, Wald LL, McNab JA (2015) The impact of gradient strength on in vivo diffusion MRI estimates of axon diameter. *Neuroimage* 106:464–472
  24. Strimbu K, Tavel JA (2010) What are biomarkers? *Curr Opin HIV AIDS* 5(6):463–466
  25. Koch P, Schulz R, Hummel FC (2016) Structural connectivity analyses in motor recovery research after stroke. *Ann Clin Transl Neurol* 3(3):233–244
  26. Schulz R, Gerloff C, Hummel FC (2013) Non-invasive brain stimulation in neurological diseases. *Neuropharmacology* 64:579–587
  27. Lotze M, Markert J, Sauseng P, Hoppe J, Plewnia C, Gerloff C (2006) The role of multiple contralesional motor areas for complex hand movements after internal capsular lesion. *J Neurosci* 26:6096–6102
  28. Granziera C, D'Arceuil H, Zai L, Magistretti PJ, Sorensen AG, de Crespigny AJ (2007) Long-term monitoring of poststroke plasticity after transient cerebral ischemia in mice using in vivo and ex vivo diffusion tensor MRI. *Open Neuroimag J* 1:10–17
  29. Ueno Y, Chopp M, Zhang L, Buller B, Liu Z, Lehman N, Liu X, Zhang Y, Roberts C, Zhang Z (2012) Axonal outgrowth and dendritic plasticity in the cortical peri-infarct area after experimental stroke. *Stroke* 43(8):2221–2228





# On the Viability of Diffusion MRI-Based Microstructural Biomarkers in Ischemic Stroke

*Ilaria Boscolo Galazzo*<sup>1\*</sup>, *Lorenza Brusini*<sup>1</sup>, *Silvia Obertino*<sup>1</sup>, *Mauro Zucchelli*<sup>1</sup>, *Cristina Granziera*<sup>2</sup> and *Gloria Menegaz*<sup>1</sup>

<sup>1</sup> Department of Computer Science, University of Verona, Verona, Italy, <sup>2</sup> Translational Imaging in Neurology Group, Department of Neurology, Basel University Hospital, Basel, Switzerland

## OPEN ACCESS

### Edited by:

Julien Valette,  
Commissariat à l'Energie Atomique et  
aux Energies Alternatives (CEA),  
France

### Reviewed by:

Matthew D. Budde,  
Medical College of Wisconsin,  
United States  
Alexandru Vlad Avram,  
National Institutes of Health (NIH),  
United States

### \*Correspondence:

Ilaria Boscolo Galazzo  
ilaria.boscologalazzo@univr.it

### Specialty section:

This article was submitted to  
Brain Imaging Methods,  
a section of the journal  
Frontiers in Neuroscience

**Received:** 30 November 2017

**Accepted:** 05 February 2018

**Published:** 21 February 2018

### Citation:

Boscolo Galazzo I, Brusini L,  
Obertino S, Zucchelli M, Granziera C  
and Menegaz G (2018) On the Viability  
of Diffusion MRI-Based  
Microstructural Biomarkers in  
Ischemic Stroke.  
Front. Neurosci. 12:92.  
doi: 10.3389/fnins.2018.00092

Recent tract-based analyses provided evidence for the exploitability of 3D-SHORE microstructural descriptors derived from diffusion MRI (dMRI) in revealing white matter (WM) plasticity. In this work, we focused on the main open issues left: (1) the comparative analysis with respect to classical tensor-derived indices, i.e., Fractional Anisotropy (FA) and Mean Diffusivity (MD); and (2) the ability to detect plasticity processes in gray matter (GM). Although signal modeling in GM is still largely unexplored, we investigated their sensibility to stroke-induced microstructural modifications occurring in the contralateral hemisphere. A more complete picture could provide hints for investigating the interplay of GM and WM modulations. Ten stroke patients and ten age/gender-matched healthy controls were enrolled in the study and underwent diffusion spectrum imaging (DSI). Acquisitions at three and two time points (*tp*) were performed on patients and controls, respectively. For all subjects and acquisitions, FA and MD were computed along with 3D-SHORE-based indices [Generalized Fractional Anisotropy (GFA), Propagator Anisotropy (PA), Return To the Axis Probability (RTAP), Return To the Plane Probability (RTPP), and Mean Square Displacement (MSD)]. Tract-based analysis involving the cortical, subcortical and transcallosal motor networks and region-based analysis in GM were successively performed, focusing on the contralateral hemisphere to the stroke. Reproducibility of all the indices on both WM and GM was quantitatively proved on controls. For tract-based, longitudinal group analyses revealed the highest significant differences across the subcortical and transcallosal networks for all the indices. The optimal regression model for predicting the clinical motor outcome at *tp3* included GFA, PA, RTPP, and MSD in the subcortical network in combination with the main clinical information at baseline. Region-based analysis in the contralateral GM highlighted the ability of anisotropy indices in discriminating between groups mainly at *tp1*, while diffusivity indices appeared to be altered at *tp2*. 3D-SHORE indices proved to be suitable in probing plasticity in both WM and GM, further confirming their viability as a novel family of biomarkers in ischemic stroke in WM and revealing their potential exploitability in GM. Their combination with tensor-derived indices can provide more detailed insights of the different tissue modulations related to stroke pathology.

**Keywords:** diffusion propagator, tensor model, 3D-SHORE model, reproducibility, tract-based, gray matter, ischemic stroke

## INTRODUCTION

In the last 30 years, diffusion magnetic resonance imaging (dMRI) has been proven to be a valuable tool for characterizing physiological and pathological conditions *in-vivo* (Le Bihan et al., 1986; Beaulieu, 2002). An increasing number of modeling methods have been proposed for inferring tissue microstructural properties from the acquired diffusion signal (for a detailed overview see Novikov et al., 2016), many of which rely only on the reconstruction of the ensemble average propagator (EAP), i.e., the probability distribution function of the water molecules displacements. The EAP, under some optimality assumptions, contains the full information about the diffusion process and therefore can inform about the underlying tissue architecture (Zucchelli et al., 2016b), leading to numerical indices that can indirectly quantify the different microstructural features.

Diffusion Tensor Imaging (DTI) (Basser et al., 1994a) was the first EAP model introduced to describe the anisotropic nature of the diffusion process in biological tissues and is still the preferred method in clinical settings thanks to its ability to estimate the principal diffusion direction from very few dMRI measurements. The scalar indices obtained from DTI, mainly the mean diffusivity (MD) and the fractional anisotropy (FA) (Pierpaoli and Basser, 1996), have become precious tools for characterizing pathological conditions such as tumors, stroke and neurodegenerative disorders (Sundgren et al., 2004). Nonetheless, DTI has an inherent strong modeling constraint related to the description of the EAP as a single multivariate Gaussian function. This assumption is rarely adequate in real conditions where complex white matter (WM) topologies featuring crossing, fanning and kissing fibers are most often encountered, severely limiting its applicability. Among the widespread EAP models proposed for circumventing this limitation, one of the most accurate is the Simple Harmonic Oscillator Based Reconstruction and Estimation (SHORE), firstly introduced in Özarlsan et al. (2008). 3D-SHORE and its extensions, as Mean Apparent Propagator (MAP)-MRI (Özarlsan et al., 2013), demonstrated good performance in detecting multiple diffusion directions and are among the most promising EAP-based models for characterizing the tissue microstructure, as recently highlighted at the SPARC-dMRI contest (Ning et al., 2015). Under some assumptions, reliable measures of tissue anisotropy can be derived from these EAP models, such as the Generalized Fractional Anisotropy (GFA) and the Propagator Anisotropy (PA), along with measures of the EAP variance (Mean Square Displacement, MSD). In addition, they provide indices that quantify various features of the three-dimensional diffusion process, namely the Return to the Origin Probability (RTOP), the Return To the Axis Probability (RTAP) and the Return To the Plane Probability (RTPP). When the diffusion time is long enough and under narrow pulse assumptions (Özarlsan et al., 2013), these indices reflect the degree of restriction of the water molecules in the voxel, which is linked to the underlying pore shape and thus represent relevant descriptors of the microstructural properties (Zucchelli et al., 2016a).

Since their first introduction, 3D-SHORE indices have been increasingly explored as novel potential biomarkers of brain

microstructure. This has been shown both on synthetic data and in *ex-vivo* experiments on a marmoset brain (Özarlsan et al., 2013) as well as in *in-vivo* studies on healthy subjects (Avram et al., 2014; Fick et al., 2015; Mendez et al., 2016; Zucchelli et al., 2016a). Very few studies have tried to pursue their potentialities as clinical biomarkers in pathologies, with promising results to date only on Alzheimer's animal models (Fick et al., 2016) and on ischemic stroke (Brusini et al., 2015; Obertino et al., 2016). In the latter case, albeit DTI scalar indices have been used to assess stroke features in several longitudinal studies (Maniega et al., 2004; Yu et al., 2009), the characterisation of the network pathophysiology with advanced EAP-based indices would add insights into the reorganization processes that can be combined with clinical information to draw a more precise picture of the disease. A recent study (Brusini et al., 2016) investigated these aspects on a group of ischemic stroke patients and assessed the performance of selected 3D-SHORE indices along WM tracts of different motor networks (cortical, subcortical, and transcallosal circuits). Results highlighted how 3D-SHORE-based indices (mainly GFA, PA, RTAP, and RTPP) could provide measurements featuring high precision and allow discriminating patients from controls, supporting their suitability for mapping longitudinal changes after stroke.

Although the available findings for these numerical indices are encouraging, a quantitative comparison with the classical tensor-derived metrics is currently lacking but essential to further probing their potentialities as biologically specific markers. Indeed, MD and FA remain the standard measures in clinical settings, especially for acute stroke imaging. Therefore, 3D-SHORE-based indices have to be carefully related to tensor-derived indices in terms of precision, consistency, discriminative and predictive power in patients, all essential requirements to be eligible as numerical biomarkers. Avram et al. (2016) reported a first attempt to assess the feasibility of novel EAP-indices (from MAP-MRI modeling rather than 3D-SHORE) in comparison to classical DTI indices, demonstrating good consistency across subjects and reproducibility in test–retest experiments on three controls. However, despite the promising results, the authors dealt with a very limited number of healthy subjects and relied only on qualitative visual comparisons, acknowledging the need for further studies on patient populations that, to the best of our knowledge, are still missing in recent literature.

Whereas a great research effort has been devoted to dMRI signal modeling in WM, its exploitability for characterizing gray matter (GM) structures is still largely unexplored. In fact, there is a growing need for a more comprehensive assessment of GM tissue changes using dMRI. The intrinsic complexity of GM microstructure which, as opposed to WM, lacks coherent tissue orientation complicates the modeling and interpretation of the diffusion process, and casts shadows on the suitability of the currently available models. Some previous studies with classical DTI indices have highlighted MD as a promising marker of GM diffusivity changes in several pathologies such as Alzheimer's disease (Weston et al., 2015), multiple sclerosis (Ceccarelli et al., 2007), and Parkinson (Kim et al., 2013). However, DTI is scarcely employed in the assessment of GM regions, especially in the cortex, and its ability of capturing

microstructural features and feature modulations in GM is still under debate. Conversely, thanks to the ability of capturing the EAP in complex tissue microstructures, the 3D-SHORE model might allow characterizing the signatures of hindered diffusion in GM regions as well as providing information about GM changes occurring over time.

The goal of this study was twofold. First, to complete the assessment of the potential of the 3D-SHORE-derived indices in capturing the microstructural feature modulations induced by ischemic stroke in WM by providing a comparative analysis of their performance with respect to the classical DTI-based FA and MD indices. Second, to start bridging WM and GM modeling by investigating the ability of the considered models (DTI and 3D-SHORE) for the identification of microstructural feature variations in GM, possibly hinting at plasticity processes.

## MATERIALS AND METHODS

### Dataset

Ten ischemic stroke patients (6 males, mean age:  $60.3 \pm 12.3$  years) and ten age- and gender-matched healthy subjects were enrolled in the study and underwent longitudinal MRI acquisitions on a 3T Siemens scanner (Trio, Siemens, Erlangen, Germany), as firstly reported in Granziera et al. (2012b). Of note, an optimized protocol and a dedicated 32-channel head coil with excellent signal-to-noise (SNR) properties (based on Wiggins et al., 2006) were employed, aiming at maximizing the SNR in the acquired data (as in Granziera et al., 2009). Acquisitions were performed at three time points in patients (within 1 week (*tp1*), 1 month ( $\pm 1$  week, *tp2*), and 6 months ( $\pm 15$  days, *tp3*) after the injury), and at two time points in controls (1 month apart, *tp1c*, and *tp2c*). The same structural imaging protocol was used in all cases. In particular, Diffusion Spectrum Imaging (DSI), a high angular resolution diffusion technique (Wedeen et al., 2005), was performed using a single-shot spin-echo echo-planar imaging (EPI) product sequence and the following parameters: TR/TE = 6,600/138 ms, FOV =  $212 \times 212$  mm<sup>2</sup>, 34 slices,  $2.2 \times 2.2 \times 3$  mm<sup>3</sup> resolution, GRAPPA = 2, scan time = 25.8 min. The sampling scheme consisted of a keyhole Cartesian acquisition with 258 diffusion directions covering a half q-space 3D grid with radial grid size of 5. Thirty-four different *b*-values (from 300 up to 8,000 s/mm<sup>2</sup>) were included in the acquisition and one image was acquired at *b* = 0 s/mm<sup>2</sup> (*b*<sub>0</sub> volume). Because of the inherent antipodal symmetry, the signal was duplicated on the other hemisphere yielding to 515 points.

In order to provide a measure of the diffusion data quality, SNR values were calculated for all the *b*<sub>0</sub> volumes as the ratio of the mean of the signal divided by the standard deviation of the underlying Gaussian noise (Descoteaux et al., 2011). A uniform ROI in the background was chosen for deriving the noise standard deviation while the mean signal was extracted from the corpus callosum, selected as representative ROI for the SNR calculation. The estimated values are reported in **Table 1**. High-resolution 3D T1-weighted images were also added to the protocol (TR/TE = 2,300/3 ms, FOV =  $256 \times 256$  mm<sup>2</sup>, 160 slices,  $1 \times 1 \times 1.2$  mm<sup>3</sup> resolution, scan time = 6.13 min). Besides MRI acquisitions, patients underwent clinical

**TABLE 1** | Signal-to-Noise (SNR) ratio for the diffusion datasets.

SNR-corporus callosum		
Controls	<i>tp1</i>	28.47 ± 5.33
	<i>tp2</i>	28.63 ± 4.38
Patients	<i>tp1</i>	28.21 ± 4.60
	<i>tp2</i>	29.65 ± 6.24
	<i>tp3</i>	27.25 ± 4.55

SNR values were calculated on the *b*<sub>0</sub> volume of each subject. In particular, a uniform ROI in the background was chosen for estimating the noise standard deviation while the mean signal was extracted from the corpus callosum, selected as representative ROI for the SNR calculation. Mean ± standard deviation values across subjects are reported, considering each time point and group separately.

neurological assessment following the National Institutes of Health Stroke Scale (NIHSS) at each *tp*. Only the motor part of the NIHSS score was retained for further analysis. Stroke volumes were derived from the individual high-resolution T1-weighted images using the statistical parametric mapping (SPM) lesion segmentation toolbox ([www.fil.ion.ucl.ac.uk/spm/](http://www.fil.ion.ucl.ac.uk/spm/)). All the subjects signed the written informed consent to the imaging in accordance with the Declaration of Helsinki and the Lausanne University Hospital approved the protocol. Patient demographics and main clinical information are reported in Supplementary Table 1.

### Signal Modeling and Microstructural Descriptors

The classical DTI (Basser et al., 1994a,b) and the 3D-SHORE (Özarslan et al., 2008, 2013) models were used to reconstruct the EAP from which the microstructural descriptors were then derived.

The EAP can be recovered from the diffusion weighted signal attenuation  $E(\mathbf{q})$  under the narrow pulse assumption (Stejskal and Tanner, 1965) via the Fourier relationship:

$$P(\mathbf{r}) = \int_{\mathbf{q} \in \mathbb{R}^3} E(\mathbf{q}) e^{i2\pi \mathbf{q} \cdot \mathbf{r}} d\mathbf{q} \quad (1)$$

where  $P(\mathbf{r})$  is the EAP, indicating the likelihood for a particle to undergo a net displacement  $\mathbf{r}$  in the unit time and  $\mathbf{q} = \mathbf{q}\mathbf{u}$  is the sampling position, with  $\mathbf{u}$  being unit vector of the reciprocal space, or *q*-space.

DTI assumes that the diffusion propagator can be described by a single 3D Gaussian distribution (Basser et al., 1994a,b) from which a  $3 \times 3$  symmetric positive-definite matrix is derived (*D*, diffusion tensor) and used to compute the classical tensor-based indices (MD and FA) as follows:

$$MD = \frac{(\lambda_1 + \lambda_2 + \lambda_3)}{3} \quad (2)$$

$$FA = \sqrt{\frac{1}{2} \frac{(\lambda_1 - \lambda_2)^2 + (\lambda_2 - \lambda_3)^2 + (\lambda_1 - \lambda_3)^2}{\lambda_1^2 + \lambda_2^2 + \lambda_3^2}} \quad (3)$$

where  $\lambda_1, \lambda_2, \lambda_3$  are the eigenvalues of  $D$ . Only  $b < 1,500 \text{ mm}^2/\text{s}$  were used for the DTI analysis, corresponding to 32 gradient directions.

The novel microstructural indices explored in this work were calculated by fitting the SHORE model (Özarslan et al., 2008, 2013) based on the solutions of the 3D quantum harmonic oscillator in the formulation using the orthonormalized basis:

$$E(\mathbf{q}) = \sum_{l=0, \text{even}}^{N_{\max}} \sum_{n=l}^{\frac{(N_{\max}+l)}{2}} \sum_{m=-l}^l c_{nlm} \Phi_{nlm}(\mathbf{q}) \quad (4)$$

In this equation,  $N_{\max}$  is the maximal order of the functions,  $\Phi_{nlm}(\mathbf{q})$  are the functions forming the 3D-SHORE orthonormal basis and are given by:

$$\Phi_{nlm}(\mathbf{q}) = \left[ \frac{2(n-l)!}{\zeta^{\frac{3}{2}} \Gamma(n+\frac{3}{2})} \right]^{\frac{1}{2}} \left( \frac{q^2}{\zeta} \right)^{\frac{l}{2}} \exp\left(\frac{-q^2}{2\zeta}\right) L_{n-l}^{l+\frac{1}{2}}\left(\frac{q^2}{\zeta}\right) Y_l^m(\mathbf{u}) \quad (5)$$

where  $\Gamma$  is the Gamma function and  $\zeta$  is a scaling parameter determined by the diffusion time and the mean diffusivity (Merlet and Deriche, 2013; Zucchelli et al., 2016a). For the 3D-SHORE model, the EAP is obtained by plugging Equation (4) into Equation (1) (Özarslan et al., 2013; Zucchelli et al., 2016a). Due to the linearity of the Fourier transform, the EAP basis is thus expressed in terms of the same set of coefficients  $c_{nlm}$  as the diffusion signal.

RTAP and RTPP (Özarslan et al., 2013) represent the integral of the EAP along the main diffusion direction and over the plane passing through the origin and perpendicular to the main diffusion direction, respectively:

$$RTAP = \int_R P(\mathbf{r}_{\parallel}) d\mathbf{r}_{\parallel} \quad (6)$$

$$RTPP = \int_{R^2} P(\mathbf{r}_{\perp}) d^2\mathbf{r}_{\perp} \quad (7)$$

where  $\mathbf{r}_{\parallel}$  is the main diffusion direction, and  $\mathbf{r}_{\perp}$  indicates the plane orthogonal to the main diffusion direction and passing through the origin. It has been shown (Özarslan et al., 2013; Zucchelli et al., 2016b) that, under the assumptions of narrow pulses and long diffusion time, RTAP and RTPP are proportional to the inverse of the mean apparent cross-sectional area and length of the compartment where diffusion takes place, respectively.

The MSD represents the mean square displacement of the water molecules in the unit time and is computed as follows:

$$MSD = \int_{R^3} P(\mathbf{r}) r^2 d^3\mathbf{r} \quad (8)$$

MSD has been proven to be closely related to the classical MD index, sharing similar patterns (Wu and Alexander, 2007).

From the EAP it is possible to derive a propagator anisotropy index, depending on the angular distance between the isotropic

part of the EAP, that is encoded in the coefficients  $c_{n00}$ , and the full EAP as in Özarslan et al. (2013):

$$PA = \sqrt{1 - \frac{\sum_{n=0}^{N_{\max}} c_{n00}^2}{\sum_{n,l,m}^{N_{\max}} c_{nlm}^2}} \quad (9)$$

Finally, the Orientation Distribution Function (ODF) can be analytically obtained from the 3D-SHORE by taking the radial integral of the EAP along a given direction (Merlet and Deriche, 2013; Özarslan et al., 2013). From the ODF it is possible to derive another measure of anisotropy, the GFA index, which can be viewed as the normalized variance of the ODF:

$$GFA = \sqrt{\frac{n \sum_{i=1}^n (ODF(\mathbf{u}_i) - \langle ODF \rangle)^2}{(n-1) \sum_{i=1}^n ODF(\mathbf{u}_i)^2}} \quad (10)$$

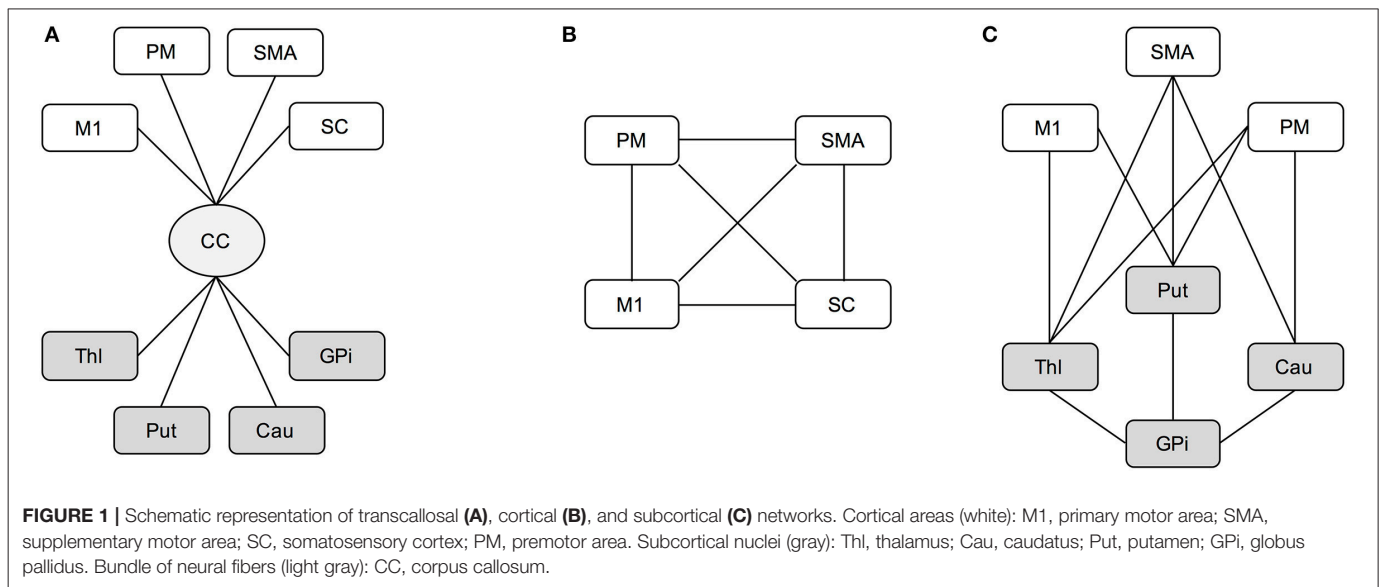
where  $ODF(\mathbf{u}_i)$  is the value of the ODF in the direction  $\mathbf{u}_i$ , and  $\langle ODF \rangle$  is the mean ODF value across all directions.

In this work, we used both classical tensor-based indices (MD, FA) along with the aforementioned 3D-SHORE-based indices (RTAP, RTPP, MSD, PA, and GFA) to detect microstructural modulations by both tract-based analyses in WM and by ROI-based analyses in GM, respectively. While the first allowed assessing the performance of the 3D-SHORE-based indices with respect to FA and MD in the motor cortical and subcortical networks, the second targets the GM in order to provide a more complete picture of changes occurring after stroke and possibly pointing at plasticity processes.

### Tract-Based Analysis of WM

The tractogram was obtained via a streamline-based algorithm with diffusion tensor ODFs computed from the DSI images (Diffusion Toolkit, CMTK, [www.connectomics.org](http://www.connectomics.org)). Individual high-resolution T1-weighted images were parcellated using Freesurfer (<http://surfer.nmr.mgh.harvard.edu/>) and the Desikan-Killiany anatomical atlas at 83-region scale (sixty-four cortical and nineteen subcortical regions) plus the corpus callosum was employed. The FLIRT tool from the FMRIB FSL software ([www.fmrib.ox.ac.uk/fsl](http://www.fmrib.ox.ac.uk/fsl)) was used for the linear (affine) registration of the T1-weighted scan to diffusion data. In particular, the diffusion baseline images (b0 volumes) were considered as reference images for estimating the registration transformation subsequently applied to back-project the subject-specific anatomical parcellation into the DSI space.

Among all the parcels, a subset of the motor regions of interest (ROIs) was considered for the analyses. For the cortical area we selected the primary motor area (M1), supplementary motor area (SMA), somatosensory cortex (SC) and premotor area (PM), which was considered as a unique region given by the joint combination of the dorsal and ventral parts from the Freesurfer parcellation, while thalamus (Thl), caudatus (Cau), putamen (Put), and globus pallidus (GPi) were selected for the subcortical part. Then, three loops involved in the motor network and linking these cortical-subcortical ROIs were considered in the analysis as in Brusini et al. (2016). In details, the transcalsal circuit (CC) gathers the set of fibers linking the corpus callosum



with each considered ROI (**Figure 1A**). The cortical loop (CORT) consists of fibers linking the four cortical ROIs (**Figure 1B**), while the subcortical loop (SUBCORT) includes the set of fibers linking cortical (except SC) with subcortical ROIs (**Figure 1C**).

Tensor-based and 3D-SHORE-based indices were finally calculated along each fiber bundle linking every pair of regions in the proposed networks. To this end, the values of the considered microstructural parameter were firstly mapped onto each fiber connecting two specific ROIs, then averaged across the whole fiber bundle. In this way, a representative microstructural value was derived for each connection of the considered network.

### Region-Based Analysis of GM

The individual high-resolution T1-weighted images were segmented into WM, GM, and cerebrospinal fluid (CSF) tissues using the SPM toolbox (Friston et al., 1995). A binary mask was derived for GM using a conservative 95% threshold on the individual probability maps.

Eighty regions from the Freesurfer parcellation were considered (brainstem and corpus callosum were excluded) and masked with the binary GM mask. Four small subcortical regions per hemisphere resulted to be empty after GM masking and were excluded from further analyses, for a total of seventy-two regions. For all indices, the mean GM value across each masked ROI was then calculated. In particular, average measures were calculated across corresponding regions in both hemispheres for controls, while averaging was constrained to the contralateral hemisphere for patients, leading in both cases to thirty-six representative GM values for each index and subject. The list of the considered regions and relative abbreviations is provided in Supplementary Table 2.

### Test-Retest Reproducibility Analysis

Before comparing the performance of the indices in the two groups and assessing their discriminative/predictive power, a preliminary step for analyzing their variability and longitudinal

stability was performed following the test-retest paradigm on controls (*tp1c* and *tp2c*). This allowed to quantitatively assess their reproducibility in physiological conditions and thus to estimate the precision of the measurements. These elements were quantified for all the microstructural indices, relying on all the representative measures coming from both tract-based and region-based analysis.

The following metrics were computed for each measure to assess the reproducibility: the intraclass correlation coefficients (ICC) and the intra- and inter-subject coefficients of variation ( $CV_{intra}$  and  $CV_{inter}$ ) (Bland and Altman, 1996; Chen et al., 2011; Pinto et al., 2016). ICC is one of the most important methods to assess the reliability of a measure, reflecting both intra- and inter-subject variability. It allows evaluating how measurements derived from the same subject are reproducible across sessions, taking into account the intra/inter-subject variability as follows:

$$ICC = \frac{\sigma_{bs}^2}{\sigma_{bs}^2 + \sigma_{ws}^2} \quad (11)$$

where  $\sigma_{bs}$  is the between-subject standard deviation and  $\sigma_{ws}$  is the within-subject standard deviation for repeated measurements. ICC levels and reliability can be evaluated using the following recommendations: poor (<0.4), fair (0.41–0.59), good (0.60–0.74) and excellent (>0.75) (Fleiss, 1981; Cicchetti, 2010).

The  $CV_{intra}$  (within-subject CV) measures the variability between sessions of the same subject, reflecting both physiological variations that can occur in a natural way and possible measurement errors (Pinto et al., 2016).  $CV_{intra}$  was computed as:

$$CV_{intra} = \frac{\sigma_{ws}}{\mu} \cdot 100 [\%] \quad (12)$$

where  $\mu$  is the mean value of the parameter across subjects and sessions (overall mean). Since only two measurements per subject

were available,  $\sigma_{ws}$  can be calculated as:

$$\sigma_{ws} = \sqrt{\left(\frac{\sum_{i=1}^k (a_{itp1} - a_{itp2})^2}{2 \times k}\right)} \quad (13)$$

where  $k$  is the number of subjects, and  $a_{itp1}$  and  $a_{itp2}$  are the measurements for subject  $i$  on test ( $tp1$ ) and retest ( $tp2$ ) sessions, respectively (Bland and Altman, 1996).

Finally, the  $CV_{inter}$  (between-subject CV) measures the stability across the group, reflecting the inter-individual variability. For each index, the  $CV_{inter}$  was initially computed for each session as follows:

$$CV_{inter_j} = \frac{\sigma_{tpj}}{\mu_{tpj}} \cdot 100 [\%] \quad (14)$$

where  $tpj$  represents the session  $j$  ( $j = 1, 2$ ),  $\mu_{tpj}$  and  $\sigma_{tpj}$  are the mean and standard deviation values, respectively, calculated across all the subjects for the considered session  $tpj$ . The representative  $CV_{inter}$  measure was then computed as the mean of the  $CV_{interj}$  from the two sessions.

For biological measurements from MRI,  $CV_{intra} \leq 10\%$  and  $CV_{inter} < 15\%$  are considered as acceptable (Heiervang et al., 2006; Marenco et al., 2006).

For tract-based measures, ICC and  $CV_{intra}$  were a single measure for each loop, as all the connections belonging to the corresponding network were grouped for providing a global representative measure of network reproducibility, in line with (Brusini et al., 2016). Conversely, the representative  $CV_{inter}$  metric was first computed for each tract and then summarized for each loop by the mean  $\pm$  standard deviation (SD) values across connections. This allowed to evaluate the stability across subjects and also the inter-subject variability across the different structural links of each network.

For region-based analysis,  $CV_{intra}$  and ICC were computed for each ROI individually (mean  $\pm$  SD values across GM ROIs), while the representative  $CV_{inter}$  metric was initially calculated for each region and then reported as mean  $\pm$  SD values across GM ROIs. This again allowed to appreciate the variability across the GM structures.

## Statistical Analysis on Tract-Based Outcomes—Patients and Controls

After the reproducibility analysis, the outcome measures from tract-based analysis were assessed for depicting possible differences between patients and controls and determining the discriminative power of the different indices. In particular, for each index and network, the percentage absolute changes in mean values between  $tp$  ( $\Delta_{tp}$ ) were calculated as in Brusini et al. (2016).

Since the Kolmogorov–Smirnov normality test confirmed the normal distribution of the percentage values, statistical comparisons with the unpaired  $t$ -test were performed to detect significant differences between delta changes in controls ( $\Delta_{tp12c}$ ) and  $\Delta_{tp12}$ ,  $\Delta_{tp23}$ ,  $\Delta_{tp13}$  calculated in the patient cohort. While in our previous work (Brusini et al., 2016) the False Discovery Rate (FDR) correction was applied to the statistical results, here a more conservative Bonferroni adjustment ( $\alpha = 0.05$ ) was used

to correct for multiple comparisons across indices. This approach was chosen in order to further strengthen the statistical findings and highly reduce false positive results.

In addition, in order to assess the predictive power of both tensor-derived and 3D-SHORE-derived indices, different linear regression models were considered and their performance in predicting the clinical motor outcome at 6 months (NIHSS at  $tp3$ ) was tested. First, a linear regression model including only clinical information at baseline (age, stroke size, and NIHSS motor scores at  $tp1$ ) as predictors was calculated for reference. Then, for each network, three types of regression models were built and compared as opposed to what was done in our previous work (Brusini et al., 2016), where a single model combining clinical information with a set of 3D-SHORE-based descriptors (GFA, PA, R, RTAP, RTOP, RTPP) was considered. In detail, the following models were considered:

- 1) *Tensor-based model (TBM)*: the average across all the connections of the considered loop at  $tp1$  was calculated for each index (MD, FA) and both mean values were included as predictors along with age, stroke size and NIHSS at  $tp1$ .
- 2) *3D-SHORE-based model (SBM)*: the average across all the connections of the considered loop at  $tp1$  was calculated for each index (GFA, PA, RTAP, RTPP, MSD) and these mean values were included as predictors along with age, stroke size and NIHSS at  $tp1$ .
- 3) *Global microstructural model (GBM)*: all the indices at  $tp1$  (both tensor-derived and 3D-SHORE-derived) were included as predictors, after having calculated their individual mean value across all the connections of the considered loop. No clinical information was included.

All the linear regression analyses were performed in SPSS, version 18 (SPSS, Inc., Chicago, Illinois), setting  $p = 0.05$  as significance threshold of the overall  $F$ -test to determine whether the regression model significantly predicts the clinical motor outcome. A backward elimination strategy was utilized to obtain a parsimonious regression model. In details, a full model that includes all the predictor variables was initially created. Then, each subsequent step removed the least significant variable in the model until all the remaining variables had individual  $p$ -values smaller than the selected criterion. The default criterion in SPSS (based on the probability of F-to-remove, with  $p_{out} = 0.10$ ) was chosen for deleting a predictor that had little or no influence on the dependent variable. For each optimal model, the calculated  $R^2$  value was adjusted for the number of predictors included, in order to perform a valid comparison across the different regression models and penalize the addition of extraneous predictors. The following equation, as implemented in SPSS (Ezekiel, 1930; Kirk, 1996), was applied:

$$R_{adj}^2 = 1 - \frac{(1 - R^2)(N - 1)}{N - k - 1} \quad (15)$$

where  $N$  is the sample size and  $k$  is the number of predictors in the corresponding model, i.e., those that were not deleted by the backward selection process, excluding the constant.

## Statistical Analysis on GM Region-Based Outcomes—Patients and Controls

In order to compare the GM region-based measures, a three-way mixed (within-between) analysis of variance (ANOVA) was firstly performed for each microstructural index to test the significance of different factors, using the mean index value as dependent variable. Three independent variables were considered: Time with two levels and Region with thirty-six levels (within-subject factors) plus Group with two levels as between-subject factor. In addition, a further two-way repeated measures ANOVA was performed on the patient group data in order to assess for the presence of longitudinal changes in contralateral GM structures across all temporal scales. Also in this case the mean value for each index was used as dependent variable in the corresponding ANOVA, while two independent variables were included: Time with three levels and Region with thirty-six levels.

For each ANOVA, Mauchly test was used to assess the sphericity assumption and Greenhouse-Geisser epsilon adjustments for non-sphericity were applied where appropriate. *Post-hoc* tests adjusted for multiple comparisons with the Bonferroni correction were used when significant interactions were found. For all statistical tests, performed in SPSS v.18,  $p < 0.05$  was considered to be significant.

## RESULTS

### Qualitative Assessment of dMRI-Based Indices

Classical tensor-derived and 3D-SHORE-derived indices were estimated in all subjects and *tp*. **Figures 2, 3** show the different maps calculated for each index across times in a representative control and a representative ischemic stroke patient, respectively. For ease of visualization and for the sake of clearer presentation, the three anisotropy measures were normalized to the respective maximum index value, while the square-root of the RTAP maps was extracted to report the values in the same range of RTPP, as in Avram et al. (2016).

All the anisotropy measures as well as RTAP and RTPP maps revealed high values in WM, while lower values were reached in GM and especially in voxels with strong CSF contribution. The opposite pattern was visible in MD and MSD maps, where WM appeared to be hypointense due to restricted diffusion while higher values were reached in GM and CSF tissues. These patterns were consistent across subjects and temporal scales. Comparing GFA, PA, and FA, both control and patient representative slices revealed a higher WM/GM contrast for the normalized 3D-SHORE-derived anisotropy measures that also appeared to be less noisy and more uniform throughout WM in comparison to the classical FA. Moreover, FA appeared to have lower values in regions with large fiber orientation dispersions where the single tensor representation precludes the possibility to cope with complex structures leading to drops. RTAP maps were hyperintense in regions of coherently packed WM fibers, while RTPP was similar in GM and WM tissues. Finally, MSD, and MD visually demonstrated a correlated behavior, appearing brighter

in regions where water particles are free to diffuse like ventricles and darker in regions of restriction like WM.

In the stroke patient reported in **Figure 3**, a large ischemic lesion can be appreciated in the left hemisphere (cortico-subcortical areas) and the modulation of tissue microstructure is visible across the different *tp*. The lesion was hypointense in GFA, PA, MSD, FA, and MD at *tp1*, while markedly brighter than the other tissues in RTAP and RTPP. After 1 month from the injury (*tp2*), the contrast was reversed for these two indices, such that the lesion appeared hypointense as in the anisotropy measures, where hyperintensities within the lesion became visible in MSD and MD. Such a trend persisted at 6 months after the initial brain damage (*tp3*).

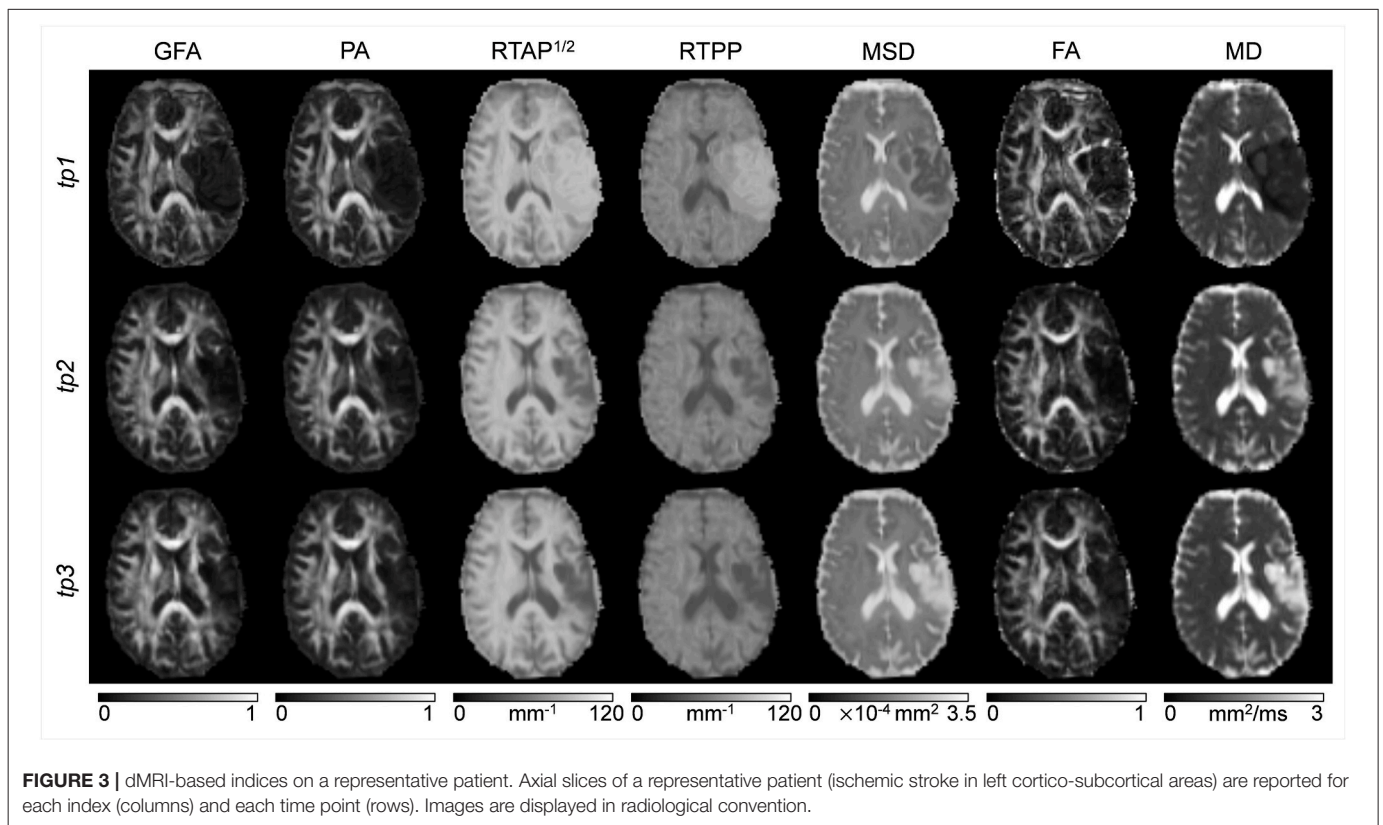
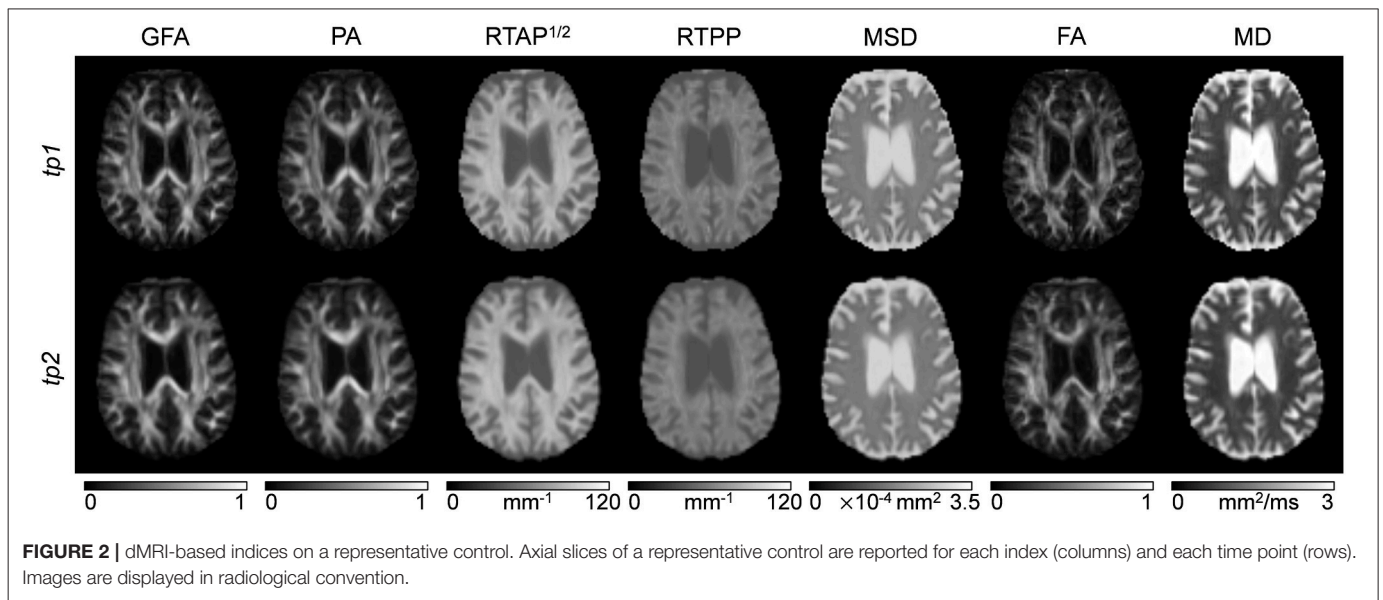
For all the subsequent quantitative analyses, we investigated the contralateral hemisphere only, where microstructural changes after stroke might be subtle and not visually detectable.

### Test-Retest Reproducibility on Healthy Controls

In terms of test-retest reproducibility, tract-based results highlighted excellent consistency across sessions in the three networks for tensor-derived as well as 3D-SHORE indices, with ICC > 0.8 in almost all cases and values close to unity for the SUBCORT loop (Supplementary Table 3). Indeed, the highest ICC was obtained for PA in SUBCORT (ICC = 0.96), followed by MSD in the same network (ICC = 0.95). Conversely, MSD together with RTPP reached the lowest values in CORT, although still amenable to be judged as having good reliability (ICC = 0.67 and ICC = 0.59, respectively). This high reliability was matched with high intra-subject stability across sessions as measured by  $CV_{intra}$  values, well below 10% and, in most of the cases, also below 5%. The lowest stability was found in the CC loop for MD ( $CV_{intra} = 7.7\%$ ), while MSD resulted to be the index with the highest stability in all the loops, reaching a remarkable 1.1% within-subject variability in the SUBCORT network.

GM region-based reproducibility results are reported in **Table 2** in terms of mean and SD values across ROIs. RTAP, RTPP, MSD, and MD reached excellent consistency, with mean ICC > 0.90 and very low SD across ROIs (<0.10). Conversely, all the anisotropy measures showed only good reliability and more variability across the different GM structures. This was further confirmed by the  $CV_{intra}$  measure, reporting mean values <10% in all cases albeit higher for GFA, PA, and FA in comparison to the other microstructural indices. Also in this case, MSD reached the lowest variability values with a limited spread around the mean.

**Figure 4** shows the inter-subject variability results ( $CV_{inter}$ ) represented as mean  $\pm$  SD across all the connections of a given loop for tract-based analysis, and across ROIs for region-based analysis on GM. As expected, the between-subject variability was higher than the within-subject, although the mean  $CV_{inter}$  values were  $\leq 15\%$  in all cases. Regarding the network analysis, similar patterns in the three loops were observed for each index, with RTPP and MSD featuring the lowest variability across subjects (RTPP:  $CV_{inter} = 4.67 \pm 2.53\%$  in CORT; MSD:  $CV_{inter} = 2.36 \pm 1.82\%$  in SUBCORT). Conversely, RTAP was the index showing



more variability in all loops, especially in CC. The same trend was observed in the ROI-based analysis on GM, where the  $CV_{inter}$  values were similar to those resulting from tract-based analysis with RTPP and MSD reaching the highest stability (RTPP:  $CV_{inter} = 4.87 \pm 1.34\%$ ; MSD:  $CV_{inter} = 6.49 \pm 1.72\%$ ). It is worthy of note that all the values were within the recommended 15% range (Heiervang et al., 2006; Marengo et al., 2006), even though tensor-derived indices featured relatively lower stability across subjects

in GM, with the highest values reached by FA ( $CV_{inter} = 11.68 \pm 3.09\%$ ).

### Quantitative Assessment on Tract-Based Outcomes—Patients and Controls

For each index and network, the mean of the percentage absolute changes between  $tp$  is reported in **Figure 5** along with SD across subjects. The  $p$ -values resulting from the statistical analysis are



shown as stars with three levels of significance ( $*p < 0.05$ ,  $**p < 0.01$ ,  $***p < 0.001$ ). In all cases, data from the control group confirmed the limited percentage changes between time points, with mean values  $< 5\%$ , in agreement with the reproducibility results from the previous section.

Regarding the CC network, all the anisotropy measures (GFA, PA, and FA) reached the highest significance when comparing  $\Delta_{tp12c}$  and  $\Delta_{tp12}$  as well as  $\Delta_{tp12c}$  and  $\Delta_{tp13}$  ( $p < 0.001$ ). Moreover, GFA and FA showed higher significance than the other microstructural indices in the comparison between  $\Delta_{tp12c}$  and  $\Delta_{tp23}$  ( $p < 0.01$ ). MSD and MD highlighted the same patterns across time and the same statistical differences, with no significant changes between  $\Delta_{tp12c}$  and  $\Delta_{tp23}$ . In the CORT network, only few significant differences were detected between controls and patients ( $\Delta_{tp12}$ ) by GFA and RTAP, while for all the other indices the longitudinal changes, although appreciable, did not reach the statistical threshold. Conversely, several significant differences were detected again in the SUBCORT loop by all the indices at multiple time scales, except for RTAP and RTPP which did not depict significant changes between  $\Delta_{tp12c}$  and  $\Delta_{tp23}$ . All the anisotropy measures confirmed the presence of marked changes over time involving also

this network, with similar patterns to the findings shown in CC.

Extending the preliminary analyses on predictive models reported in Brusini et al. (2016), the tract-based results in patients were further used to predict the clinical motor outcome at  $tp3$  by relying on several regression models. The reference linear regression model including only clinical variables at baseline (age, stroke size and NIHSS motor score at  $tp1$ ) and avoiding microstructural indices could predict the NIHSS outcome at  $tp3$  with low correlation ( $R^2 = 0.546$ ; adjusted  $R^2 = 0.489$ ;  $p < 0.05$ ). The TBM, enclosing MD-FA at  $tp1$  plus the clinical variables, allowed increasing the prediction capability of the reference model in the CORT and SUBCORT networks (Figure 6, first row). In detail, the TBM for SUBCORT presented the best performance ( $R^2 = 0.975$ ; adjusted  $R^2 = 0.955$ ;  $p < 0.001$ ) holding MD, FA, stroke size and age as relevant predictors. In the case of the CORT network, a higher correlation than the reference model was found with the TBM retaining only stroke size and MD as significant predictors ( $R^2 = 0.700$ ; adjusted  $R^2 = 0.614$ ;  $p < 0.05$ ). Conversely, the TBM for CC did not include any microstructural index, returning the reference model as the optimal one.

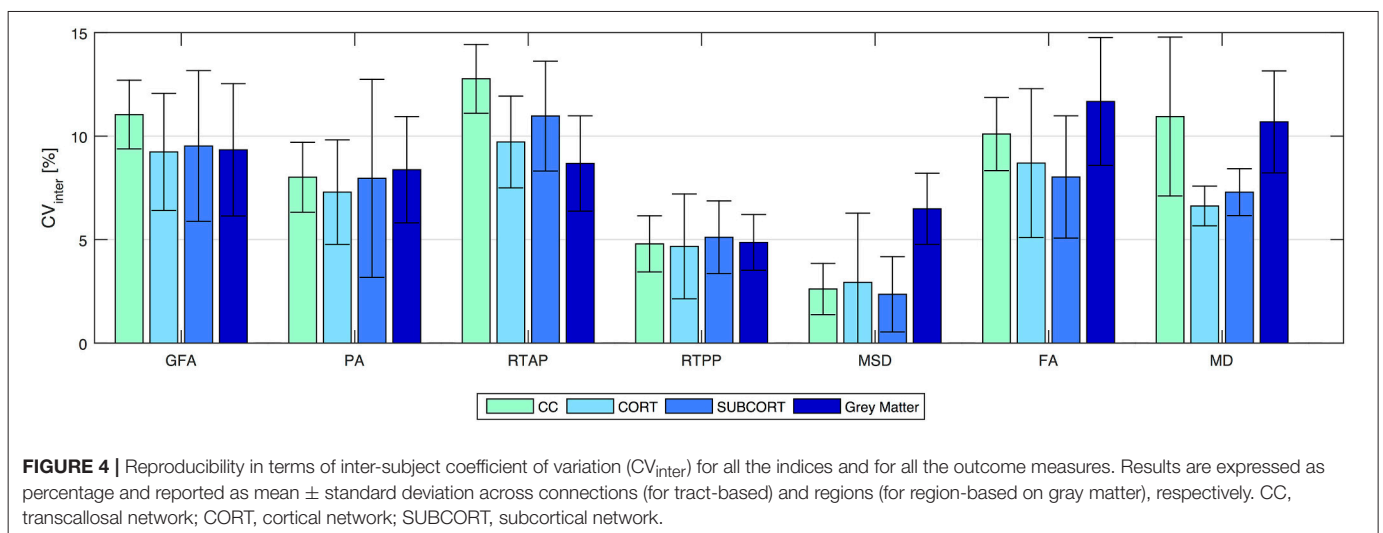
The SBM, embedding the five 3D-SHORE indices at  $tp1$  plus the clinical variables, reached the highest correlation in the SUBCORT network ( $R^2 = 1$ ; adjusted  $R^2 = 0.998$ ;  $p < 0.001$ ) (Figure 6, second row). The optimal predictive model held clinical variables plus GFA, MSD, RTPP, and PA as significant predictors. The SBM for CORT excluded all the microstructural indices, leading to the reference model as the optimal one. Finally, in the CC network the SBM presented a slightly lower correlation than the reference ( $R^2 = 0.454$ ; adjusted  $R^2 = 0.385$ ;  $p < 0.05$ ) but highlighting RTPP as the only significant predictor.

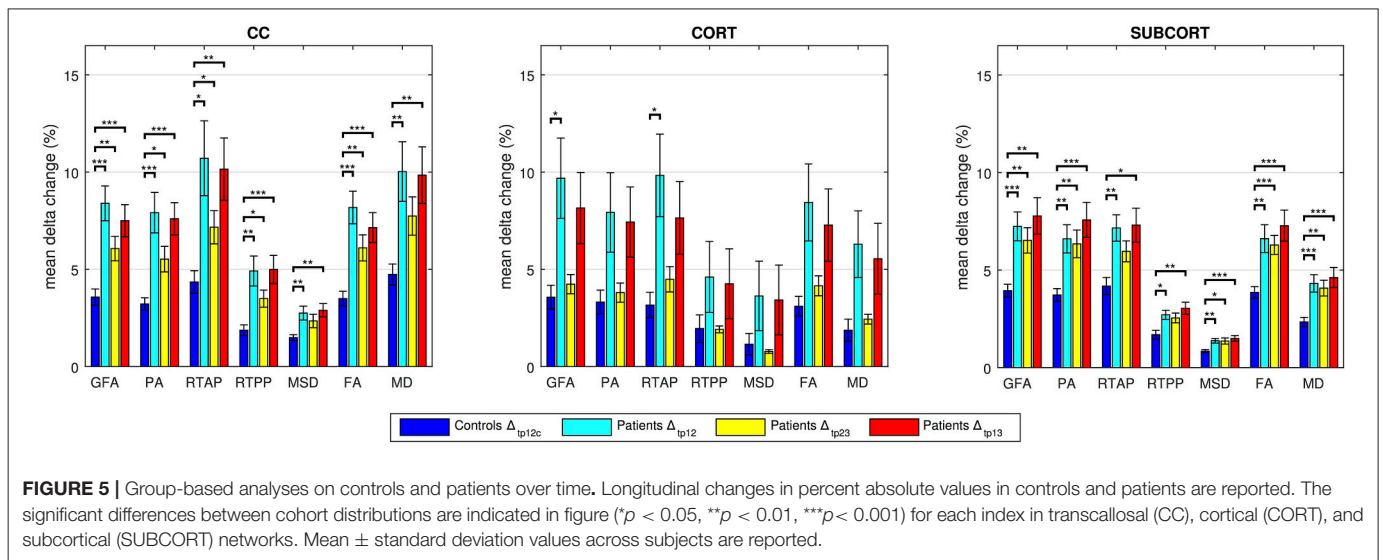
The GBM, including only the dMRI-based indices, allowed to substantially increase the capability to timely predict the motor outcome compared to the clinical reference model (Figure 6, third row). In detail, the SUBCORT network provided again the highest correlation ( $R^2 = 0.728$ ; adjusted  $R^2 = 0.694$ ;  $p < 0.01$ ) keeping only RTPP as significant predictor. The predictive

**TABLE 2 |** Reproducibility for gray matter (GM) outcomes.

	ICC	CV <sub>intra</sub> %
GFA	0.63 ± 0.22	7.36 ± 2.96
PA	0.61 ± 0.24	6.82 ± 2.42
RTAP	0.91 ± 0.07	3.40 ± 1.63
RTPP	0.92 ± 0.07	1.73 ± 0.78
MSD	0.93 ± 0.09	1.97 ± 0.75
FA	0.66 ± 0.17	9.25 ± 3.59
MD	0.94 ± 0.08	3.09 ± 1.71

Results are quantified in terms of intra-class correlation coefficient (ICC) and intra-subject coefficient of variation (CV<sub>intra</sub>) for all the indices. In particular, mean ± standard deviation values across all the considered GM regions are reported.





model for the CC network also featured high correlation ( $R^2 = 0.713$ ; adjusted  $R^2 = 0.631$ ;  $p < 0.05$ ) maintaining MD and RTPP as predictors, while GFA, RTAP, and MD were retained in the predictive model for CORT. This network led to the GBM with the lowest correlation ( $R^2 = 0.724$ ; adjusted  $R^2 = 0.586$ ;  $p < 0.05$ ), but still higher than the reference model. Further details on the predictive models and the retained predictors are reported in the Supplementary Tables 4.

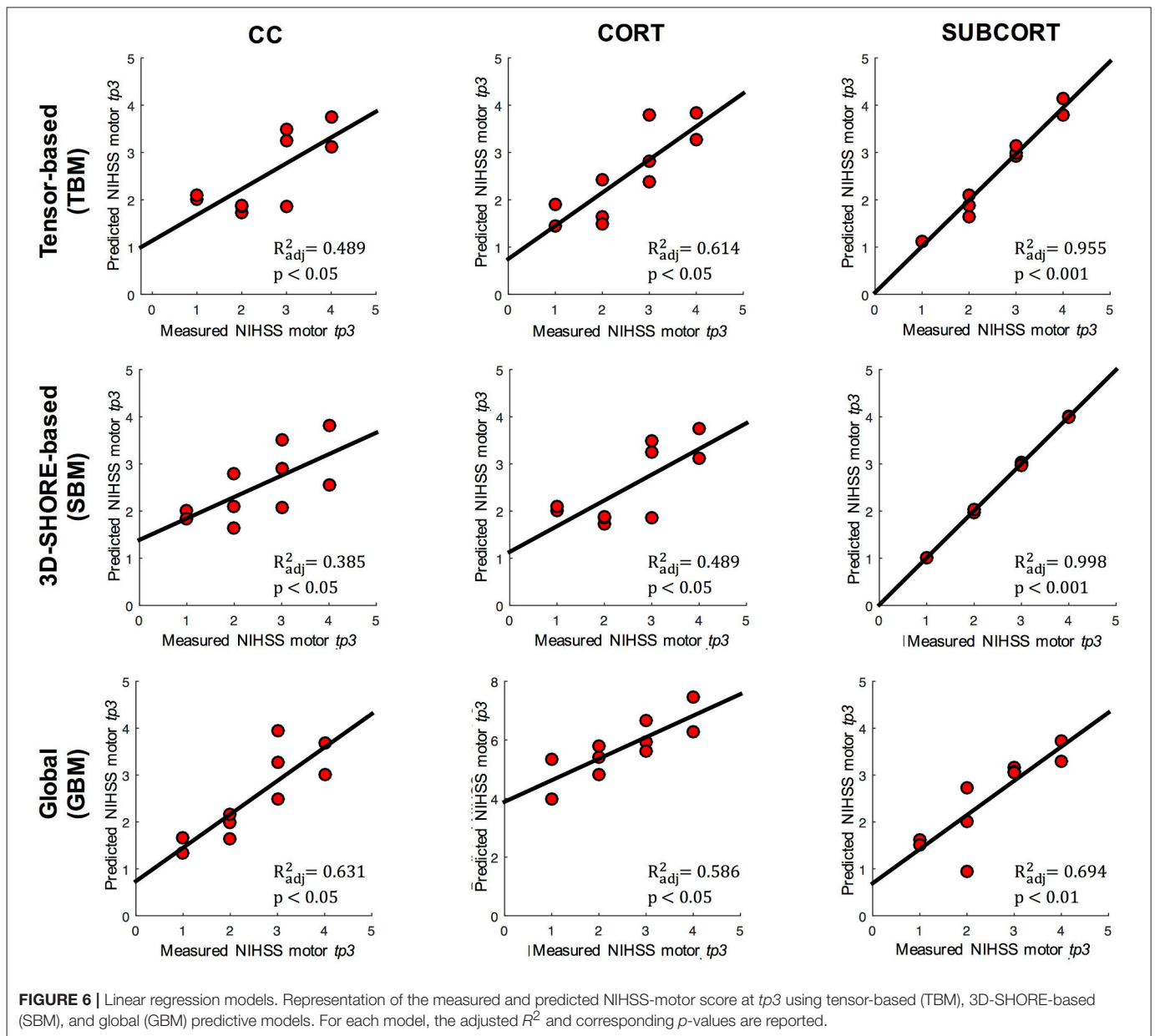
## Quantitative Assessment on GM Region-Based Outcomes—Patients and Controls

Regarding the control vs. patient analyses on the outcomes from the region-based quantification in GM tissues, the mixed ANOVA revealed a significant three-way interaction between Group, Time (TP) and Region (ROI) for all the anisotropy measures (GFA, PA, and FA) and RTPP. Details about these statistical results are reported in **Table 3**. For the four indices, *post-hoc* Bonferroni tests revealed significant between-group differences in several regions at both time scales, showing in these cases higher values in patients than controls (**Figure 7**). While the most widespread changes were detected in terms of anisotropy at  $tp1$ , four common regions were identified as significantly altered (Patients > Controls) also by RTPP. In detail, the inferior temporal gyrus (ITG) and the lateral occipital cortex (LOC) were in common at both  $tp$ , while the lateral orbitofrontal cortex (lOFC) and the middle temporal gyrus (MTG) presented high significance ( $p \leq 0.01$ ) at  $tp1$  and  $tp2$  in GFA, PA, and RTPP and only at  $tp1$  in FA (**Figure 7**). RTPP changes were more visible at  $tp2$ , with several regions showing higher values in patients compared to controls and non-significant anisotropic differences. The remaining indices failed to reach a significant three-way interaction even though control vs. patient differences can be visually appreciated in **Figure 7A**. In particular, for RTAP a similar trend to the anisotropy measures was detected in all the regions, especially at  $tp1$  over motor areas and subcortical

nuclei as PM, SMA, SC, M1 and Thal, Cau and Put (Patients > Controls). For MSD, while few ROIs presented relatively higher values in patients at  $tp1$ , there was an overall increase in all regions at  $tp2$  (Patients > Controls), except for the temporal pole where lower values were found over time in this group. Finally, MD patterns were in line with MSD results, although with less marked changes between groups.

Moving a step backward in the mixed ANOVA, all the indices except RTAP revealed a significant two-way interaction between Group and ROI confirming that, considering the overall time scales, there were differences in specific GM regions between the two groups (**Table 3**; Supplementary Figure 1). The anisotropy measures were highly consistent, with FA highlighting more widespread increased values in GM for patients as before. Finally, only GFA, PA, and FA revealed an overall significant main effect of Group (between-subject factor), as reported in **Table 3**.

Considering the longitudinal analysis on the patient measures only, again all the anisotropy indices along with RTPP and MD revealed a significant interaction between TP and ROI. In details, for GFA  $F_{(70, 630)} = 1.61$ ,  $p = 0.002$ ; for PA  $F_{(70, 630)} = 1.52$ ,  $p = 0.006$ ; for RTPP  $F_{(70, 630)} = 1.47$ ,  $p = 0.01$ ; for FA  $F_{(70, 630)} = 1.92$ ,  $p < 0.0001$ ; and for MD  $F_{(70, 630)} = 1.76$ ,  $p = 0.0003$  (Supplementary Table 5). *Post-hoc* Bonferroni tests (**Figure 8**) highlighted for the three anisotropy measures consistently significant differences over the lingual gyrus (LgG) for  $tp1$  vs.  $tp2$ , and in the medial orbitofrontal cortex (mOFC) for  $tp1$  vs.  $tp3$ . Moreover, FA presented LgG differences for  $tp1$  vs.  $tp3$ , and in the precuneus (PCN) for both  $tp1$  vs.  $tp2$  and  $tp1$  vs.  $tp3$ . In all these statistically significant changes, higher values were detected just after the stroke event ( $tp1$ ) in comparison to  $tp2$  and  $tp3$ . Conversely, an opposite trend was found for RTPP detecting a single region [frontal pole (FP)] with higher values at  $tp2$  compared to  $tp1$ . For MD, despite the significant interaction no regions survived the Bonferroni corrections of the *post-hoc* paired tests (**Figure 8**). When using a less conservative approach [Least Significant Different (LSD) *post-hoc* tests], five regions, including PM, SC, and Thal, turned



out to be significantly increased at *tp3* compared to *tp2* and *tp1* (Supplementary Figure 2). Applying LSD *post-hoc* tests also to the other indices, the anisotropy measures revealed more widespread regions of increased values in the early phase (*tp1*) in comparison to the other two time points, consistently with the results from the mixed ANOVA. GFA and PA, in addition, showed higher values at *tp3* compared to *tp2* over two motor regions, e.g., Put and M1, respectively. Finally, RTPP confirmed a significant increase over time (both *tp2* and *tp3*) in comparison to *tp1* in the FP region.

Regarding the other two indices that did not show a significant interaction (RTAP and MSD) and were thus precluded to be evaluated with *post-hoc* tests, a different trend was visible across time with a series of appreciable longitudinal differences (Figure 8A). In particular, RTAP revealed a similar behavior to

the anisotropy measures, with higher values at *tp1* that decreased over time, especially at *tp3*. Conversely, MSD highlighted higher values over time, as in the case of MD, with marked visual increases at *tp3* over several regions (as PM, SC, FP, Thal, Put, Cau).

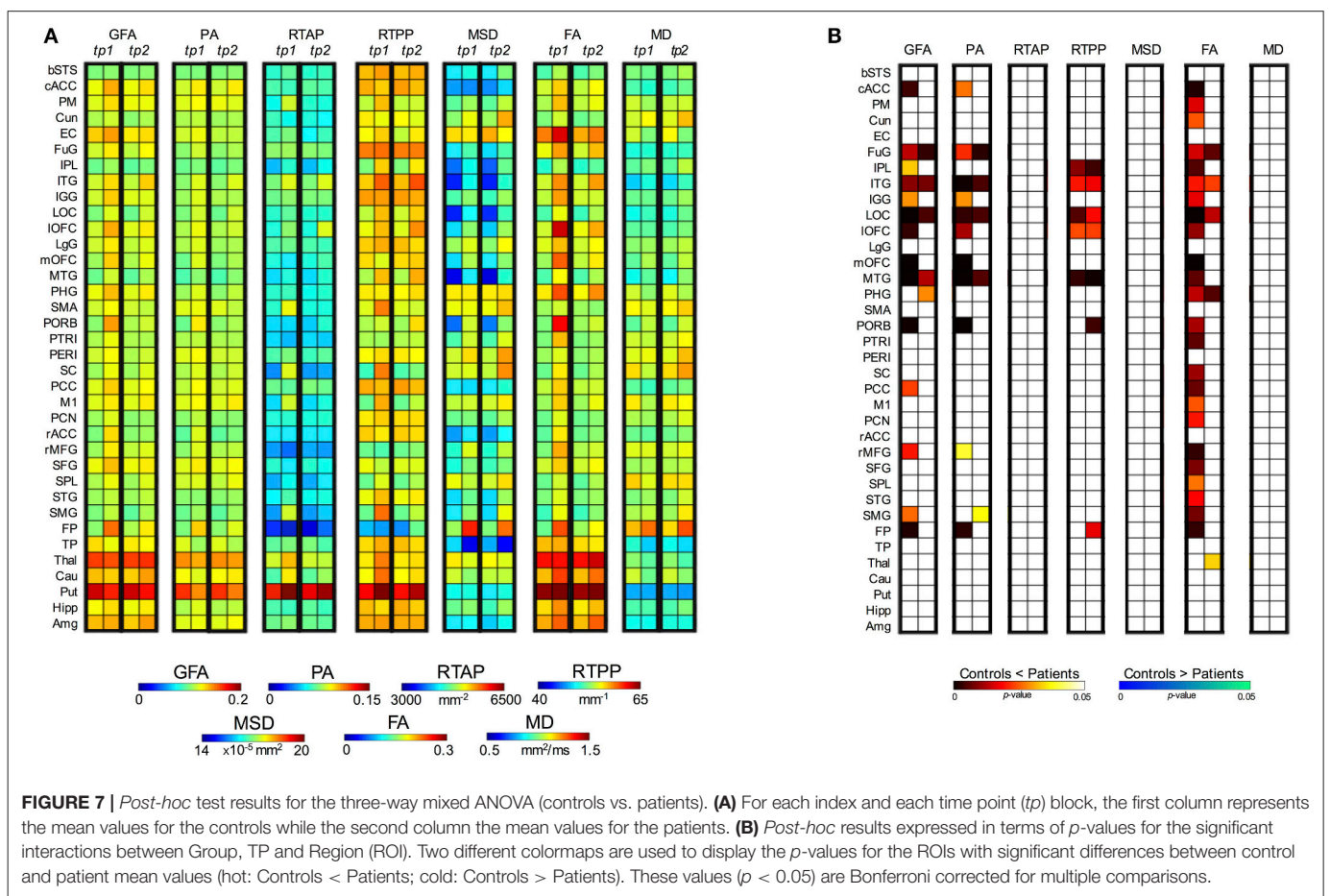
## DISCUSSION

In this study, our results suggest that 3D-SHORE-based microstructural descriptors obtained from DSI data are capable to quantify the remodeling of WM tracts and GM regions involved in motor recovery after ischemic stroke. 3D-SHORE-based indices proved to perform similarly to the classical DTI indices (FA and MD) and revealed common patterns across the networks and ROI evaluated in the analyses.

**TABLE 3** | ANOVA results (three-way mixed ANOVA) for the control vs. patient comparison of gray matter outcomes.

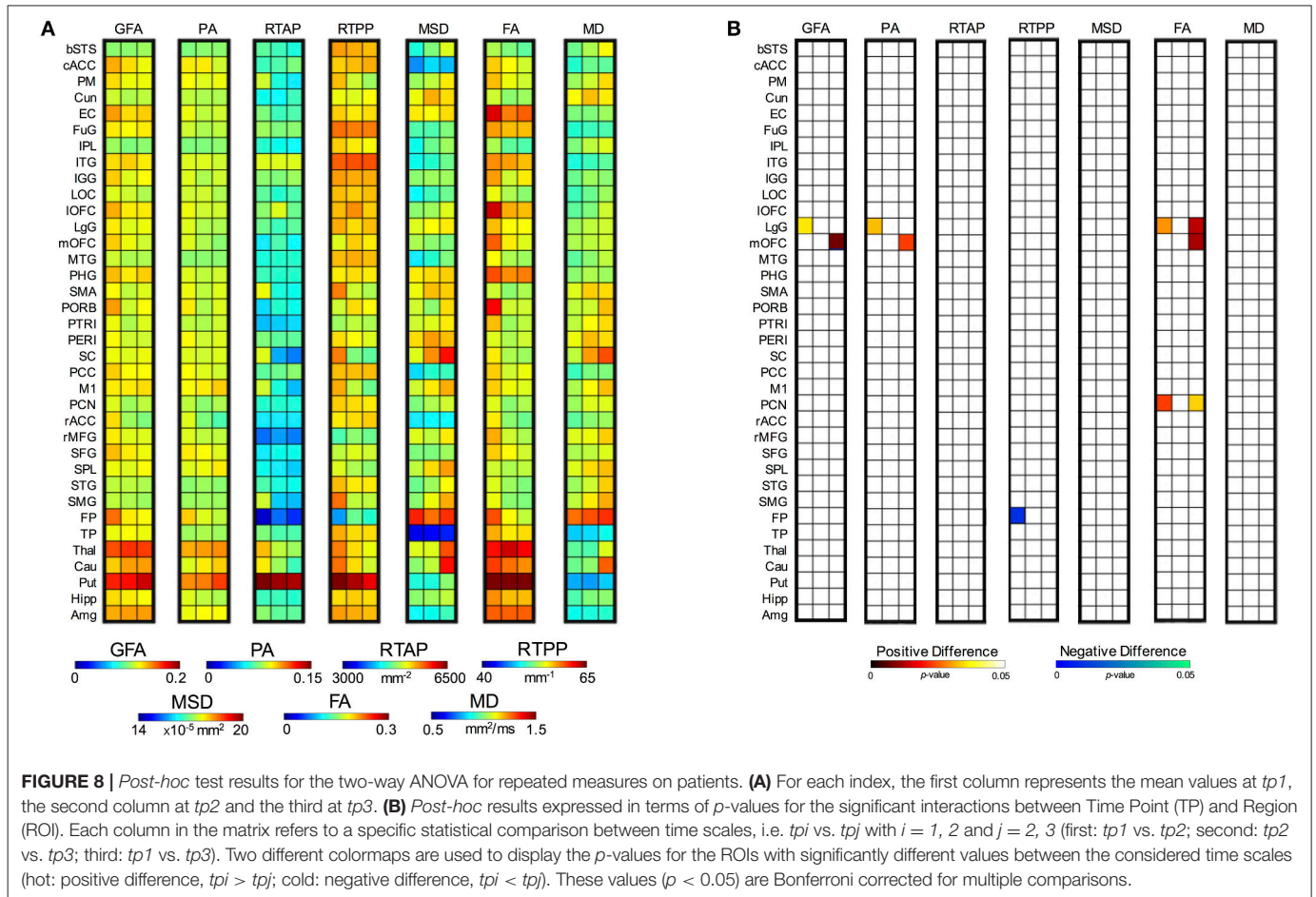
	Between-subject		Within-subject			
	Group		Group*ROI		Group*TP*ROI	
	F-ratio (1, 18)	p-value	F-ratio (35, 630)	p-value	F-ratio (35, 630)	p-value
GFA	6.205	0.023*	2.340	<0.001*	2.235	<0.001*
PA	6.256	0.022*	2.218	<0.001*	1.669	0.010*
RTAP	1.548	0.229	1.249	0.157	1.326	0.102
RTPP	2.064	0.168	2.152	<0.001*	1.843	0.003*
MSD	2.681	0.119	2.601	<0.001*	0.552	0.990
FA	7.346	0.014*	2.082	<0.001*	2.731	<0.001*
MD	0.186	0.671	1.825	0.003*	1.105	0.314

The three independent variables were Group (between-subject factor), Time Point (TP) and Region (ROI) (within-subject factors), while the dependent variable was the mean index value. Group, along with Group\*ROI and Group\*TP\*ROI interactions, are expressed in terms of F-ratio (degree of freedom, error) and p-values. \*, significant values.



Considering their performance and different nature, their combination in clinical studies would allow to provide a more detailed and specific tissue characterization, allowing to disentangle different conditions where tensor-based indices take the same values. For instance, DTI cannot distinguish between a reduction of FA caused by crossing fibers and one caused by a decrease of neural density in a voxel. Conversely, the joint exploitation of RTAP and RTPP can allow disentangling such

ambiguity, as RTAP and RTPP both diminish in the case of neuronal density reduction, while RTAP decreases and RTPP increases for crossing fibers, as previously reported (Zucchelli et al., 2016a). In addition, the combination of tensor-based and SHORE-based indices in the linear regression models allowed to greatly increase their ability to predict the clinical motor outcome in all the considered networks. To the best of our knowledge, this is the first study focusing on the



quantitative comparison between 3D-SHORE-based and tensor-based descriptors in healthy subjects and in a patient population, aiming at demonstrating their behavior in different brain conditions/tissues and accomplishing an essential step toward their applicability as viable tissue markers.

## Qualitative Assessment of dMRI-Based Indices

A growing body of literature is currently reporting the advantages of using multiple b-values in terms of both detecting fiber crossings (Sotiropoulos et al., 2013; Jeurissen et al., 2014) and recovering the tissue microstructure (Assaf and Basser, 2005; Zhang et al., 2012; Kaden et al., 2016). Because of these facts, nowadays, sampling schemes presenting higher b-values (as DSI and multi-shell) are becoming popular in research and started to appear also in clinical application. In order to fully exploit advanced dMRI datasets, reconstruction models that require multiple b-values such as the 3D-SHORE are necessary and therefore will become more common in this field. In this context, it is therefore necessary to provide an extensive characterization of these indices in describing tissues in physiological and pathological condition, as we did for stroke patients. In line with the findings firstly described by Özarlan et al. (2008, 2013), our results suggest that 3D-SHORE-based indices can provide a wide set of information, reflecting meaningful tissue

properties as visually appreciable from the different maps. In particular, the values estimated in our healthy population for each index and their spatial distribution across the different anatomical structures appear to be in agreement with the available literature results (Özarlan et al., 2013; Avram et al., 2016; Zucchelli et al., 2016a), with a high consistency across subjects and time. These 3D-SHORE-based metrics are able to provide accurate microstructural information especially in brain regions characterized by complex architectures and geometries, to which the classical indices have low sensitivity. GFA and PA represent alternative measures of anisotropy to the classical FA, based on different mathematical formulations. Indeed, while GFA is a measure of the ODF variance, PA is derived from the EAP as a measure of its deviation from the isotropic component, and FA is computed from the tensor eigenvalues. In consequence, they provide different descriptors of the diffusion anisotropy with a high degree of correlation. However, GFA and PA are able to more properly quantify the anisotropy, presenting more contrast between the GM and regions with multiple fiber crossings in which the FA usually results in the same value. The two zero-displacement probability measures derived from SHORE reflect diffusion restriction in different directions, respectively radially (RTAP) and axially (RTPP) to the main diffusion direction (Özarlan et al., 2013). Consistently, RTAP maps exhibited high values in regions of coherently packed WM fibers, as the corpus

callosum which is less contaminated by partial volume effects. RTPP values were similar in both GM and WM tissues featuring less WM/GM contrast. This could suggest similar apparent axial diffusivity for WM and GM, even though the mapping of this measurement to real tissue microstructural properties is still an open issue. Finally, MSD and MD were consistently higher in regions featuring free diffusion, like the CSF and in areas with ischemic oedema (Alexander et al., 2007). These two indices are directly related via the Einstein diffusion equation as reported in the works of Wu and Alexander (2007) and Hosseinbor et al. (2013) and, accordingly, are visually correlated.

Evaluating qualitatively the longitudinal maps derived from the stroke patients, the microstructural indices exhibited a different behavior in the voxels belonging to the damaged area but with a consistent pattern. Indeed, while all the anisotropy measures revealed low values within the lesion that persisted over time, RTAP and RTPP shifted from initial hyperintensities toward hypointensities after 1 month from the event (*tp2*), highlighting an opposite trend for anisotropy and restriction. This stresses the complementarity of the information brought by those indices. Furthermore, considering their opposite trend in comparison to MSD and MD (from hypo- to hyperintensities) and the ischemic nature of the stroke, these findings support the hypothesis of Avram et al. (2016) according to which the zero-displacement measures are more specific biomarkers of the presence of restricting barriers to diffusion. Interestingly, RTAP and RTPP featured the highest values at *tp1* highlighting restricted diffusion in the lesion. Moreover, we found MSD to be more contrasted than MD inside the ischemic lesion in all cases. In particular, this index seems to identify and characterize different portions of the lesion, while MD appears to be more homogeneous in the same areas. Some patients (mainly those with extensive lesions) also revealed increased MSD values in the periphery. However, as this pattern was not confirmed in all cases, a larger sample size and more focused analyses on the stroke lesion would be necessary to draw robust conclusions on this aspect, possibly pointing at an inflammatory reaction which has been previously described (Wang et al., 2007; Kim et al., 2016). Finally, the heterogeneous patterns of RTAP, RTPP, and MSD visible within the lesion 1 week after stroke could be of help for distinguishing the ischemic core from the penumbra area. This issue deserves further investigation.

## Reproducibility Analyses on Controls

The quantitative analysis of possible plasticity processes was focused on the contralateral hemisphere to the stroke. The contralesional GM and WM tissues have been widely considered as normal appearing, although the plasticity and compensatory processes that might take place in the non-injured areas are still not well understood. First of all, several complementary aspects were evaluated on healthy controls in order to quantify the reliability of these microstructural indices through a test-retest paradigm and their potentialities as novel biomarkers for stroke recovery. In particular, both 3D-SHORE-based and DTI indices exhibited high reproducibility, as quantified by ICC, and high stability, as quantified by intra/inter-subject CV parameters, on both tract and region-based outcomes.

Interestingly, for tract measures the 3D-SHORE index MSD, rarely considered in previous studies, showed the lowest intra-subject variability ( $CV_{intra}$ ) in all cases, and the highest reliability (ICC) in CC and SUBCORT. Conversely, it revealed lower, although still good, ICC values in CORT along with RTPP that resulted to be the index with the lowest reliability in this network. This is possibly related to the fact that these two indices exhibited here a relatively higher within-subject SD for repeated measurements than in the other cases, which resulted to be closer to the between-subject SD values and therefore led to lower ICC values for this loop. Despite this consideration concerning the CORT loop only, the reliability and discriminative power of MSD and RTPP were not compromised as further proven by the other group-based analyses performed in this study. To note that beside Brusini et al. (2016), where some of these indices were initially evaluated along WM tracts, no other studies have quantified the reproducibility of 3D-SHORE-based metrics across subjects and sessions. Moreover, the previous reports aiming at quantifying the reliability of classical tensor-based measures generally focused only on few major fiber tracts (e.g., corpus callosum, cingulum, fornix and arcuate fasciculus) (Heiervang et al., 2006; Danielian et al., 2010; Wang et al., 2012) rather than considering specific brain networks with different sets of tracts. Despite this main difference, our findings are in line with the results of these studies, which demonstrated reliable measurements for FA and MD featuring both inter-session  $CV_{intra} \leq 10\%$  and  $ICC \geq 0.70$ , with some variability related to the considered tract.

Regarding region-based outcomes, the reproducibility analysis in GM ROIs revealed a higher intra-subject variability for the three anisotropy measures (GFA, PA, and FA) in comparison to the other indices, with mean values still well within the 10% range, matched with a good reliability from ICC. This is possibly due to the lack of directed orientation in a tissue as GM (Basser and Ozarslan, 2009) and is in agreement with previous studies showing a two-three times higher variation of FA in regions of GM compared to WM structures (Vollmar et al., 2010; Bouix et al., 2013). Conversely, MSD and RTPP appeared again as featuring the lowest intra-subject variability and, along with MD, reached the highest ICC reliability values. The performance of FA for GM ROIs appears to be in line with previous reports evaluating DTI indices in this tissue (Veenith et al., 2013; Grech-Sollars et al., 2015), showing higher  $CV_{intra}$  values for the whole GM than for MD (8–11% vs. 2–5%, respectively) and a wide range of variation across the different GM structures (3.3–19.2%). Conversely, no studies have previously quantified the measurement precision of 3D-SHORE-based indices in GM regions, therefore our findings add an important step to the current literature on the topic and their reassurance in terms of reliability encourages their use for evaluating GM tissues as well.

Considering as additional reliability measure the between-subject variability, we found average  $CV_{inter}$  values well below the 15% threshold for both tract- and region-based outcome. Among the seven variables, RTPP and MSD generally had lower  $CV_{inter}$  than the other metrics with average values  $\leq 6\%$ . Tensor-based measures revealed overall lower between-subject stability than 3D-SHORE-based indices, especially in the GM ROIs where the

average values were around 10%. Previous studies have indicated FA and MD as the measures with lower  $CV_{inter}$  in different WM fiber tracts, for example Wang et al. (2012) reported average values in the range 2.4–7.6% for FA and 1.7–9.9% for MD respectively, while Grech-Sollars et al. (2015) showed mean inter-subject values <6% for the whole GM and WM regions (not tracts). Our results confirmed the good inter-subject stability for FA and MD but demonstrated that the 3D-SHORE-based indices improve on the classical measures in terms of between-subject variability in most of the cases. The latter observation demonstrated the gain in using a multi-b-values model such as 3D-SHORE. In particular, GFA and MSD were already defined the analogs of FA and MD for multi-b-values acquisitions by Hosseinbor et al. (2013). The combined high stability over time, relatively higher inter-subject variability ( $CV_{intra} \ll CV_{inter}$ ) shown by the 3D-SHORE based indices, which is a pattern that can help detecting group differences between subjects, and excellent inter-session ICC values for most of the cases reinforce their potentialities as microstructural biomarkers for revealing longitudinal changes.

## Quantitative Analyses on Tract-Based Outcomes of WM

Longitudinal group-based analyses were performed to statistically compare the mean absolute changes between time points calculated for each network. Regarding 3D-SHORE-based indices, the Bonferroni corrected *t*-tests revealed several highly significant differences between patients and controls in the SUBCORT and CC networks, also for the newly introduced MSD index. These findings further confirm and strengthen our preliminary results on a subset of 3D-SHORE indices (Brusini et al., 2016), where the *t*-tests were corrected for multiple comparisons with FDR. Conversely, a more conservative correction was employed here in order to quantify with additional confidence the longitudinal changes detected by the different indices and to reduce false positive results. Tensor-derived indices also exhibited similar patterns to 3D-SHORE descriptors, in terms of both evolutions of changes over time and level of significance.

In all cases, the highest levels of significance were reached in the patient group for the *tp1-tp2* and *tp1-tp3* relative changes, suggesting the presence of marked modifications in the contralateral hemisphere just 1 week after the stroke event (*tp1*). Interestingly, 3D-SHORE-based indices appeared to be the only capable of depicting statistically significant changes across the CORT loop. Indeed, only GFA and RTAP found a significant patient vs. control difference in the first phase (*tp1-tp2*), further highlighting the relevance of this time scale in the course of the disease.

These findings are in line with the few previous works reporting changes in the WM tracts of the contralesional hemisphere after stroke. Indeed, the possible modifications in the contralateral hemisphere with respect to the lesion have been scarcely investigated in literature, especially in humans, as these tissues have been widely disregarded as considered healthy and not directly involved in any rearrangement process (Maniega et al., 2004; Ozsunar et al., 2004). However, as the field

moved forward, it became apparent that also the non-injured hemisphere undergoes marked changes and has a fundamental role in stroke recovery, as recognized by several authors relying on different MRI techniques (Ward et al., 2003; Gerloff et al., 2006; Crofts et al., 2011; Granziera et al., 2012b; Lin et al., 2015). Specifically, Crofts et al. (2011) showed how communicability values, derived from complex network analysis, were reduced in both ipsilateral and homologous contralateral regions. Moreover, Granziera et al. (2012a) reported significantly increased apparent diffusion coefficient (ADC) values in the infarct region (in both GM and WM tissues) moving from acute to chronic, whereas WM FA significantly decreased in the mirror regions. Our study extends the available literature on the topic and the novel biomarkers derived by the 3D-SHORE model possibly add new metrics that can be employed in this context (for a detailed overview see Kim and Winstein, 2017).

In addition, the predictive power of all the microstructural indices for patient motor outcome at *tp3* were investigated relying on the tract-based values and comparing several regression models for the prediction. Notably, among the three loops, the SUBCORT was the only one for which all the three types of models created (tensor-based model, 3D-SHORE-based model, global microstructural model) reached excellent performance. In particular, the 3D-SHORE-based model, combining a subset of these indices together with clinical patient information, led to the best linear regression model featuring a very high predictive power ( $R_{adj}^2 = 0.998$ ,  $p < 0.001$ ), which slightly outperformed the optimal model we found in our previous work ( $R_{adj}^2 = 0.988$ ,  $p = 0.009$ ) (Brusini et al., 2016). The set of indices in the optimal model of this work embeds MSD, suggesting that this index holds a higher potential in probing stroke-induced microstructural changes during the early phase.

The model using all the microstructural indices led to the best performance in the SUBCORT loop, reaching the highest correlation score ( $R_{adj}^2 = 0.694$ ,  $p < 0.01$ ) and keeping RTPP as key predictor. The relevance of RTPP for subcortical WM tracts appears to be coherent with another observation of Avram et al. (2016) according to which RTPP is very sensitive to deep structures, showing higher intensity in nuclei like thalamus. RTPP also highlighted high predictive power in CC, contributing to the optimal model for both the 3D-SHORE-based and global model, in combination with MD in this latter case. These results, jointly with the high precision and the ability to detect significant changes between patients and controls, stress the potential of this index in the considered task.

## Quantitative Analyses on ROI-Based Outcomes of GM

Besides evaluating the performance of the different indices along the WM connections of specific brain networks, we performed a quantitative comparison of their patterns within contralateral GM regions. GM tissue changes related to the disease are generally quantified by volume or density analyses and are very rarely investigated with dMRI-based indices. A growing body of literature is emerging to endorse the use of dMRI techniques for detecting microscopic changes in GM in different disorders.

Indeed, the analysis of diffusivity GM changes using MD has shown to be promising for detecting abnormalities in Alzheimer disease (Weston et al., 2015) and multiple sclerosis (Ceccarelli et al., 2007). GM FA alterations were also demonstrated in schizophrenic patients in Situ et al. (2015), reporting increased MD and decreased FA values in patients compared to controls. In stroke patients, studies in GM are less consistent and generally consider the tissues in the contralateral hemisphere as normal appearing, although regions remote (upstream or downstream) from the infarct have been demonstrated to undergo marked changes over a time course of 2 days to 1 year (Sotak, 2002). In one of these studies using the contralateral part as reference, Maniega et al. (2004) showed a trend of increased MD/decreased FA values within the lesion, which just started the first week from the event.

In our study, the longitudinal analyses on the patient group demonstrated a similar pattern but in the contralateral hemisphere, revealing an increase in MD values over time which mainly involved GM motor regions. Conversely, FA exhibited an initial widespread increase at *tp1* over temporo-frontal and motor areas, followed by a gradual decrease toward normality at *tp3*. This was further confirmed by the group-based comparisons with ANOVA, highlighting in most of these regions significantly higher FA values at *tp1* in patients vs. controls, whereas the increased pattern remained restricted to few ROIs when *tp2* values were evaluated. Similar patterns of alterations were detected also by SHORE-based indices, in particular by GFA, PA, RTPP and MSD. The group comparisons 1 week after the stroke revealed several GM regions (cACC, FuG, IGG, mOFC, PORB, rMFG, FP, ITG, LOC, IOFC, MTG) in which the patients exhibit significantly higher values for all the anisotropy indices (GFA, PA, FA) with respect to the controls. Considering that in the same regions, at the same time point, the MD and MSD appear to be increasing (**Figure 7A**), although not significantly, we can speculate that we are observing a general increase of the diffusivity along the main diffusion direction in the GM. More difficult to interpret is the simultaneous increase of the RTPP in some of these regions (ITG, LOC, IOFC, MTG). RTPP is generally inversely proportional to anisotropy in WM, e.g., RTPP is low in single fiber bundle areas such as the CC, and higher in crossing regions (Özarslan et al., 2013; Avram et al., 2016; Zucchelli et al., 2016a). Understanding the possible causes of this contemporary increase of RTPP and anisotropy in the GM will be one of the aims of our future works.

Contralateral changes in GM involved not only regions in the motor systems, but also areas playing an important role in cognition and behavior, as the FP and frontal areas, supporting the hypothesis of extensive rearrangements during stroke recovery. These indices therefore confirm their potentialities in describing not only WM but also GM properties, with high reliability and discriminative power. However, RTAP and MSD, which resulted to be suitable to characterize WM tracts in all the networks, appeared to be less sensitive to GM changes. Indeed, these indices failed to highlight statistically significant differences in the GM areas, especially when comparing the patient data over time. However, they deserve further investigations considering their good stability over time and their physiological relevance.

It is worth mentioning that the impact of partial volume effects was minimized by restricting the analysis to voxels where the GM contribution was above the 95%. This further enhances the hypothesis of extensive contralateral changes involving also the GM, reducing the contamination by other tissues.

As a side note, we also extracted for each patient and time point the average volumes of GM ROIs (results not shown). However, when statistically compared by means of a two-way repeated measure ANOVA, no significant changes were detected, possibly because of the small sample size and the limitations of such morphometric measure that might be not sensitive enough to subtle changes in the contralateral hemisphere. A larger sample size and more sophisticated analyses, for example based on cortical thickness measures or voxel-based morphometry, might be more suitable for depicting GM longitudinal changes following stroke, as often done in literature (Stebbins et al., 2008; Brodtmann et al., 2012). Our results, though preliminary, support the hypothesis that SHORE-based indices might hold the potential of revealing GM plasticity processes in the contralesional stroke area. We are aware of the fact that the interpretation in terms of geometrical restriction of the diffusion of the SHORE-derived indices in GM is prone to criticism because the real tissue architecture cannot be directly mapped to the underlying reference model (i.e., the pore). However, the fact that differences across time within a patient population and across groups can be detected using such indices provide evidence in favor of their exploitability as potential numerical biomarkers for GM plasticity in disease, leaving their interpretation in terms of microstructural properties an open issue.

Some limitations have to be acknowledged. This work has to be considered as a preliminary comparison between DTI and SHORE-based EAP derived indices in stroke. Here, we considered only the two most used DTI derived indices (FA and MD) and some of the principal EAP derived indices (RTAP, RTPP, MSD, PA, GFA). However, it will be interesting to extend the analyses to further indices that can be derived, e.g., the radial and axial diffusivity for the DTI, RTOP and the MAP-MRI non-gaussianity for the EAP. Moreover, our findings are based on the comparison between 10 healthy subjects and 10 ischemic stroke patients. A higher number of subjects would be necessary in future studies to fully exploit the potentialities and discriminative/predictive power of these rather novel indices. In particular, the linear regression analyses have to be carefully evaluated bearing in mind they are preliminary, although encouraging, findings. Indeed, the limited sample size precluded the possibility of identifying the optimal model in a subset of the population and testing it in a different validation cohort, as normally does in the machine learning/classification field. Moreover, a large number of predictors was initially included in the models, possibly leading to over-fitting problems that should be carefully considered when dealing with a limited number of subjects. Adding more data will allow to increase the power of the statistical analyses performed in this work and to further validate the promising findings about contralateral WM and GM changes suggesting the presence of plasticity processes.



## CONCLUSIONS

In conclusion, this work provided new evidence in favor of the suitability of dMRI-based microstructural indices for probing WM modifications and highlighted their potential as descriptors of microstructural feature changes in GM in ischemic stroke patients. To the best of our knowledge this is the first attempt of using 3D-SHORE-derived indices for studying microstructure in GM in both controls and patients, contributing a first step in bridging WM and GM diffusion signal modeling. In particular, the RTPP seems to be able to convey relevant information while being consistent across groups and time.

From the clinical point of view, our results provide additional evidence in favor of the hypothesis of the contralateral remodeling after stroke. The 3D-SHORE-derived indices performed as well as classical tensor-derived indices (FA and MD), achieving a high predictive power for clinical outcome over cortico-subcortical connections and a good discrimination between patients and controls at different time scales, further confirming their viability in ischemic stroke. Their combination can allow to convey a more detailed microstructural description, marking a step forward in the definition of a novel family of

biomarkers. Finally, the detection of significant changes in GM across groups and in the patient longitudinal comparison provides a new perspective along the path of characterizing disease-related microstructural modulations which deserves further investigation.

## AUTHOR CONTRIBUTIONS

IBG and GM conceived and designed the experiments, interpreted the results of experiments and wrote the manuscript. IBG performed part of the statistical analyses. LB and SO analyzed the data and drafted the manuscript. MZ wrote the code for deriving all the indices, interpreted the results and drafted the manuscript. CG was involved in the design of the study and in data acquisition, interpreted the results of experiments, and drafted the manuscript.

## SUPPLEMENTARY MATERIAL

The Supplementary Material for this article can be found online at: <https://www.frontiersin.org/articles/10.3389/fnins.2018.00092/full#supplementary-material>

## REFERENCES

- Alexander, A. L., Eun Lee, J., Lazar, M., and Field, A. S. (2007). Diffusion tensor imaging of the brain. *Neurotherapeutics* 4, 316–329. doi: 10.1016/j.nurt.2007.05.011
- Assaf, Y., and Basser, P. J. (2005). Composite hindered and restricted model of diffusion (CHARMED) MR imaging of the human brain. *Neuroimage* 27, 48–58. doi: 10.1016/j.neuroimage.2005.03.042
- Avram, A. V., Barnett, A. S., and Basser, P. J. (2014). “The Variation of MAP—MRI Derived Parameters Along White Matter Fiber Pathways in the Human Brain,” in *ISMRM 22nd Annual Meeting*, (Milan), 2587.
- Avram, A. V., Sarlls, J. E., Barnett, A. S., Özarslan, E., Thomas, C., Irfanoglu, M. O., et al. (2016). Clinical feasibility of using mean apparent propagator (MAP) MRI to characterize brain tissue microstructure. *Neuroimage* 127, 422–434. doi: 10.1016/j.neuroimage.2015.11.027
- Basser, P. J., Mattiello, J., and Le Bihan, D. (1994a). Estimation of the effective self-diffusion tensor from the NMR spin echo. *J. Magn. Reson. B* 103, 247–254. doi: 10.1006/jmrb.1994.1037
- Basser, P. J., Mattiello, J., and Le Bihan, D. (1994b). MR diffusion tensor spectroscopy and imaging. *Biophys. J.* 66, 259–267. doi: 10.1016/S0006-3495(94)80775-1
- Basser, P. J., and Ozarslan, E. (2009). “Introduction to diffusion MR,” in *Diffusion MRI: From Quantitative Measurement to In-vivo Neuroanatomy*, eds H. Johansen-Berg and E. J. Timothy (Oxford: Academic Press), 2–10.
- Beaulieu, C. (2002). The basis of anisotropic water diffusion in the nervous system—a technical review. *NMR Biomed.* 15, 435–455. doi: 10.1002/nbm.782
- Bland, J., and Altman, D. (1996). Statistics notes: measurement error. *BMJ* 312:774.
- Bouix, S., Pasternak, O., Rathi, Y., Pelavin, P. E., Zafonte, R., and Shenton, M. E. (2013). Increased gray matter diffusion anisotropy in patients with persistent post-concussive symptoms following mild traumatic brain injury. *PLoS ONE* 8:e66205. doi: 10.1371/journal.pone.0066205
- Brodthmann, A., Pardoe, H., Li, Q., Lichter, R., Ostergaard, L., and Cumming, T. (2012). Changes in regional brain volume three months after stroke. *J. Neurol. Sci.* 322, 122–128. doi: 10.1016/j.jns.2012.07.019
- Brusini, L., Obertino, S., Boscolo Galazzo, I., Zucchelli, M., Krueger, G., Granziera, C., et al. (2016). Ensemble average propagator-based detection of microstructural alterations after stroke. *Int. J. Comp. Assist. Radiol. Surg.* 11, 1585–1597. doi: 10.1007/s11548-016-1442-z
- Brusini, L., Obertino, S., Zucchelli, M., Galazzo, I. B., Krueger, G., Granziera, C., et al. (2015, October). “Assessment of mean apparent propagator-based indices as biomarkers of axonal remodeling after stroke,” in *International Conference on Medical Image Computing and Computer-Assisted Intervention*. Munich: Springer International Publishing, 199–206.
- Ceccarelli, A., Rocca, M. A., Falini, A., Tortorella, P., Pagani, E., Rodegher, M., et al. (2007). Normal-appearing white and grey matter damage in MS. *J. Neurol.* 254, 513–518. doi: 10.1007/s00415-006-0408-4
- Chen, Y., Wang, D. J., and Detre, J. A. (2011). Test–retest reliability of arterial spin labeling with common labeling strategies. *J. Magn. Reson. Imaging* 33, 940–949. doi: 10.1002/jmri.22345
- Cicchetti, D. V. (2010). Methodological commentary the precision of reliability and validity estimates re-visited: distinguishing between clinical and statistical significance of sample size requirements. *J. Clin. Exp. Neuropsychol.* 23, 695–700. doi: 10.1076/jcen.23.5.695.1249
- Crofts, J. J., Higham, D. J., Bosnell, R., Jbabdi, S., Matthews, P. M., Behrens, T. E. J., et al. (2011). Network analysis detects changes in the contralesional hemisphere following stroke. *Neuroimage* 54, 161–169. doi: 10.1016/j.neuroimage.2010.08.032
- Danielian, L. E., Iwata, N. K., Thomasson, D. M., and Floeter, M. K. (2010). Reliability of fiber tracking measurements in diffusion tensor imaging for longitudinal study. *Neuroimage* 49, 1572–1580. doi: 10.1016/j.neuroimage.2009.08.062
- Descoteaux, M., Deriche, R., Le Bihan, D., Mangin, J. F., and Poupon, C. (2011). Multiple q-shell diffusion propagator imaging. *Med. Image Anal.* 15, 603–621. doi: 10.1016/j.media.2010.07.001
- Ezekiel, M. (1930). *Methods of Correlation Analysis*. New York, NY: John Wiley and Sons.
- Fick, R. H. J., Daianu, M., Pizzolato, M., Wassermann, D., Jacobs, R. E., Thompson, P. M., et al. (2016). “Comparison of biomarkers in transgenic Alzheimer rats using multi-shell diffusion MRI,” in *MICCAI 2016 Workshop on Computational Diffusion MRI (CDMRI'16)* (Athens).
- Fick, R. H. J., Zucchelli, M., Girard, G., Descoteaux, M., Menegaz, G., and Deriche, R. (2015). “Using 3D-SHORE and MAP-MRI to obtain both tractography and microstructural contrast from a clinical DMRI acquisition,” in *Biomedical Imaging (ISBI), 2015 IEEE 12th International Symposium on IEEE* (New York, NY), 436–439.

- Fleiss, J. L. (1981). *Methods for Rates and Proportions, 2nd Edn.* New York, NY: Wiley.
- Friston, K. J., Holmes, A. P., Worsley, K. J., Poline, J.-P., Frith, C. D., and Frackowiak, R. S. J. (1995). Statistical parametric maps in functional imaging: a general linear approach. *Hum. Brain Mapp.* 2, 189–210. doi: 10.1002/hbm.460020402
- Gerloff, C., Bushara, K., Sailer, A., Wassermann, E. M., Chen, R., Matsuoka, T. D., et al. (2006). Multimodal imaging of brain reorganization in motor areas of the contralesional hemisphere of well recovered patients after capsular stroke. *Brain* 129, 791–808. doi: 10.1093/brain/awh713
- Granziera, C., Ay, H., Koniak, S. P., Krueger, G., and Sorensen, A. G. (2012a). Diffusion tensor imaging shows structural remodeling of stroke mirror region: results from a pilot study. *Eur. Neurol.* 67, 370–376. doi: 10.1159/000336062
- Granziera, C., Daducci, A., Meskaldji, D. E., Roche, A., Maeder, P., Michel, P., et al. (2012b). A new early and automated MRI-based predictor of motor improvement after stroke. *Neurology* 79, 39–46. doi: 10.1212/WNL.0b013e31825f25e7
- Granziera, C., Schmahmann, J. D., Hadjikhani, N., Meyer, H., Meuli, R., and Wedeen, V., et al. (2009). Diffusion spectrum imaging shows the structural basis of functional cerebellar circuits in the human cerebellum *in vivo*. *PLoS ONE* 4:e5101. doi: 10.1371/journal.pone.0005101
- Grech-Sollars, M., Hales, P. W., Miyazaki, K., Raschke, F., Rodriguez, D., Wilson, M., et al. (2015). Multi-centre reproducibility of diffusion MRI parameters for clinical sequences in the brain. *NMR Biomed.* 28, 468–485. doi: 10.1002/nbm.3269
- Heiervang, E., Behrens, T. E. J., Mackay, C. E., Robson, M. D., and Johansen-Berg, H. (2006). Between sessions reproducibility and between subject variability of diffusion MR and tractography measures. *Neuroimage* 33, 867–877. doi: 10.1016/j.neuroimage.2006.07.037
- Hosseini, A. P., Chung, M. K., Wu, Y. C., and Alexander, A. L. (2013). Bessel fourier orientation reconstruction (bfor): an analytical diffusion propagator reconstruction for hybrid diffusion imaging and computation of q-space indices. *Neuroimage* 64, 650–670. doi: 10.1016/j.neuroimage.2012.08.072
- Jeurissen, B., Tournier, J. D., Dhollander, T., Connelly, A., and Sijbers, J. (2014). Multi-tissue constrained spherical deconvolution for improved analysis of multi-shell diffusion MRI data. *Neuroimage* 103, 411–426. doi: 10.1016/j.neuroimage.2014.07.061
- Kaden, E., Kelm, N. D., Carson, R. P., Does, M. D., and Alexander, D. C. (2016). Multi-compartment microscopic diffusion imaging. *Neuroimage* 139, 346–359. doi: 10.1016/j.neuroimage.2016.06.002
- Kim, B., and Winstein, C. (2017). Can neurological biomarkers of brain impairment be used to predict poststroke motor recovery? A Systematic Review. *Neurorehabil. Neural. Repair* 31, 3–24. doi: 10.1177/1545968316662708
- Kim, H. J., Kim, S. J., Kim, H. S., Choi, C. G., Kim, N., Han, S., et al. (2013). Alterations of mean diffusivity in brain white matter and deep gray matter in Parkinson's disease. *Neurosci. Lett.* 550, 64–68. doi: 10.1016/j.neulet.2013.06.050
- Kim, J. Y., Park, J., Chang, J. Y., Kim, S. H., and Lee, J. E. (2016). Inflammation after ischemic stroke: the role of leukocytes and glial cells. *Exp. Neurobiol.* 25, 241–251. doi: 10.5607/en.2016.25.5.241
- Kirk, R. E. (1996). Practical significance: a concept whose time has come. *Educ. Psychol. Meas.* 56, 746–759. doi: 10.1177/0013164496056005002
- Le Bihan, D., Breton, E., Lallemand, D., Grenier, P., Cabanis, E., and Laval-Jeantet, M. (1986). MR imaging of intravoxel incoherent motions: application to diffusion and perfusion in neurologic disorders. *Radiology* 161, 401–407. doi: 10.1148/radiology.161.2.3763909
- Lin, Y. C., Daducci, A., Meskaldji, D. E., Thiran, J. P., Michel, P., Meuli, R., et al. (2015). Quantitative analysis of myelin and axonal remodeling in the uninjured motor network after stroke. *Brain Connect.* 5, 401–412. doi: 10.1089/brain.2014.0245
- Maniega, S. M., Bastin, M. E., Armitage, P. A., Farrall, A. J., Carpenter, T. K., Hand, P. J., et al. (2004). Temporal evolution of water diffusion parameters is different in grey and white matter in human ischaemic stroke. *J. Neurol. Neurosurg. Psychiatry* 75, 1714–1718. doi: 10.1136/jnnp.2003.033852
- Marengo, S., Rawlings, R., Rohde, G. K., Barnett, A. S., Honea, R. A., Pierpaoli, C., et al. (2006). Regional distribution of measurement error in diffusion tensor imaging. *Psychiatry Res.* 147, 69–78. doi: 10.1016/j.psychres.2006.01.008
- Mendez, A., Obertino, S., and Menegaz, G. (2016). “Shore-based microstructural indices: do they tell us more?” in *Pattern Recognition in Neuroimaging (PRNI), 2016 International Workshop on IEEE* (Trento), 1–4.
- Merlet, S. L., and Deriche, R. (2013). Continuous diffusion signal, EAP and ODF estimation via compressive sensing in diffusion MRI. *Med. Image Anal.* 17, 556–572. doi: 10.1016/j.media.2013.02.010
- Ning, L., Laun, F., Gur, Y., DiBella, E. V., Deslauriers-Gauthier, S., Megherbi, T., et al. (2015). Sparse reconstruction challenge for diffusion MRI: validation on a physical phantom to determine which acquisition scheme and analysis method to use? *Med. Image Anal.* 26, 316–331. doi: 10.1016/j.media.2015.10.012
- Novikov, D. S., Jespersen, S. N., Kiselev, V. G., and Fieremans, E. (2016). Quantifying brain microstructure with diffusion MRI: theory and parameter estimation. *arXiv:1612.02059*.
- Obertino, S., Brusini, L., Boscolo Galazzo, I., Zucchelli, M., Granziera, C., and Cristani, M., et al. (2016). “Shore-based biomarkers allow patient versus control classification in stroke,” in *Biomedical Imaging (ISBI), 2016 IEEE 13th International Symposium on IEEE* (Prague), 1097–1100.
- Özarslan, E., and Koay, C. G., Basser, P. J. (2008). “Simple harmonic oscillator based estimation and reconstruction for one-dimensional q-space MR,” in *Proceedings of the International Society for Magnetic Resonance in Medicine* (Toronto, ON), Vol 16. 35.
- Özarslan, E., Koay, C. G., Shepherd, T. M., Komlosh, M. E., Irfanoglu, M. O., Pierpaoli, C., et al. (2013). Mean apparent propagator (MAP) MRI: a novel diffusion imaging method for mapping tissue microstructure. *Neuroimage* 78, 16–32. doi: 10.1016/j.neuroimage.2013.04.016
- Ozsunar, Y., Grant, P. E., Huisman, T. A., Schaefer, P. W., Wu, O., Sorensen, A. G., et al. (2004). Evolution of water diffusion and anisotropy in hyperacute stroke: significant correlation between fractional anisotropy and T2. *AJNR Am. J. Neuroradiol.* 25, 699–705.
- Pierpaoli, C., and Basser, P. J. (1996). Toward a quantitative assessment of diffusion anisotropy. *Magn. Reson. Med.* 36, 893–906. doi: 10.1002/mrm.1910360612
- Pinto, J., Jorge, J., Sousa, I., Vilela, P., and Figueiredo, P. (2016). Fourier modeling of the BOLD response to a breath-hold task: optimization and reproducibility. *Neuroimage* 135, 223–231. doi: 10.1016/j.neuroimage.2016.02.037
- Situ, W., Liao, H., Zhou, B., Xia, X., and Tan, C. (2015). Application of diffusion tensor imaging for detecting structural changes in the brain of schizophrenic patients. *Int. J. Psychiatry Clin. Pract.* 19, 114–118. doi: 10.3109/13651501.2014.988270
- Sotak, C. (2002). The role of diffusion tensor imaging in the evaluation of ischemic brain injury a review. *NMR Biomed.* 15, 561–569. doi: 10.1002/nbm.786
- Sotiropoulos, S. N., Jbabdi, S., Xu, J., Andersson, J. L., Moeller, S., Auerbach, E. J., et al. (2013). Advances in diffusion MRI acquisition and processing in the human connectome project. *Neuroimage* 80, 125–143. doi: 10.1016/j.neuroimage.2013.05.057
- Stebbins, G. T., Nyenhuis, D. L., Wang, C., Cox, J. L., Freels, S., and Bangen, K., et al. (2008). Gray matter atrophy in patients with ischemic stroke with cognitive impairment. *Stroke* 39, 785–793. doi: 10.1161/STROKEAHA.107.507392
- Stejskal, E., and Tanner, J. (1965). Spin diffusion measurements: spin echoes in the presence of a time-dependent field gradient. *J. Chem. Phys.* 42, 288–292. doi: 10.1063/1.1695690
- Sundgren, P. C., Dong, Q., Gómez-Hassan, D., Mukherji, S. K., Maly, P., and Welsh, R. (2004). Diffusion tensor imaging of the brain: review of clinical applications. *Neuroradiology* 46, 339–350. doi: 10.1007/s00234-003-1114-x
- Veenith, T. V., Carter, E., Grossac, J., Newcombe, V. F., Outtrim, J. G., Lupson, V., et al. (2013). Inter subject variability and reproducibility of diffusion tensor imaging within and between different imaging sessions. *PLoS ONE* 8:e65941. doi: 10.1371/journal.pone.0065941
- Vollmar, C., O'Muircheartaigh, J., Barker, G. J., Symms, M. R., Thompson, P., Kumari, V., et al. (2010). Identical, but not the same: intra-site and inter-site reproducibility of fractional anisotropy measures on two 3.0T scanners. *Neuroimage* 51, 1384–1394. doi: 10.1016/j.neuroimage.2010.03.046
- Wang, J. Y., Abdi, H., Bakhadirov, K., Diaz-Arrastia, R., and Devous, M. Sr. (2012). A comprehensive reliability assessment of quantitative diffusion tensor tractography. *Neuroimage* 60, 1127–1138. doi: 10.1016/j.neuroimage.2011.12.062
- Wang, Q., Tang, X. N., and Yenari, M. A. (2007). The inflammatory response in stroke. *J. Neuroimmunol.* 184, 53–68. doi: 10.1016/j.jneuroim.2006.11.014

- Ward, N. S., Brown, M. M., Thompson, A. J., and Frackowiak, R. S. J. (2003). Neural correlates of motor recovery after stroke: a longitudinal fMRI study. *Brain* 126, 2476–2496. doi: 10.1093/brain/awg245
- Wedeen, V. J., Hagmann, P., Tseng, W. Y., Reese, T. G., and Weisskoff, R. M. (2005). Mapping complex tissue architecture with diffusion spectrum magnetic resonance imaging. *Magn. Reson. Med.* 54, 1377–1386. doi: 10.1002/mrm.20642
- Weston, P. S. J., Simpson, I. J. A., Ryan, N. S., Ourselin, S., and Fox, N. C. (2015). Diffusion imaging changes in grey matter in Alzheimer's disease: a potential marker of early neurodegeneration. *Alzheimers Res. Ther.* 7, 47–55. doi: 10.1186/s13195-015-0132-3
- Wiggins, G. C., Triantafyllou, C., Potthast, A., Reykowski, A., Nittka, M., and Wald, L. L. (2006). 32-channel 3 Tesla receive-only phased-array head coil with soccer-ball element geometry. *Magn. Reson. Med.* 56, 216–223. doi: 10.1002/mrm.20925
- Wu, Y. C., and Alexander, A. L. (2007). Hybrid diffusion imaging. *Neuroimage* 36, 617–629. doi: 10.1016/j.neuroimage.2007.02.050
- Yu, C., Zhu, C., Zhang, Y., Chen, H., Qin, W., Wang, M., et al. (2009). A longitudinal diffusion tensor imaging study on Wallerian degeneration of corticospinal tract after motor pathway stroke. *Neuroimage* 47, 451–458. doi: 10.1016/j.neuroimage.2009.04.066
- Zhang, H., Schneider, T., Wheeler-Kingshott, C. A., and Alexander, D. C. (2012). NODDI: practical *in vivo* neurite orientation dispersion and density imaging of the human brain. *Neuroimage* 61, 1000–1016. doi: 10.1016/j.neuroimage.2012.03.072
- Zucchelli, M., Brusini, L., Méndez, C. A., Daducci, A., Granziera, C., and Menegaz, G. (2016a). What lies beneath? Diffusion EAP-based study of brain tissue microstructure. *Med. Image Anal.* 32, 145–156. doi: 10.1016/j.media.2016.03.008
- Zucchelli, M., Fick, R. H. J., Deriche, R., and Menegaz, G. (2016b). “Ensemble average propagator estimation of axon diameter in diffusion MRI: implications and limitations,” in *Biomedical Imaging (ISBI), 2016 IEEE 13th International Symposium* (Prague), 465–468.

**Conflict of Interest Statement:** The authors declare that the research was conducted in the absence of any commercial or financial relationships that could be construed as a potential conflict of interest.

Copyright © 2018 Boscolo Galazzo, Brusini, Obertino, Zucchelli, Granziera and Menegaz. This is an open-access article distributed under the terms of the Creative Commons Attribution License (CC BY). The use, distribution or reproduction in other forums is permitted, provided the original author(s) and the copyright owner are credited and that the original publication in this journal is cited, in accordance with accepted academic practice. No use, distribution or reproduction is permitted which does not comply with these terms.

---

## References

1. Francisco Aboitiz, Arnold B Scheibel, Robin S Fisher, and Eran Zaidel. Fiber composition of the human corpus callosum. *Brain research*, 598(1):143–153, 1992.
2. Flavio Dell’ Acqua, Giovanna Rizzo, Paola Scifo, Rafael Alonso Clarke, Giuseppe Scotti, and Ferruccio Fazio. A model-based deconvolution approach to solve fiber crossing in diffusion-weighted mr imaging. *Biomedical Engineering, IEEE Transactions on*, 54(3):462–472, 2007.
3. Monika Albert, Jack Antel, Wolfgang Brück, and Christine Stadelmann. Extensive cortical remyelination in patients with chronic multiple sclerosis. *Brain Pathology*, 17(2):129–138, 2007.
4. Andrew L Alexander, Jee Eun Lee, Mariana Lazar, and Aaron S Field. Diffusion tensor imaging of the brain. *Neurotherapeutics*, 4(3):316–329, 2007.
5. Daniel C Alexander and Tim B Dyrby. Diffusion imaging with stimulated echoes: signal models and experiment design. *arXiv preprint arXiv:1305.7367*, 2013.
6. Daniel C. Alexander, Penny L. Hubbard, Matt G. Hall, Elizabeth A. Moore, Maurice Ptito, Geoff J.M. Parker, and Tim B. Dyrby. Orientationally invariant indices of axon diameter and density from diffusion MRI. *NeuroImage*, 52(4):1374 – 1389, 2010.
7. Daniel C Alexander, Penny L Hubbard, Matt G Hall, Elizabeth A Moore, Maurice Ptito, Geoff JM Parker, and Tim B Dyrby. Orientationally invariant indices of axon diameter and density from diffusion mri. *Neuroimage*, 52(4):1374–1389, 2010.
8. Eva Alonso-Ortiz, Ives R Levesque, and G Bruce Pike. Mri-based myelin water imaging: A technical review. *Magnetic resonance in medicine*, 73(1):70–81, 2015.
9. Katrin Amunts, Axel Schleicher, and Karl Zilles. Cytoarchitecture of the cerebral cortex more than localization. *Neuroimage*, 37(4):1061–1065, 2007.
10. Adam W Anderson. Measurement of fiber orientation distributions using high angular resolution diffusion imaging. *Magnetic Resonance in Medicine*, 54(5):1194–1206, 2005.
11. Ingrid Åslund, Agnieszka Nowacka, Markus Nilsson, and Daniel Topgaard. Filter-exchange pgse nmr determination of cell membrane permeability. *Journal of Magnetic Resonance*, 200(2):291–295, 2009.
12. Yaniv Assaf and Peter J. Basser. Composite hindered and restricted model of diffusion (charmed) {MR} imaging of the human brain. *NeuroImage*, 27(1):48 – 58, 2005.
13. Yaniv Assaf, Tamar Blumenfeld-Katzir, Yossi Yovel, and Peter J Basser. Axciliber: a method for measuring axon diameter distribution from diffusion mri. *Magnetic Resonance in Medicine*, 59(6):1347–1354, 2008.

14. Yaniv Assaf, Raisa Z Freidlin, Gustavo K Rohde, and Peter J Basser. New modeling and experimental framework to characterize hindered and restricted water diffusion in brain white matter. *Magnetic Resonance in Medicine*, 52(5):965–978, 2004.
15. Yaniv Assaf, Raisa Z. Freidlin, Gustavo K. Rohde, and Peter J. Basser. New modeling and experimental framework to characterize hindered and restricted water diffusion in brain white matter. *Magnetic Resonance in Medicine*, 52(5):965–978, 2004.
16. Haz-Edine Assemlal, David Tschumperl, and Luc Brun. Efficient and robust computation of {PDF} features from diffusion {MR} signal. *Medical Image Analysis*, 13(5):715 – 729, 2009.
17. Alexandru V Avram, Alan S Barnett, Evren Ozarslan, Joelle E Sarlls, M Okan Irfanoglu, Elizabeth Hutchinson, Carlo Pierpaoli, and Peter J Basser. Characterizing human brain microstructure with mean apparent propagator (map) mri. In *Proc. Intl. Soc. Mag. Reson. Med*, volume 22, page 2605, 2014.
18. Alexandru V Avram, Joelle E Sarlls, Alan S Barnett, Evren Özarslan, Cibu Thomas, M Okan Irfanoglu, Elizabeth Hutchinson, Carlo Pierpaoli, and Peter J Basser. Clinical feasibility of using mean apparent propagator (map) mri to characterize brain tissue microstructure. *NeuroImage*, 127:422–434, 2016.
19. Jérôme Badaut, Stephen Ashwal, Arash Adami, Beatriz Tone, Rebecca Recker, David Spagnoli, Béatrice Ternon, and Andre Obenaus. Brain water mobility decreases after astrocytic aquaporin-4 inhibition using rna interference. *Journal of Cerebral Blood Flow & Metabolism*, 31(3):819–831, 2011.
20. Frederik Barkhof and Marianne van Walderveen. Characterization of tissue damage in multiple sclerosis by nuclear magnetic resonance. *Philosophical Transactions of the Royal Society of London B: Biological Sciences*, 354(1390):1675–1686, 1999.
21. AV Barzykin, K Hayamizu, WS Price, and M Tachiya. Pulsed-field-gradient nmr of diffusive transport through a spherical interface into an external medium containing a relaxation agent. *Journal of Magnetic Resonance, Series A*, 114(1):39–46, 1995.
22. Peter J Basser. Inferring microstructural features and the physiological state of tissues from diffusion-weighted images. *NMR in Biomedicine*, 8(7):333–344, 1995.
23. Peter J Basser, James Mattiello, and Denis LeBihan. Estimation of the effective self-diffusion tensor from the nmr spin echo. *Journal of Magnetic Resonance, Series B*, 103(3):247–254, 1994.
24. Peter J Basser, James Mattiello, and Denis LeBihan. MR diffusion tensor spectroscopy and imaging. *Biophys J*, 66(1):259, 1994.
25. Peter J Basser and Evren Ozarslan. Introduction to diffusion mr. *Diffusion MRI: From quantitative measurement to in-vivo neuroanatomy*, 2009.
26. Gregory T Baxter and Lawrence R Frank. A computational model for diffusion weighted imaging of myelinated white matter. *Neuroimage*, 75:204–212, 2013.
27. T.E.J. Behrens, M.W. Woolrich, M. Jenkinson, H. Johansen-Berg, R.G. Nunes, S. Clare, P.M. Matthews, J.M. Brady, and S.M. Smith. Characterization and propagation of uncertainty in diffusion-weighted mr imaging. *Magnetic Resonance in Medicine*, 50(5):1077–1088, 2003.
28. Timothy EJ Behrens, H Johansen Berg, Saad Jbabdi, Matthew FS Rushworth, and Mark W Woolrich. Probabilistic diffusion tractography with multiple fibre orientations: What can we gain? *Neuroimage*, 34(1):144–155, 2007.
29. Michael Sh Birman and Mikhail Zakharovich Solomjak. *Spectral theory of self-adjoint operators in Hilbert space*, volume 5. Springer Science & Business Media, 2012.
30. J Martin Bland and Douglas G Altman. Statistics notes: measurement error. *Bmj*, 313(7059):744, 1996.

31. Ilaria Boscolo Galazzo, Lorenza Brusini, Silvia Obertino, Mauro Zucchelli, Cristina Granziera, and Gloria Menegaz. On the viability of diffusion mri-based microstructural biomarkers in ischemic stroke. *Frontiers in Neuroscience*, 12:92, 2018.
32. Sylvain Bouix, Ofer Pasternak, Yogesh Rathi, Paula E Pelavin, Ross Zafonte, and Martha E Shenton. Increased gray matter diffusion anisotropy in patients with persistent post-concussive symptoms following mild traumatic brain injury. *PloS one*, 8(6):e66205, 2013.
33. Matthew Brett, Ingrid S Johnsrude, and Adrian M Owen. The problem of functional localization in the human brain. *Nature reviews neuroscience*, 3(3):243–249, 2002.
34. Amy Brodtmann, Heath Pardoe, Qi Li, Renee Lichter, Leif Ostergaard, and Toby Cumming. Changes in regional brain volume three months after stroke. *Journal of the neurological sciences*, 322(1):122–128, 2012.
35. Robert Brown. Xxvii. a brief account of microscopical observations made in the months of june, july and august 1827, on the particles contained in the pollen of plants; and on the general existence of active molecules in organic and inorganic bodies. *Philosophical Magazine Series 2*, 4(21):161–173, 1828.
36. Kenneth R Brownstein and CE Tarr. Importance of classical diffusion in nmr studies of water in biological cells. *Physical Review A*, 19(6):2446, 1979.
37. Lorenza Brusini, Silvia Obertino, Ilaria Boscolo Galazzo, Mauro Zucchelli, Gunnar Krueger, Cristina Granziera, and Gloria Menegaz. Ensemble average propagator-based detection of microstructural alterations after stroke. *International journal of computer assisted radiology and surgery*, 11(9):1585–1597, 2016.
38. Lorenza Brusini, Silvia Obertino, Mauro Zucchelli, Ilaria Boscolo Galazzo, Gunnar Krueger, Cristina Granziera, and Gloria Menegaz. Assessment of mean apparent propagator-based indices as biomarkers of axonal remodeling after stroke. In *International Conference on Medical Image Computing and Computer-Assisted Intervention*, pages 199–206. Springer, 2015.
39. Menegaz G Brusini, L and M Nilsson. Monte carlo simulations of diffusion in myelin spirals: Impact on diffusional water exchange. In *ISMRM*, Paris, France, 2018.
40. Matthew D Budde and Joseph A Frank. Neurite beading is sufficient to decrease the apparent diffusion coefficient after ischemic stroke. *Proceedings of the National Academy of Sciences*, 107(32):14472–14477, 2010.
41. Frédéric Buffon, Nicolas Molko, Dominique Hervé, Raphaël Porcher, Isabelle Denghien, Sabina Pappata, Denis Le Bihan, Marie-Germaine Bousser, and Hugues Chabriat. Longitudinal diffusion changes in cerebral hemispheres after mca infarcts. *Journal of Cerebral Blood Flow & Metabolism*, 25(5):641–650, 2005.
42. Lauren M Burcaw, Els Fieremans, and Dmitry S Novikov. Mesoscopic structure of neuronal tracts from time-dependent diffusion. *NeuroImage*, 114:18–37, 2015.
43. Paul T. Callaghan. *Principles of nuclear magnetic resonance microscopy*. Oxford University Press on Demand, 1993.
44. Paul T Callaghan. Pulsed-gradient spin-echo nmr for planar, cylindrical, and spherical pores under conditions of wall relaxation. *Journal of magnetic resonance, Series A*, 113(1):53–59, 1995.
45. Paul T Callaghan. A simple matrix formalism for spin echo analysis of restricted diffusion under generalized gradient waveforms. *Journal of Magnetic Resonance*, 129(1):74–84, 1997.
46. Paul T Callaghan, Andrew Coy, David MacGowan, Ken J Packer, and Fernando O Zelaya. Diffraction-like effects in nmr diffusion studies of fluids in porous solids. *Nature*, 351(6326):467–469, 1991.
47. Paul T Callaghan, D MacGowan, KJ Packer, and FO Zelaya. High-resolution q-space imaging in porous structures. *Journal of Magnetic Resonance (1969)*, 90(1):177–182, 1990.

48. PT Callaghan and Istvan Furo. Diffusion-diffusion correlation and exchange as a signature for local order and dynamics. *The Journal of chemical physics*, 120(8):4032–4038, 2004.
49. Roberto Caminiti, Filippo Carducci, Claudia Piervincenzi, Alexandra Battaglia-Mayer, Giuseppina Confalone, Federica Visco-Comandini, Patrizia Pantano, and Giorgio M Innocenti. Diameter, length, speed, and conduction delay of callosal axons in macaque monkeys and humans: comparing data from histology and magnetic resonance imaging diffusion tractography. *Journal of Neuroscience*, 33(36):14501–14511, 2013.
50. Roberto Caminiti, Hassan Ghaziri, Ralf Galuske, Patrick R Hof, and Giorgio M Innocenti. Evolution amplified processing with temporally dispersed slow neuronal connectivity in primates. *Proceedings of the National Academy of Sciences*, 106(46):19551–19556, 2009.
51. Emmanuel Caruyer and Rachid Deriche. Optimal regularization for mr diffusion signal reconstruction. In *Biomedical Imaging (ISBI), 2012 9th IEEE International Symposium on*, pages 50–53. IEEE, 2012.
52. Neil A Castle. Aquaporins as targets for drug discovery. *Drug discovery today*, 10(7):485–493, 2005.
53. Antonia Ceccarelli, Maria A Rocca, Andrea Falini, Paola Tortorella, Elisabetta Pagan, Mariemma Rodegher, Giancarlo Comi, Giuseppe Scotti, and Massimo Filippi. Normal-appearing white and grey matter damage in ms. *Journal of neurology*, 254(4):513–518, 2007.
54. Kae-Jiun Chang, Stephanie A Redmond, and Jonah R Chan. Remodeling myelination: implications for mechanisms of neural plasticity. *Nature neuroscience*, 19(2):190, 2016.
55. Yufen Chen, Danny JJ Wang, and John A Detre. Test-retest reliability of arterial spin labeling with common labeling strategies. *Journal of Magnetic Resonance Imaging*, 33(4):940–949, 2011.
56. J. Cheng, T. Jiang, and R. Deriche. Theoretical Analysis and Practical Insights on EAP Estimation via a Unified HARDI Framework. In *MICCAI Workshop on Computational Diffusion MRI (CDMRI)*, Toronto, Canada, 2011.
57. Jian Cheng, Aurobrata Ghosh, Rachid Deriche, and Tianzi Jiang. Model-free, regularized, fast, and robust analytical orientation distribution function estimation. *Medical Image Computing and Computer-Assisted Intervention-MICCAI 2010*, pages 648–656, 2010.
58. Jian Cheng, Aurobrata Ghosh, Tianzi Jiang, and Rachid Deriche. Model-free and analytical eap reconstruction via spherical polar fourier diffusion mri. pages 590 – 597, 2010.
59. Sarah L Codd and Paul T Callaghan. Spin echo analysis of restricted diffusion under generalized gradient waveforms: planar, cylindrical, and spherical pores with wall relaxivity. *Journal of Magnetic Resonance*, 137(2):358–372, 1999.
60. Marc-Alexandre Côté, Gabriel Girard, Arnaud Boré, Eleftherios Garyfallidis, Jean-Christophe Houde, and Maxime Descoteaux. Tractometer: towards validation of tractography pipelines. *Medical image analysis*, 17(7):844–857, 2013.
61. Jonathan J Crofts, Desmond J Higham, Rose Bosnell, Saâd Jbabdi, Paul M Matthews, TEJ Behrens, and Heidi Johansen-Berg. Network analysis detects changes in the contralesional hemisphere following stroke. *Neuroimage*, 54(1):161–169, 2011.
62. Laura E Danielian, Nobue K Iwata, David M Thomasson, and Mary Kay Floeter. Reliability of fiber tracking measurements in diffusion tensor imaging for longitudinal study. *Neuroimage*, 49(2):1572–1580, 2010.

63. Silvia De Santis, Derek K Jones, and Alard Roebroeck. Including diffusion time dependence in the extra-axonal space improves in vivo estimates of axonal diameter and density in human white matter. *NeuroImage*, 130:91–103, 2016.
64. Sean CL Deoni. Quantitative relaxometry of the brain. *Topics in magnetic resonance imaging: TMRI*, 21(2):101, 2010.
65. Maxime Descoteaux, Elaine Angelino, Shaun Fitzgibbons, and Rachid Deriche. Regularized, fast, and robust analytical q-ball imaging. *Magnetic resonance in medicine*, 58(3):497–510, 2007.
66. Maxime Descoteaux, Rachid Deriche, Denis Le Bihan, Jean-Francois Mangin, and Cyril Poupon. Multiple q-shell diffusion propagator imaging. *Medical Image Analysis*, 15(4):603 – 621, 2011. Special section on {IPMI} 2009.
67. Thijs Dhollander, David Raffelt, and Alan Connolly. Unsupervised 3-tissue response function estimation from single-shell or multi-shell diffusion mr data without a co-registered t1 image. In *Proc ISMRM Workshop on Breaking the Barriers of Diffusion MRI*, volume 5, 2016.
68. Rick M Dijkhuizen and Klaas Nicolay. Magnetic resonance imaging in experimental models of brain disorders. *Journal of Cerebral Blood Flow & Metabolism*, 23(12):1383–1402, 2003.
69. Macleod M Davis SM Donnan GA, Fisher M. Stroke. *Lancet*, 371:1612–1623, 2008.
70. William Alexander Newman Dorland. *Dorland’s medical dictionary*. Saunders, 1968.
71. Richard D Dortch, Kevin D Harkins, Meher R Juttukonda, John C Gore, and Mark D Does. Characterizing inter-compartmental water exchange in myelinated tissue using relaxation exchange spectroscopy. *Magnetic resonance in medicine*, 70(5):1450–1459, 2013.
72. Gwenaëlle Douaud, Saâd Jbabdi, Timothy EJ Behrens, Ricarda A Menke, Achim Gass, Andreas U Monsch, Anil Rao, Brandon Whitcher, Gordon Kindlmann, Paul M Matthews, et al. Dti measures in crossing-fibre areas: increased diffusion anisotropy reveals early white matter alteration in mci and mild alzheimer’s disease. *Neuroimage*, 55(3):880–890, 2011.
73. Adrienne N Dula, Daniel F Gochberg, Holly L Valentine, William M Valentine, and Mark D Does. Multiexponential t2, magnetization transfer, and quantitative histology in white matter tracts of rat spinal cord. *Magnetic resonance in medicine*, 63(4):902–909, 2010.
74. Tim B Dyrby, Matt G Hall, Maurice Ptito, Daniel Alexander, et al. Contrast and stability of the axon diameter index from microstructure imaging with diffusion mri. *Magnetic resonance in medicine*, 70(3):711–721, 2013.
75. Julia M. Edgar and Ian R. Griffiths. Chapter 7 - white matter structure: A microscopists view. In Heidi Johansen-Berg, , and Timothy E.J. Behrens, editors, *Diffusion MRI (Second Edition)*, pages 127 – 153. Academic Press, San Diego, second edition edition, 2014.
76. Albert Einstein. Über die von der molekularkinetischen theorie der wärme geforderte bewegung von in ruhenden flüssigkeiten suspendierten teilchen. *Annalen der physik*, 322(8):549–560, 1905.
77. Albert Einstein. *Investigations on the Theory of the Brownian Movement*. Courier Corporation, 1956.
78. Yan X Min X Wang L Feng, Z. Effects of echo time on diffusion quantification of prostate. In *ISMRM*, Honolulu, Hawaii, USA, 2017.
79. H.J. Fick, Rutger, Demian Wassermann, Gonzalo Sanguinetti, and Rachid Deriche. Laplacian-Regularized MAP-MRI: Improving Axonal Caliber Estimation. In *International Symposium on BIOMEDICAL IMAGING: From Nano to Macro*, Brooklyn, New York City, United States, April 2015.



80. R.H.J. Fick, M. Zucchelli, G. Girard, M. Descoteaux, G. Menegaz, and R. Deriche. Using 3D-SHORE and MAP-MRI to Obtain Both Tractography and Microstructural Contrast from a Clinical DMRI Acquisition. In *International Symposium on Biomedical Imaging: From Nano to Macro*, Brooklyn, New York City, United States, 2015.
81. Els Fieremans, Lauren M Burcaw, Hong-Hsi Lee, Gregory Lemberskiy, Jelle Veraart, and Dmitry S Novikov. In vivo observation and biophysical interpretation of time-dependent diffusion in human white matter. *NeuroImage*, 129:414–427, 2016.
82. Els Fieremans, Jens H Jensen, and Joseph A Helpert. White matter characterization with diffusional kurtosis imaging. *Neuroimage*, 58(1):177–188, 2011.
83. Els Fieremans, Dmitry S Novikov, Jens H Jensen, and Joseph A Helpert. Monte carlo study of a two-compartment exchange model of diffusion. *NMR in Biomedicine*, 23(7):711–724, 2010.
84. Joseph L Fleiss, Bruce Levin, and Myunghee Cho Paik. *Statistical methods for rates and proportions*. John Wiley & Sons, 2013.
85. Karl J Friston, Andrew P Holmes, Keith J Worsley, J-P Poline, Chris D Frith, and Richard SJ Frackowiak. Statistical parametric maps in functional imaging: a general linear approach. *Human brain mapping*, 2(4):189–210, 1994.
86. Herbert S Gasser and Joseph Erlanger. The role played by the sizes of the constituent fibers of a nerve trunk in determining the form of its action potential wave. *American Journal of Physiology—Legacy Content*, 80(3):522–547, 1927.
87. Christian Gerloff, Khalaf Bushara, Alexandra Sailer, Eric M Wassermann, Robert Chen, Takahiro Matsuoka, Daniel Waldvogel, George F Wittenberg, Kenji Ishii, Leonardo G Cohen, et al. Multimodal imaging of brain reorganization in motor areas of the contralesional hemisphere of well recovered patients after capsular stroke. *Brain*, 129(3):791–808, 2005.
88. Christian Gerloff, Khalaf Bushara, Alexandra Sailer, Eric M Wassermann, Robert Chen, Takahiro Matsuoka, Daniel Waldvogel, George F Wittenberg, Kenji Ishii, Leonardo G Cohen, et al. Multimodal imaging of brain reorganization in motor areas of the contralesional hemisphere of well recovered patients after capsular stroke. *Brain*, 129(3):791–808, 2005.
89. Aurobrata Ghosh and Rachid Deriche. From second to higher order tensors in diffusion-mri. *Tensors in Image Processing and Computer Vision*, pages 315–334, 2009.
90. Aurobrata Ghosh and Rachid Deriche. A survey of current trends in diffusion mri for structural brain connectivity. *Journal of neural engineering*, 13(1):011001, 2015.
91. John C Gore, Junzhong Xu, Daniel C Colvin, Thomas E Yankeelov, Edward C Parsons, and Mark D Does. Characterization of tissue structure at varying length scales using temporal diffusion spectroscopy. *NMR in Biomedicine*, 23(7):745–756, 2010.
92. Ay H. Koniak S. P. Krueger G. Sorensen A. G. Granziera, C. Diffusion tensor imaging shows structural remodeling of stroke mirror region: results from a pilot study. *European neurology*, 67(6):370–376, 2012.
93. C Granziera, H DArceuil, L Zai, PJ Magistretti, AG Sorensen, and AJ De Crespigny. Long-term monitoring of post-stroke plasticity after transient cerebral ischemia in mice using in vivo and ex vivo diffusion tensor mri. *The open neuroimaging journal*, 1:10, 2007.
94. Cristina Granziera, Alessandro Daducci, Djalel E Meskaldji, Alexis Roche, Philippe Maeder, Patrik Michel, Nouchine Hadjikhani, A Gregory Sorensen, Richard S Frackowiak, Jean-Philippe Thiran, et al. A new early and automated mri-based predictor of motor improvement after stroke. *Neurology*, 79(1):39–46, 2012.

95. Denis S Grebenkov. Laplacian eigenfunctions in nmr. i. a numerical tool. *Concepts in Magnetic Resonance Part A*, 32(4):277–301, 2008.
96. Denis S Grebenkov. Laplacian eigenfunctions in nmr. ii. theoretical advances. *Concepts in Magnetic Resonance Part A*, 34(5):264–296, 2009.
97. Matthew Grech-Sollars, Patrick W Hales, Keiko Miyazaki, Felix Raschke, Daniel Rodriguez, Martin Wilson, Simrandip K Gill, Tina Banks, Dawn E Saunders, Jonathan D Clayden, et al. Multi-centre reproducibility of diffusion mri parameters for clinical sequences in the brain. *NMR in Biomedicine*, 28(4):468–485, 2015.
98. Jiasong Guo, Leiming Wang, Yang Zhang, Jiawen Wu, Sezgi Arpag, Bo Hu, Beat A Imhof, Xinxia Tian, Bruce D Carter, Ueli Suter, et al. Abnormal junctions and permeability of myelin in pmp22-deficient nerves. *Annals of neurology*, 75(2):255–265, 2014.
99. Patric Hagmann, Lisa Jonasson, Philippe Maeder, Jean-Philippe Thiran, Van J Wedeen, and Reto Meuli. Understanding diffusion mr imaging techniques: from scalar diffusion-weighted imaging to diffusion tensor imaging and beyond. *Radio-graphics*, 26(suppl\_1):S205–S223, 2006.
100. Matt G Hall and Daniel C Alexander. Convergence and parameter choice for monte-carlo simulations of diffusion mri. *IEEE transactions on medical imaging*, 28(9):1354–1364, 2009.
101. KD Harkins and MD Does. Simulations on the influence of myelin water in diffusion-weighted imaging. *Physics in medicine and biology*, 61(13):4729, 2016.
102. Kevin D Harkins, Adrienne N Dula, and Mark D Does. Effect of intercompartmental water exchange on the apparent myelin water fraction in multiexponential t2 measurements of rat spinal cord. *Magnetic resonance in medicine*, 67(3):793–800, 2012.
103. E Heiervang, TEJ Behrens, CE Mackay, MD Robson, and H Johansen-Berg. Between session reproducibility and between subject variability of diffusion mr and tractography measures. *Neuroimage*, 33(3):867–877, 2006.
104. Christopher P Hess, Pratik Mukherjee, Eric T Han, Duan Xu, and Daniel B Vigneron. Q-ball reconstruction of multimodal fiber orientations using the spherical harmonic basis. *Magnetic Resonance in Medicine*, 56(1):104–117, 2006.
105. A Pasha Hosseinbor, Moo K Chung, Yu-Chien Wu, and Andrew L Alexander. Bessel fourier orientation reconstruction (bfor): An analytical diffusion propagator reconstruction for hybrid diffusion imaging and computation of q-space indices. *NeuroImage*, 64:650–670, 2013.
106. Scott N Hwang, Chih-Liang Chin, Felix W Wehrli, and David B Hackney. An image-based finite difference model for simulating restricted diffusion. *Magnetic Resonance in Medicine*, 50(2):373–382, 2003.
107. Giorgio M Innocenti. Exuberant development of connections, and its possible permissive role in cortical evolution. *Trends in neurosciences*, 18(9):397–402, 1995.
108. Giorgio M Innocenti. Network causality, axonal computations, and poffenberger. *Experimental Brain Research*, pages 1–9, 2017.
109. Giorgio M Innocenti and Roberto Caminiti. Axon diameter relates to synaptic bouton size: structural properties define computationally different types of cortical connections in primates. *Brain Structure and Function*, 222(3):1169–1177, 2017.
110. Giorgio M Innocenti, Roberto Caminiti, and Patrick R Hof. Fiber composition in the planum temporale sector of the corpus callosum in chimpanzee and human. *Brain structure and function*, 215(2):123–128, 2010.
111. Giorgio M Innocenti, Patricia Lehmann, and Jean-Christophe Houzel. Computational structure of visual callosal axons. *European Journal of Neuroscience*, 6(6):918–935, 1994.

112. Ileana O Jelescu, Jelle Veraart, Els Fieremans, and Dmitry S Novikov. Degeneracy in model parameter estimation for multi-compartmental diffusion in neuronal tissue. *NMR in Biomedicine*, 29(1):33–47, 2016.
113. Jens H Jensen, Joseph A Helpert, Anita Ramani, Hanzhang Lu, and Kyle Kaczynski. Diffusional kurtosis imaging: The quantification of non-gaussian water diffusion by means of magnetic resonance imaging. *Magnetic resonance in medicine*, 53(6):1432–1440, 2005.
114. Ben Jeurissen, Alexander Leemans, Jacques-Donald Tournier, Derek K Jones, and Jan Sijbers. Investigating the prevalence of complex fiber configurations in white matter tissue with diffusion magnetic resonance imaging. *Human brain mapping*, 34(11):2747–2766, 2013.
115. Ben Jeurissen, Jacques-Donald Tournier, Thijs Dhollander, Alan Connelly, and Jan Sijbers. Multi-tissue constrained spherical deconvolution for improved analysis of multi-shell diffusion mri data. *NeuroImage*, 103:411–426, 2014.
116. Enrico Kaden, Nathaniel D Kelm, Robert P Carson, Mark D Does, and Daniel C Alexander. Multi-compartment microscopic diffusion imaging. *NeuroImage*, 139:346–359, 2016.
117. Enrico Kaden, Thomas R Knösche, and Alfred Anwander. Parametric spherical deconvolution: Inferring anatomical connectivity using diffusion mr imaging. *NeuroImage*, 37(2):474–488, 2007.
118. J Kärger. Principles and applications of self-diffusion measurements by nuclear magnetic resonance. *Adv Magn Reson*, 12:1–89, 1988.
119. Jörg Kärger. Nmr self-diffusion studies in heterogeneous systems. *Advances in Colloid and Interface Science*, 23:129–148, 1985.
120. Bokkyu Kim and Carolee Winstein. Can neurological biomarkers of brain impairment be used to predict poststroke motor recovery? a systematic review. *Neurorehabilitation and neural repair*, 31(1):3–24, 2017.
121. Hengjun J Kim, Sang Joon Kim, Ho Sung Kim, Choong Gon Choi, Namkug Kim, Seungbong Han, Eun Hye Jang, Sun J Chung, and Chong Sik Lee. Alterations of mean diffusivity in brain white matter and deep gray matter in parkinson’s disease. *Neuroscience letters*, 550:64–68, 2013.
122. Jong Youl Kim, Joohyun Park, Ji Young Chang, Sa-Hyun Kim, and Jong Eun Lee. Inflammation after ischemic stroke: the role of leukocytes and glial cells. *Experimental neurobiology*, 25(5):241–251, 2016.
123. Gordon Kindlmann, Raul San Jose Estepar, Marc Niethammer, Steven Haker, and Carl-Fredrik Westin. Geodesic-loxodromes for diffusion tensor interpolation and difference measurement. In *International Conference on Medical Image Computing and Computer-Assisted Intervention*, pages 1–9. Springer, 2007.
124. Cheng Guan Koay, Lin-Ching Chang, John D Carew, Carlo Pierpaoli, and Peter J Basser. A unifying theoretical and algorithmic framework for least squares methods of estimation in diffusion tensor imaging. *J Magn Reson*, 182(1):115–125, 2006.
125. Philipp Koch, Robert Schulz, and Friedhelm C Hummel. Structural connectivity analyses in motor recovery research after stroke. *Annals of clinical and translational neurology*, 3(3):233–244, 2016.
126. Valery N Kornienko and Igor Nicolaevich Pronin. Demyelinating diseases of the central nervous system. *Diagnostic Neuroradiology*, pages 1033–1073, 2009.
127. Björn Lampinen, Filip Szczepankiewicz, Johan Mårtensson, Danielle van Westen, Pia C Sundgren, and Markus Nilsson. Neurite density imaging versus imaging of microscopic anisotropy in diffusion mri: a model comparison using spherical tensor encoding. *Neuroimage*, 147:517–531, 2017.
128. Samo Lasič, Markus Nilsson, Jimmy Lätt, Freddy Ståhlberg, and Daniel Topgaard. Apparent exchange rate mapping with diffusion mri. *Magnetic resonance in medicine*, 66(2):356–365, 2011.

129. Cornelia Laule, Irene M Vavasour, Shannon H Kolind, David KB Li, Tony L Troubsee, GR Wayne Moore, and Alex L MacKay. Magnetic resonance imaging of myelin. *Neurotherapeutics*, 4(3):460–484, 2007.
130. Denis Le Bihan and E Breton. Imagerie de diffusion in-vivo par résonance magnétique nucléaire. *Comptes-Rendus de l'Académie des Sciences*, 93(5):27–34, 1985.
131. Jing-Huei Lee and Charles S Springer. Effects of equilibrium exchange on diffusion-weighted nmr signals: The diffusigraphic shutter-speed. *Magnetic resonance in medicine*, 49(3):450–458, 2003.
132. Ives R Levesque and G Bruce Pike. Characterizing healthy and diseased white matter using quantitative magnetization transfer and multicomponent t2 relaxometry: A unified view via a four-pool model. *Magnetic resonance in medicine*, 62(6):1487–1496, 2009.
133. Daniel Liewald, Robert Miller, Nikos Logothetis, Hans-Joachim Wagner, and Almut Schüz. Distribution of axon diameters in cortical white matter: an electron-microscopic study on three human brains and a macaque. *Biological cybernetics*, 108(5):541–557, 2014.
134. Mu Lin, Hongjian He, Qiqi Tong, Qiuping Ding, Xu Yan, Thorsten Feiweier, and Jianhui Zhong. Effect of myelin water exchange on dti-derived parameters in diffusion mri: Elucidation of te dependence. *Magnetic Resonance in Medicine*, 2017.
135. Ying-Chia Lin, Alessandro Daducci, Djalel Eddine Meskaldji, Jean-Philippe Thiran, Patrik Michel, Reto Meuli, Gunnar Krueger, Gloria Menegaz, and Cristina Granziera. Quantitative analysis of myelin and axonal remodeling in the uninjured motor network after stroke. *Brain connectivity*, 5(7):401–412, 2015.
136. Martin Lotze, Jochen Markert, Paul Sauseng, Julia Hoppe, Christian Plewnia, and Christian Gerloff. The role of multiple contralesional motor areas for complex hand movements after internal capsular lesion. *Journal of Neuroscience*, 26(22):6096–6102, 2006.
137. Alex Mackay, Kenneth Whittall, Julian Adler, David Li, Donald Paty, and Douglas Graeb. In vivo visualization of myelin water in brain by magnetic resonance. *Magnetic Resonance in Medicine*, 31(6):673–677, 1994.
138. S Munoz Maniega, ME Bastin, PA Armitage, AJ Farrall, TK Carpenter, PJ Hand, V Cvorovic, CS Rivers, and JM Wardlaw. Temporal evolution of water diffusion parameters is different in grey and white matter in human ischaemic stroke. *Journal of Neurology, Neurosurgery & Psychiatry*, 75(12):1714–1718, 2004.
139. Stefano Marengo, Robert Rawlings, Gustavo K Rohde, Alan S Barnett, Robyn A Honea, Carlo Pierpaoli, and Daniel R Weinberger. Regional distribution of measurement error in diffusion tensor imaging. *Psychiatry Research: Neuroimaging*, 147(1):69–78, 2006.
140. David W McCall, Dean C Douglass, and Ernest W Anderson. Self-diffusion studies by means of nuclear magnetic resonance spin-echo techniques. *Berichte der Bunsengesellschaft für physikalische Chemie*, 67(3):336–340, 1963.
141. Sylvain L Merlet and Rachid Deriche. Continuous diffusion signal, eap and odF estimation via compressive sensing in diffusion mri. *Medical image analysis*, 17(5):556–572, 2013.
142. Partha P Mitra and Bertrand I Halperin. Effects of finite gradient-pulse widths in pulsed-field-gradient diffusion measurements. *Journal of Magnetic Resonance, Series A*, 113(1):94–101, 1995.
143. ME Moseley, Y Cohen, J Mintorovitch, L Chileuitt, H Shimizu, J Kucharczyk, MF Wendland, and PR Weinstein. Early detection of regional cerebral ischemia in cats: comparison of diffusion-and t2-weighted mri and spectroscopy. *Magnetic resonance in medicine*, 14(2):330–346, 1990.

144. James M Mountz, Hong-Gang Liu, and Georg Deutsch. Neuroimaging in cerebrovascular disorders: measurement of cerebral physiology after stroke and assessment of stroke recovery. In *Seminars in nuclear medicine*, volume 33, pages 56–76. Elsevier, 2003.
145. JS Murday and Robert M Cotts. Self-diffusion coefficient of liquid lithium. *The Journal of Chemical Physics*, 48(11):4938–4945, 1968.
146. Gemma L Nedjati-Gilani, Torben Schneider, Matt G Hall, Niamh Cawley, Ioana Hill, Olga Ciccarelli, Ivana Drobnjak, Claudia AM Gandini Wheeler-Kingshott, and Daniel C Alexander. Machine learning based compartment models with permeability for white matter microstructure imaging. *NeuroImage*, 150:119–135, 2017.
147. CH Neuman. Spin echo of spins diffusing in a bounded medium. *The Journal of Chemical Physics*, 60(11):4508–4511, 1974.
148. M Nilsson, H Hagslätt, D Van Westen, R Wirestam, F Ståhlberg, and J Lätt. A mechanism for exchange between intraaxonal and extracellular water: Permeable nodes of ranvier. In *Proc Intl Soc Mag Reson Med*, volume 18, page 1570, 2010.
149. Markus Nilsson, Erik Alerstam, Ronnie Wirestam, F Sta, Sara Brockstedt, Jimmy Lätt, et al. Evaluating the accuracy and precision of a two-compartment karger model using monte carlo simulations. *Journal of Magnetic Resonance*, 206(1):59–67, 2010.
150. Markus Nilsson, Samo Lasič, Ivana Drobnjak, Daniel Topgaard, and Carl-Fredrik Westin. Resolution limit of cylinder diameter estimation by diffusion mri: The impact of gradient waveform and orientation dispersion. *NMR in Biomedicine*, 30(7), 2017.
151. Markus Nilsson, Jimmy Lätt, Emil Nordh, Ronnie Wirestam, Freddy Ståhlberg, and Sara Brockstedt. On the effects of a varied diffusion time in vivo: is the diffusion in white matter restricted? *Magnetic resonance imaging*, 27(2):176–187, 2009.
152. Markus Nilsson, Jimmy Lätt, Danielle van Westen, Sara Brockstedt, Samo Lasič, Freddy Ståhlberg, and Daniel Topgaard. Noninvasive mapping of water diffusional exchange in the human brain using filter-exchange imaging. *Magnetic resonance in medicine*, 69(6):1572–1580, 2013.
153. Lipeng Ning, Frederik Laun, Yaniv Gur, Edward VR DiBella, Samuel Deslauriers-Gauthier, Thinhinane Megherbi, Aurobrata Ghosh, Mauro Zucchelli, Gloria Menegaz, Rutger Fick, et al. Sparse reconstruction challenge for diffusion mri: Validation on a physical phantom to determine which acquisition scheme and analysis method to use? *Medical image analysis*, 26(1):316–331, 2015.
154. David G Norris. The effects of microscopic tissue parameters on the diffusion weighted magnetic resonance imaging experiment. *NMR in Biomedicine*, 14(2):77–93, 2001.
155. Dmitry S Novikov, Jens H Jensen, Joseph A Helpert, and Els Fieremans. Revealing mesoscopic structural universality with diffusion. *Proceedings of the National Academy of Sciences*, 111(14):5088–5093, 2014.
156. Silvia Obertino, Lorenza Brusini, I Boscolo Galazzo, Mauro Zucchelli, Cristina Granziera, Marco Cristani, and Gloria Menegaz. Shore-based biomarkers allow patient versus control classification in stroke. In *Biomedical Imaging (ISBI), 2016 IEEE 13th International Symposium on*, pages 1097–1100. IEEE, 2016.
157. E Ozarslan, C Koay, TM Shepherd, SJ Blackb, and PJ Basser. Simple harmonic oscillator based reconstruction and estimation for three-dimensional q-space mri. 2009.
158. E Özarslan, CG Koay, and PJ Basser. Simple harmonic oscillator based estimation and reconstruction for one-dimensional q-space mr. In *Proc. Intl. Soc. Mag. Reson. Med*, volume 16, page 35, 2008.

159. E. Ozarslan, C.G. Koay, T.M. Shepherd, M.E. Komlosh, M.O. Irfanoglu, C. Pierpaoli, and P.J. Basser. Mean apparent propagator (map) mri: A novel diffusion imaging method for mapping tissue microstructure. *NeuroImage*, 78:16 – 32, 2013.
160. Yelda Ozsunar, P Ellen Grant, Thierry AGM Huisman, Pamela W Schaefer, Ona Wu, A Gregory Sorensen, Walter J Koroshetz, and R Gilberto Gonzalez. Evolution of water diffusion and anisotropy in hyperacute stroke: significant correlation between fractional anisotropy and t2. *American journal of neuroradiology*, 25(5):699–705, 2004.
161. Michael Paquette, Sylvain Merlet, Rachid Deriche, and Maxime Descoteaux. Dsi 101: Better odds for free! page 7018, 2014.
162. Richard E Passingham, Klaas E Stephan, and Rolf Kötter. The anatomical basis of functional localization in the cortex. *Nature Reviews Neuroscience*, 3(8):606–616, 2002.
163. T Paus, DL Collins, AC Evans, G Leonard, B Pike, and A Zijdenbos. Maturation of white matter in the human brain: a review of magnetic resonance studies. *Brain research bulletin*, 54(3):255–266, 2001.
164. Tomáš Paus. Growth of white matter in the adolescent brain: myelin or axon? *Brain and cognition*, 72(1):26–35, 2010.
165. Sharon Peled. New perspectives on the sources of white matter dti signal. *IEEE transactions on medical imaging*, 26(11):1448–1455, 2007.
166. Gaby S Pell, Regula S Briellmann, Anthony B Waites, David F Abbott, David P Lewis, and Graeme D Jackson. Optimized clinical t2 relaxometry with a standard cpng sequence. *Journal of Magnetic Resonance Imaging*, 23(2):248–252, 2006.
167. Josef Pfeuffer, Ulrich Flögel, Wolfgang Dreher, and Dieter Leibfritz. Restricted diffusion and exchange of intracellular water: theoretical modelling and diffusion time dependence of 1h nmr measurements on perfused glial cells. *NMR in Biomedicine*, 11(1):19–31, 1998.
168. Carlo Pierpaoli, Alan Barnett, Sinisa Pajevic, Robert Chen, LaRoy Penix, Anette Virta, and Peter Basser. Water diffusion changes in wallerian degeneration and their dependence on white matter architecture. *Neuroimage*, 13(6):1174–1185, 2001.
169. Joana Pinto, João Jorge, Inês Sousa, Pedro Vilela, and Patrícia Figueiredo. Fourier modeling of the bold response to a breath-hold task: Optimization and reproducibility. *Neuroimage*, 135:223–231, 2016.
170. Jim Pipe. Pulse sequences for diffusion-weighted mri. *Diffusion MRI: From quantitative measurement to in-vivo neuroanatomy*, pages 12–35, 2009.
171. Wen Qin, Chun Shui Yu, Fan Zhang, Xiang Ying Du, Heng Jiang, Yu Xia Yan, and Kun Cheng Li. Effects of echo time on diffusion quantification of brain white matter at 1.5 t and 3.0 t. *Magnetic resonance in medicine*, 61(4):755–760, 2009.
172. James D Quirk, G Larry Bretthorst, Timothy Q Duong, Avi Z Snyder, Charles S Springer, Joseph JH Ackerman, and Jeffrey J Neil. Equilibrium water exchange between the intra-and extracellular spaces of mammalian brain. *Magnetic resonance in medicine*, 50(3):493–499, 2003.
173. David Raffelt, J-Donald Tournier, Stephen Rose, Gerard R Ridgway, Robert Henderson, Stuart Crozier, Olivier Salvado, and Alan Connelly. Apparent fibre density: a novel measure for the analysis of diffusion-weighted magnetic resonance images. *Neuroimage*, 59(4):3976–3994, 2012.
174. David G Regan and Philip W Kuchel. Mean residence time of molecules diffusing in a cell bounded by a semi-permeable membrane: Monte carlo simulations and an expression relating membrane transition probability to permeability. *European Biophysics Journal*, 29(3):221–227, 2000.
175. Anne K Rehme and Christian Grefkes. Cerebral network disorders after stroke: evidence from imaging-based connectivity analyses of active and resting brain states in humans. *The Journal of physiology*, 591(1):17–31, 2013.

176. Axel Riecker, Klaus Gröschel, Hermann Ackermann, Sonja Schnaudigel, Jan Kas-subek, and Andreas Kastrup. The role of the unaffected hemisphere in motor recovery after stroke. *Human brain mapping*, 31(7):1017–1029, 2010.
177. Baldwin Robertson. Spin-echo decay of spins diffusing in a bounded region. *Physical review*, 151(1):273, 1966.
178. WAH Rushton. A theory of the effects of fibre size in medullated nerve. *The Journal of physiology*, 115(1):101–122, 1951.
179. Judith D Schaechter, Zachary P Fricker, Katherine L Perdue, Karl G Helmer, Mark G Vangel, Douglas N Greve, and Nikos Makris. Microstructural status of ip-silesional and contralesional corticospinal tract correlates with motor skill in chronic stroke patients. *Human brain mapping*, 30(11):3461–3474, 2009.
180. B. Scherrer and S.K. Warfield. Why multiple b-values are required for multi-tensor models. evaluation with a constrained log-euclidean model. In *Biomedical Imaging: From Nano to Macro, 2010 IEEE International Symposium on*, pages 1389–1392, 2010.
181. Robert Schulz, Christian Gerloff, and Friedhelm C Hummel. Non-invasive brain stimulation in neurological diseases. *Neuropharmacology*, 64:579–587, 2013.
182. Pabitra N Sen and Peter J Basser. A model for diffusion in white matter in the brain. *Biophysical journal*, 89(5):2927–2938, 2005.
183. Weijun Situ, Haiyan Liao, Bin Zhou, Xibin Xia, and Changlian Tan. Application of diffusion tensor imaging for detecting structural changes in the brain of schizophrenic patients. *International journal of psychiatry in clinical practice*, 19(2):114–118, 2015.
184. C.H. Sotak. The role of diffusion tensor imaging in the evaluation of ischemic brain injury a review. *NMR in Biomedicine*, 15(7-8):561–569, 2002.
185. Stamatios N Sotiropoulos, Saad Jbabdi, Junqian Xu, Jesper L Andersson, Steen Moeller, Edward J Auerbach, Matthew F Glasser, Moises Hernandez, Guillermo Sapiro, Mark Jenkinson, et al. Advances in diffusion MRI acquisition and processing in the human connectome project. *Neuroimage*, 80:125–143, 2013.
186. Greg J Stanisz, Graham A Wright, R Mark Henkelman, and Aaron Szafer. An analytical model of restricted diffusion in bovine optic nerve. *Magnetic Resonance in Medicine*, 37(1):103–111, 1997.
187. Glenn T Stebbins, David L Nyenhuis, Changsheng Wang, Jennifer L Cox, Sally Freels, Katherine Bangen, Kumar Sripathirathan, Michael Moseley, David A Turner, John DE Gabrieli, et al. Gray matter atrophy in patients with ischemic stroke with cognitive impairment. *Stroke*, 39(3):785–793, 2008.
188. Edward O Stejskal and John E Tanner. Spin diffusion measurements: spin echoes in the presence of a time-dependent field gradient. *The journal of chemical physics*, 42(1):288–292, 1965.
189. Andrew J Steven, Jiachen Zhuo, and Elias R Melhem. Diffusion kurtosis imaging: an emerging technique for evaluating the microstructural environment of the brain. *American journal of roentgenology*, 202(1):W26–W33, 2014.
190. Wendy A Stewart, Alex L Mackay, Kenneth P Whittall, GR Moore, and Donald W Paty. Spin-spin relaxation in experimental allergic encephalomyelitis. analysis of cpmg data using a non-linear least squares method and linear inverse theory. *Magnetic resonance in medicine*, 29(6):767–775, 1993.
191. Aaron Szafer, Jianhui Zhong, and John C Gore. Theoretical model for water diffusion in tissues. *Magnetic resonance in medicine*, 33(5):697–712, 1995.
192. Ali Tabesh, Jens H Jensen, Babak A Ardekani, and Joseph A Helpert. Estimation of tensors and tensor-derived measures in diffusional kurtosis imaging. *Magnetic resonance in medicine*, 65(3):823–836, 2011.

193. Matthew J Tait, Samira Saadoun, B Anthony Bell, and Marios C Papadopoulos. Water movements in the brain: role of aquaporins. *TRENDS in Neurosciences*, 31(1):37–43, 2008.
194. John E Tanner. Use of the stimulated echo in nmr diffusion studies. *The Journal of Chemical Physics*, 52(5):2523–2526, 1970.
195. John E Tanner and Edward O Stejskal. Restricted self-diffusion of protons in colloidal systems by the pulsed-gradient, spin-echo method. *The Journal of Chemical Physics*, 49(4):1768–1777, 1968.
196. Rudrapatna U S Witzel T Tax, C M and D K Jones. Disentangling in two dimensions in the living human brain: feasibility of relaxometry-diffusometry using ultra-strong gradients. In *ISMRM*, Honolulu, Hawaii, USA, 2017.
197. Simone Tomasi, Roberto Caminiti, and Giorgio M Innocenti. Areal differences in diameter and length of corticofugal projections. *Cerebral Cortex*, 22(6):1463–1472, 2012.
198. Henry C Torrey. Bloch equations with diffusion terms. *Physical review*, 104(3):563, 1956.
199. J-Donald Tournier, Fernando Calamante, and Alan Connelly. Robust determination of the fibre orientation distribution in diffusion mri: non-negativity constrained super-resolved spherical deconvolution. *NeuroImage*, 35(4):1459–1472, 2007.
200. J-Donald Tournier, Fernando Calamante, David G Gadian, and Alan Connelly. Direct estimation of the fiber orientation density function from diffusion-weighted mri data using spherical deconvolution. *NeuroImage*, 23(3):1176–1185, 2004.
201. J-Donald Tournier, Chun-Hung Yeh, Fernando Calamante, Kuan-Hung Cho, Alan Connelly, and Ching-Po Lin. Resolving crossing fibres using constrained spherical deconvolution: validation using diffusion-weighted imaging phantom data. *Neuroimage*, 42(2):617–625, 2008.
202. David S Tuch. Q-ball imaging. *Magnetic resonance in medicine*, 52(6):1358–1372, 2004.
203. David S. Tuch, Timothy G. Reese, Mette R. Wiegell, Nikos Makris, John W. Belliveau, and Van J. Wedeen. High angular resolution diffusion imaging reveals intravoxel white matter fiber heterogeneity. *Magnetic Resonance in Medicine*, 48(4):577–582, 2002.
204. Yuji Ueno, Michael Chopp, Li Zhang, Benjamin Buller, Zhongwu Liu, Norman L Lehman, Xian Shuang Liu, Yi Zhang, Cynthia Roberts, and Zheng Gang Zhang. Axonal outgrowth and dendritic plasticity in the cortical peri-infarct area after experimental stroke. *Stroke*, 43(8):2221–2228, 2012.
205. P Vangelder, D DesPres, PCM Vanzijl, and CTW Moonen. Evaluation of restricted diffusion in cylinders. phosphocreatine in rabbit leg muscle. *Journal of Magnetic Resonance, Series B*, 103(3):255–260, 1994.
206. Irene M Vavasour, Kenneth P Whittall, Alex L Mackay, David KB Li, Galina Vorobeychik, and Donald W Paty. A comparison between magnetization transfer ratios and myelin water percentages in normals and multiple sclerosis patients. *Magnetic resonance in medicine*, 40(5):763–768, 1998.
207. Tonny V Veenith, Eleanor Carter, Julia Grossac, Virginia FJ Newcombe, Joanne G Outtrim, Victoria Lupson, Guy B Williams, David K Menon, and Jonathan P Coles. Inter subject variability and reproducibility of diffusion tensor imaging within and between different imaging sessions. *PloS one*, 8(6):e65941, 2013.
208. Jelle Veraart, Dmitry S Novikov, and Els Fieremans. Te dependent diffusion imaging (teddi) distinguishes between compartmental t2 relaxation times. *NeuroImage*, 2017.
209. AS Verkman. Water permeability measurement in living cells and complex tissues. *The Journal of membrane biology*, 173(2):73–87, 2000.



210. Christian Vollmar, Jonathan O’muircheartaigh, Gareth J Barker, Mark R Symms, Pamela Thompson, Veena Kumari, John S Duncan, Mark P Richardson, and Matthias J Koepp. Identical, but not the same: intra-site and inter-site reproducibility of fractional anisotropy measures on two 3.0 t scanners. *Neuroimage*, 51(4):1384–1394, 2010.
211. Elisabeth AH von dem Hagen and R Mark Henkelman. Orientational diffusion reflects fiber structure within a voxel. *Magnetic Resonance in Medicine*, 48(3):454–459, 2002.
212. Jun Yi Wang, Hervé Abdi, Khamid Bakhadirov, Ramon Diaz-Arrastia, and Michael D Devous. A comprehensive reliability assessment of quantitative diffusion tensor tractography. *Neuroimage*, 60(2):1127–1138, 2012.
213. Qing Wang, Xian Nan Tang, and Midori A Yenari. The inflammatory response in stroke. *Journal of neuroimmunology*, 184(1):53–68, 2007.
214. NS Ward, MM Brown, AJ Thompson, and RSJ Frackowiak. Neural correlates of motor recovery after stroke: a longitudinal fmri study. *Brain*, 126(11):2476–2496, 2003.
215. Van J Wedeen, Patric Hagmann, Wen-Yih Isaac Tseng, Timothy G Reese, and Robert M Weisskoff. Mapping complex tissue architecture with diffusion spectrum magnetic resonance imaging. *Magnetic resonance in medicine*, 54(6):1377–1386, 2005.
216. Van J Wedeen, Patric Hagmann, Wen-Yih Isaac Tseng, Timothy G Reese, and Robert M Weisskoff. Mapping complex tissue architecture with diffusion spectrum magnetic resonance imaging. *Magnetic resonance in medicine*, 54(6):1377–1386, 2005.
217. Van J Wedeen, Patric Hagmann, Wen-Yih Isaac Tseng, Timothy G Reese, and Robert M Weisskoff. Mapping complex tissue architecture with diffusion spectrum magnetic resonance imaging. *Magnetic resonance in medicine*, 54(6):1377–1386, 2005.
218. VJ Wedeen, TG Reese, DS Tuch, MR Weigel, JG Dou, RM Weiskoff, and D Chessler. Mapping fiber orientation spectra in cerebral white matter with fourier-transform diffusion mri. In *Proceedings of the 8th Annual Meeting of ISMRM, Denver*, page 82, 2000.
219. Cornelius Weiller, François Chollet, Karl J Friston, Richard JS Wise, and Richard SJ Frackowiak. Functional reorganization of the brain in recovery from striatocapsular infarction in man. *Annals of neurology*, 31(5):463–472, 1992.
220. C-F Westin, Stephan E Maier, Hatsuho Mamata, Arya Nabavi, Ferenc A Jolesz, and Ron Kikinis. Processing and visualization for diffusion tensor mri. *Medical image analysis*, 6(2):93–108, 2002.
221. Philip SJ Weston, Ivor JA Simpson, Natalie S Ryan, Sebastien Ourselin, and Nick C Fox. Diffusion imaging changes in grey matter in alzheimers disease: a potential marker of early neurodegeneration. *Alzheimer’s research & therapy*, 7(1):47, 2015.
222. Kenneth P Whittall, Alex L Mackay, Douglas A Graeb, Robert A Nugent, David KB Li, and Donald W Paty. In vivo measurement of t2 distributions and water contents in normal human brain. *Magnetic resonance in medicine*, 37(1):34–43, 1997.
223. Yu-Chien Wu and Andrew L Alexander. Hybrid diffusion imaging. *NeuroImage*, 36(3):617–629, 2007.
224. Junzhong Xu, Hua Li, Kevin D Harkins, Xiaoyu Jiang, Jingping Xie, Hakmook Kang, Mark D Does, and John C Gore. Mapping mean axon diameter and axonal volume fraction by mri using temporal diffusion spectroscopy. *NeuroImage*, 103:10–19, 2014.
225. H. Zhang, Schneider T., C.A.N. Wheeler-Kingshott, and D.C. Alexander. NODDI: Practical in vivo neurite orientation dispersion and density imaging of the human brain. *Neuroimage*, 61(4):1000–1016, 2012.

226. Hui Zhang, Penny L Hubbard, Geoff JM Parker, and Daniel C Alexander. Axon diameter mapping in the presence of orientation dispersion with diffusion mri. *Neuroimage*, 56(3):1301–1315, 2011.
227. Hui Zhang, Torben Schneider, Claudia A Wheeler-Kingshott, and Daniel C Alexander. Noddi: practical in vivo neurite orientation dispersion and density imaging of the human brain. *Neuroimage*, 61(4):1000–1016, 2012.
228. JR Zimmerman and W E. Brittin. Nuclear magnetic resonance studies in multiple phase systems: lifetime of a water molecule in an adsorbing phase on silica gel. *The Journal of Physical Chemistry*, 61(10):1328–1333, 1957.
229. Mauro Zucchelli, Lorenza Brusini, C Andrés Méndez, Alessandro Daducci, Cristina Granziera, and Gloria Menegaz. What lies beneath? diffusion eap-based study of brain tissue microstructure. *Medical image analysis*, 32:145–156, 2016.
230. Mauro Zucchelli, Andrés Méndez, C, and Gloria Menegaz. Multi-tensor mapmri: how to estimate microstructural information from crossing fibers. In Nassir Navab, Joachim Hornegger, WilliamM. Wells, and AlejandroF. Frangi, editors, *Inproceedings of "Medical Image Computing and Computer Assisted Intervention (MICCAI), Workshop on Computational Diffusion MRI (CDMRI)*, Lecture Notes in Computer Science. Springer International Publishing, 2015.

---

## Acknowledgements

Towards the end of this work there are several people to whom my gratitude goes because without them I would not be where and especially as I am now.

The first thanks goes to my supervisor, Gloria. The hours spent looking at a multitude of signal curves to discover the secrets of permeability in the dMRI have taught me the tenacity and perseverance that come from loving our own work. Your example has always encouraged me to give value and cultivate my skills, pushing me to always look beyond, turning obstacles into challenges and not into problems.

I am also very grateful to Prof. Markus Nilsson, I particularly appreciated the free availability, patience and humility in listening and teaching, not at all obvious. An affectionate thought goes also to your family that welcomed me so warmly.

Thanks also to Prof. Rachid Deriche, without your hospitality I would not have been able to discover the beauty of a science that has no geographical boundaries and rather enriches itself with diversity.

To my colleagues Mauro, Ilaria, Silvia that I learned to know and appreciate working side by side every day, thank you because without your support this job would have been certainly more difficult. Moreover, this work would have been even less cheerful if I had not shared spaces, lunches, coffee and especially laughter with Eda, Gabriele, Francesca, Alberto, Federica, Michele, Alberto, Vincenzo and Samuele and Silvia.

To Ginevra, Chiara and Elisa I owe an excuse as well as a thank you... I know that among the sacrifices that my choices have often involved, you have often ended up among them and I'm sorry about that. Thank you for being better friends for me than I deserve! Thanks Ginny because the special place you have in my heart you never tire of cultivating it in a totally disinterested way. Thanks Chiara because you can always surprise me with your love. Thanks Elisa because the communion of ideals in diversity of character makes me grow. And to Chiara and Chiara, because even if we do not often see each other, two words are enough for seeming that we have left each other for no more than a moment.

And to Bax, Deto, Pippo, Cesco, Silvia, J, Otty, Giulia, Gio, Carlo, Cate, Lillo, Ciccio, Tommy, Kazzho and all friends. I did not write all the names that I have in mind: I could stay here to make an infinite list for so many people with whom I share my world and that color it. Thank you.

I have met many of them thanks to scouting, and I'm still meeting many others wonderful people thanks to it. Therefore, thanks to all these old and younger road mates, with uniform and without, with whom I'm lucky to walk thanks to mutual trust and above all thanks to Someone.

But we know that the fundamental people are held last. Even only because they will be the only ones to have the patience to read until the end! I had the grace to grow up in a fairly large family. I felt obliged to thank them one by one starting from each uncle and cousin and arriving to my grandparents and Fabios family. I can not or I should really add a chapter to this thesis. So I will thank them simply because you have always made me feel loved, in one way or another, and although I do not see each other every day I always carry your affection with me. Thanks Ambra and Cristian, because despite being so different I think I have never again received such a beautiful gift in my life of you two brothers. To Hicham, because you are another brother and you take care of her and of my two beautiful nephews who bring so much joy in our lives! To Elisa, because instead you take care of him and I want to place my trust in you. But above all thanks to my father and my mother. Thank you Dad because you're not a chatterer, you're a rock, a person helpful until the abnegation, with a look free of prejudice and arrogance. Thank you Mom because you are instead a chatterer, you are the soul of the family, honest and sincere, you would throw yourself on a fire for all of us despite we often do not deserve it. I repeat, you are fundamental. I owe also you my excuse as well as my thanks. I am sorry to being not able to show you my love for you how you would hope. I love you so much.

And finally to my husband. I should write a book. I limit myself to thanking you for bringing me in your life as your bride. With the grace of Christ, you promise to be always faithful, in joy and pain, in health and in sickness, and to love and honor me every day of your life. Not yesterday neither tomorrow but today, always. You gained a bit of this thesis!

---

## Sommario

L'imaging di risonanza magnetica in diffusione (dMRI) consente una caratterizzazione in vivo non invasiva del tessuto. Il discernimento di ciascuna proprietà microstrutturale riflessa sul segnale dMRI totale è uno degli argomenti più caldi del settore. Le tecniche di ricostruzione dMRI si basano su ipotesi sul modello del segnale e considerano gli assoni neuronali come cilindri impermeabili. Tuttavia, le interazioni con l'ambiente sono una caratteristica della vita biologica e avviene uno scambio d'acqua attraverso le membrane cellulari. La mielina avvolge gli assoni con più strati costituendo una barriera che modula lo scambio tra l'assone e il tessuto extracellulare. A causa del breve tempo di rilassamento trasversale ( $T_2$ ) dell'acqua intrappolata tra gli strati, il contributo della mielina al segnale di diffusione è spesso trascurato. Questa tesi punta a esplorare come lo scambio influenza il segnale dMRI e come questo può essere informativo sulla struttura della mielina. Abbiamo anche cercato di esplorare come le recenti tecniche di ricostruzione del segnale dMRI potrebbero essere applicate in clinica, proponendo una strategia per indagare il potenziale dei descrittori tissutali derivati come biomarcatori.

Il primo obiettivo della tesi è stato affrontato effettuando simulazioni Monte Carlo di un sistema con tre compartimenti: intra-assonale, spirale mielinica e extra-assonale. Gli esperimenti hanno mostrato che il tempo di scambio tra i compartimenti intra ed extra-assonale era inferiore al secondo (e quindi possibilmente osservabile) per geometrie con piccolo diametro assonale e basso numero di involucri come nel cervello del bambino e nelle malattie demielinizzanti. Il secondo obiettivo della tesi è stato raggiunto caratterizzando gli indici derivati dalla ricostruzione e stima basate sull'oscillatore armonico semplice tridimensionale (3D-SHORE) applicate all'ictus. Sono state eseguite le analisi basate sul tratto coinvolgendo le reti motorie e basate sulle regioni in sostanza grigia (GM). Gli indici 3D-SHORE si sono rivelati sensibili alla plasticità sia in sostanza bianca (WM) che in GM, evidenziando la loro potenzialità come biomarcatori nell'ictus.

Lo studio complessivo può considerarsi il punto di partenza per una futura indagine sull'interdipendenza di diversi fenomeni come scambio e rilassamento correlati agli indici dMRI stabiliti. Questo è utile per l'accurata interpretazione dei dati dMRI in tessuti eterogenei e in diverse condizioni fisiologiche.